Spatial and subcellular gene expression patterns in myogenic differentiation and muscle pathology

Katarzyna Maria Chwalenia

Department of Paediatrics

St Cross College, University of Oxford

Thesis submitted for the degree of

Doctor of Philosophy

Trinity Term 2024

Declaration

The work presented in this thesis was undertaken in Professor Matthew Wood's laboratory at the Department of Paediatrics, University of Oxford, between 2020 and 2024. I, Katarzyna Chwalenia, hereby declare that all work presented is my own with the following exceptions. Assistance in mouse tissue harvest of animals utilised in Chapter I was provided by Nicole Hemmer and Ambra Speciale. Assistance in preparations of tissue cryosections in Chapters I and II was provided by Viviyun Feng, Nicole Hemmer and Nina Ahlskog. Serum miRNA analysis in Chapter I was performed by Viviyun Feng. Intravenous injections and mouse tissue harvest of animals utilised in Chapter I were performed by Yulia Lomonosova. The dystrophin western blot and correlation analyses in Chapter II were performed in collaboration with Dr Jacopo Oieni. Data collection and preparation of Figure 1 in Chapter III was performed by Dr Thomas Roberts and Dr Sofia Stenler (unpublished manuscript). This work has not been submitted for any other degree at this university or any other institute of learning. My thesis includes text excerpts and figures from my first-author and co-authored articles published throughout my DPhil as listed in section 8.1. Where required, permission from individual journals was obtained.

Acknowledgments

First, I would like to express my gratitude to Prof Matthew Wood for accommodating me in his lab throughout my DPhil journey. I'm grateful for your support in building a unique research skill set which has empowered me to develop my own scientific ideas. I’m especially thankful to Dr Thomas Roberts for being my day-to-day guide, supervisor, and mentor throughout the years. Thank you for your guidance in technical, philosophical, practical aspects of science and research. I deeply appreciate all the opportunities to engage with the experts in the field you have provided. Thank you for cultivating an encouraging atmosphere, that helped me grow both professionally and personally. I’m grateful to be the part of the RNA medicine team.

Thank you to my generous funders, who turned my long-lasting ambition of pursuing a PhD into reality: the Clarendon Fund, St Cross College (Juel-Jensen scholarship), and Medical Research Council. I’m particularly grateful to Medical Research Council for supporting my visiting position at Prof. Eric Wang lab (University of Florida) during second year of the program. This 2-month learning experience had a fundamental impact on the direction and quality of my research.

Thank you to the whole Wood lab – past and present members who complimented my research journey with and incredible atmosphere of collaboration and support. I’m grateful for all personal and professional advice which shaped my priorities and ambitions. Thank you to Britt Hanson who supported and inspired me initially as a colleague, and now as a long-lasting friend. I’m very grateful for all the memories we keep building together. Thank you to Ambra Speciale for unwavering support and tons of help in and outside of the lab. Thank you for empowering me at all stages of my journey. Thank you to Amarjit Bhomra for the incredible amount of the practical and personal support through the years. You are the pillar of the group, providing the most essential day-to-day guidance on (literally) everything. Thank you to Nina Ahlskog, Nicole Hemmer, Viviyun Feng, Yulia Lomonosova

and Jacopo Oieni for supporting my experimental work. Thank you to other students: Ania Kordala, Dora Markati, Jess Stoodley for your companionship and motivation. Thank you to all post-docs in the Wood lab for stimulating conversations and encouragement in pursuing my research goals. To the members of Wang lab – Prof Eric Wang, Chase Kelley, Belinda Pinto, Kiril Poukalov for welcoming me to your space and taking the time to teach me the techniques that greatly advanced my research. Thank you to all the friends outside of the lab that were central to my Oxford student experience. I am grateful for each formal dinner, college lunch, ball, and other events we have had a chance to enjoy together. Thank you to my friends of more than 14 years: Agata, Agata and Karolina who supported me throughout all the major milestones of my life. I am grateful for your constant motivation and the many moments of recharge that keep me going strong.

Thank you to my family: Mariola, Stanisław, Krzysztof and Barbara for the biggest support (both financial and emotional) and endless motivation. Thank you for instilling in me the persistence and strong work ethics that guided me through my doctoral degree. I am grateful that you have enabled me to pursue the highest degree in the institution of my choice. Thank you to my grandma Helena for your wisdom, generosity, and unconditional support that is as strong today as it was when you first walked me to primary school. Finally, I am deeply grateful to my partner Lucas Mangas Araujo, for bringing me laughs, joy and comfort throughout my studies. Thank you for the understanding and motivation that pushed me in the critical moments of my studies. My Oxford experience would not be the same without you.

Abstract

Duchenne muscular dystrophy (DMD) is a debilitating muscle-wasting disorder caused by lack of dystrophin protein. Promising dystrophin-restoration therapies such as gene editing using the CRISPR-Cas9 system and antisense oligonucleotide-mediated exon skipping using peptide-phosphorodiamidate morpholino oligomers (PPMOs) are currently in development. The efficacy of these approaches is typically assessed in terms of the amount of dystrophin restored, while correct sarcolemmal localisation of the protein has largely been assumed.

Our prior work revealed that CRISPR-Cas9-mediated exon excision results in a spatially restricted, patchy pattern of dystrophin expression. In this thesis, a novel DMD mouse model (*mdx52-Xist*$^{\Delta hs}$) was developed, characterised by chimeric myofibres, consisting of both dystrophin-expressing and non-dystrophin-expressing nuclei as a consequence of skewed X-chromosome inactivation. Non-uniform dystrophin localisation along myofibres of *mdx52-Xist*$^{\Delta hs}$ animals mirrors the pattern observed in CRISPR-Cas9-treated animals. These observations are consistent with the myonuclear domain theory which posits that every nucleus in syncytial myofiber controls a specific amount of cytoplasm around it. Analysis of centrally nucleated myofibres as well as serum myomiR biomarkers (miR-1, miR-133 and miR-206) reveals that patchy dystrophin positively modifies but does not prevent the muscle degeneration. Moreover, disorganisation of microtubule network in dystrophic mice is only partially rescued by the presence of dystrophin positive myonuclear domains. Additionally, visualisation of aged *mdx52-Xist*$^{\Delta hs}$ muscle shows that the non-uniform pattern of dystrophin distribution and myofibre central nucleation do not resolve with age. Furthermore, single myofibre analysis reveals the presence of distinct myofibre classes in *mdx52-Xist*$^{\Delta hs}$ muscle differentiated by the position of their respective myonuclei. Systematic classification of individual *mdx52-Xist*$^{\Delta hs}$ myofibres shows profound differences associated with central nucleation. These include higher numbers of myonuclei and the more substantial disorganisation of the microtubule

network in centrally nucleated myofibres. Intriguingly, analysis of dystrophin expression in centrally nucleated regions of *mdx52-Xist*$^{\Delta hs}$ myofibres reveals that dystrophin is translationally repressed in these areas.

In contrast to non-uniform dystrophin expression in *mdx52-Xist*$^{\Delta hs}$ and CRISPR-Cas9 treated mice, treatment with PPMO exon skipping compound restores dystrophin uniformly at the sarcolemma in *mdx* dystrophic animals. Notably, this uniform pattern is observed regardless of the PPMO dose. Additionally, exon skipping, and levels of dystrophin protein rescue are inversely correlated with serum myomiRs abundance, emphasising their utility as pharmacodynamic markers for dystrophin restoration strategies.

Within the muscle tissue myomiRs are known to regulate the process of myogenesis which supports skeletal muscle turnover in DMD. Canonically, microRNAs have been considered to function only in the cytoplasm. However, analyses in murine and human muscle cells shows that myomiRs are abundant and specifically upregulated in the nucleus during myogenic differentiation. Moreover, the majority of myomiRs localise to the nucleoplasm and are bound to the effector AGO2 protein. Accordingly, AGO2 protein localises primarily to the nucleus of the differentiating mouse muscle cells. These results reveal a previously unappreciated aspect of myomiRs function during muscle formation.

List of figures

List of Tables

List of Abbreviations

α/β-DG	α/β-Dystroglycan
A-band	Anisotropic band
AAV	Adeno-associated virus
ADP	Adenosine diphosphate
ANOVA	Analysis of variance
ASO	Antisense oligonucleotide
ATP	Adenosine triphosphate
BMD	Becker muscular dystrophy
bp	Base pair
C/CYT	Cytoplasmic fraction
C57	C57Bl6 or C57Bl10 wild-type mouse
Cas9	CRISPR-associated protein 9
CDC	Cardiosphere derived cells
cDNA	Complementary DNA
CH	Chromatin
CK	Creatine kinase
CLASH	Cross-linking anf sequencing of hybrids
CN	Centrally-nucleated
CNF	Centrally nucleated fibre
CNM	Centronuclear myopathy
CPP	Cell penetrating peptides
CRISPR	Clustered regularly interspaced short palindromic repeats
crRNA	CRISPR RNA
CSA	Cross-section area
CXMD	Canine X-linked animal model
CYT	Cytoplasm
DAPC	Dystrophin associated protein complex
DAPI	4',6-diamidino-2-phenylindole
DGCR8	DiGeorge syndrome critical region gene 8
dKO	Dystrophin/utrophin double knock out mouse
DM	Differentiation media
DMD	Duchenne muscular dystrophy
DMEM	Dulbecco's Modified Eagle Medium
DRP	Dystrophin related protein
DSB	Double-strand break
DTNA	α-dystrobrevin
ECM	Extracellular matrix
EDB	Extensor digitorum brevis
EDL	Extensor digitorum longus
EDTA	Ethylenediaminetetraacetic acid
eMHC	Embryonic myosin heavy chain
eNOS	Endothelial nitric oxide synthase
ER	Endoplasmic reticulum
EU	European Union

F-actin	Filamentous actin
FBS	Foetal bovine serum
FCS	Foetal calf serum
FDA	Food and Drug Administration
FISH	Fluorescence *in situ* hybridisation
Fmoc	9-fluorenylmethoxy carbonyl
FWD	Forward
GAPDH	Glyceraldehyde 3-phosphate dehydrogenase
GE	Golgi elements
GFP	Green fluorescent protein
GM	Growth media
H3K27me3	Trimethylation of lysine 27 on histone H3
HCR	Hybridisation chain reaction
HDR	Homology directed repair
HEPES	4-(2-hydroxyethyl)-1-piperazineethanesulfonic acid)
His	Histidine
HLB	Hypotonic lysis buffer
hnRNP	heterogeneous nuclear RNP
HRP	Horseradish peroxidase
HS	Horse serum
I-band	Isotropic band
IgG	Immunoglobulin G
IgM	Immunoglobulin M
IPO8	Importin 8
ITR	Inverted terminal repeats
kb	Kilobase
kDa	Kilo dalton
LDS	Lithium dodecyl sulfate
lncRNA	Long non-coding RNA
Lys	Lysine
M-line	Myosin line
MB	Myoblasts
Met	Methonine
MHC	Myosin heavy chain
miRNA	microRNA
MOPS	3-(N-Morpholino) propanesulfonic acid SDS running buffer
MRF	Myogenic regulatory factor
mRNA	Messenger RNA
MT	Myotubes
MTOC	Microtubule organising centre
MWC	Modified Wuarin-Schibler buffer
N/NUC	Nuclear fraction
NA	Numerical aperture
NGS	Normal goat serum
NHEJ	Non-homologous end joining
NLS	Nuclear localisation signal
NMD	Neuromuscular disorders
NMD	Nonsense-mediated decay

NMJ	Neuromuscular junction
nNOS	Nitric oxide synthase
NO	Nitric oxide
NP	Nucleoplasm
NSAA	North Star Ambulatory Assessment
nt	Nucleotide
OCT	Optimal cutting temperature
OMIM	Online mendelian inheritance in man
ORF	Open reading frame
PB	Piggy bac
PBS	Phosphate-buffered saline
PBST	Phosphate-buffered saline with 0.1% Tween-20 detergent
PCR	Polymerase chain reaction
PFA	Paraformaldehyde
PI	Protease inhibitor cocktail
PMO	Phosphorodiamidate morpholino oligonucleotide
PN	Phosphoryl guanidine linkage
PPMO	Peptide-conjugated PMO
PRC2	Polycomb repressive complex 2
Pre-miRNA	Precursor miRNA
Pri-miRNA	Primary miRNA
PSA	Penicillin, Streptomycin and Amphotericin B
PTC	Premature translation termination codon
PTGS	Post-transcriptional gene silencing
PVDF	Polyvinylidene fluoride
qPCR	Quantitative polymerase chain reaction
rAAV	Recombinant adeno-associated viral vectors
REV	Reverse
RIPA	Radio-Immunoprecipitation Assay
RISC	RNA-induced silencing complex
RNAi	RNA interference
ROS	Reactive oxygen species
rpm	Revolutions per cycle
RT	Reverse transcription
rtTA	Reverse transcriptional activator
SC	Satellite cell
SDS	Sodium dodecyl sulfate
SG	Sarcoglycan
sgRNA	Short guide RNA
snRNA	Small nuclear RNA
sqRNA	Short guide RNA
SSC	Saline-sodium citrate
SSCT	Saline-sodium citrate with 0.1% Tween-20 detergent
SV40	Simian virus 40
TA	Tibialis anterior
TALEN	Transcription activator-like effector nucleases
TBST	Tris-buffered saline with 0.1% Tween-20 detergent
tcDNA	Tri-cyclo DNA

TeDT	Texture detection technique
TGF-β	Transforming growth factor β
tracrRNA	Trans activating CRISPR RNA
TRE	Trans regulatory element
tRNA	Transfer RNA
TTN	Titin
UTR	Untranslated region
WC	Whole cell
WT	Wild-type
XCI	X-chromosome inactivation
Xist	X-inactive specific transcript
XLDC	X-linked dilated cardiomyopathy
XPO5	Exportin 5
ZNFs	Zinc finger nucleases
ATCC	American Type Culture Collection

Table of contents

1 Introduction

1.1 Neuromuscular disorders

Neuromuscular disorders (NMDs) are a group of distinct genetic diseases affecting peripheral nerves, lower motor neurons, neuromuscular junctions (NMJs) and skeletal muscle [1]. As such, these diseases are generally characterised by neurodegeneration and muscle weakness often leading to speech, swallowing and respiratory difficulties as well as cardiac impairment. Ninety percent of NMDs are characterised as rare with an incidence of less than 5 in 10,000 individuals on average, and exhibit wide heterogeneity in terms of disease severity, age of onset and progression [2].

Myopathies, a subset of NMDs primarily affecting muscle tissue, encompass the group of muscular dystrophies which are characterised by a progressive muscle degeneration [3,4]. Muscular dystrophies were initially classified by the clinical features such as the age of onset or affected muscle type [5]. However, since cloning and description of the dystrophin gene as the causative locus for Duchenne muscular dystrophy in 1987, significant research efforts have elucidated the genetic basis of other disorders. To date, mutations in over 40 genes, the majority of which encode diverse muscle proteins, are linked to the muscular dystrophies [3]. Elucidation of their pathogenic mechanisms, driven by the advances in molecular biology techniques, has facilitated the rapid development of novel, targeted therapeutic approaches. Recent years have witnessed the approval of several innovative drugs, with many more in clinical development [6–10]. These therapeutics, while not providing a cure, modify disease progression, improving functional outcomes thus enhancing patient quality of life.

1.2 Duchenne Muscular Dystrophy

Duchenne muscular dystrophy (DMD, OMIM # 310200) is a severe form of inherited muscular dystrophy in children. It is an X-linked disorder caused by loss of the dystrophin protein affecting 1:3,500 - 5,000 boys worldwide [11]. The disease is named after Dr Guillaume-Benjamin-Amand Duchenne, a 19th-century French neurologist [12,13]. Dr Duchenne meticulously observed and described the progressive nature of muscle weakness as well as characteristic calf enlargement in his patients around 1868 [12,13]. His observations paved the way for future research and diagnostics of DMD. DMD can be inherited from an asymptomatic carrier mother, although, due to its large size, dystrophin gene is characterised by a high mutational rate which contributes to the significant occurrence of *de novo* mutations in a third of the DMD cases [14]. Two allelic forms of DMD are reported: Becker muscular dystrophy (BMD, OMIM # 300376), characterised by later onset and milder disease progression and X-linked dilated cardiomyopathy (XLDC, # 302045) which affects the heart but not skeletal muscle. Together, these disorders are classified as dystrophinopathies of which DMD is the most common, followed by BMD with an incidence of 1:18,000 males [15–17]. The prevalence of XLDC is currently unclear.

1.2.1 Genetic basis of DMD

DMD is caused by a spectrum of loss-of-function mutations in the dystrophin gene (*DMD,* human; *Dmd,* mouse*)* which is located at the small arm of the X-chromosome (Xp21.1) [11]. *DMD* is one of the largest genes of the human genome, spanning 2.4 Mb, encoding 79-exons, 11.4 kb full-length mRNA which encodes for a 427 kDa dystrophin protein. More than 99% of its sequence is non-coding, comprised of introns ranging from 107 bp to 360 kb in length [18]. The transcription of *Dmd* takes 16 hours with splicing occurring co-transcriptionally and non-sequentially [18,19]. Adding to the genetic complexity, *Dmd* expression is driven by seven separate, tissue-specific promoters. The first three, located upstream of exon 2 produce three full-length dystrophin isoforms in

muscle (Dp427m), brain (Dp427b), and Purkinje cells (Dp427p). The Dp427m is the main skeletal and cardiac muscle isoform which is also expressed to some extent in glial cells. Four additional promoters, located downstream of exon 29, produce short N-terminally truncated dystrophin isoforms. These include Dp260, Dp140, Dp116, and Dp71 and are characteristic to various non-muscle tissues such as the retina (Dp260, Dp140, Dp71), brain (Dp140, Dp71), kidneys (Dp140, Dp71), peripheral nerves (Dp116) cardiac muscle (Dp71) [20].

The mutational spectrum of DMD is complex and poses challenges in clinical management, severity prediction, and development of targeted therapies. As of April 2024, over 8,500 unique DNA variants of the *DMD* gene have been identified in humans (https://www.dmd.nl/) [21]. A detailed analysis of 7,000 *DMD* mutations showed that deletions or duplications spanning ≥1 exon are most frequently observed (up to 80%), the remainder being small deletions, duplications, insertions, or point mutations [22]. Such distribution of mutations applies to both DMD and BMD patients, while the specific diagnosis largely depends on whether the open reading frame (ORF) is preserved [16,17,23]. Specifically, DMD is caused by frameshift mutations which lead to production of defective, prematurely terminated protein variants. Conversely, BMD patients typically maintain the translation reading frame, producing an internally deleted, yet partially functional, pseudo-dystrophin, which underlies the milder disease progression. The presence of pseudo-dystrophin in BMD demonstrates that complete, full-length protein is to some extent dispensable for functional compensation. The most remarkable example of this phenomenon comes from a BMD patient lacking 46% of the dystrophin gene who presented only mild symptoms and was ambulant at the age of 61 [24].

Although mutations span the entire dystrophin gene, the majority (80% of deletions) cluster within two hot spots: exons 45-55 encoding the central part of the dystrophin and exons 2–20 encoding the N-terminus [21,22]. These account for around 47% and 15% of total DMD mutations, respectively, reflecting the majority of affected individuals [17,21,22].

It has been suggested that the nature of repetitive sequences within these regions as well as their propensity for recombination lead to increased replication errors in the hot spot regions [25,26]. Notably, the ORF rule holds true for 90% of *DMD* mutations with some in-frame deletions causing a severe phenotype [16,17]. For example, in-frame deletion of exons 45-46 results in a severe DMD progression with profound cardiomyopathy which presented a decade earlier than observed for patients with 45-48 and 45-51 deletions [27]. Conversely, several out-of-frame mutations were found in BMD patients with dystrophin partially present in the muscle [17]. Therefore, in addition to the reading frame preservation rule, mutation-specific effects likely play a role in overall disease progression. It has been shown that mutations located in the 5′ end of the gene correlate with severe progression and earlier onset of symptoms in BMD [17,28]. Additionally, differences between dystrophin levels in patients carrying the same mutations have been observed, pointing to individual variations in intronic sequences that potentially affect the splicing efficacy [29]. Accordingly, Beggs *et al*. have shown that patients carrying similar multi-exon deletions (e.g., exons 45-47, 45-48, 45-49, and 45-53) have contrastingly different disease progression courses with some of them ambulant at 42, and some presenting severe motor delay at 4 years of age [28]. The clinical phenotype of BMD is thus highly variable and depends on several factors including the specific location and extent of the mutation, particularly in cases of multi-exon deletions [30]. These lead to production dystrophin proteins of varying lengths and compositions, which directly influence the functional capability of the protein [31]. Notably, beyond dystrophin, certain genes can act as disease modulators (e.g. transforming growth factor β (TGF-β) or osteopontin) modifying the disease progression regardless of mutation, further contributing to observed clinical heterogeneity of dystrophinopathy [32].

1.2.2 Clinical manifestation of DMD

In DMD, dystrophin deficiency results in extreme vulnerability of muscles to contraction-induced damage. As such, daily physical function initiates a detrimental cascade of degeneration-regeneration cycles ultimately leading to muscle wasting and thus

loss of function [33]. DMD typically manifests in early childhood, around 2-3 years of age, with primary muscle weakness affecting the proximal and trunk muscles. At this stage, DMD boys often present with general clumsiness, waddling gait, positive Gower's sign, difficulty in climbing the stairs, toe walking, and enlarged calves [34]. As the disease progresses, degeneration affects also distal muscles, ultimately leading to the loss of ambulation by the age of ~15 [35]. The primary muscle weakness leads to several secondary complications. Many patients develop contractures and require spinal surgery to correct scoliosis caused by poor mobility and weakness of trunk muscles [36]. Furthermore, the progressive wasting of intercostal muscles and diaphragm leads to profound ventilatory problems in early adulthood when patients often start to rely on mechanical ventilatory support [36–38]. Additionally, as the cardiac muscle weakens, heart function rapidly declines during adolescence with almost all DMD patients eventually developing a form of dilated cardiomyopathy, often leading to end-stage heart failure [36,39,40]. Currently, cardiac dysfunction is the main cause of death for dystrophic patients, typically in the third decade of life [41]. In contrast, BMD generally presents with much milder severity and slower disease progression with patients remaining ambulant well into adulthood, and with some never requiring wheelchair use [17,24,29,42]. The need for ventilatory support and severe cardiomyopathy is also uncommon in BMD patients [16,17].

The clinical DMD symptoms are always accompanied by an extreme elevation of serum creatine kinase (CK) levels [17,43]. Muscle relies on CK to phosphorylate creatine. Phosphocreatine acts as an immediate energy reserve in the muscle, readily transferring the high-energy phosphate group to adenosine diphosphate (ADP), and thus regenerating the adenosine triphosphate (ATP) energy carrier during contraction. Muscle damage is known to cause a significant leakage of CK into the circulation [43]. In DMD patients, serum levels of CK are up to 100 times higher than in healthy boys reaching their maximum level between 2–5 years of life and followed by a steady decline afterwards [43]. While BMD patients generally exhibit lower levels of serum CK than DMD, suggesting less extensive

muscle damage, significant variability in CK levels exists within both BMD and DMD populations [17,43]. In DMD patients, higher CK levels were shown to be associated with earlier age of ambulation loss and worsened respiratory function. [17,44]. Nevertheless, while elevated CK remains one of the main DMD diagnostic markers, its intraindividual, seasonal, and activity-dependent fluctuations, as well as marked decrease with age position it as a poor pharmacodynamic biomarker [45].

1.2.3 Dystrophin and associated proteins

Dystrophin was first described by the group of Prof. Louis M. Kunkel in 1987, nearly 130 years after the first descriptions of DMD pathology [11–13]. Subsequent biochemical studies characterised dystrophin as a large, rod-shaped and multidomain protein [46]. In healthy muscle, dystrophin is localised underneath the muscle cell membrane (sarcolemma) where it assembles and maintains the dystrophin-associated protein complex (DAPC) (Figure 1.1) [47]. The DAPC is composed of several functionally coupled proteins: α/β-dystroglycan (α/β-DG), the sarcoglycan (SG) complex, dystrobrevin (DTNA), syntrophins, and neuronal nitric oxide synthase (nNOS). Four distinct domains of dystrophin are involved in the assembly of the complex: the amino-terminal domain, the central rod domain comprised of 24 spectrin-like repeats, the cysteine-rich domain, and the carboxy-terminal domain. The N-terminal part of dystrophin faces the myofibre core, providing a link to the cytoskeleton by binding to filamentous actin (F-actin) [48]. This connection is further reinforced by two additional actin and microtubule binding sites located within the rod domain (repeats 11–17 and 20–23 respectively) [49,50]. Repeats 16–17 also serve as a docking site for the nNOS signalling protein, tethering it to the membrane with the help of cytoplasmic syntrophins [51,52]. Syntrophins directly bind to two sites in dystrophin C-terminus, serving as an adapter capable of bridging various protein families to DAPC [52,53]. Additionally, the C-terminus of dystrophin binds to DTNA, which in turn directly interacts with syntrophins as well as other cytoskeletal proteins (e.g., syncoilin and synemin) [54,55]. Dystrophin is anchored to the sarcolemma via a dual mechanism. Firstly, the

cysteine-rich domain binds to the transmembrane β-DG [56]. Secondly, multiple independent, direct interactions of the rod domain with membrane phospholipids further stabilise the association of dystrophin with the membrane [57]. β-DG non-covalently binds to the extracellular α-DG which directly interacts with extracellular matrix (ECM) proteins, such as laminin [58]. Within the membrane, β-DG directly interacts with the sarcoglycan complex composed of α-, β-, γ-, and δ-sarcoglycan isoforms [59]. In the absence of dystrophin, the DAPC does not correctly assemble, and the expression of its protein components is significantly reduced [60].

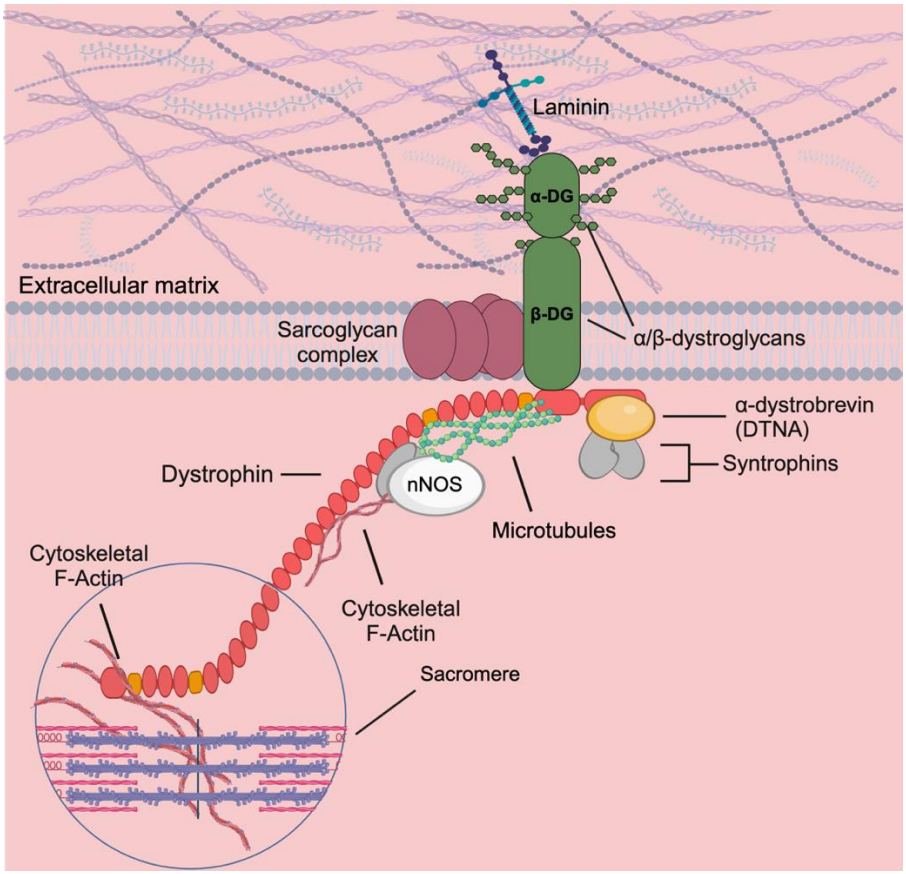

Figure 1.1 Dystrophin-associated protein complex (DAPC) structure.

Dystrophin localises beneath the muscle cell membrane, where it plays a key role in the organisation of DAPC. Dystrophin is anchored to the sarcolemma through cysteine-rich domain interaction with β-dystroglycan (β-DG). β-DG is bound to α-dystroglycan (α-DG) which directly interacts with extracellular matrix (ECM) laminin. Within the membrane, β-DG

directly interacts with the sarcoglycan complex. N-terminus of dystrophin as well as central rod domain repeats 11-17 bind cytoskeletal filamentous actin (F-actin), which further interacts with sarcomeres. Repeats 16-17 neuronal nitric oxide synthase (nNOS). Repeats 20-23 bind microtubules. The C-terminus of dystrophin interacts with α-dystrobrevin (DTNA) and syntrophins. Image not to scale, created with BioRender.com

Dystrophin functions as the foundation and central component of the costamere which is a highly specialised, muscle-specific focal adhesion point [61]. Costameres are localised in the subsarcolemmal space in a muscle-characteristic striated pattern aligning with the structure of internal contractile machinery (sarcomeres) [61,62]. Accordingly, costameres physically connect sarcomeres with the sarcolemma and ECM. As such they serve as anchors and intermediaries, transmitting contractile force generated within the myofibre core outward to the ECM. This efficient transfer of force is further dissipated through tendons and bones, enabling coordinated muscle-body movement [63]. Accordingly, costameres function also as mechano-sensing hubs facilitating the conversion of mechanical stretch/tension cues into biochemical signalling that regulates muscle homeostasis. While dystrophin and its associated proteins are important for their central role in costamere function, many other proteins work together to ensure the correct force transduction and sensing (reviewed in [61–63]). These include structural proteins, such as the vinculin-talin-integrin complex or desmin on the sarcolemmal side, as well as actin, titin, and telethonin within the sarcomere [61].

The absence of dystrophin disrupts the intricate costameric network, severing a crucial link between internal contractile machinery and surrounding ECM. This disruption has profound consequences visible not only through DMD pathology but also in other disorders caused by deficiencies in costameric components. Many costameric proteins lead to muscle disease when not functioning correctly [61]. For example, loss of α7 integrin, results in severe muscular dystrophy and significantly exacerbates the pathology of the dystrophic animal model leading to a premature death [64,65]. Similarly, the lack of

sarcoglycan family members results in a spectrum of limb-girdle muscular dystrophies while impaired α-DG binding to its extracellular partners causes dystroglycanopathies [59,66,67]. The importance of a functional costamere is further highlighted by the fact that simply restoring DAPC to the sarcolemma, without linking it to F-actin through dystrophin N-terminus, fails to recover the pathological phenotype [68].

1.2.3.1 Functions of dystrophin and associated proteins in muscle

By directly binding to the cytoskeleton, dystrophin forms a continuous pathway for transmitting the lateral force generated through the muscle contraction to the ECM [63]. At the same time, it efficiently prevents the excessive stress being exerted on the sarcolemma while force is transmitted [69,70]. This role is possible in part due to the large central rod domain which distributes the force through conformational changes of spectrin-like repeats [69]. The inherent elasticity of the rod domain allows it to effectively dissipate sudden increases in force, meaning that dystrophin is considered to be a molecular shock absorber of the muscle cell [69].

In addition to well-established force transduction and protective roles, dystrophin, and the DAPC act as signalling hubs [53]. Dystrophin signalling functions are primarily mediated through syntrophin proteins which contain several separate binding domains allowing for anchoring of various protein partners to the DAPC [53]. For example, nNOS binding and thus its correct function within the muscle relies on syntrophin-mediated anchoring to the DAPC [52]. In healthy skeletal muscle, nNOS plays a pivotal role through the production of nitric oxide (NO) which readily diffuses within the myofibre and proximal micro-vessels [71,72]. At rest, NO levels in the muscle are low, rising significantly during contraction, stimulated by increased calcium (Ca^{2+}) influx, among other factors [71,73]. Subsequently, actively produced NO diffuses to the nearby capillaries where it regulates the flow of blood into the active muscle [74,75]. This mechanism ensures that the contracting tissue receives vital oxygen and nutrients crucial for sustained contraction and fatigue resistance [75]. Within the myofibre, NO modulates a plethora of processes including contractile function

itself, as well as mitochondrial respiration, calcium handling, and glucose uptake, among others (reviewed in [71,76]). Additionally, NO has been implicated in the regulation of skeletal muscle repair, directly activating muscle stem cells shortly after myofibre damage [77,78]. In DMD patients and animal models, nNOS expression is reduced and the protein is displaced from the sarcolemma to the cytoplasm [79]. This results in a dramatic decrease in NO production, causing general metabolic defects in the cell, as well as disrupted blood flow regulation leading to muscle functional ischemia [74,80]. In addition to regulation of NO signalling, dystrophin facilitates the correct membrane organisation of multiple membrane ion channels including the voltage-gated calcium channel necessary for proper muscle contraction [81]. Through those interactions, dystrophin affects stretch-induced cationic flux across the sarcolemma, as well as calcium signalling, required for correct cellular function [81,82].

1.2.3.2 Utrophin – a dystrophin related protein

Utrophin (or dystrophin related protein, DRP) is a 376 kDa autosomal paralogue of dystrophin. Encoded by the *UTRN* gene on the 6q24 chromosome in humans and chromosome 10 in mice, it shares 86% of sequence homology with dystrophin, despite a smaller size of 900 kb in the genome [83–85]. Utrophin mRNA is 13 kb in length and is composed of 74 exons [86]. The sequence and amino acid similarity to dystrophin spans throughout the length of the protein with C-terminal and N-terminal being the most conserved at 80% of homology [83,86]. Accordingly, utrophin retains the F-actin, β-DG and DTNA binding domains and assembles the DAPC, protecting the sarcolemma against contraction-induced damage [84,86–89]. The main differences between utrophin and dystrophin are found in the central rod domain [84]. In contrast to dystrophin, utrophin contains only 22 spectrin-like repeats, lacking the equivalent dystrophin repeats 15 and 19 [84,90]. This absence leads to loss of the interaction with nNOS and microtubules, reducing functionality when compared to dystrophin [50,91].

In skeletal muscle, the highest levels of utrophin are observed during development when it is expressed throughout the sarcolemma of newly formed myofibres [92–94]. Subsequently, utrophin expression progressively declines, ultimately being replaced by dystrophin at the adult muscle membrane [93,95]. As such, in healthy adult skeletal muscle, utrophin expression is restricted to the neuromuscular (NMJ, site of motor neuron connection to the myofiber) and myotendinous junctions (MTJ, site of muscle-tendon connection) [88,92,96–99]. However, consistent with its developmental expression pattern, utrophin re-appears at the sarcolemma of newly formed, regenerating adult myofibres [100–102]. Accordingly, utrophin levels increase significantly in dystrophic muscle which undergoes extensive degeneration and repair cycles [87,92,94,101]. Importantly, in dystrophic conditions, this upregulation is not limited to regenerating myofibres, as utrophin has been detected at the sarcolemma of dystrophic muscle independent of regeneration [89,94,96,97,99,103]. Notably, utrophin and dystrophin proteins bind the same sites at the sarcolemma, as evidenced by electron microscopy detection of both proteins in the muscle of transgenic mice [104]. While these results suggest a compensatory role for utrophin in protecting the dystrophic muscle against contraction-induced damage, the protein levels in patients are insufficient to fully prevent degeneration. Accordingly, the correlation between utrophin levels and disease progression remains unclear [87,96]. However, the lack of utrophin localisation to the sarcolemma has been recently connected to an unusually severe DMD progression [105]. Specifically, a DMD patient lacking exons 10-60 due to an in-frame *DMD* mutation exhibited correct localisation of dramatically truncated dystrophin protein to the sarcolemma [105]. While utrophin was upregulated in the muscles of that patient, its localisation was restricted to the cytoplasm [105]. The patient exhibited an exceptionally severe phenotype of the disease, ultimately succumbing to cardiac arrest at the age of 9 years 7 months [105]. This study provided the first direct human evidence that utrophin can compensate for dystrophin, competing for sarcolemma binding in DMD patients.

1.2.4 Molecular pathophysiology of DMD

The absence of dystrophin results in the skeletal muscle membrane being inherently susceptible to mechanical stress and damage [70]. This vulnerability triggers a chronic, contraction-induced cascade of myofibre death and regeneration, ultimately leading to muscle functional loss. Dystrophic sarcolemma fragility manifests through the physical disruption of the membrane with observable microscopic tears termed “delta lesions” localising along the cell [23,106]. These render the myofibre leaky to the extracellular contents as identified by the potent accumulation of exogenous dyes, as well as serum components like albumin or large antibodies such as IgG (150 kDa) and IgM (900 kDa) in damaged myofibres [68]. Accordingly, the disrupted sarcolemma is permissive for the release of cytoplasmic contents, including creatine kinase or muscle-specific microRNA into the circulation [43,107,108]. Increased membrane permeability is also partially responsible for the intracellular Ca^{2+} overload in DMD muscle [82,109]. Increased levels of Ca^{2+} lead to intensified proteolytic damage of essential muscle proteins, and digestion of membranes [82]. In parallel, elevated calcium uptake by mitochondria results in disruption of mitochondrial membrane potential and increased production of reactive oxygen species (ROS) [82,110]. In turn, ROS further contribute to muscle degeneration through irreversible oxidative damage of proteins, membrane lipids, and DNA [111]. The consequences of a disrupted sarcolemma ultimately converge in myofibre death, which is sensed by inflammatory cells that infiltrate the damaged area. Within hours of damage occurring, neutrophils appear at the site of necrosis amplifying the response by recruiting pro-inflammatory M1 macrophages [112]. These are further replaced by M2 anti-inflammatory macrophages, which are essential for the completion of muscle regeneration [112]. Regeneration of myofibres is initiated by the activation of quiescent resident muscle stem cells (satellite cells, SC) that are nested between the basal lamina and sarcolemma [113]. Upon injury, these $Pax7^{+}$ cells rapidly expand, differentiate and fuse with each other, forming a new set of myofibres in a process mirroring the formation of embryonic muscle [114,115].

Newly formed myofibres are characterised by a small cross-sectional area, centrally located nuclei, and expression of developmental myogenic factors such as embryonic myosin heavy chain (eMHC) and utrophin [102,116]. Importantly, the proportion of regenerating myofibres (indicating the scope of muscle damage) is directly correlated with the disease severity of BMD and DMD patients [87]. Over time, regenerated myofibres lose the expression of developmental marker proteins, are subjected to radial growth, and reposition the myonuclei to the periphery [117].

Owing to the presence of satellite cells, muscle regenerative capacity is generally remarkably efficient [118]. However, continuous myonecrosis resulting in repetitive bouts of degeneration and repair of fragile DMD muscle cells eventually leads to regeneration failure. Excessive ECM deposition is driven by chronic inflammation, persistent repair processes, and upregulation of TGF-β results in the progressive formation of fibrotic scar and fatty tissue deposits within dystrophic muscle [112,119]. These pathological changes significantly contribute to muscle weakness and dysfunction. As such, muscle fibrosis is highly correlated with the level of motor impairment in DMD patients [119]. Beyond the ECM and inflammatory milieu, dysfunctional satellite cells and the unfavourable dystrophic environment further contribute to the failure of muscle repair mechanisms [33,120,121]. These mechanisms together with other secondary processes such as oxidative stress and functional muscle ischemia are the hallmarks of DMD pathology [23]. Their interplay leads to rapidly progressing functional decline, compromising the lifespan and life quality of DMD patients.

1.2.5 DMD mouse models

Animal models play a vital role in understanding the pathology of DMD, offering mechanistic insights, and potential for testing experimental therapeutics. Over the years, multiple dystrophin-deficient models, that include at least 8 different species, have been developed [122]. Nevertheless, due to their practicality, affordability and well-characterised genetics, murine models remain the preferred choice for pre-clinical DMD research. The first described dystrophic mouse strain (termed *mdx* after X chromosome-linked muscular dystrophy) was identified based on elevated serum pyruvate and creatine kinase levels in an enzymatic screen [123,124]. Lesions characteristic of muscular dystrophy observed in these mice were later attributed to a spontaneous point mutation in exon 23 of dystrophin, which leads to the generation of a premature translation termination codon (PTC) located 27% of the way along the protein sequence [124]. The presence of the PTC triggers the nonsense-mediated decay (NMD) machinery components to bind to faulty transcripts marking them for degradation [125]. Nevertheless, the internal *Dmd* promoters located downstream of exon 23 (which initiate transcription of the Dp260, Dp140, Dp116, and Dp71 isoforms) remain functional. As such, full-length Dp427 is missing in these animals, while expression of other isoforms is unperturbed.

Although some dystrophic symptoms are observed already in embryonic development, *mdx* mice are characterised by extensive myonecrosis occurring at 2-4 weeks of age [126–128]. In parallel, a massive infiltration of mononuclear immune cells is observed [127]. Subsequently, small in diameter, centrally nucleated fibres appear around 6 weeks of age, indicating that active regeneration is occurring [126,127,129]. The repeated bouts of muscle turnover peak around 12 weeks of life and further plateau, shifting from extensive myonecrosis to robust, satellite cell-driven regeneration [130–132]. In parallel, injury-induced chronic inflammation leads to enhanced activation of resident fibroblasts and abnormal, progressive accumulation of EMC components (primarily collagen) [119,131]. The increased deposition of fibrotic tissue (fibrosis) results in muscle stiffness and

weakness, further contributing to the phenotype [131]. The majority of *mdx* myofibres are centrally nucleated at 2 months, and almost all are centrally nucleated by 4 months of age, indicating that most of the myofibres underwent degeneration and have been regenerated by that time [126,127,129]. Along with cycles of degeneration and regeneration, *mdx* mice experience substantial myofibre hypertrophy [129]. As such, *mdx* muscles are characterised by a significant variability in myofibre size, reflecting the co-occurrence of small, recently regenerated, and large, hypertrophied muscle cells [126]. CK levels are also markedly increased in *mdx* animals up to ~ 6 months of age, falling in older animals, and reaching normal levels by 12th month of age [126].

Although many pathological features of DMD are shared between mice and humans, there are several key differences to be noted. In comparison to DMD patients, *mdx* mice exhibit milder disease progression with only a slightly reduced (~ 20%) lifespan [133]. Additionally, diminished regenerative capacity is observed in humans versus mouse models. Specifically, in DMD patients, muscle regeneration was recently shown to cease around 10 years of age, after which point, no functional myofibres are formed, while muscles are progressively replaced by fibrotic and fatty deposits [33,134]. In contrast, regeneration is more prominent in the *mdx* mouse, continuing through the majority of its life [126,135,136]. As such, it has been suggested that DMD-specific calf enlargement in patients reflects the *mdx* myofibre hypertrophy only at initial stages and that fibrosis is responsible for the enlarged calf at later stages (pseudohypertrophy) [137]. Accordingly, fibrotic changes are less pronounced in *mdx* animals than in patients [126]. The relatively mild phenotype of *mdx* animals has been attributed to persistent expression of utrophin in the muscles of these animals, which was confirmed by severe progression and death at 12 weeks of age of dystrophin/utrophin double knock-out (dKO) animals [138]. Accordingly, dystrophic mice engineered to overexpress utrophin are fully protected against the contraction-induced muscle damage [139]. Regardless of these commonly recognised

differences, the *mdx* mouse model is currently the most widely used animal model in DMD research.

Notably, while serving as a valuable tool, *mdx* point mutation in exon 23 is not directly relevant to the mutational spectrum of DMD patients [21,22]. Significant additional mouse models have been generated to better resemble patient genetics for more accurate evaluation of therapeutic strategies. Among these, *mdx52* animals were generated by a targeted deletion of exon 52, which is a patient-relevant mutation as exon 52 localises to the most frequently affected hot-spot region of *DMD* [21,22,140]. The muscular phenotype progression in *mdx* and *mdx52* is overall similar, although an earlier peak in the number of centrally nucleated fibres (i.e. regeneration) is observed for *mdx52* mice (before 2 months versus before 6 months) [136]. Both *mdx* and *mdx52* animals continue to regenerate throughout the lifespan as demonstrated by declining but present eMHC staining up to 18 months of age [136]. In contrast, the *mdx52* model does not express Dp260 and Dp140 dystrophin isoforms and thus presents with altered retinal function in comparison to *mdx* [140,141]. Nevertheless, both models share a similar progressive decline in muscle function due to ongoing myofibre damage, inflammation, and accumulating fibrosis observed in humans [135,140].

1.2.6 Therapeutic dystrophin levels

The topic of clinically relevant levels of dystrophin protein is complex. The link between dystrophin expression levels and disease severity is generally well-established, whereby lower levels are associated with more pronounced symptoms while complete loss with typical DMD progression [17,29,42]. However, inconsistencies have been observed in BMD patients expressing high levels of dystrophin and characterised by severe muscular dystrophy and vice versa, suggesting that other factors contribute to the dystrophic phenotype [96,142]. The dystrophin threshold effect proposes a minimum functional dystrophin level necessary for observing clinical improvement in muscular dystrophy. [142,143]. For example, BMD patients with less than 10% dystrophin were shown to exhibit

significantly diminished strength and more rapid symptom onset relative to those expressing > 10% dystrophin [142]. In patients with XLDC, dystrophin mutations lead to a complete absence of dystrophin in the heart, and diminished but not halted production in skeletal muscle [143]. Analysis of dystrophin levels in this cohort revealed that the production of full-length, uniformly distributed dystrophin from birth at 30% is sufficient to prevent muscle pathology [143]. However, other studies show that levels as low as 0.5% of wild-type dystrophin correlate with delayed loss of ambulation, the lack of need for spinal surgery, and cardiac impairment severity in DMD [144,145]. Exceptionally, two patients with < 0.5% of dystrophin were ambulant until 73 and 66 years of age respectively [144]. In animals, expression of 20-30% of full-length or truncated dystrophin expressed from birth is sufficient to reduce muscle pathology [146]. Similarly, restoration of 15% dystrophin in 12-week-old *mdx* mice was shown to protect the muscle against contraction-induced sarcolemma damage [147]. Additionally, 3.3% expression of near full-length dystrophin in the heart of *mdx*^{3cv} (carrying a mutation in intron 65 of *Dmd*), improves the heart function relative to dystrophin-null controls [148]. It is therefore widely acknowledged that some dystrophin is better than none, however, the concept of threshold effect requires further investigations. Nevertheless, clinical variability between patients as well as available animal data consistently suggests that other factors than dystrophin quantity (i.e., protein quality, stability, environmental, disease-modifying genes, and epigenetic factors) are likely to contribute to the downstream effect of dystrophin on myofibre function.

Notably, the majority of the dystrophic patients (around 50%) and animal models display sporadic, dystrophin-positive myofibres in their skeletal muscle termed revertant fibres (Figure 1.2) [136,145,149,150]. These were first described in 1990 and are thought to arise from spontaneous, multi-exon skipping (up to 30 exons) events which override the genomic dystrophin mutation leading to the production of internally deleted pseudo-dystrophin proteins [151,152]. Revertant fibres are present in newborn *mdx* at the sarcolemma of singular cells but expand with age leading to a formation of dystrophin-

positive myofibre clusters composed of ~ 100 cells [151,153]. They also increase in length, initially spanning ~ 10 µm of sarcolemma at the perinatal stage and > 1 mm in 18-month-old animals [151]. Notably, the revertant fibre frequency in dystrophic animals differs between mutants, with *mdx* mice containing significantly higher amounts than the *mdx52* model [136]. The expression of functional dystrophin in these fibres is thought to occur at the satellite cell stage and grow via clonal expansion of the revertant cell through degeneration/regeneration cycles in *mdx* animals [153]. Other mechanisms, such as diffusion of specific splicing factors within revertant fibre territory, secondary DNA mutation, and stability (and thus accumulation) of dystrophin-positive fibres have been later proposed [136]. In contrast, no increase in size or number of revertant fibres with age is observed in DMD patients, which is thought to reflect the diminished regenerative capacity of human DMD muscle [149]. Notably, besides clearly positive, sporadic revertant myofibres, some DMD patients exhibit weak dystrophin signal at the sarcolemma of a high proportion of fibres referred to as “dystrophin traces” [145,149]. These seem to be specific to humans, as a similar phenomenon has not been reported in mice [149]. Even though initially believed to be beneficial, residual dystrophin levels were, more recently, shown not to correlate with functional muscle improvements in DMD patients [145,149].

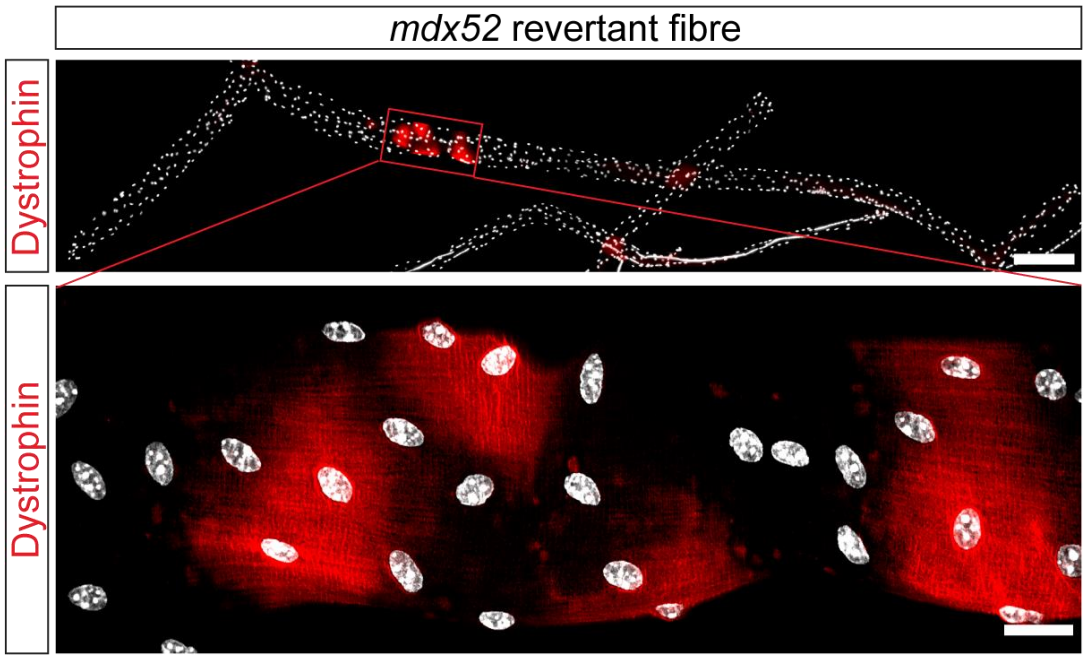

Figure 1.2 Revertant mouse myofibre from *mdx52* dystrophic model.

Dystrophin staining in single extensor digitorum longus (EDL) revertant myofibre isolated from 12-week-old *mdx52* mouse. Tiled image taken at ×10 magnification and stitched using LAS X software (Leica) (top). Scale bar represents 200 μm. High-resolution image of the revertant region (bottom) taken at ×25 magnification. Scale bar represents 20 μm.

1.2.7 X chromosome inactivation and DMD female carriers

X chromosome inactivation (XCI) is a mechanism of dosage compensation, that relies on the X-inactive specific transcript (*Xist*) long non-coding RNA (lncRNA) that randomly silences one of the X chromosomes in XX cells [154–156]. The *Xist* transcript initiates X chromosome inactivation by spreading across the chromosome in *cis*, recruiting the Polycomb repressive complex 2 (PRC2) to induce repressive histone modifications (i.e., H3K27me3) and DNA methylation, ultimately leading to transcriptional silencing [156–158]. Normally, this process leads to a balanced 50:50 ratio of active maternal and paternal chromosomes across the body [159,160]. However, in some cases one chromosome is silenced in a higher proportion of cells than the other, leading to a non-random X-inactivation pattern (i.e. skewed XCI) ranging from mild (40:60) to extreme (15:85) [159–163].

Skewed X chromosome inactivation in adults arises either from primary or secondary mechanisms [164]. Primary skewed X-inactivation is linked to the preferential silencing of one X chromosome and is usually attributed to mutations in *Xist* locus [164,165]. Secondary non-random inactivation is linked to the effects of X-linked mutations on cell survival. X chromosome inactivation is established at the stage when the embryo is composed of 10-20 cells and is subsequently maintained in all somatic cell progeny [166–168]. In the secondary non-random inactivation mechanism, the initial choice of which X chromosome to silence is random, with a 50:50 chance in each cell [155,169,170]. However, some X-linked mutations leading to cell growth disadvantage, e.g. diminished proliferation or pronounced cell death, will result in depletion of these cells during subsequent division cycles [162,171,172]. This results in a limited number of cells with active, mutation containing X chromosome in the adult organism, resulting in the observed skewed XCI pattern [160,162,166,171–174]. The cell selection mechanism was demonstrated for X-linked intellectual disability carriers heterozygous for a mutation in *ATRX* gene, where preferential selection of cells expressing the wild-type allele resulted in skewed XCI (≥ 80:20) [171,173]. Similar observations have been made in obligate Wiskott-Aldrich and Rett

syndrome carriers [172,174]. Conversely, a favourable selection of cells with the active, mutation-carrying (p.Arg384X) X chromosome was suggested as a cause of severe haemophilia B in a female carrier [175].

Females are generally less susceptible than males to X-linked disorders, due to the presence of a healthy allele on the second X chromosome (reviewed in [176]). Thus, the majority of DMD female carriers are considered asymptomatic [176,177]. Nonetheless, the severity of symptoms in DMD carriers can be highly variable [178]. Skewed X chromosome inactivation has been linked to more severe muscle pathology in some female DMD carrier cases [179,180]. For example, severe dystrophic changes (i.e. highly elevated CK and moderate/severe muscle weakness) were observed in a patient with 90:10 skewed XCI towards preferential inactivation of the healthy allele [179]. Moreover, classic DMD symptoms (i.e. motor delay, contractures, muscle weakness, and positive Gower's sign) were reported for a carrier with skewed XCI whose non-manifesting twin sister exhibited random X-inactivation pattern [181]. Additionally, it has been demonstrated that random XCI results in expression of > 60%, while skewed XCI lead to less than 30% of dystrophin protein levels relative to healthy control [180]. Similar results were obtained by others, suggesting that dystrophin expression levels, and thus the severity of symptoms in DMD female carriers, are connected to XCI [179–183]. However, a more recent study in monozygotic carrier DMD twins, both of whom presented with non-random X chromosome inactivation with preferential silencing of healthy, maternal X chromosome (paternal: maternal expression ratios of 81:19 and 76:24 respectively) revealed a different pattern [184]. Specifically, only one sister was a manifesting carrier with elevated CK levels and observable calf enlargement, implying that while skewed X chromosome inactivation contributes to the extent of symptoms in female DMD carriers, other factors (e.g., differentially expressed disease-modifying genes) could also play a role [32,184].

1.3 Therapeutic strategies for DMD

Current standards of care in DMD focus on multidisciplinary approaches aimed at slowing disease progression and optimising quality of life [185,186]. One of the most widely used pharmaceutical interventions are corticosteroids such as prednisone, deflazacort and, more recently, vamorolone [187,188]. These drugs are believed to modulate the disease course in DMD through pleiotropic anti-inflammatory and metabolic effects, resulting in a slowdown of muscle function decline. Corticosteroids have been shown to improve pulmonary function, ambulation, and reduce the risk of scoliosis (reviewed in [186,187]). Other disease management approaches include physical therapy, psychosocial management, ventilatory support, or the use of angiotensin-converting enzyme inhibitors for improved heart function [185,186]. However, over recent years, a significant scientific effort has been dedicated to the development of drugs which aim to treat the underlying cause of the disease. Aside from corticosteroids, there are five DMD therapeutic interventions approved by USA Food and Drug Administration (FDA). These include four exon-skipping antisense oligonucleotides, and a gene replacement therapy.

Ataluren (Translarna, PTC Therapeutics) was the first conditionally approved DMD therapeutic in the EU for patients with nonsense mutations in the dystrophin gene. It acts through a stop codon read-through mechanism, allowing ribosomes to translate past the PTC and produce a functional protein, potentially mitigating the severity of muscle weakness [189]. However, in late 2023, the marketing authorisation of Ataluren was not renewed, after no sufficient benefit was observed in ambulatory patients [190]. Corticosteroids are currently the main pharmaceutical intervention available for DMD patients in the EU.

1.3.1 Antisense oligonucleotide mediated exon skipping

Antisense oligonucleotide (ASO)-mediated exon skipping is one of the most promising therapeutic strategies for DMD [6]. ASOs are single-stranded nucleic acid polymers (20-30 nt in length) designed to bind the splice signals of a selected exon via Watson-Crick base pairing [6,191–193]. Exon skipping aims to elicit a milder, BMD-like form of the disease in DMD patients. Specifically, ASOs are strategically designed to modulate the pre-mRNA splicing of the dystrophin gene, restoring the open reading frame, and resulting in a production of an internally deleted but functional pseudo-dystrophin protein [6,194]. Effectively ASOs hide the targeted sequence from splicing machinery leading to the exclusion of selected exon from mature mRNA and restoration of functional protein [6,191]. Thus, ASO-mediated exon skipping is a mutation-specific approach [22,194]. Analysis of DMD patients mutations revealed that exon skipping strategy is applicable to 55% of all patient mutations [22,194]. Since *DMD* deletions tend to cluster in hotspot regions, skipping just a few exons could benefit a substantial proportion of patients [22,194]. For example, in theory, exon 51 skipping is applicable to the largest group of DMD patient mutations (~ 14%) [22,194]. Conversely, skipping of exon 77 would be applicable to only 0.02% of mutations [194]. This includes single or double exon skipping for deletions, duplications, and small mutations [194]. Notably, this strategy does not apply to very large deletions or mutations in regions critical for dystrophin cysteine-rich domain or actin-binding sites [194].

Due to their inherent susceptibility to nucleases and poor target binding affinity, unmodified ASOs based on natural DNA and RNA chemistry have limited clinical use [192]. As such, diverse ASO chemistries have been developed to optimise pharmacokinetics, target specificity, and the overall therapeutic efficacy [192]. For example, in the case of phosphorodiamidate morpholino oligonucleotide (PMO) ASOs the sugar-phosphate backbone of natural nucleic acids is replaced with morpholine rings and phosphorodiamidate linkages for increased stability [195]. This results in PMO exhibiting a significant resistance to many biofluid enzymes (i.e. nucleases, proteases, esterases and

others) as well as reduced binding affinity for proteins resulting in their excellent safety profile [196]. As of 2024, four PMO antisense drugs have been approved by the FDA for treatment of DMD (Table 1.1). These include Eteplirsen, Golodirsen, Viltolarsen and Casimersen [7,8,10,197,198]. All these target exons skipping of which could benefit the highest number of patients (i.e. exon 51, 53 and 45). Notably, the efficacy of currently approved exon-skipping ASOs is low. Specifically, weekly Eteplirsen injections for almost 3.5 years resulted in the expression of ~ 1% of wild-type dystrophin [197]. The approval of Eteplirsen by FDA in 2016 was highly controversial, as it was solely based on the minimal dystrophin restoration which was doubted to elicit any functional benefit [199]. Similar results were obtained with other approved ASOs (Table 1.1). Dystrophin restoration levels were the highest for Viltolarsen with 5.9% of dystrophin expression achieved after 25 weeks of treatment [198]. However, this is subjected to change as several clinical trials for Viltolarsen are still ongoing [200]. Notably, none of the FDA-approved ASOs for DMD have been approved by European Medicine Agency mainly due to their low efficacy. Other ASO chemistries have also been tested in clinical trials. Wave Life Sciences developed a stereopure ASO with phosphorothioate backbone to induce *DMD* exon 51 skipping (Suvodirsen) [201]. Despite promising pre-clinical results, Suvodirsen failed to meet the primary endpoint (i.e. an increase in dystrophin protein expression) in a phase II clinical trial, and its development was subsequently discontinued [202]. Similarly, a 2′-O-methyl ASO with phosphorothioate backbone, developed by BioMarin (Drisapersen) did not receive marketing authorisation by the FDA [203]. This decision based on limited efficacy (i.e. lack of functional improvement) and adverse events including injection site reactions, thrombocytopenia, and proteinuria [204]. Notably, Wave Life Sciences are currently conducting a phase 1/2 trial (NCT04906460) of an ASO (WVE-N531) based on phosphoryl guanidine (PN)-containing backbone chemistry [205]. This chemistry has been shown to improve the delivery and overall therapeutic potency in animals, including the severely affected dKO mice [206,207].

Interestingly, multi-exon skipping has been proposed as a strategy that could benefit over 60% of DMD patients [208]. This approach utilises a cocktail of oligos targeting sites between exons 45-55 for exclusion of the whole hot-spot region. Aoki *et. al* successfully used a mixture of 10 PMO ASOs to restore up to 15% of dystrophin in the *mdx52* mouse model, which improved the muscle strength and histopathology [209]. In contrast, a similar study utilising 2'-O-methyl phosphorothioate ASOs in DMD patient myoblasts resulted in a minimal efficiency of the targeted region skipping [210]. The multi-exon skipping strategy has not yet reached the clinical trial stage.

ASO	Target exon	Dystrophin protein restoration	Chemistry	Company	Approval Year	Source
Eteplirsen	51	0.9% after 180 weeks	PMO	Sarepta	FDA 2016	[197]
Golodirsen	53	1% after 48 weeks	PMO	Sarepta	FDA 2019	[8,211]
Viltolarsen	53	5.9% after 25 weeks	PMO	NS Pharma	FDA 2020	[10,198]
Casimersen	45	4.25% after 48 weeks	PMO	Sarepta	FDA 2021	[7,212]

Table 1.1 Approved antisense oligonucleotide-based therapeutic strategies for DMD.

A key advantage of clinically approved PMO chemistry is the favourable safety profile resulting from their low plasma protein binding properties [192,193]. However, the same characteristic leads to rapid plasma clearance of the PMO from the system [192,193,200,213,214]. This results not only in the requirement for weekly dosing for prolonged periods but also in limited uptake by targeted cells. As such, the efficient delivery of PMO to the muscle (and especially heart) presents a significant challenge to the field. In addition to different ASO chemistries designed for improved delivery and target engagement, other approaches have been developed to overcome these issues. One of the most promising technologies for improved tissue targeting and uptake is conjugation of the PMO with cell-penetrating peptides (CPP) [213,214]. CPPs are short (< 30 amino acids), often positively charged sequences that possess the remarkable ability to cross cell membranes, making them valuable tools for delivering therapeutic molecules [215]. An extensive series of peptide-conjugated PMOs (PPMOs) has been developed and pre-clinically tested in the context of DMD [213]. In comparison to unconjugated PMOs, PPMOs demonstrate enhanced efficacy as splicing correctors at lower doses, enabling systemic administration to achieve widespread dystrophin restoration in skeletal muscles [213].

Currently, three clinical trials of PPMO for DMD are ongoing. These are sponsored by Sarepta Therapeutics (NCT04004065, SRP-5051 Vesleteplirsen), PepGen (NCT06079736, PGN-EDO51) and Entrada (ENTR-601-44-101, ENTR-601-44).

1.3.2 Gene replacement therapy

Gene replacement therapy for DMD aims to deliver a functional copy of the dystrophin gene into the muscle. Recombinant adeno-associated viral (AAV) vectors have emerged as a leading approach for gene transfer in DMD [216–218]. AAV is a single-stranded DNA virus of low immunogenicity in humans and is thus considered safe for therapeutic purposes [218]. Such viruses have been extensively used in therapeutic development with several AAV-based therapies approved, including Delandistrogene moxeparvovec (Elevidys) which

recently received marketing authorisation in the US for the treatment of DMD patients aged 4-6 [9]. Elevidys delivers a highly internally deleted, sequence-optimised version of the dystrophin protein (138 kDa) lacking spectrin-like repeats 4-23, as well as the C-terminal domain [219]. Such extensive manipulation of dystrophin mRNA sequence is necessary due to the limited packaging capacity of AAV vectors of ~ 4.7 kb [218]. As such, delivery of full-length dystrophin cDNA (~ 14 kb) is not feasible, and the strategy utilises shorter mini- and micro-dystrophins. These are highly internally truncated versions of the protein containing the most important domains (including the N-terminus and the cysteine-rich domain) [6,216]. The usefulness of mini- and micro-dystrophins stems directly from observations in BMD patients who carry large multi-exon deletions but exhibit relatively mild symptoms, showing that not all dystrophin domains are crucial for its function [24]. However, comparing the expression of full-length and truncated dystrophin constructs in *mdx* mice revealed that the truncated protein is less effective at preventing muscle degeneration [220]. As such, although internally deleted pseudo-dystrophins have therapeutic effects, their ability to phenocopy the functionality of the wild-type protein heavily depends on the construct design [220]. Multiple iterations of mini- and micro-dystrophin sequences have been investigated for the best efficiency [6,216]. Similarly, several different transgene promoters as well as AAV serotypes have been tested for improved tissue targeting [6,216]. In contrast to ASO-based therapeutics, AAV-micro-dystrophin therapy can in theory be applicable to all DMD patients, however in reality some exclusion criteria (patients with exon 8-11 deletions, pre-existing immunity to AAV virus) were introduced due to immune reaction to the transgene or presence of neutralizing antibodies against the AAV vector [221]. Several other clinical gene therapy clinical trials for DMD, utilising different micro-dystrophin constructs are currently ongoing (Table 1.2).

Notably, AAV-mediated gene therapies face several challenges beyond limited packaging capacity, including large-scale vector production and efficient tissue targeting [216]. The majority of natural AAV capsids transduce the liver very efficiently and thus tend

to accumulate in that organ [218]. As such, capsid modifications resulting in improved muscle targeting are being developed (e.g. MyoAAV) [222]. Importantly, AAV-mediated gene therapy presents safety problems associated with anti-vector immunity [223]. To achieve sufficient transgene expression in skeletal muscle and heart, extremely high doses of viral vector (i.e. 10^{14} vector genomes / kg of body weight) are being used [223]. While in mouse models the AAV vectors elicit minimal immune response, similar doses in humans can trigger significant immune responses such as complement activation and T cell-mediated toxicity [224]. This can further lead to serious complications such as myocarditis or fatal hepatotoxicity [224]. In fact, four patients have died in a AAV gene therapy trial for X-linked myotubular myopathy (developed by Astellas Pharma) due to progressive liver failure [223]. More recently, dosing was paused in a DMD micro-dystrophin gene therapy trial (sponsored by Pfizer, NCT04281485) due to the occurrence of a patient death one year after dosing [225]. Notably, this was the second death reported in a clinical trial investigating the PF-06939926 micro-dystrophin [225].

Name	Sponsor	Clinical trial ID	Phase	Primary completion date (estimated)
PF-06939926	Pfizer	NCT04281485	III	2024-04
SGT-001	Solid Biosciences	NCT03368742	I/II	2026-12
GNT0004	Genethon	2020-002093-27	I/II/III	undisclosed
RGX-202	REGENXBIO	NCT05693142	I/II	2025-12

Table 1.2 Current gene replacement clinical trials for DMD.

1.3.3 CRISPR-Cas9 gene editing

Clustered regularly interspaced short palindromic repeats (CRISPR) – CRISPR-associated protein 9 (Cas9) systems form a natural defence mechanism in bacteria and archaea [226,227]. They evolved to protect against invaders like bacteriophages by capturing fragments of foreign DNA during infection and incorporating them into the CRISPR elements of the bacterial genome [227–229]. The CRISPR element consists of short, identical DNA sequences (palindromic repeats) interspaced with unique, acquired, bacteriophage-derived spacer sequences [230,231]. Therefore, it comprises a heritable record of past infections that drives the adaptive genomic immune memory [227,228,232]. The CRISPR region is transcribed into precursor CRISPR RNA (pre-crRNAs) that are further cleaved into small ~57 nt long crRNAs [228]. In *Streptococcus pyogenes*-derived CRISPR-Cas9, this cleavage is facilitated by binding of the *trans*-activating CRISPR RNA (tracrRNA) [233]. Formation of the tracrRNA:pre-crRNA complex drives the RNase III-mediated cleavage of the pre-crRNA and facilitates subsequent Cas9 binding [233,234]. The Cas9 protein is an RNA-guided, bacterial DNA endonuclease [235]. The mature crRNA, formed from a 20-nt long guide unit, directs the Cas9 to the complementary DNA sequence [233]. Upon target recognition, Cas9 induces a double-strand break (DSB) within the guide-complementary region of viral DNA [226,228,234]. This results in an immediate, targeted disruption of the viral genome, effectively abrogating its replicative and functional capacity.

Although not naturally occurring in higher organisms, CRISPR-Cas9 has been successfully adapted for use as a powerful genome editing tool in eukaryotic cells [226]. This ground-breaking work by Emmanuelle Charpentier and Jennifer Doudna was awarded the 2020 Nobel Prize in Chemistry [236]. The main change introduced to the system was replacement of dual tracrRNA:crRNA with single, short guide RNA (sgRNA) chimera which can be designed to direct the Cas9 for DNA cleavage at a desired sequence of interest within the genome [226]. This created a simple, readily adaptable method which surpasses previously used genome engineering tools like TALENs (Transcription activator-like effector

nucleases) or ZNFs (Zinc finger nucleases) in its practicality, versatility, and affordability [226,237].

Within the eukaryotic cell, the Cas9-induced DSBs are resolved by one of the DNA repair pathways: non-homologous end joining (NHEJ) or homology director repair (HDR) [238]. The error-prone NHEJ joins the loose DNA ends with a high potential of introducing insertion-deletion mutations within the targeted region [238]. Conversely, HDR utilises the homologous DNA strand as a template to precisely repair double-strand breaks in a template-directed manner [238]. As such, CRISPR-Cas9 DSBs enable HDR-mediated precise mutation correction or NHEJ-driven indel formation that potentially corrects the disease-causing lesions. This capacity of CRISPR-Cas9 as a gene editing tool sparked significant interest in its therapeutic application for various diseases, including DMD [6,239,240].

In DMD, strategies of CRISPR-Cas9-mediated exon deletion, exon skipping, or exon reframing of the dystrophin gene are currently being investigated [6,239,240]. These can be achieved by either single (one sgRNA) or dual-cut (two sgRNAs) strategy and rely mostly on the NHEJ DNA repair pathway since HDR activity is negligible in post-mitotic cells and thus not applicable to the terminally differentiated myofibres [239,240]. The proof-of-concept study was performed by Long and colleagues in 2014 who successfully edited the dystrophin gene in *mdx* zygotes thus achieving dystrophin re-expression in all major muscle groups [241]. They used a dual-cut strategy where two sgRNAs flanking exon 23 facilitate excision of the mutated region and thus restoration of the dystrophin open reading frame [241]. Two years later, another three studies independently confirmed this strategy, restoring dystrophin expression up to 8% of the wild-type levels in *mdx* mice [242–244]. Another interesting approach used a panel of sgRNAs targeting multiple sequences with the exon 45-55 hot spot region for multi-exon exclusion [245]. Although potentially beneficial for approximately half of DMD patients (i.e. patients with mutations in 45-55 hot spot region), this method was noted to be significantly less efficient than the correction of a single exon

[240,245]. Encouragingly, studies employing a single-cut strategy with sgRNA targeting the exon 51 splice site demonstrated efficient exon skipping and gene reframing, leading to the production of nearly 90% of wild-type dystrophin levels in mice with exon 50 deletion [246]. Notably, this approach yielded similar results in a canine dystrophic model lacking exon 50, achieving a remarkable restoration of 90% of wild-type dystrophin expression [247].

Currently, Vertex Pharmaceuticals and Sarepta are conducting early-stage, pre-clinical development of CRISPR-Cas9-based therapeutics for DMD. However, a recent, first-in-human (*n* = 1) clinical trial evaluating safety and preliminary efficacy of CRD-TMH-001 compound was recently conducted (NCT05514249). The compound aimed to upregulate the cortical isoform of dystrophin using the modified dCas9 (“dead”) which is enzymatically inactive, but fused to a transcription activation protein VP64 and thus can induce the expression of the target sequence [248]. The compound was developed by Cure Rare Disease non-profit organisation. However, the 27-year-old patient developed severe adverse effects including acute respiratory stress and died 6 days after receiving treatment [249].

Importantly since currently developed strategies utilise AAV vectors to deliver CRISPR-Cas9 machinery components, these will face similar safety challenges as the gene replacement approach [224]. Moreover, inclusion of a bacterial protein in the system (i.e. Cas9) further complicates the safety profile of the gene editing approach, raising the risk of severe immune response and fatal adverse events [250]. Additionally, reliance on error-prone NHEJ mechanism for gene editing in non-dividing myofibers increases the risk of introducing non-productive indels and thus lowering the efficiency of genetic correction and rendering the myonuclei refractory to further manipulations [251]. Moreover, the off-target effects of the CRISPR-Cas9 system could lead to unintended or adverse alterations to the genome further resulting in changes in gene expression with unintended effects [250]. While the CRISPR-Cas9 strategy holds promise for eliminating the underlying cause of disease,

its widespread clinical implementation faces several challenges that must be overcome to ensure both safety and success on a large scale.

1.3.4 Cell therapy

Cell therapy for DMD is based on autologous or heterologous transplantation of genetically modified or healthy muscle precursor cells expressing functional dystrophin protein into the patient's muscle. It utilises large numbers of donor cells administered via intramuscular or systemic injection [6,252]. The transplanted cells undergo fusion with each other and existing myofibres leading to the formation of mosaic myofibres containing host and donor myonuclei. This approach was pioneered by Partridge *et al.* in 1986 who successfully transplanted healthy myoblasts into *mdx* muscles, obtaining mosaic myofibres expressing 30-40% of wild-type dystrophin protein [253,254]. The efficacy of the transplant was further enhanced to 60-80% dystrophin re-expression by muscle irradiation which abolished the proliferation of resident muscle stem cells [254]. Soon after, Law *et al.* injected healthy myoblasts (from culture or healthy donors) into the extensor digitorum brevis (EDB) muscle of DMD patients [255]. They observed an improvement in muscle tension and histopathology concluding that cell therapy is a safe and efficient method to alleviate pathological features of dystrophic muscle in patients [255]. This was followed by larger studies of intramuscular injections (up to 48 injections) of high numbers of healthy myoblasts (up to 5 billion) in DMD patients [256,257]. These initial results were encouraging as improvement in muscle strength and detection of dystrophin-positive myofibres was observed [255–257]. However, while most of the subsequent studies in DMD patients demonstrated an increase in dystrophin expression levels, the majority showed no evidence of muscle function restoration (reviewed in [258,259]). The consistently observed lack of efficacy of cell therapies was connected to limited migration and extensive death of donor cells as well as immune response towards injected myoblasts [252,259,260]. In fact, in a study by Skuk *et al.* multiple intramuscular injections of healthy donor cells resulted in very restricted production of dystrophin-positive myotubes and/or myofibres around the area of

injection accompanied by a great variability of dystrophin restoration levels among the patients [261]. Moreover, it was estimated that only ~ 1% of donor cells survive after transplant [256,262–264]. Given the fact that muscle is the largest tissue of the human body, poor survival of donor stem cells is especially challenging also from the perspective of donor cell production. Notably, besides myoblasts other donor cell types have been tested including $CD133^+$ stem cells, bone marrow mononuclear cells, mesangioblasts, mesenchymal stem cells or cardiosphere derived cells (CDCs) [258]. While myoblasts and satellite cells do not pass through endothelium of vascular cells some of the alternatives do (e.g. $CD133^+$ stem cells or mesangioblasts) which makes them suitable for systemic delivery [260].

Notably, a human clinical trial utilising mesangioblasts as donor cells demonstrated the safety of four consecutive intra-arterial infusions in DMD patients aged 8-12 years [265]. However, the efficacy of the treatment was minimal, with the donor cell engraftment efficacy calculated between 0 and 0.69% [265]. This was attributed to advanced muscle pathology in treated patients (i.e. lack of regeneration and pronounced fibrosis) as well as low total cell dose used, and effects of anti-inflammatory and immunosuppressive therapies on cell engraftment [265]. The results of that trial were interpreted as evidence that the cell therapy approach, targeting skeletal muscle is ineffective for DMD, which results in successful engraftment of only a small percentage of donor cells [266]. Currently a phase III clinical trial of CDCs (CAP-1002) developed by Capricor Therapeutics (HOPE-3, NCT05126758) is ongoing [267]. CDCs are cardiac progenitor cells that have been shown to benefit cardiac and skeletal muscle function through the release of cargo-containing exosomes (i.e. extracellular vehicles) in *mdx* mice [267]. They are believed to slow the disease progression through anti-fibrotic and anti-inflammatory properties rather than by direct restoration of dystrophin protein [267]. Results from phase II trial demonstrated improvement in cardiac and upper limb function in DMD patients [267].

1.3.5 Utrophin upregulation therapies

Due to high sequence homology driving the similarities in function between utrophin and dystrophin, upregulation of utrophin expression in DMD patients is considered a promising therapeutic approach [6]. While basal utrophin expression in DMD patients is insufficient to protect against muscle pathology, enhanced utrophin levels are postulated to have a significant clinical benefit. The role of utrophin in the modulation of pathology progression in mice was clearly shown by knock-out and overexpression studies in *mdx* animals [88,138]. While dramatically worsened pathology progression results in premature death of dKO animals, utrophin overexpression on a dystrophin-null background results in restoration of DAPC at the skeletal muscle and diaphragm sarcolemma, restoration of normal muscle histology, improvement in muscle function as well as calcium homeostasis [88,138,139,268]. These initial studies in mice paved the way for identification and characterisation of small molecules capable of utrophin upregulation in human muscle. In 2011, out of thousands of potential candidates, SMT C1100 (Ezutromid, developed further by Summit Therapeutics) was identified through a luciferase reporter, cell-based assay designed to activate the human utrophin promoter [269]. Daily oral dosage of Ezutromid over 28 days resulted in an increase in utrophin mRNA and protein levels in skeletal muscle, and heart of *mdx* mice and a significant reduction of pathological features as well as an improvement in muscle function [269]. Subsequent phase I studies in healthy volunteers and DMD patients reported a favourable safety profile of Ezutromid but revealed high variability in target exposure with DMD patients exhibiting lower plasma concentrations of the drug than expected [270–272]. Phase II interim results were encouraging and demonstrated utrophin upregulation as well as a decrease in muscle damage, however, the study failed to meet the primary and secondary endpoints leading to discontinuation of the clinical development [273]. This was later attributed to the rapid metabolism of Ezutromid and thus increased clearance in DMD patients which resulted in a lack of sustained clinical

benefit in DMD trials [272,274]. Currently, second-generation utrophin upregulation compounds with improved physicochemical properties are being developed [275].

Notably, using small molecules to upregulate utrophin has several benefits over other DMD therapeutic strategies. Firstly, this is a mutation-independent approach and thus applicable to all DMD patients. Secondly, in comparison to ASOs (e.g., Eteplirsen with a size of 10 kDa) and CRISPR-Cas9 machinery (Cas9 with the size of 160 kDa) small molecules are indeed small with size ranging from 0.2-0.5 kDa [276]. Moreover, small molecules exhibit generally good intracellular delivery and bioavailability in comparison to ASOs or gene therapy and can be administered orally which makes them easily accessible to a wide range of patients [276].

1.4 The myofibre as a therapeutic target

Mature human myofibres are long multinucleated cells that support muscle contraction [277]. Each cell is built from ~ 2,000 protein-dense myofibrils which occupy most of the cytoplasmic volume while the rest of the cell organelles are squeezed between them or, as in case of nuclei, against the sarcolemma [277]. Myofibrils are comprised of sarcomeres, which are formed during the stepwise process of myofibrillogenesis (Figure 1.3) [278–281]. Within the sarcomere, actin filaments extend inwards from the Z-disc towards the centre, while thick myosin filaments are arranged in a staggered pattern, anchored to the Z-disc with titin (Figure 1.3) [282]. In the centre of the sarcomere, the M-line (M standing for myosin) stabilises the myosin filaments. The M-line composition is dynamic and variable in different muscle types [283]. A single sarcomere is delineated by the Z-disc. The Z-disc is composed of various proteins including titin, telethonin and α-actinin, which are directly connected with the multiprotein structure of the costamere (Figure 1.3 and Figure 1.4) [61,282,284].

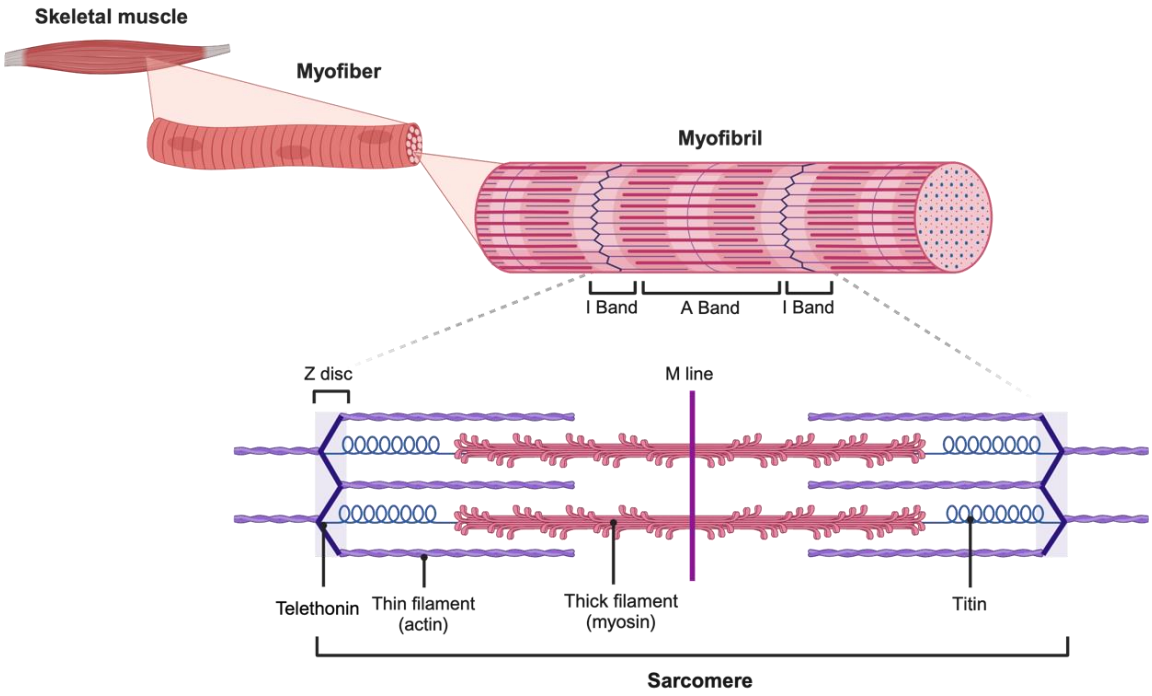

Figure 1.3 Structure of the skeletal muscle.

Skeletal muscle is composed of elongated syncytial myofibres which cytoplasm (sarcoplasm) is packed with protein-dense myofibrils. Myofibrils are comprised of sarcomeres - the fundamental contractile units. Z-disc demarcate each sarcomere, which contains a precisely arranged lattice of thick myosin and thin actin filaments. The critical interaction between these filaments underlies muscle contraction. The giant protein titin is anchored in Z-disc and extends to the M-line maintaining the precise alignment and length of the sarcomere. Telethonin interacts with titin N-terminus on Z-discs further stabilises the contractile unit structure. I-band (isotropic band) corresponds to the thin filament region of the sarcomere. A-band (anisotropic band) comprises both thin and thick filaments. Image created with BioRender.com.

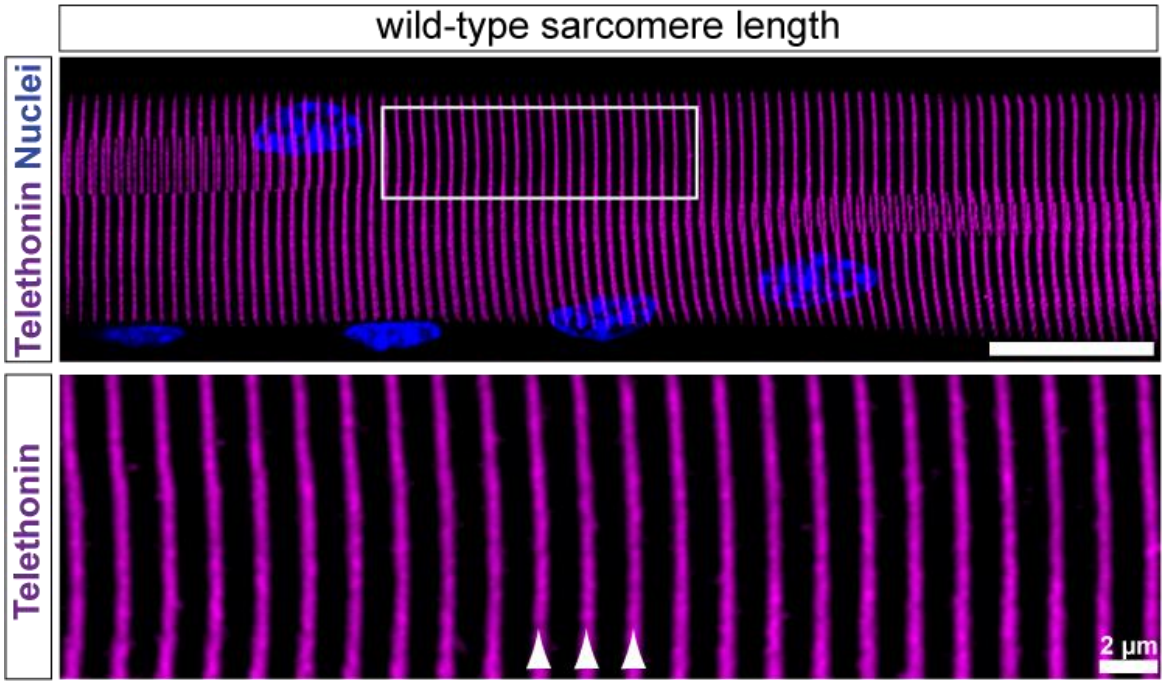

Figure 1.4 Sarcomere organisation in healthy mouse myofibre.

Representative immunostaining for telethonin in single myofibre isolated from EDL muscle of wild-type mouse. The bottom image represents enlarged inset marked with a white rectangle on the top image. White arrows indicate three consecutive Z-discs. Images taken at ×40 magnification. Scale bar represents 20 µm (top), and 2 µm (bottom). 2 µm is the average sarcomere length.

Sarcomere formation occurs concurrently with myoblast fusion [285]. Initially, Z-bodies containing α-muscle actinin accumulate at the site of protocostamere which is comprised of the integrin-vinculin-talin multiprotein complex [286]. Z-bodies, together with the muscle actin and non-muscle myosin II, form pre-myofibrils where they exhibit a random or oblique orientation with respect to the longitudinal axis of the cell [280,287]. Pre-myofibrils grow and mature into nascent myofibrils which include the incorporation of titin and the replacement of non-muscle myosin with muscle myosin II. At this stage, nascent myofibril organisation is non-striated due to the unordered overlap of thick myosin filaments [280,285]. Finally, the Z-bodies transform into Z-discs, and muscle myosin II filaments become precisely aligned within the A-bands (anisotropic bands) encompassing the

segment between two neighbouring Z-discs (Figure 1.3) [279,280,285]. This well-defined organisation of proteins creates the characteristic striated pattern of mature myofibrils with alternating light and dark bands [280,285]. The length of a single mature sarcomere (i.e. the distance between Z-discs) ranges from 0.5 μm in pre-myofibrils to 2-2.5 μm in mature myofibrils (Figure 1.4) [279,281,288].

The myofibre cytoskeleton forms a complex network composed of microtubules, intermediate filaments (primarily desmin), and actin microfilaments [289]. The microtubules can be divided into two domains based on their localisation: cortical microtubules surrounding the myofibre centre (core), found within the limited space between the contractile units and sarcolemma and sporadic longitudinal microtubules located in the myofibre core [290,291]. In healthy myofibres, cortical microtubules form a well-organised, grid-like network with distinct longitudinal and transverse components (Figure 1.5) [49,290,292–294]. The extensive cortical microtubule network is formed through the polymerisation of α/β-tubulin dimers nucleating from the microtubule organising centre (MTOC) [295]. In myoblasts, similarly to other mononucleated, proliferating cells, the MTOC is organised at the single centrosome (nuclear membrane-associated structure composed of two centrioles) [293,296]. However, upon differentiation, the MTOC is drastically redistributed with centrosome proteins (e.g. PCM-1) re-localising to the nuclear envelope but also being dispersed through the myofibre [291,293,294,296,297]. Accordingly, polarised Golgi complexes, which also serve as MTOC, become fragmented into Golgi elements (GE) which spread throughout the cell and form characteristic GE rows between the myonuclei [291,296,298]. The cortical microtubule network aligns with the sarcomeres at the Z-disc and M-lines and is thought to act as a scaffold for positioning myosin filaments during sarcomere formation [291,297,299]. Notably, inhibition of microtubule network polymerisation resulted in disassembly of myotubes into mononucleated cells *in vitro* [300]. Recent studies have demonstrated essential role of the microtubule network for the correct active transport of mRNAs and proteins within both cardiac and skeletal muscle cells

[301,302]. Importantly, dystrophin plays a role in stabilisation of the network, through direct interaction of spectrin-like repeats 20-23 with microtubules [49,50]. Accordingly, disruption of the microtubule network in dystrophic animals has been previously reported [49,50,290,292,294,303].

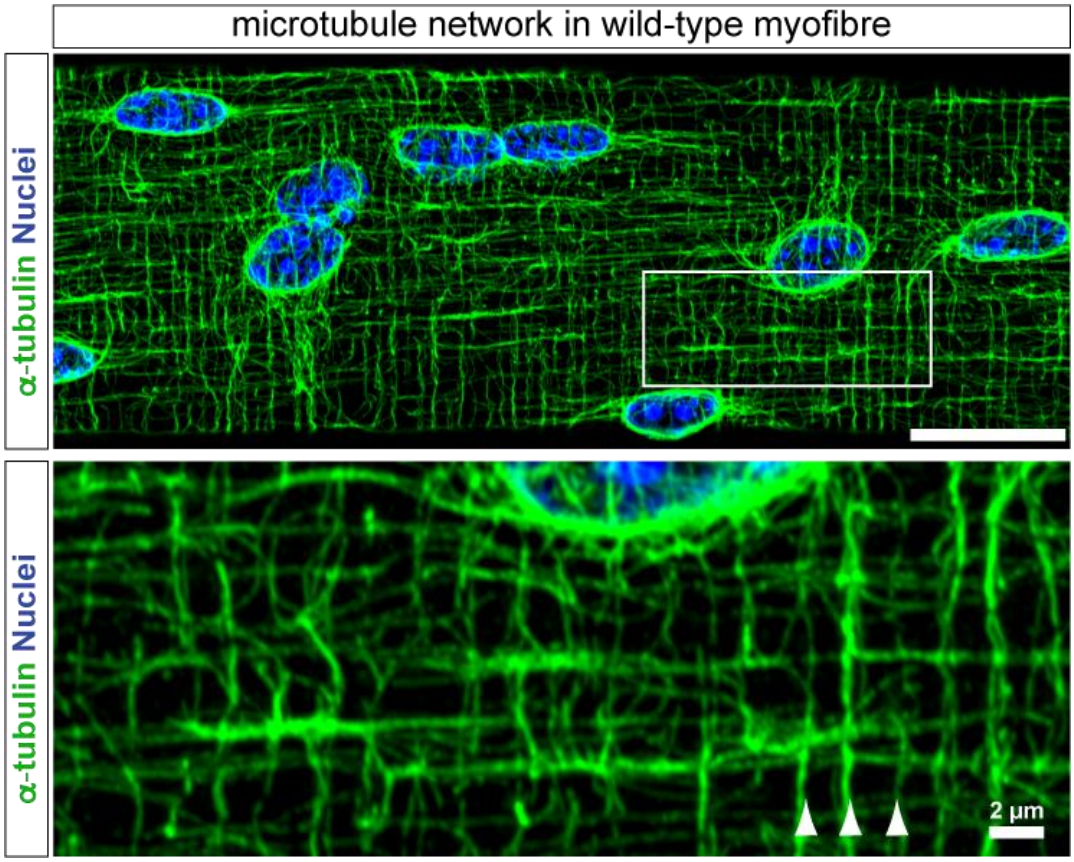

Figure 1.5 Microtubule network organisation in healthy mouse myofibre.

Representative immunostaining for α-tubulin polymers in single myofibre isolated from EDL muscle of wild-type mouse. The bottom image represents enlarged inset marked with white rectangle on the top image. White arrows indicate the overlap between three consecutive Z-discs. Images taken at ×40 magnification. Scale bar represents 20 μm (top), and 2 μm (bottom).

Additionally, at the mature myofibre sarcolemma, costameres are remarkably organised, resembling a rib-like lattice integrated into the membrane. They are positioned overlaying the Z-discs and M-lines of the sarcomere fulfilling the roles of mechanical anchor, force transduction and signalling hub [61]. Accordingly, dystrophin presents a characteristic organisation at the sarcolemma, with the majority of the protein aligning with the Z-disc, M-line, and microtubules, but also present in the longitudinal lines (Figure 1.6) [49,291].

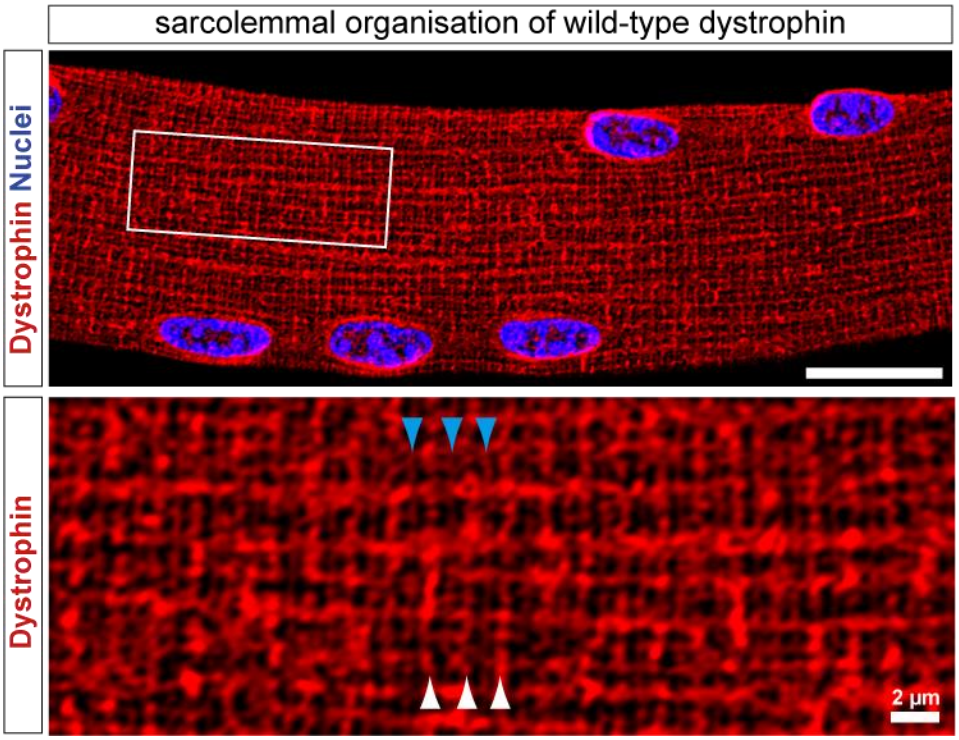

Figure 1.6 Dystrophin organisation in healthy mouse myofibre.

Representative immunostaining for dystrophin in single myofibre isolated from EDL muscle of wild-type mouse. The bottom image represents enlarged inset marked with white rectangle on the top image. White arrows indicate the overlap between three consecutive Z-discs. Blue arrows indicate the overlap between three consecutive M-lines. Images taken at × 40 magnification. Scale bar represents 20 µm (top), and 2 µm (bottom).

1.4.1 The myonuclear domain theory

The peripheral positioning of myonuclei is a hallmark of mature muscle cells [281]. Most myonuclei are 10 μm in diameter and are evenly dispersed throughout the myofibre ~ 30 μm apart [281,302,304]. With a myofibre length of up to 45 cm in the adult body, a large number of nuclei (~ 100 nuclei/mm) is needed to support the whole cytoplasmic volume of the cell [277,305]. The myonuclear domain theory posits that every nucleus within the syncytial myofibre controls a specific amount of cytoplasm that surrounds it [306]. This concept of nuclear territories was proposed over 50 years ago [306]. Since then, the myonuclear domain has been mostly studied in the context of myofibre hypertrophy and atrophy [305,307,308]. Recent work has provided some valuable insights into nuclei-dependent myofibre growth, where the expansion of myofibres relies on the accretion of nuclei to maintain the cytoplasm-to-DNA ratio [305,308]. These studies show that maintaining the correct myonuclear domain is a crucial feature of myofibre physiology. Conversely, others have reported that the myonuclear domain is flexible, showing that myofibres can adapt to reduced nuclear numbers through upregulation of global mRNA production in healthy mice [309]. This increase is not infinite, but rather capped at a certain volume referred to as the ‘myonuclear domain ceiling’ beyond which a single myonucleus is unable to effectively support the volume cytoplasm around it [307,310]. As such, it has been suggested that myonuclei do not synthesise mRNA at their full capacity in normal conditions and thus can increase their transcriptional output to a certain extent when needed [310].

Perhaps the best-known examples of myonuclear domain restriction of gene expression products come from research of highly specialised NMJ myonuclei [311–314]. NMJ is a chemical synapse formed between a motor neuron and a myofibre which transmits the nerve impulse, triggering the muscle contraction [315–317]. Each myofibre is typically innervated by a single NMJ, which comprises approximately four nuclei expressing a unique set of genes essential for NMJ function [316]. For example, it is well-established that NJM

nuclei exhibit selective expression and clustering of acetylcholine receptors, which bind the motor neuron-secreted acetylcholine allowing for transmission of action potential through the muscle [311–314]. Additionally, several other studies in heterokaryon cell models demonstrated myonuclear-domain restricted localisation of gene expression products [318,319]. Pavlath *et al.* showed that sarcomeric MHC and 5.1H11 cell surface antigen proteins are expressed in the proximity of their myonuclei of origin in differentiated muscle heterokaryons *in vitro* [319]. Analogously, mRNAs encoding nuclear, cytoplasmic, or endoplasmic reticulum (ER)-bound proteins were shown to localise within 100 μm of the nucleus that produces them [318]. Nevertheless, the importance of the myonuclear domain concept has been relatively overlooked in the context of DMD therapeutics.

Notably, studies from our group have speculated that myonuclear domain theory might be directly applicable to dystrophin re-expressed at the sarcolemma upon CRISPR-Cas9-mediated gene editing treatment [251,320–322]. Specifically, it has been postulated that restricted dystrophin expression will be observed at the sarcolemma adjacent to the nucleus where successful editing event has occurred. Indeed, we have recently directly shown this in longitudinal sections of the dKO muscle treated with CRISPR-Cas9 machinery which exhibit within-fibre non-uniform, patchy dystrophin re-expression [251].

1.5 Myogenesis

Myogenesis is the process that supports muscle development and the regeneration of injured or diseased adult muscle (as in the case of DMD). During myogenesis, mononuclear muscle progenitors undergo cell cycle arrest and fuse together to form syncytial myofibres. This complex process is governed by a highly coordinated network of signalling molecules, transcription factors, and microRNAs (reviewed in [323,324]).

1.5.1 Embryonic myogenesis

During the early embryonic development in mice, a mesoderm-derived cluster of Pax3-positive muscle progenitor cells mark the regions where skeletal muscle will be established around embryonic day 8 [115,325]. At that point, cells commit to the muscle lineage and two waves of myogenic differentiation take place: primary (embryonic) and secondary (foetal) myofibre formation [326,327]. The primary myotubes, spanning from tendon to tendon, are formed by an autonomous and synchronic fusion of embryonic myoblasts [327]. These cells then serve as a scaffold for the second myogenic differentiation phase, whereby Pax7-expressing foetal myoblasts proliferate and fuse to each other as well as to the primary myotubes, forming secondary myofibres [326]. During the secondary myotube formation, neuromuscular and myotendinous junctions, as well as the basal lamina (a thin, non-cellular layer surrounding each myofibre, composed mainly of collagen and glycoproteins) are established [315,327]. Through further growth and nuclei accretion, secondary myotubes ultimately comprise most of the adult skeletal muscle tissue, while foetal $Pax7^+$ myoblasts establish the satellite cell pool [326]. Newly formed myofibres are characterised by expression of embryonic and neonatal myosin isoforms which are replaced by adult myosin a few days after birth [328]. At around the 3rd week of life, the myofibre formation process plateaus, the syncytia mature, and further adult muscle growth relies solely on the radial growth of the myofibre as well as the formation of new myofibril [115,315].

Myogenesis is orchestrated by a set of well-established myogenic regulatory factors (MRFs) which are tissue-specific, basic helix-loop-helix transcription factors. These include Myf5, MyoD, Myogenin, and MRF4 which are characterised by a conserved DNA binding domain motif that recognises the enhancer box of muscle-specific gene promoters [329]. At the onset of primary myofibre formation, progenitor cells commit to the myogenic lineage through activation of Myf5 and MyoD markers [329,330]. While these MRFs share a large subset of targets in proliferating myoblasts, they can exert different functions [331]. Myf5 is effective at regulating cell commitment and expansion, while MyoD is additionally capable of inducing differentiation by regulating expression of genes crucial for that process, including myogenin and myosin heavy chain (MHC) isoforms [331]. Beyond regulating myogenin expression, MyoD collaborates with it to drive terminal myofibre differentiation by regulating the expression of genes characteristic for that stage [332]. These include upregulation of the cell cycle inhibitor p21 leading to cell cycle withdrawal [333–335]. Subsequently, myogenin induces the expression of contractile apparatus proteins and regulates correct myoblast fusion [334]. Two myogenin-regulated proteins are crucial for the formation of syncytial myotubes: myomaker (*TMEM8C*) and myomerger (*MYMX*) [336,337]. Myomaker is a transmembrane protein that initiates cell fusion by promoting their adhesion and apposition, while myomerger promotes formation of the pore between two cells, which further expands allowing for two myoblasts to fuse [338,339]. Notably, immediately after myoblast fusion nuclei undergo localisation to the centre of the newly formed cell in a microtubule-driven process of centration [281,340]. Accumulated nuclei align longitudinally and subsequently spread before being dispersed to the periphery by contracting myofibrils [281,341].

1.5.2 Adult muscle regeneration

Adult muscle, unlike many other tissues, possesses a remarkable capacity to regenerate. This ability is maintained thanks to the presence of satellite cells (SCs) established during embryonic development which support muscle repair, including in DMD

[113,114]. In the healthy state, SCs (characterised by Pax7 expression) are mitotically quiescent and located between the sarcolemma and basal lamina [118]. Upon myofibre damage, injury-induced growth factors (e.g., insulin-like growth factors and fibroblast growth factors) and inflammatory signals (e.g., interleukin-6) induce the expression of MyoD triggering SCs re-entry into the cell cycle (i.e. SCs activation) [342]. Proliferating SCs express Pax7, Myf5, and MyoD (with peak MyoD induction 24 hr after activation) which are marks of myogenic lineage commitment [118]. Pax7 is subsequently downregulated while, analogously to embryonic development, myogenin and MyoD trigger terminal differentiation and satellite cell fusion [118,343]. Accordingly, recently formed myofibres in adult muscle can be identified by expression of embryonic myosin forms and/or utrophin protein, in addition to the central localisation of nuclei [102,328].

Notably, SC divisions can be symmetric or asymmetric [323]. During symmetric cell division, satellite cells replicate to generate two daughter cells with identical stem cell potential. In contrast, asymmetric cell division produces one committed muscle progenitor differentiation and one self-renewing stem cell [344]. This is important for long-term stem cell pool maintenance, while simultaneously generating progenitors for immediate muscle repair. Notably, dystrophin protein has been reported to regulate asymmetric division of SCs [345]. Specifically, dystrophin protein was shown to interact with Mark2, thereby ensuring the correct cell polarity and mitotic spindle (i.e. the microtubule-based chromosome separation machinery) orientation [345]. Accordingly, SCs of *mdx* animals were shown to exhibit diminished asymmetric division rates alongside a loss of polarity and defective mitotic spindle formation [345]. As such, dystrophin-null satellite cells are considered defective (i.e. not able to produce sufficient amount of dedicated muscle progenitors) and thus contribute to the dystrophic pathology [121,345]. However, a study by Boldrin *et al.* provided contrasting results whereby SCs isolated from young and aged *mdx* mice transplanted into the pre-irradiated 3-week-old *mdx* mice showed that these cells retain their

regenerative capacity regardless of age [121]. As such, it appears that intrinsic nature of the dystrophic environment (i.e. satellite cells niche) contributes to SCs dysfunction [344].

1.6 MicroRNAs in myogenic differentiation and disease

1.6.1 MicroRNA biogenesis and function

MicroRNAs (miRNAs) are short, ~ 22 nucleotides (nt) long, endogenous, non-coding RNAs that are crucial for post-transcriptional gene expression regulation in all eukaryotic cells [346]. They drive the RNA interference (RNAi) mechanism within the cell, guiding an assembly of effector proteins to target mRNA, subsequently inducing its silencing [347].

miRNAs are widely expressed and transcribed from various genomic regions: predominantly from introns, but also from exons and intergenic sequences [348,349]. Their biogenesis begins with the transcription of primary-miRNA (pri-miRNA) by RNA polymerase II, producing a precursor transcript that can be up to several kilobases in length [349,350]. Pri-miRNAs are subsequently processed in the nucleus by the RNase III enzyme DROSHA and DGCR8 (DiGeorge syndrome critical region gene 8), which cleaves off a ~70 nt long stem-loop precursor-miRNA (pre-miRNA) [349,351]. Pre-miRNAs are then exported to the cytoplasm by exportin-5 (XPO5) [352], where its terminal loop is cleaved by the second RNase III enzyme Dicer [353]. The released miRNA duplex is loaded onto the Argonaute protein (AGO), which comprises a functional centre of the RNA-induced silencing complex (RISC) [354]. Upon AGO loading, one of the miRNA duplex strands, known as the passenger strand, is passively discarded and degraded [355]. The remaining, guide strand, directs the mature RISC to mRNA targets through complementary base pairing.

More than 60% of human protein-coding genes have a miRNA binding site located in 3' untranslated region (3' UTR) of the mature mRNA [356]. Upon miRNA binding, the target can be silenced through various mechanisms that include translational repression,

direct cleavage (slicer activity of AGO2), and slicer-independent transcript downregulation. The specific mechanism of miRNA action depends not only on the degree of miRNA-mRNA mismatches but also AGO isoform incorporated into the RISC complex [357–360]. Mammals ubiquitously express four AGO proteins (AGO1–4) [358]. While all AGO isoforms incorporate small RNA duplexes, only AGO2 has a catalytic endonuclease activity allowing for direct cleavage of the target mRNA [358,361]. Such a mechanism requires extensive (i.e. full complementarity) base pairing between miRNA and target, limiting it to highly complementary interactions [362]. Nevertheless, the majority of guide miRNAs bind to target sites with mismatches, triggering translational repression and mRNA degradation through alternative, indirect mechanisms [357].

1.6.2 Regulation of myogenic differentiation by microRNAs

The majority of miRNAs exhibit variable but widespread expression throughout the body. However, certain miRNA subsets exhibit more tissue-restricted patterns of expression [363]. As such, muscle-enriched set of miRNAs: miR-1, miR-133, miR-206 (myomiRs) are crucial for correct muscle formation [324,364,365]. Driven by the central regulators of myogenesis, myomiRs are upregulated during muscle differentiation and regeneration [366–370].

Two miRNA subfamilies: 1) miR-1 and miR-206, and 2) miR-133 (miR-133a-1, miR-133b) play a crucial role in regulation of myogenesis [371,372]. miR-133a and miR-1 are co-transcribed from two, identical bi-cistronic clusters: miR-133a-1/miR-1-2 and miR-133a-2/miR-1-2 on chromosomes 18 and 2 respectively [372,373]. Similarly, miR-206 is co-expressed with miR-133b from one locus located on chromosome 1 [372–374]. While miR-133a/miR-1 are expressed in both skeletal and cardiac muscle, miR-206/miR-133b expression is restricted only to skeletal muscle [373–375]. The mature members of miR-1 and miR-133a have identical sequences within subfamilies, while miR-133a differs from miR-133b by one nucleotide at the 3' end [372,373]. Sequences of miR-206 and miR-1 differ by four nucleotides, although their seed sequence remains the same resulting in a similar

pool of targets [374]. Given their distinct muscle tissue specificity, collectively these microRNAs are labelled as myomiRs.

MyoD and myogenin directly drive the expression of myomiRs by binding to their promoter regions [376,377]. This regulation coincides with the observed increase in myomiRs abundance during muscle development in both humans and mice [368,375]. miR-1 and miR-206 share the same seed sequence, allowing them to regulate expression of Pax7 and connexin 43, and thus impacting lineage commitment, communication, and fusion of myogenic precursors [369,375,378]. Both miRNAs directly downregulate histone deacetylase 4, facilitating the expression of MyoD controlled genes [378–380]. Additionally, miR-206 specifically induces cell cycle withdrawal by downregulating DNA polymerase α1, thereby inhibiting DNA synthesis [369]. Notably, miR-206 has been shown to bind and downregulate utrophin mRNA, consistent with developmental pattern of utrophin expression [92,377]. In contrast, miR-133 plays an antagonistic role, inhibiting the expression of terminal differentiation markers through increased myoblast proliferation [380]. This is achieved through repression of serum response factor which is a transcription factor positively regulating myogenic differentiation [380]. As such, inhibition of miR-1 and miR-206 but not miR-133 results in continued DNA synthesis and lack of differentiation markers expression [369].

As in the case of MRF expression, myomiRs are indispensable for correct adult muscle regeneration. Their critical role is supported by the fact, that Dicer-null satellite cells exhibit significantly increased cell death and diminished differentiation upon activation [378]. Notably, while most myomiRs are upregulated in activated satellite cells, their expression is markedly reduced in injured and dystrophic mouse skeletal muscle [378]. Additionally, premature induction of miR-1 and miR-206 restricts satellite cell proliferation and induces differentiation by limiting Pax7 expression [378].

1.6.3 miRNA in DMD pathology

Given their importance for correct muscle development, it is not surprising that myomiRs expression is dysregulated in many muscle disorders including DMD [365,366,381]. Multiple studies have reported changes in myomiR expression in the muscles of DMD patients and animal models relative to healthy controls [108,382,383]. Our group and others demonstrated that miR-206 is significantly upregulated in most of the dystrophic mouse tissues, including the heart and diaphragm, at 8 weeks of age [108,383]. In contrast, miR-1 expression is reduced in most dystrophic mouse tissues at 8 weeks of age [108]. This agreed with a previously published study by Yuasa *et al.* who also showed that miR-1 levels in *mdx* TA muscle remain steady at later time points [383]. Interestingly, miR-133a levels are relatively unchanged or modestly downregulated in *mdx* tissues [108,383]. Similar myomiRs expression profiles were obtained in the dystrophic $CXMD_J$ canine model [383].

Intriguingly, results from our group demonstrated that despite variation in expression profiles across dystrophic tissues, all three myomiRs show a remarkable ~ 50-fold upregulation in *mdx* serum [108]. This is supported by several independent studies which consistently reported elevated serum myomiR levels in both DMD patients and animal models [107,384–389]. The presence of serum myomiRs in dystrophic conditions has typically been ascribed to passive leakage from damaged myofibres [384,385,388,389]. As such, serum myomiRs are usually thought to mirror the extent of myonecrosis in dystrophic muscle [381,384,390]. Several studies have investigated the potential of circulating myomiRs as biomarkers for DMD progression, with inconclusive results [384,387,389,391]. Reported correlations between serum myomiRs and the North Star Ambulatory Assessment (NSAA) functional test score, commonly used to measure disease progression in DMD patients, have been inconsistent between studies [387,391]. However, one of the studies demonstrated a higher level of serum myomiRs in ambulant vs. non-ambulant DMD patients [387]. A more recent study showed a positive correlation between circulating myomiRs and

lower limb distal muscle strength, regardless of patient age [384]. Moreover, similarly to CK, a negative correlation between serum myomiRs levels and DMD patient age was also reported [387,389,392]. Nevertheless, larger scale studies are needed to definitively establish the relationships between DMD progression and serum myomiRs abundance.

Although elevated serum CK levels are used to diagnose neuromuscular diseases including DMD, these peak in early childhood and progressively decrease after 6 years of age in DMD patients [393,394]. This is connected to the replacement of functional muscle with fibrotic tissue in patients [394]. As such CK levels are not suitable to measure the disease progression or response to therapy. Notably, several studies from our group reported serum myomiRs restoration after single-dose PPMO-mediated exon skipping in *mdx* mice [107,108,320,395]. Similar results were obtained with chimeric AAV antisense U1 small nuclear RNA (U1-snRNA) restoration of dystrophin by exon skipping [396]. Other disease interventions, e.g. reconstitution of NO signalling through gene transfer of constitutively active endothelial NOS (eNOS) also restored the myomiR signature towards wild-type levels [382]. Based on these results, circulating myomiRs have been proposed as effective pharmacodynamic serum biomarkers, that mirror the effective dystrophin restoration in muscle upon therapeutic interventions [390].

1.7 Thesis aims and hypotheses

In this thesis, I hypothesise that:

1. Dystrophin distributed non-uniformly at the sarcolemma exerts profound changes on the myofibre morphology and biology, leading to an intermediate cell phenotype (i.e. between healthy and dystrophic). Furthermore, I propose that this pattern of dystrophin expression will not prevent myofibre turnover due to the presence of sarcolemma regions unprotected by dystrophin.
2. ASO-mediated exon skipping of mutant dystrophin will result in a uniform dystrophin expression at the sarcolemma. Moreover, dystrophin restoration will result in a dose-dependent restoration of DMD serum biomarkers towards wild-type levels.
3. Upregulation of myomiRs during myogenic differentiation *in vitro* occurs mainly in the nuclear compartment of the cells.

2 Materials and methods

2.1 Animal work

Animals were housed in the University of Oxford Biomedical research building (until November 2023) and Institute of Developmental and Regenerative Medicine animal facility (from November 2023). All experimental procedures were authorised and approved by animal facility managers and UK home office, under the project license number PP6777529 in accordance with the Animals (Scientific Procedures) Act 1986. Animals were housed in groups in individually ventilated cages under 12 hr light / 12 hr dark conditions with food and water provided *ad libitum*.

Xist$^{\Delta hs}$ animals were a kind gift from Prof. Annemieke Aartsma-Rus and Dr. Maaike van Putten (Leiden University Medical Center, Leiden, Netherlands) and Prof. Neil Brockdorff who developed the colony (Department of Biochemistry, University of Oxford, Oxford, UK) [164]. *Xist*$^{\Delta hs}$ animals contain a deletion of DNase hypersensitivity region upstream of P_1 promoter of the *Xist* gene encoding for lncRNA that drives the X-chromosome inactivation process. This results in preferential silencing of the mutation-containing chromosome. In heterozygous animals, mutated X-chromosome is inactivated in up to 90% of the cells [164].

Dystrophic *mdx52* (C57BL/6J129S-Dmd^{tm1Mok}) animals were provided by Dr. Yoshitsugu Aoki (Department of Molecular Therapy, National Centre of Neurology and Psychiatry, Tokyo, Japan). The line was generated by Dr. Motoya Katsuki group by a targeted replacement of exon 52 in the dystrophin gene with a neomycin resistance transgene cassette (in the antisense orientation) [140]. This disrupted expression of full-length Dp427m and shorter isoforms Dp260 and Dp160, but not Dp116 (peripheral nerves) and Dp71 (brain and retina).

Dystrophic *mdx* animals (C57BL/10ScSn-Dmd^{mdx}/J) were obtained from Jackson's Laboratory (Bar Harbour, ME, USA). These animals harbour a point mutation in the exon

23 of dystrophin gene causing a C-to-T transition at position 3185, resulting in a termination codon in place of a glutamine codon. This mutation i produces a truncated protein. [124].

Wild-type C57BL/6JOlaHsd (C57BL/6) and C57BL/10ScSn mice were obtained from Envigo (Inotiv; London, England) and served as control animals.

Dystrophin/utrophin double knock-out (dKO, 10ScSn.Cg-Utrn^{tm1Ked}Dmd^{mdx}/J) mice were obtained by inbreeding of the animals heterozygous for utrophin knock-out (Utrn^{tm1Ked}) and hemizygous or homozygous for dystrophin knock-out mutation (Dmd^{mdx}) [138]. The breeders were obtained from Jackson's Laboratory (Stock no: 014563). The utrophin knock-out line (Utrn^{tm1Ked}) was originally developed by Deconinck *et al.*, by 1.6 kb insertion of the neomycin cassette into exon 7 of the utrophin gene [397]. The *mdx* model was developed as described above.

2.2 Dystrophin and utrophin protein isolation and Western Blotting

2.2.1 Protein extraction from muscle tissue

Dystrophin protein quantification was performed on Tibialis anterior (TA) lysates. For protein extraction muscles were either homogenised using a Precellys homogeniser (Bertin Technologies, Paris, France (4 × 5,000 rpm, 30 sec), or through lysis of ~ 200 of 8 µm TA sections. In both cases, lysis was performed in modified Radio-Immunoprecipitation Assay (RIPA) buffer (50 mM Tris pH 8, 150 mM NaCl, 1% IGEPAL CA-630, 0.5% sodium deoxycholate, 10% SDS) containing 1× cOmplete proteinase inhibitors (Merck, NJ, USA). Homogenised samples were heated for 3 min at 4°C and centrifuged at room temperature for 10 min at 15,800 *g*. Protein concentration was measured using Pierce BCA Protein Assay Kit (Thermo Fisher Scientific, MA, USA) according to the manufacturer's instructions.

2.2.2 Dystrophin and utrophin Western Blotting

20-40 µg of total protein were mixed with NuPAGE sample reducing agent and NuPAGE LDS sample buffer (both Thermo Fisher Scientific) and denatured for 10 min at 75°C. Standards were prepared as a mix of defined different protein ratios isolated from

positive control, wild-type C57 and negative control, dystrophic (*mdx* or *mdx52*) mouse TA. All samples were loaded onto a pre-cast, NuPAGE 3 to 8% Tris-Acetate 1 mm gel (Thermo Fisher Scientific) and electrophoresis run at 130 V for 1 hr 45 min in 1× NuPAGE Tris-Acetate SDS Running Buffer (Thermo Fisher Scientific). Protein was electrotransferred onto 0.45 µm polyvinylidene fluoride (PVDF) membrane (Merck) for 1 hr at 30 V followed by 1 hr at 100 V in 1× NuPAGE Transfer Buffer (Thermo Fisher Scientific) supplemented with 0.1 g/l of SDS (Sigma-Aldrich, MO, USA) and 20% methanol. To assess the transfer efficiency, membrane was rinsed with MQ water and incubated in 0.0005% w/v Fast Green stain (Sigma) diluted in wash solution (6.7% acetic acid, 30% methanol, 63.3% ddH_2O). Total protein was visualised using a ChemiDoc Imaging system (Bio-Rad, CA, USA) measuring fluorescence at 700 nm. The membrane was then rinsed in water and blocked with Odyssey blocking buffer (LI-COR Biosciences, NE, USA). Membranes were incubated with mouse anti-dystrophin, mouse anti-utrophin or mouse anti-vinculin primary antibody (Table 2.3) overnight in Odyssey blocking buffer + 0.1% Tween-20 v/v (Sigma-Aldrich) at 4°C. Membranes were washed in tris-buffered saline buffer with 0.1% Tween-20 v/v (TBST) and incubated with anti-mouse IgG horseradish peroxidase (HRP) linked antibody (Table 2.3) in blocking buffer + 0.1% Tween-20 at room temperature for 1 hr. Chemiluminescent signal was detected using Clarity Western electrogenerated chemiluminescence (ECL) substrate (Bio-Rad). If membrane re-probing was necessary for the detection of proteins of similar molecular mass (e.g. dystrophin and utrophin) or using different antibodies from the same host, the membrane was stripped in 0.2 M sodium hydroxide (NaOH) for 30 min - 2 hr at room temperature. Stripping of secondary antibodies was confirmed by additional chemiluminescence detection. Subsequently, blocking step, primary and secondary antibody incubation and HRP-based detection were performed as described above.

2.3 Serum miRNA analysis

2.3.1 Serum collection

Serum was harvested from the jugular vein blood sample collected into capillary blood collection tube Microvette CB 300 (Sarstedt, Nümbrecht, Germany) immediately after animal was culled. Samples were allowed to clot for 30 – 60 min at room temperature and centrifugation at 10,000 *g* for 10 min at room temperature. Serum supernatant was transferred into a new tube and stored at - 80° C until ready for analysis.

2.3.2 Serum RNA extraction

Serum miRNAs were quantified using the small RNA TaqMan method, described in detail previously [398,399]. RNA was extracted from 50 µl of serum with TRIzol LS (Thermo Fisher Scientific) according to the manufacturer's instructions with minor modification. Specifically, 150 µl RNase-free water (Life Technologies, CA, USA) was added to the mixture to increase the volume of aqueous phase. Additionally, 3 µl of 5 nM exogenous spike mix was added per sample. The exogenous spike mix is an equimolar mixture of synthetic 5′-phosphorylated RNA oligonucleotide mimics of *C. elegans* and *A. thaliana* miRNAs (Table 2.1) purchased from Integrated DNA Technologies (IDT, Leuven, Belgium), and allowed to control for variation of RNA extraction from biofluids. The RNA was precipitated in isopropanol with addition of 1 µl of RNAse-free glycogen (Roche, Welwyn Garden City, UK) for increased extraction efficacy. RNA pellets were washed twice with 75% molecular biology grade ethanol (EtOH). The pellets were air dried at room temperature, 30 µl of RNase-free water (Life Technologies) was added and samples were incubated at 55°C for 10 min, to improve the RNA solubilisation. RNA samples were stored at - 80°C.

Exogenous miRNA	Sequence (5' to 3')
cel-miR-39-3p	UCACCGGGUGUAAAUCAGCUUG
cel-miR-54-3p	UACCCGUAAUCUUCAUAAUCCGAG
cel-miR-238-3p	UUUGUACUCCGAUGCCAUUCAGA
cel-miR-2-3p	UAUCACAGCCAGCUUUGAUGUGC
cel-lin-4-5p	UCCCUGAGACCUCAAGUGUGA
ath-miR159a	UUUGGAUUGAAGGGAGCUCUA

Table 2.1 Sequences of exogenous spike-in RNAs used in this study.

2.3.3 Serum miRNA RT-qPCR

10 µl of serum RNA was reverse transcribed (RT) using the Applied Biosystems TaqMan MicroRNA Reverse Transcription Kit (Thermo Fisher Scientific) according to manufacturer's instructions. The assay employs miRNA-specific stem-loop primers, which binds and extends 3' end of miRNA facilitating binding of universal reverse primer along with miRNA specific probe and forward primer in subsequent qPCR amplification step (Figure 2.1, [398]). The RT product (complementary DNA, cDNA) was diluted 1:5 in RNase free water. The qPCR was performed on Step-One Plus Real-Time PCR instrument with TaqMan Universal PCR Master Mix (both Thermo Fisher Scientific, Applied Biosystems) according to the manufacturer's instructions. 2 µl of RT product was used per 20 µl qPCR reaction. Transcript levels were quantified relative to external cel-miR-39 amounts using the Pfaffl method [400]. TaqMan miRNA assays used in the present study are listed in Table 2.2.

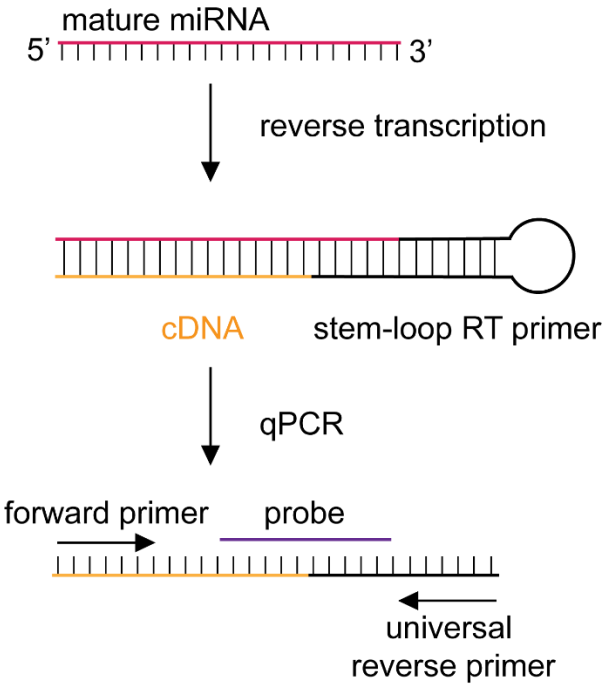

Figure 2.1 miRNA detection using TaqMan MicroRNA Reverse Transcription Kit

miRNA TaqMan assay	detection channel	assay ID
mmu-miR-1a-3p	FAM	002222
mmu-miR-133a-3p	FAM	002246
mmu-miR-206-3p	FAM	000510
cel-miR-39	FAM	000200

Table 2.2 List of miRNAs TaqMan assays used in this study.

2.4 Tibialis anterior immunofluorescence

2.4.1 Sample preparation and sectioning

Fresh frozen tibialis anterior (TA) muscles were mounted onto corks with Tissue-TEK optimal cutting temperature (OCT) Compound (Sakura, Japan) and cryosectioned (8 μm) in transverse and longitudinal orientations. Sections were transferred onto SuperFrost Plus microslides (VWR), left to dry for 10 min at RT, and stored at -80°C until ready to analyse.

2.4.2 Tissue immunofluorescence

On the day of staining, slides were air-dried and soaked in phosphate-buffered saline (PBS, Thermo Fisher Scientific) for 10 min at room temperature. Sections were blocked in blocking buffer composed of PBS supplemented with 20% foetal calf serum (FCS, Thermo Fisher Scientific) and 20% normal goat serum (NGS, MP Biomedicals, CA, USA) for 2 hr room temperature. Subsequently, slides were incubated with primary antibodies (listed in Table 2.3) in blocking buffer for 2 hr at room temperature. After washing 3 times with PBS slides were incubated with secondary fluorescent antibodies (listed in Table 2.4) in PBS or blocking buffer for 1 hr at room temperature in darkness. Slides were then washed 3 times with PBS, incubated with 4',6-diamidino-2-phenylindole (DAPI) in PBS (1:5000, Thermo Fisher Scientific), washed with PBS once more and mounted using Dako, Fluorescence Mounting Medium (Agilent Technologies, CA, USA) or SlowFade Diamond Antifade Mountant (Thermo Fisher Scientific).

2.5 Microscopy

Immunofluorescence microscopy of tissue sections was performed using either wide-field Leica DMIRB Inverted Microscope (Leica Microsystems, Germany) with MetaMorph imaging software (Molecular Devices, CA, USA) or wide-field Leica DMi8 fluorescence microscope with LAS X Microscope Science Software Platform (both Leica Microsystems). For each protein staining, optimal exposure time was chosen based on negative staining

control where samples were incubated with II° antibodies only, to account for background noise and autofluorescence of tissues. All images were processed using Fiji software [401]. Standard image processing for tissue section images included background subtraction (based on rolling ball with radius of 50 pixels) and brightness and contrast adjustment.

2.6 Lists of antibodies used in this study

Target protein	Host (clone)	Product ID	Manufacturer	Application	Dilution
α-dystrobrevin	rabbit pAb	α-1CTFP	In-house (gift from Prof. K.E. Davies) [402]	IF	1:100
α-tubulin	mouse mAb (AA13)	T8203	Sigma Aldrich	IF	1:1,000
α-tubulin	rat mAb (YOL1/34)	ab6161	Abcam	IF	1:250
α-tubulin	rabbit mAb (EP1332Y)	ab52866	Abcam	IF	1:250 – 1:500
Argonaute 2	rabbit pAb	ab32381	Abcam	WB	1:500
Calreticulin	rabbit pAb	2891S	Cell Signalling	WB	1:500
Dystrophin (C-terminal)	rabbit pAb	ab15277	Abcam	IF	1:1,000
Dystrophin (rod domain)	mouse mAb (Dy4/6D3)	NCL-DYS1	Leica Biosystems	WB	1:100
F-actin	phalloidin probe conjugated with Alexa Fluor 568	A12380	Thermo Fisher Scientific	IF	1: 200,000
GAPDH	rabbit pAb	G9545	Sigma Aldrich	WB	1:2000 – 1:5000
Histone H3	rabbit pAb	ab1791	Abcam	WB	1:10,000
hnRNPa1	rabbit pAb	ab137780	Abcam	WB	1:500
lamin A/C	mouse mAb (131C3)	ab8984	Abcam	WB	1:1,500
Laminin subunit α-2	rat mAb (4H8-2)	L0663	Sigma-Aldrich	IF	1:250
Myosin heavy chain (embryonic)	mouse mAB (F1.652)	F1.652	DSHB	IF	2-5 ug/ml
Myosin heavy chain	Mouse mAB (MF20)	MF20	DSHB	IF	1:20
nNOS	rabbit mAb	ab76067	Abcam	IF	1:100
Telethonin	rabbit mAb (EPR8375)	ab133646	Abcam	IF	1:1,000
Titin	mouse mAb (9D10)	9 D10	DSHB	IF	2-5 ug/ml
Utrophin	goat pAB	URD40	In-house (Gift from Prof. K.E Davies) [403]	IF	1:400 – 1:500

Vinculin	mouse mAb (hVIN-1)	V9131	Sigma	WB	1:100,000
β-Dystroglycan	mouse mAb (43DAG1/8D5)	NCL-b-DG	Leica Biosystems	IF	1:100

Table 2.3 List of primary antibodies used in this study.

II° antibody	Product ID	Manufacturer	Application	Dilution
Donkey anti-goat IgG Alexa Fluor 488	A11055	Thermo Fisher Scientific	IF	1:500 – 1:1000
Goat anti-mouse IgG Alexa Fluor-568	A11004	Thermo Fisher Scientific	IF	1:500 – 1:1000
Goat anti-mouse IgG Alexa Fluor-647	A21235	Thermo Fisher Scientific	IF	1:500 – 1:1000
Goat anti-mouse IgG Alexa Fluor-488	A28175	Thermo Fisher Scientific	IF	1:500 – 1:1000
Goat anti-rabbit IgG HRP-linked Antibody	7074	Cell Signalling	WB	1: 10,000
Goat anti-rabbit IgG Alexa Fluor-594	ab150080	Abcam	IF	1:500 – 1:1000
Goat anti-rabbit IgG Alexa Fluor-488	A11008	Thermo Fisher Scientific	IF	1:500 – 1:1000
Goat anti-rabbit IgG Alexa Fluor-568	A11011	Thermo Fisher Scientific	IF	1:500 – 1:1000
Goat anti-rat IgG Alexa Fluor-488	ab150157	Abcam	IF	1:500 – 1:1000
Goat anti-rat IgG Alexa Fluor-647	A21247	Thermo Fisher Scientific	IF	1:500 – 1:1000
Horse anti-mouse IgG HRP-linked Antibody	7076S	Cell Signalling	WB	1: 10,000

Table 2.4 List of secondary antibodies used in this study.

3 Results I: Spatial biology of dystrophin in muscle pathology and regeneration

3.1 Introduction

The efficacy of DMD therapeutic approaches is usually considered in terms of the amount of restored protein, largely assuming efficient distribution of both the therapeutic agent and the corrected gene expression products within the syncytium. However, it is known that the intricately organised architecture of the myofibre presents a major obstacle to the passive transport of mRNAs and proteins throughout the syncytium [288]. Specifically, the myofibre core is filled with protein-dense myofibrils which occupy ~ 80% of the whole cell volume, significantly hindering free macromolecule diffusion [288]. This is further amplified by the organisation of other subcellular organelles (i.e. nuclei, sarcoplasmic reticulum, mitochondria) which are effectively pushed to the myofibre periphery and are thus concentrated in the remaining 20% volume of the cell [288]. Accordingly, the accumulation of mRNAs and proteins in a myonuclear domain-restricted manner, rather than their widespread distribution, has been demonstrated as a feature of multinucleated myofibres *in vitro* and *in vivo* [319,404].

Spatial restriction of gene expression products presents a challenge for DMD restoration strategies. Specifically, the limited diffusion of corrected dystrophin within a fibre could indicate that a high number of nuclei must be corrected to achieve full protection of dystrophin against contraction-induced damage. Notably, we have recently reported that CRISPR-Cas9-mediated gene editing, which resulted in the correction of a limited number of nuclei, restored dystrophin non-uniformly at the sarcolemma [251]. In particular, myofibres of CRISPR-Cas9 treated animals presented with dystrophin-positive sarcolemma adjacent to dystrophin-negative regions within the same cell [251]. Shortly after, these findings were independently confirmed by Morin *et al*. in a similar study [405].

Notably, patchy dystrophin expression can be modelled in mice. For example, heterozygous *mdx* females, exhibit discontinuous localisation of dystrophin at the sarcolemma [406]. However, these animals express > 50% of wild-type dystrophin levels which is considered high, and thus present very few dystrophic features including lack of elevated serum myomiRs levels [321]. As such heterozygote *mdx* are rarely considered as feasible DMD model [321,407]. Recently the *mdx-Xist*$^{\Delta hs}$ mouse model, mimicking the restricted pattern of dystrophin expression at levels below 50% was developed by breeding the *mdx* male with *Xist*$^{\Delta hs}$ female by our group and others [321,407–409]. Heterozygous *Xist*$^{\Delta hs}$ animals contain a deletion upstream of the *Xist* promoter region which results in preferential silencing of the *Xist* mutation-containing X-chromosome [164]. As such, the F1 female offspring of homozygous *Xist*$^{\Delta hs}$ females and dystrophic hemizygous *mdx* males contain one predominantly inactive X-chromosome expressing wild-type dystrophin (derived from *Xist*$^{\Delta hs}$) and the second X-chromosome which does not produce functional protein (derived from *mdx*). Accordingly, our group and others have shown that this mosaic pattern of skewed XCI leads to the expression of variable, low levels of dystrophin distributed non-uniformly along the sarcolemma [321,407]. The *mdx-Xist*$^{\Delta hs}$ model has been primarily used to assess the effects of low dystrophin amounts on muscle function, thereby addressing the question of therapeutically significant dystrophin amounts. As such, dystrophin level-dependent improvement in physiological performance tests (i.e., hanging wire and grip tests) and muscle histology have been reported [407]. The same group further showed that low-level patchy dystrophin levels are insufficient to restore correct NMJ function, but able to improve the dystrophic heart pathology [408,409]. Similar results were obtained in animals expressing patchy dystrophin on a utrophin-null background (*mdx/utrn*$^{-/-}$*/ Xist*$^{\Delta hs}$) [410]. However, while addressing the question of therapeutically relevant dystrophin levels is of key importance, it is worth noting that patchy, and uniform dystrophin myofibres expressing similar amounts of total dystrophin are likely non-equivalent in terms of function. A study from our group demonstrated that extracellular myomiRs biomarkers and muscle turnover were restored in PPMO-treated *mdx* animals with uniform dystrophin

but not in *mdx-Xist*$^{\Delta hs}$ model expressing similar levels of patchy dystrophin [321]. Importantly, Torelli *et al*. showed that low in staining intensity (comparable to severe BMD phenotype) but uniformly distributed dystrophin (as opposed to the pattern observed in severe BMD patients) correlated with milder, intermediate muscular dystrophy phenotype in patients [411]. Together, despite the observed benefits, the extent to which patchy dystrophin can replicate the function and biology of healthy muscle remains unclear. It is possible that non-uniform dystrophin defines a novel class of myofibres potentially exhibiting divergent characteristics compared to their fully dystrophin-protected counterparts. Specifically, spatially-restricted localisation of dystrophin at the sarcolemma can have several downstream effects on myofibre morphology and molecular biology. For example, DAPC-mediated signalling function is likely maintained in dystrophin positive myonuclear domains. Conversely, downstream signalling pathways may be disrupted in dystrophin-lacking regions. In turn, this could lead to local differences in gene expression profiles within the same myofibre. Moreover, a lack of the protective sarcomere-ECM link in dystrophin negative myonuclear domains renders the patchy myofibre partially susceptible to contraction induced damage at unprotected regions. Additionally, other differences, for example in the cytoskeleton organisation or utrophin expression, may be characteristic of patchy dystrophin myofibres. Nevertheless, the effects of localised, non-uniform dystrophin coverage at the sarcolemma are currently not well understood. This chapter investigates the impact of patchy dystrophin distribution on muscle tissue pathology, as well as the structure and function of individual myofibres.

3.2 Materials and Methods

3.2.1 CNF and CSA quantification in transverse tissue sections

The proportion of centrally nucleated fibres (CNF) and myofibre cross-section area (CSA) was analysed in transverse TA muscle sections using an open-source Fiji plugin: MuscleJ2 [412]. MuscleJ2 is an automated, multi-parametric tool which facilitates quantitative analysis of morphological features within immunofluorescence images of skeletal muscle sections. The plugin employs thresholding and morphological operations to segment structures like nuclei and myofibres within assigned channel of the input image. Following segmentation, MuscleJ2 extracts quantitative features like area, intensity, and count, allowing for customisable downstream analysis and data visualisation [412].

Fresh frozen TA sections were prepared and stained as described in section 2.4. Immunofluorescence was performed using primary antibodies against α2-laminin to mark the muscle membrane (Table 2.3), and nuclei were labelled with DAPI (Thermo Fisher Scientific). Tiled images of the whole muscle sections were acquired with inverted, wide-field Leica DMi8 fluorescence microscope. Each image was stitched in LAS X Microscope Science Software (Leica Microsystems), background signal was subtracted using the rolling ball Fiji function with radius of 50 pixels and contrast was adjusted for each channel to facilitate correct image segmentation. The MuscleJ2 plugin was applied according to the developers' instructions [412]. Within the plugin, sample pathophysiology setting was set as damaged to account for variable myofibre area size in dystrophic animals. 2 - 5 whole TA sections were analysed per animal. For CNF proportion analysis, all analysed sections were considered separately. For analysis of correlation between dystrophin and CNF percentage results obtained from each animal were averaged.

3.2.2 Single myofibre isolation

Extensor digitorum longus (EDL) single myofibre isolation was performed according to an established protocol [413]. EDL muscles were dissected tendon-to-tendon and placed in 0.2% collagenase II (Worthington, NJ, USA) diluted in filter-sterilised DMEM (Thermo Fisher Scientific, pre-warmed at 37°C). Muscle was digested for 45-52 minutes at 37°C. Digestion was stopped by transferring the muscle into a 3.5 cm cell culture dish, pre-coated with heat inactivated horse serum (Thermo Fisher Scientific) containing Fluorobrite media (Thermo Fisher Scientific) supplemented with containing 1% Antibiotic-Antimycotic (PSA: Penicillin, Streptomycin and Amphotericin B; Thermo Fisher Scientific) pre-warmed at 37°C. Single myofibres were released from the muscle by gentle flushing using a 200 µl pipette under a stereomicroscope. At all times, the dish was kept at room temperature for maximum of 10 min at the time, after which it was returned to a pre-warmed (37°C) incubator allowing for the temperature to equilibrate. Flushing was repeated until the desired number of myofibres was released from the muscle. For subsequent staining and imaging, freshly isolated myofibres were transferred using a 200 µl pipette and tip into spot plate containing 4% ultrapure paraformaldehyde solution (PFA, Electron Microscopy Sciences, PA, USA) for fixation for 10 min at room temperature. Fixed myofibres were washed twice with ultrapure PBS for 5 min at room temperature. Immunofluorescence and/or hybridisation chain reaction-based RNA in situ hybridisation (HCR-RNA FISH) were performed directly after fixation and PBS washes.

3.2.3 Single myofibre immunofluorescence and HCR-FISH RNA detection

3.2.3.1 Protein detection in single isolated myofibres

If protein immunodetection and HCR RNA-FISH were performed on the same sample, staining for protein was performed first. PFA-fixed myofibres were permeabilised with 1% Triton-X100 (Sigma) for 10 min at room temperature followed by a single wash with PBS (Thermo Fisher Scientific) for 5 min. Subsequently, blocking was performed for 30 min at

room temperature with blocking buffer containing either 1% bovine serum albumin (BSA, Sigma) diluted in ddH_2O if only protein immunodetection was performed or 1% ultrapure BSA with RiboLock RNase Inhibitor at 1 U/µl (both Thermo Fisher Scientific) if protein detection was followed by RNA HCR-FISH. Myofibres were then incubated with primary antibodies (Table 2.3) diluted in blocking buffer for 2 hr at room temperature. After that time, myofibres were washed 3 times with PBS (Thermo Fisher Scientific) containing 0.1% v/v of Tween-20 (PBST, Sigma-Aldrich) at room temperature. Subsequently, myofibres were incubated with secondary fluorescent antibodies (Table 2.4) for 2 hr at room temperature in darkness.

If only protein detection was performed, samples were washed 3 times with PBST and either incubated with DAPI (Thermo Fisher Scientific) diluted in PBS for at least 2 min at room temperature. Myofibres were transferred using tweezers onto the SuperFrost Plus microslides (VWR) containing 35 µl of SlowFade Diamond Antifade Mountant (Thermo Fisher Scientific) and covered with High Precision Cover Glasses, 1.5 mm thickness (Thorlabs, NJ, USA). Stained myofibres were imaged on the following day and/or stored at -20 °C for repeated imaging.

If HCR RNA-FISH was subsequently performed samples were washed once with PBS and fixed with 4% PFA (Electron Microscopy Sciences) at room temperature.

Single myofibre imaging was performed with ZEISS LSM 980 confocal microscope equipped with Airyscan2 detector (ZEISS, Oberkochen, Germany). Depending on the application following objectives were used: ×40 Plan-Apochromat oil objective (numerical aperture NA = 1.4), ×25 Plan-Apochromat (NA = 0.8) or ×20 Plan-Apochromat (NA = 0.8). The choice of the objective was based on the field of view and detail required in each experiment. The magnification used is stated within each figure caption. The Airyscan post-processing step was applied in all cases, resulting in improved image resolution [414].

3.2.3.2 mRNA detection in single isolated myofibres by HCR RNA-FISH

RNA was detected using HCR RNA-FISH products purchased from Molecular Instruments (CA, USA), following the generic sample in solution protocol with modifications. PFA-fixed myofibres were washed twice with PBS (Thermo Fisher Scientific) for 5 min at room temperature. Subsequently, samples were incubated with 2× ultrapure saline-sodium citrate (SSC) buffer diluted in ultrapure H_2O (both Thermo Fisher Scientific) for 5 min at room temperature. Then, samples were incubated in pre-warmed at 37°C hybridisation buffer (Molecular Instruments) for 30 min at 37°C. Humidified conditions were maintained by wrapping the spot plate in cling film and placing it in a plastic bag containing H_2O-soaked filter paper. Subsequently, HCR probe sets were added to fresh, pre-warmed (37°C) hybridisation buffer at 1.25 nM/sample. Myofibres were incubated with probe sets at 37°C in humidified conditions for 12 – 16 hr. Samples were washed with pre-warmed (37°C) wash buffer (Molecular Instruments) 5 times for 10 min at 37°C followed by a wash with 5× SSCT (SSC supplemented with 0.1% v/v Tween-20) twice at room temperature. Samples were incubated with amplification buffer (Molecular Instruments) for 30 min at room temperature (pre-amplification). At the same time HCR hairpin amplifiers (h1 and h2) were thawed and 2 µl of each amplifier per sample was aliquoted. Hairpin amplifiers were heated at 95°C for 90 sec and cooled to room temperature darkness for 30 min. After pre-amplification, samples were incubated with hairpin amplifiers mixed in amplification buffer for 3.5 – 4 hr at room temperature in darkness. Subsequently, samples were washed 5 times with 5× SSCT for 10 min and incubated with DAPI diluted in PBS (both Thermo Fisher Scientific) for at least 2 min at room temperature. Myofibres were transferred using tweezers onto the SuperFrost Plus microslides (VWR) containing 35 µl of SlowFade Diamond Antifade Mountant (Thermo Fisher Scientific) and covered with High Precision Cover Glasses, 1.5 mm thickness (Thorlabs). Stained myofibres were imaged on the following day and/or stored at -20 °C for repeated imaging.

3.2.4 Analysis of dystrophin mRNA distribution within single myofibres

For each dystrophin HCR-FISH experiment, z-stack images were acquired with a ZEISS LSM 980 confocal microscope equipped with Airyscan2 detector (ZEISS). A ×40 Plan-Apochromat oil objective (NA = 1.4) was used in all cases. Images were acquired with 1.5 scan zoom in Airyscan SR-8Y mode and processed using ZEN software (ZEISS). The Airyscan post-processing step was applied in all cases, resulting in improved image resolution [414].

Analysis of dystrophin mRNA distribution among subcellular compartments within acquired imaged was performed using a Python 3-based method established by Dr. Chase P. Kelley, described in detail previously [302]. The method implements a custom image analysis pipeline designed specifically for analysis RNA FISH signal within single myofibre images. The pipeline performs myofibre and nuclei segmentation followed by defining the nuclear, perinuclear, and cytoplasmic regions using morphological operations. It further identifies RNA spots in designated channel and assigns them to subcellular compartments. Subsequently, number and density of spots is calculated for each compartment and exported as a csv file for downstream analysis [302]. The original code is publicly available at https://github.com/cpkelley94/muscle-FISH. Minor adjustments to the code were performed, to account for differences in metadata organisation between Zen Black and Zen Blue imaging software (ZEISS) used in different facilities. The pipeline utilises well-validated and widely used image analysis methodologies. The voxel dimensions as well as channel wavelengths are extracted from the image metadata. Nuclei are segmented from the DAPI channel using Otsu's thresholding method in each image. The myofibre area is segmented using Li's automatic threshold selection. The perinuclear compartment is defined as a 2 µm region around the segmented and thresholded nuclei. RNA FISH spots detection was performed using scikit-image (v.0.22.0) module skimage.feature.blob_log, which identifies 'blob'-like structures in a grayscale image using Laplacian of Gaussian filtering method

[415]. The detected signal was assigned to the subcellular compartment based on pixel position relative to segmented masks.

3.2.5 Analysis of the microtubule network organisation.

Microtubule intersection angle was analysed using TeDT direction v2017 software according to the developer's instructions [290]. Two to three cortical microtubule regions per myofibre segment were analysed from z-stack images acquired at ×40 magnification. Pre-analysis Image processing included the z-projection of cortical microtubule region and background subtraction (radius = 50 pixels). Images were arranged so that transverse microtubules were positioned at 90° angle with respect to the longitudinal axis of the myofibre. The isotropic areas of microtubule nucleation around myonuclei have been excluded from the analysis [290,297]. In total *n* = 60, 79 and 65 regions from 32 (C57 WT), 40 (*mdx52-Xist*$^{\Delta hs}$) and 31 (*mdx52*) myofibers were analysed respectively. The histogram of proportion of microtubule directionality angles for each genotype was prepared using averaged and 0-1 normalised values of fractions of microtubules at 0 - 176° in 4° intervals from each region. These values and vertical directionality score were obtained directly from the TeDT software results sheet.

3.2.6 Classification of centrally nucleated, segmented and non-centrally nucleated myofibres

Classification into non-centrally nucleated (non-CNF), segmented and centrally nucleated (CNF) fibres was performed on myofibres isolated from *mdx52-Xist*$^{\Delta hs}$ mice aged between 12 and 17 weeks. Myofibres were isolated and stained as described above, using the antibodies listed in Table 2.3. The myofibre isolation efficiency was between 40 – 199 myofibres per mouse. In total 11 animals were used, and 24 slides (i.e. separate immunofluorescence stainings) were analysed. Each slide containing between 20 and 86

myofibres was scanned using the wide-field Leica DMi8 fluorescence microscope to visualise all myofibres. Each myofibre was visually examined for nuclei (DAPI), dystrophin and/or β-DG signal at the sarcolemma and classified according to a pre-defined decision chart (Figure 3.1). Myofibres were classified into non-CNF, segmented and CNF groups based on nuclear DAPI staining. All myofibres were first classified based on the presence of centrally nucleated myofibres, if no centrally nucleated chains were observed myofibre was classified as non-CNF. If centrally nucleated chains were observed, myofibre was further classified as CNF (central nuclei chains spanning whole myofibre) or segmented (central nuclei chain region adjacent to non-CNF segment). DAPC expression in each CNF and segmented myofibre class was examined based on dystrophin or β-DG signal. Both myofibre classes were further grouped into DAPC-expressing and non-expressing groups. Within segmented myofibres DAPC localisation was subsequently examined according to the myofibre region i.e. centrally nucleated (CN) or non-centrally nucleated (non-CN) segment. Within each slide, uniformity, and intensity of DAPC of non-centrally nucleated myofibres, representing the expected staining pattern for each animal served as a reference point in the classification of segmented myofibres. Due to the observation that DAPC is present at the NMJ and MTJ of almost all *mdx52-Xist*$^{\Delta hs}$ myofibres junctional sarcolemma was excluded from the analysis.

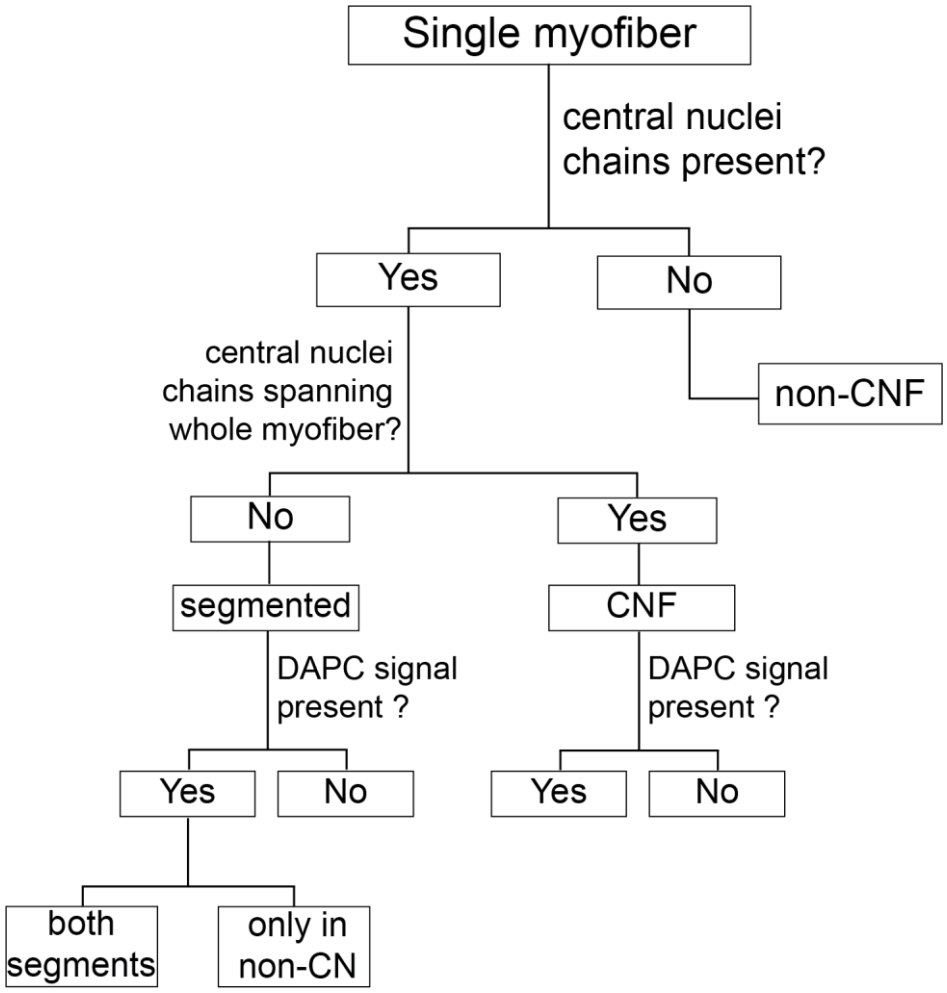

Figure 3.1 Decision tree of *mdx52-Xist*$^{\Delta hs}$ myofibre classification.

Myofibre classes: non-CNF (non-centrally nucleated fibre), segmented (containing centrally nucleated region adjacent to non-centrally nucleated segment) and CNF (centrally nucleated fibre) were assigned based on the position of nuclei. DAPC expression was evaluated based on the presence of either dystrophin or β-dystroglycan at the sarcolemma. The signal observed in NMJ and MTJ was excluded from the analysis.

3.2.7 Quantification of nuclei in myofibre segments

Nuclei from centrally nucleated and non-centrally nucleated were quantified manually from z-projections of myofibre images acquired with ZEISS LSM 980 confocal microscope equipped with Airyscan2 detector. All images were acquired at the same settings using the ×40 Plan-Apochromat oil objective (NA = 1.4) with 1.5 scan zoom in Airyscan SR-8Y mode and processed using ZEN software (ZEISS) to ensure analysis of the same myofibre volume.

3.3 Results

3.3.1 Development of *mdx52-Xist*$^{\Delta hs}$ mouse model

Spatial restriction of dystrophin in skeletal myofibres is a noteworthy phenomenon, relevant not only to CRISPR-Cas9 but also to cell therapy approaches where fusion of healthy myoblast to dystrophic muscle results in spatially restricted dystrophin expression [253,263,416,417]. Notably, beyond therapeutic interventions, patchy dystrophin expression is also characteristic for heterozygous dystrophic female muscle, and thus relevant in the context of DMD carriers [180,181,418,419]. Besides the general analysis of *mdx-Xist*$^{\Delta hs}$ animal physiology discussed above, not much is known concerning how patchy dystrophin affects the molecular biology and function of myofibres. To investigate the downstream effects of non-uniform dystrophin *mdx52-Xist*$^{\Delta hs}$ model was established, by crossing female *Xist*$^{\Delta hs}$ with male dystrophin-deficient *mdx52* mice (Figure 3.2). Similarly to *mdx-Xist*$^{\Delta hs}$ mice, *Xist*$^{\Delta hs}$ mutation leads to preferential silencing of maternal X chromosome expressing wild-type dystrophin resulting in expression of variable, low protein levels [164]. As opposed to a point mutation in *mdx*, the lack of whole exon in *mdx52* constitutes a patient-relevant mutation [22,140]. Additionally, *mdx52* animals contain fewer revertant myofibres than the *mdx* model [136]. Revertant myofibres express dystrophin in a positive patch along the sarcolemma (Figure 1.2) and as such, are impossible to discriminate from non-uniform dystrophin myofibres resulting from skewed XCI. This could potentially bias the visual analysis of *mdx-Xist*$^{\Delta hs}$ myofibres. Moreover, lack of 118 bp-long exon 52 in *mdx52* model allows for easier differentiation between mutant and healthy dystrophin mRNA, which co-occur within the same myofibre.

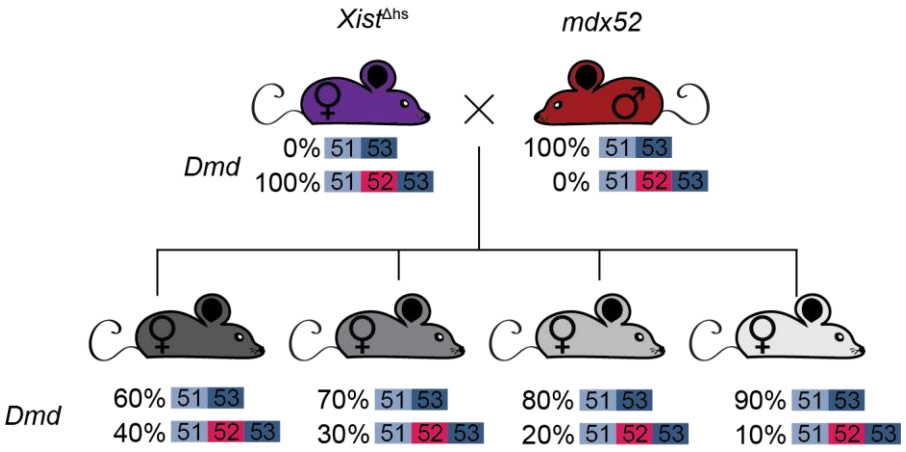

Figure 3.2 Breeding scheme of *mdx52-Xist*$^{\Delta hs}$ mice.

Female *Xist*$^{\Delta hs}$ mice containing a mutation in the *Xist* gene were crossed with male *mdx52* animals lacking exon 52 of the dystrophin gene. The *Xist* mutation results in primary, skewed X-chromosome inactivation thus silencing the *Dmd* in mutation-containing chromosome in 60 – 90% of the cases. The F1 female *mdx52-Xist*$^{\Delta hs}$ offspring express dystrophin in varying amounts.

To determine the levels of dystrophin expression in *mdx52-Xist*$^{\Delta hs}$ model, female mice were sacrificed at 6 weeks of age (adult, *N* = 20), and skeletal muscle tissues were harvested. Female *mdx52*, wild-type C57 and *Xist*$^{\Delta hs}$ mice were sacrificed in parallel as controls (*n* = 4-5 for each group). Total protein was extracted from tibialis anterior (TA) muscles and dystrophin protein was measured by western blot and quantified as a percentage of wild-type C57 levels (Figure 3.3 A). *mdx52-Xist*$^{\Delta hs}$ dystrophin expression levels fell in the range of 1-41% of wild-type dystrophin levels (Figure 3.3 B, C). Each *mdx52-Xist*$^{\Delta hs}$ animal was retrospectively assigned to low (~1-8%), medium (~11-17%), and high (~23-41%) dystrophin-expressing groups *post-mortem* accordingly (Figure 3.3 A, C). These results demonstrate, that *mdx52-Xist*$^{\Delta hs}$ animals exhibit variable dystrophin expression from birth, with a maximum level reaching 41% of the wild-type transcript amounts.

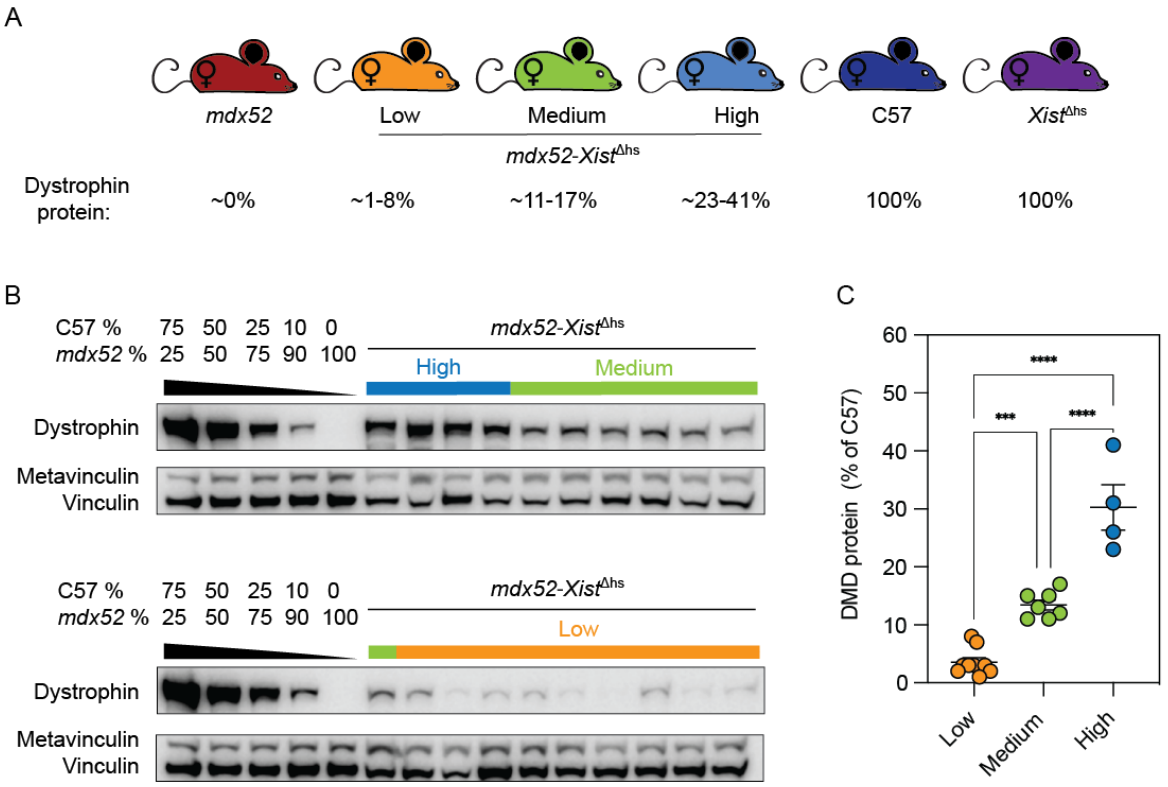

Figure 3.3 Quantification of dystrophin protein expression in adult *mdx52-Xist*$^{\Delta hs}$ muscle.

(**A**) *mdx52*, *mdx52-Xist*$^{\Delta hs}$, C57 and *Xist*$^{\Delta hs}$ animals were grouped based on the relative amount of dystrophin expression in tibialis anterior (TA) muscle. (**B**) Western blot analysis of dystrophin protein in TA muscle from adult, 6-week-old C57, *mdx52*, and *mdx52-Xist*$^{\Delta hs}$. Vinculin was utilised as a loading control, standard curves consisted of mixtures of C57 wild-type and *mdx52* TA lysates. (**C**) Quantification of dystrophin western blot as a percentage of wild-type dystrophin levels. *mdx52-Xist*$^{\Delta hs}$ were assigned to low, medium, or high dystrophin expression groups. Statistical analysis: one-way analysis of variance (ANOVA) with Bonferroni *post hoc* test. *** $P < 0.001$, ** $P < 0.01$, * $P < 0.05$.

3.3.2 Dystrophin distribution is patchy along myofibres of mdx52-Xist$^{\Delta hs}$ animals

Dystrophin localisation in *mdx52-Xist*$^{\Delta hs}$ myofibres was analysed by immunofluorescence in longitudinal and transverse TA sections (Figure 3.4). Imaging analysis revealed that adult *mdx52-Xist*$^{\Delta hs}$ mice exhibit a non-uniform pattern of dystrophin distribution, with incomplete staining observed throughout the length of myofibres in all three groups (high, medium, and low dystrophin expressing animals, Figure 3.4 white arrows). In contrast, dystrophin localisation in C57 wild-type and *Xist*$^{\Delta hs}$ muscles was uniform. Together, these results confirm that the novel *mdx52-Xist*$^{\Delta hs}$ animal model expresses variable levels of dystrophin that is non-uniformly distributed at the sarcolemma. These results agree with data obtained from previously used *mdx-Xist*$^{\Delta hs}$ model, and mirror the pattern observed upon dystrophin restoration with CRISPR-Cas9 and cell therapy approaches [251,253,321,405,408].

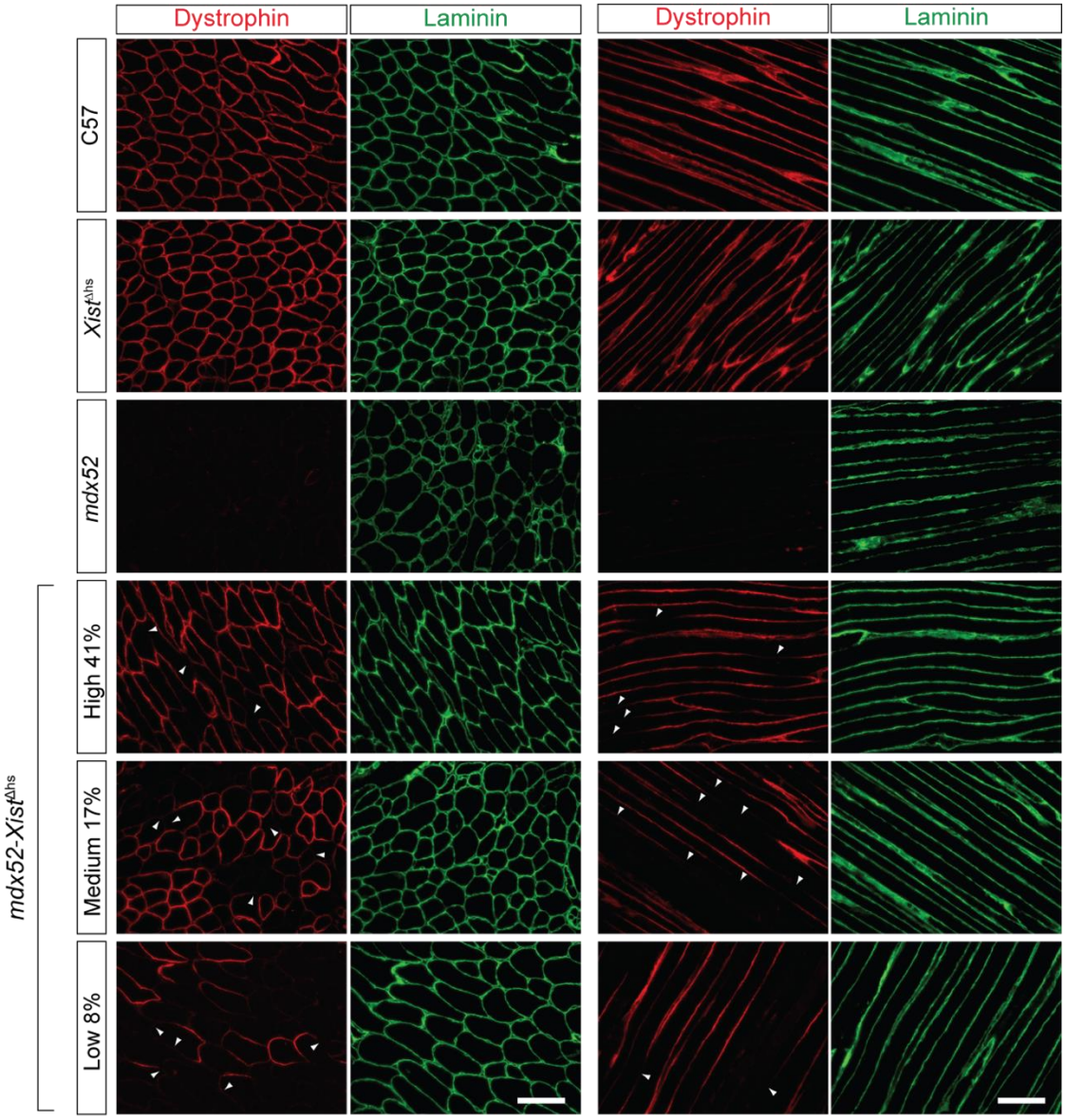

Figure 3.4 Dystrophin protein localisation in adult control and *mdx52-Xist*$^{\Delta hs}$ TA muscle.

Representative immunofluorescence staining of dystrophin and laminin in transverse and longitudinal tibialis anterior muscle sections of 6-week-old C57 wild-type, *Xist*$^{\Delta hs}$, *mdx52*, and *mdx52-Xist*$^{\Delta hs}$ animals from high, medium, and low dystrophin groups. Within-fibre, patchy dystrophin expression resulting from skewed X chromosome inactivation indicated with arrowheads. Scale bar indicates 100 μm, images taken at ×20 magnification. The percentage indicates total dystrophin quantification in the animals from which the sections were derived.

3.3.3 DAPC components follow the patchy distribution of dystrophin expression in *mdx52-Xist*$^{\Delta hs}$

Dystrophin exerts its muscle-protective and signalling functions by forming a multiprotein DAPC at the sarcolemma which directly links the sarcomere to the extracellular matrix. To assess the pattern of the DAPC assembly in *mdx52-Xist*$^{\Delta hs}$ animals, immunofluorescence analysis was performed for dystrophin, β-DG, DTNA and nNOS in isolated extensor digitorum longus (EDL) myofibres from adult wild-type C57 and *mdx52-Xist*$^{\Delta hs}$ animals. β-DG and DTNA were non-uniformly distributed in *mdx52-Xist*$^{\Delta hs}$ myofibres (Figure 3.5 A), and co-staining of β-DG with dystrophin revealed their colocalisation to the same membrane regions (Figure 3.5 B, *N* = 217 myofibres). In contrast, analysed DAPC components were present along the entire length of the C57 wild-type healthy sarcolemma, forming a characteristic 'rib'-like lattice of the costameres (Figure 3.5 A). Surprisingly, in all analysed *mdx52-Xist*$^{\Delta hs}$ myofibres (*N* = 260) nNOS signal was present and uniformly distributed, suggesting a differential regulatory mechanism for nNOS localisation in the *mdx52-Xist*$^{\Delta hs}$ model (Figure 3.5 A, C). Together, these results confirm that functional DAPC is formed only in the presence of dystrophin at the sarcolemma. However, the expression and distribution of nNOS does not fully depend on dystrophin in the *mdx52-Xist*$^{\Delta hs}$ mice.

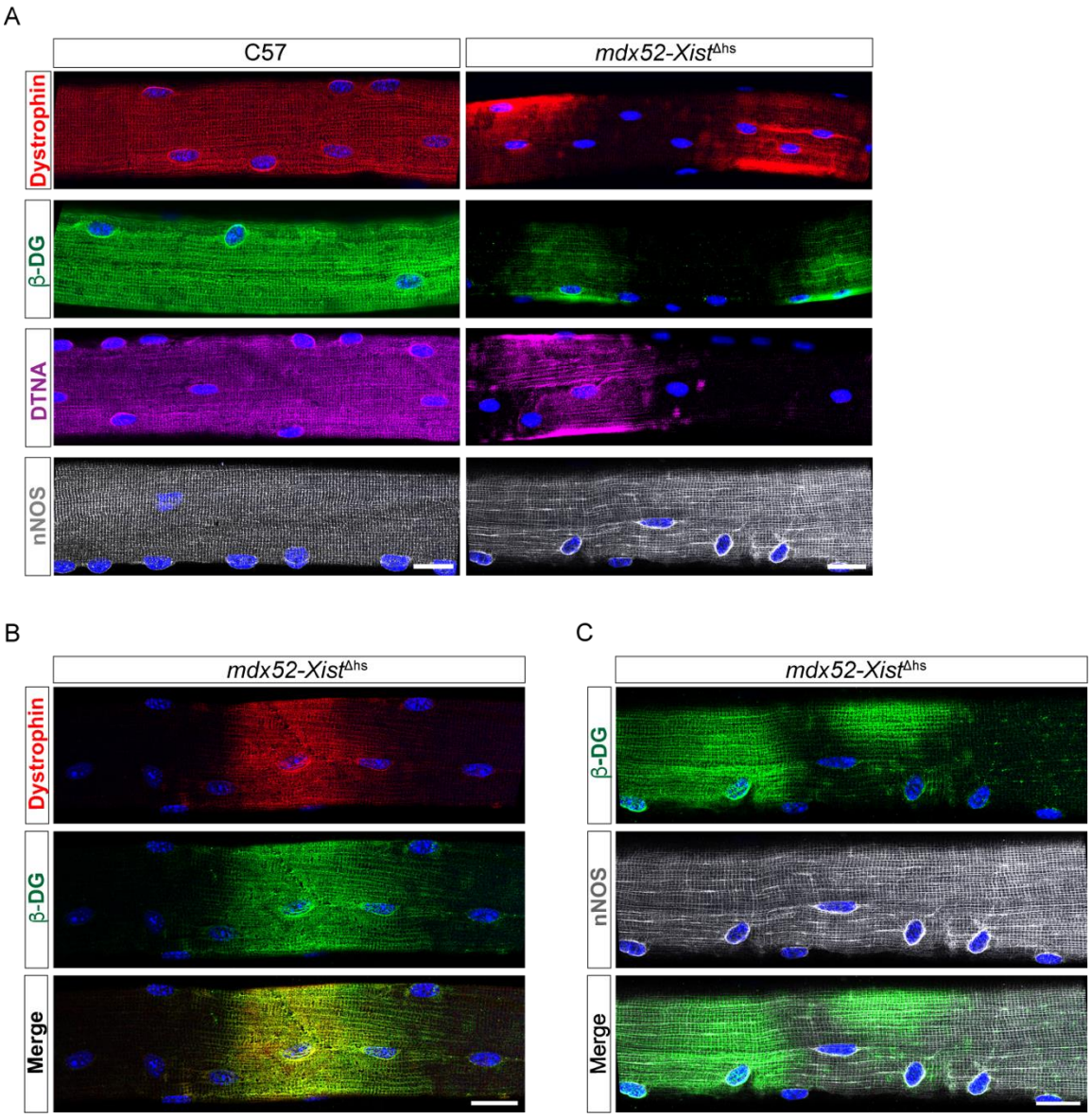

Figure 3.5 Localisation of DAPC in single isolated myofibres of wild-type and patchy-dystrophin expressing *mdx52-Xist*$^{\Delta hs}$.

(**A**) Representative immunofluorescence staining of β-dystroglycan (β-DG), α-dystrobrevin (DTNA) and nitric oxide synthase (nNOS) in single isolated EDL myofibres of C57 (wild type) and *mdx52-Xist*$^{\Delta hs}$. Representative co-staining of dystrophin with β-DG (**B**) and (**C**) β-DG with nNOS in the isolated single myofibre of *mdx52-Xist*$^{\Delta hs}$ animals. Scale bar indicates 20 µm, images taken at ×25 magnification.

Analogously, immunofluorescent detection of DAPC components was performed in transverse and longitudinal TA sections of dKO animals treated with CRISPR-Cas9 gene editing machinery [251] (Figure 3.6, Figure 3.7,Figure 3.8). Double-cut CRISPR-Cas9 strategy designed to excise exon 23 and restore dystrophin expression was delivered intravenously or intraperitoneally to dKO animals on day 2 after birth [251]. This resulted in the restoration of dystrophin expression at ~2% of wild-type levels in TA muscle [251]. Patchy dystrophin restoration pattern after CRISPR-Cas9 treatment was visible in analysed sections (Figure 3.6), confirming non-uniform dystrophin restoration with gene editing. In accordance with *mdx52-Xist*$^{\Delta hs}$ data, β-DG, and DTNA were non-uniformly distributed along the TA sarcolemma (Figure 3.7). In contrast, the distribution of nNOS followed a similar patchy distribution pattern (Figure 3.8).

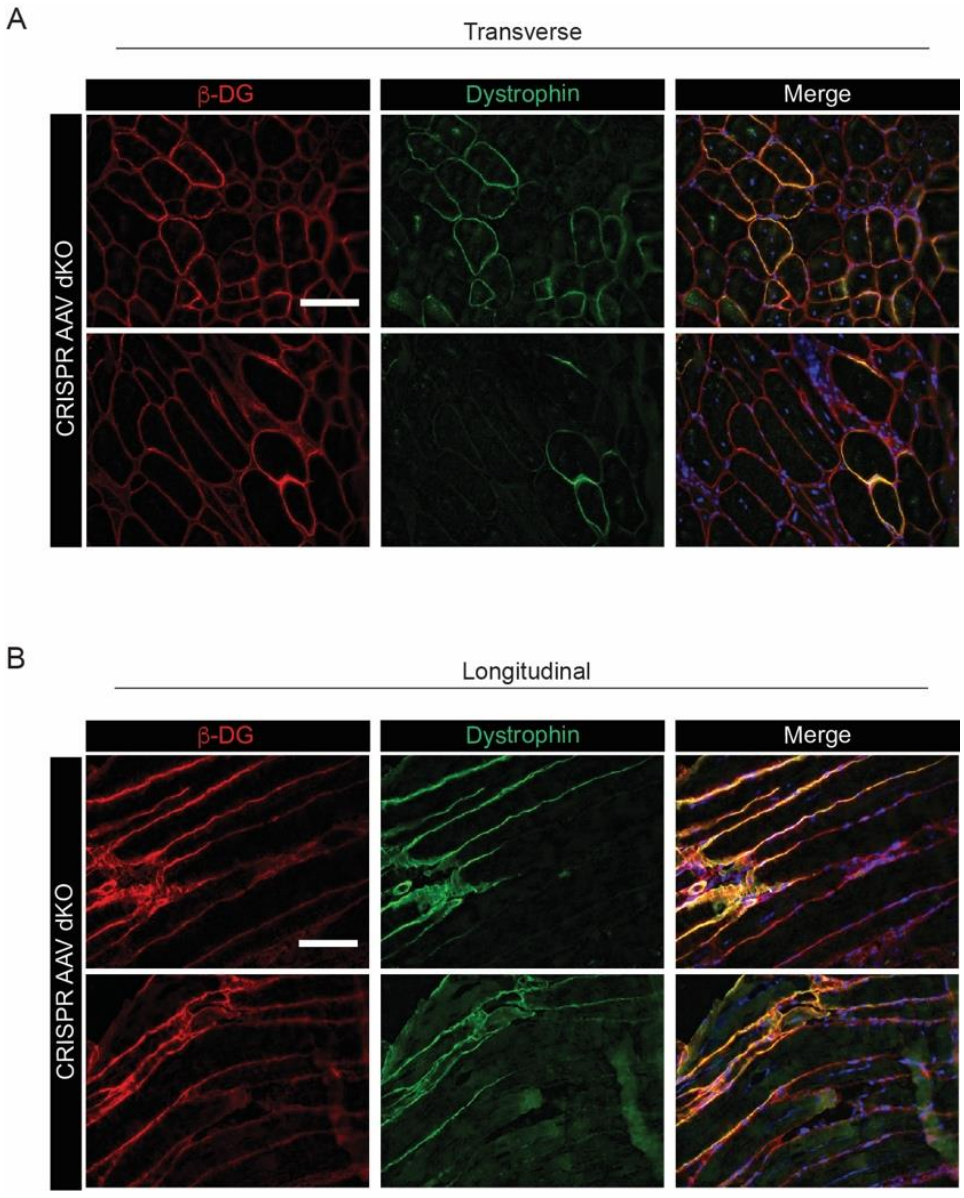

Figure 3.6 Dystrophin and β-DG localisation at the sarcolemma of CRISPR-Cas9 treated dKO animals.

Representative immunofluorescence staining of β-DG and dystrophin in transverse (**A**) and longitudinal (**B**) TA muscle sections of CRISPR-Cas9 treated dKO animals. Scale bar indicates 100 μm, images taken at ×20 magnification.

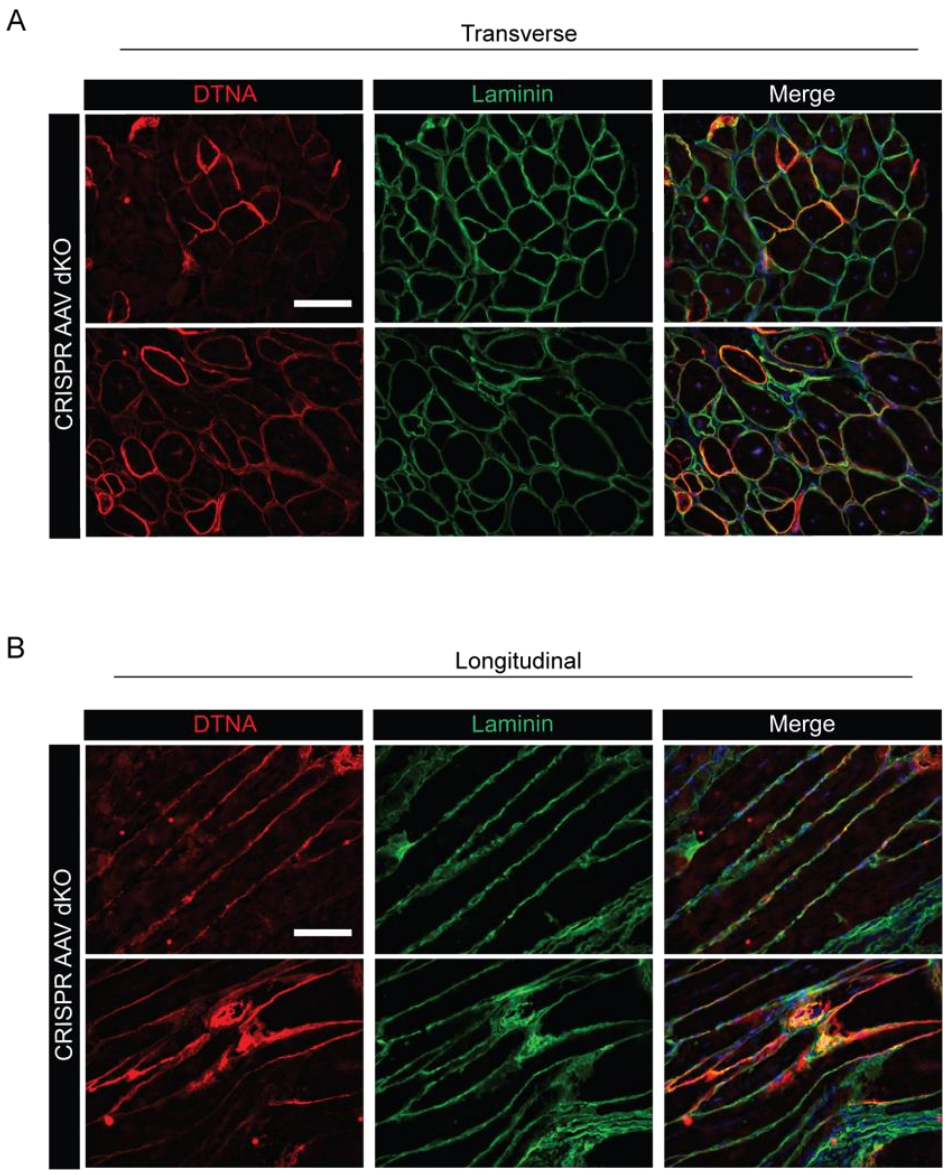

Figure 3.7 DTNA localisation at the sarcolemma of CRISPR-Cas9 treated dKO animals.

Representative immunofluorescence staining of DTNA and laminin (control) transverse (**A**) and longitudinal (**B**) TA muscle sections of CRISPR-Cas9 treated dKO animals. Scale bar indicates 100 μm, images taken at ×20 magnification.

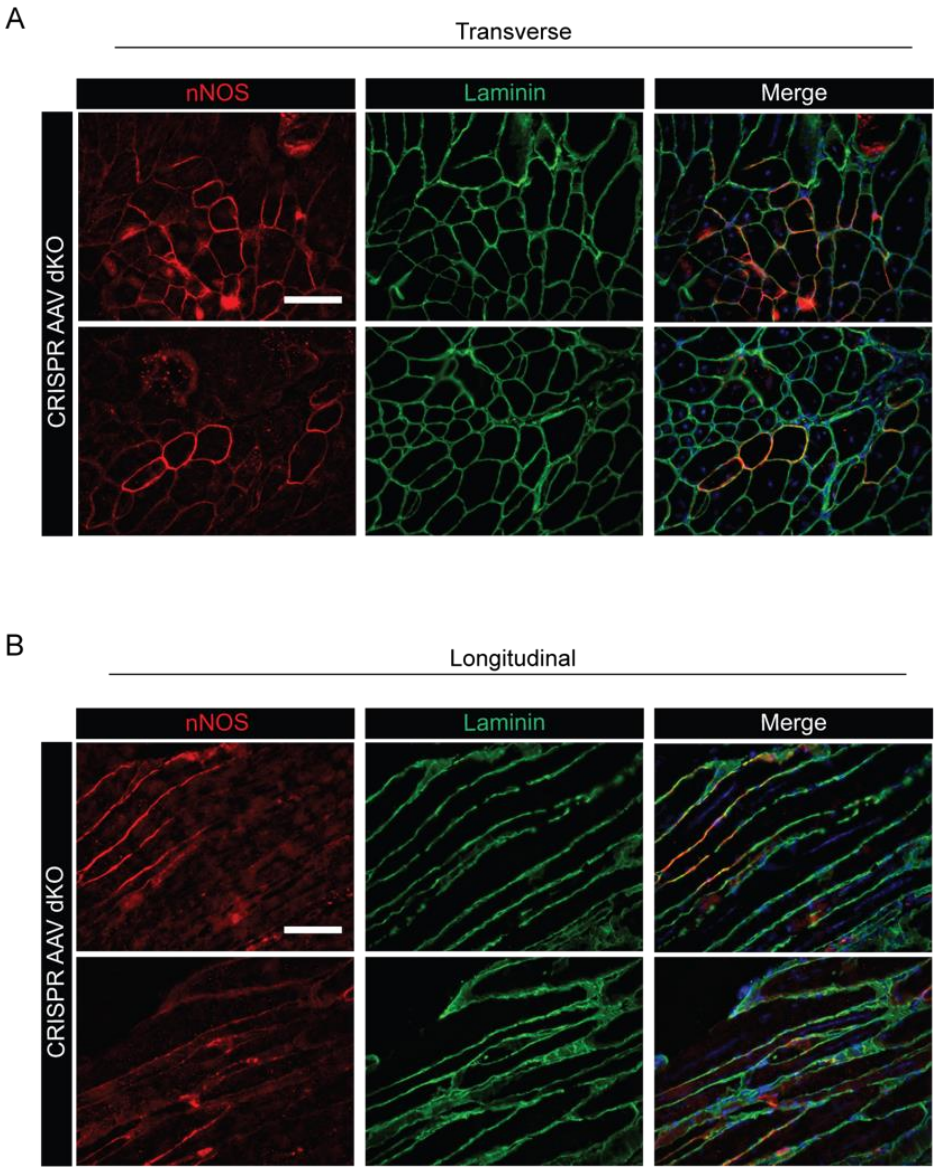

Figure 3.8 nNOS localisation at the sarcolemma of CRISPR-Cas9 treated dKO animals.

Representative immunofluorescence staining of nNOS and laminin (control) in transverse (**A**) and longitudinal (**B**) TA muscle sections of CRISPR-Cas9 treated dKO animals. Scale bar indicates 100 μm, images taken at ×20 magnification.

3.3.4 Dystrophin mRNA does not accumulate within dystrophin-positive myonuclear domains

The observation of patchy dystrophin distribution in *mdx52-Xist*$^{\Delta hs}$ confirms that this protein does not move freely within the myofibre and suggests that dystrophin is produced and deposited at the sarcolemma locally. A clear accumulation of mRNA within the vicinity of the nucleus was previously reported with very characteristic signal aggregation around the nucleus of origin for exogenous β-galactosidase and green fluorescent protein (GFP) mRNAs [318,420]. Endogenously, transcriptional activation of specific genes within myonuclei might occur in demand-driven bursts, signalled by the local environment (e.g., within the myonuclear domain) as well as external signalling stimuli released by the extracellular environment locally to the myofibres. Indeed, heterogeneous, and uncoordinated transcriptional activity of myonuclei within the same myofibre is a well-established phenomenon [421–423]. Accordingly, it is plausible that increased transcription and shuttling of dystrophin mRNA could occur in positive (high production rate) or negative (high demand) myonuclear domains.

Fluorescence *in situ* hybridisation (FISH) detection of RNAs based on hybridisation chain reaction (HCR-FISH) is a robust method of mRNA imaging within cells and tissues [424]. High-resolution imaging was used to analyse dystrophin mRNA distribution in isolated single myofibres using an HCR-FISH 30-probe cocktail targeting the entire transcript. This revealed a characteristic dystrophin expression pattern: a high-density nuclear ’blob’ reflecting a large, continuously transcribed genomic locus, and smaller, dispersed cytoplasmic dots confirming the HCR method (Figure 3.9 top panel). Notably, the observed dystrophin transcript abundance was substantially lower as compared to mRNA encoding titin (TTN), a protein of 3,800 kDa encoded by 363-exon long mRNA, in agreement with previously published results by Denes *et al.* (Figure 3.9 bottom panel) [302]. Imaging of dystrophin transcripts in isolated single myofibres of 8-week-old *mdx52-Xist*$^{\Delta hs}$

demonstrated that the non-nuclear *Dmd* transcripts were relatively evenly distributed throughout the cytoplasm at low levels (*N* = 37 myofibres from 7 animals, Figure 3.10).

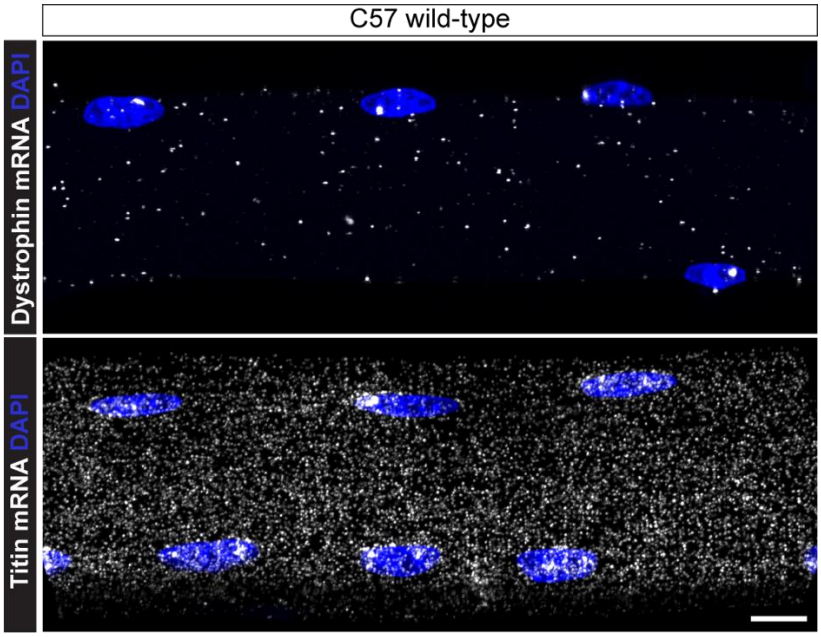

Figure 3.9 HCR-RNA FISH signal of dystrophin and titin mRNA in healthy myofibre. Representative images of HCR-FISH-based detection of dystrophin (top) and titin (bottom) full-length mRNA within single EDL myofibres of a healthy mouse. Images taken at 40× magnification, scale bar represents 10 µm.

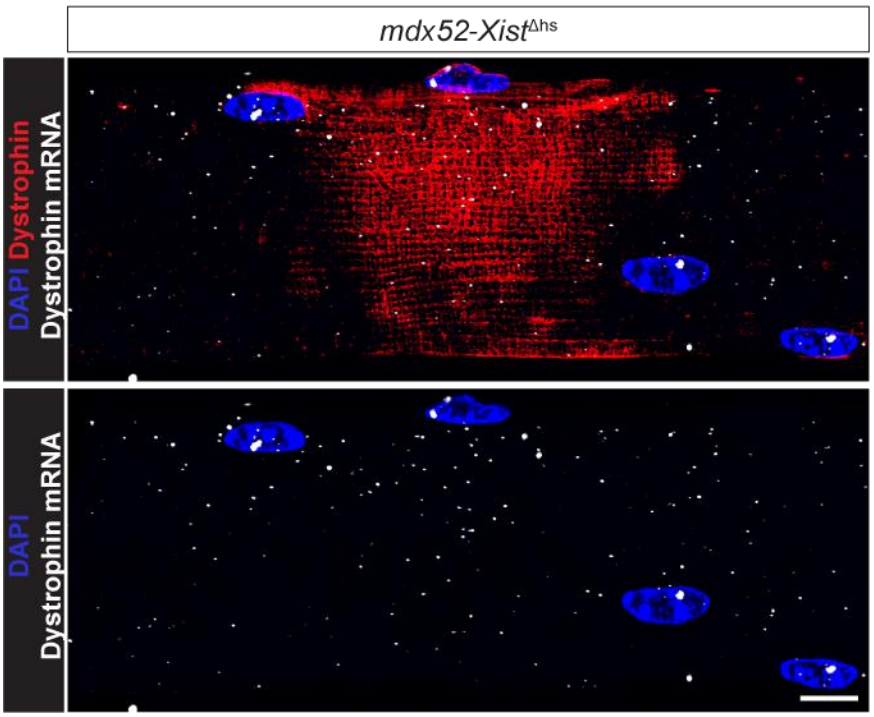

Figure 3.10 Comparison of full-length dystrophin mRNA spot density in patchy *mdx52-Xist*$^{\Delta hs}$ myofibres.

Representative images of dystrophin immunofluorescence combined HCR-FISH based detection of dystrophin mRNA in a single isolated EDL myofibre from 8-week-old *mdx52-Xist*$^{\Delta hs}$ animal. Both images show the same myofibre including (top) or excluding (bottom) dystrophin-positive myonuclear domain visualisation for clarity. Images taken at 40× magnification, scale bar represents 10 µm.

Additionally, a workflow developed by Denes *et al*. combining HCR-FISH imaging and bioinformatic signal quantification within subcellular compartments of isolated myofibres was applied to assess overall dystrophin mRNA abundance and distribution in patchy *mdx52-Xist*$^{\Delta hs}$ muscle and controls [302]. Total dystrophin mRNA counts were normalised to the myofibre volume to account for differences in myofibre size. The dystrophin transcript counts within specific subcellular compartments (cytoplasm, nucleus, perinuclear region) were measured relative to their volume. Both *mdx52* and *mdx52-Xist*$^{\Delta hs}$ displayed reduced dystrophin mRNA levels compared to healthy controls, indicative of either suppressed

transcription or enhanced transcript degradation in dystrophic conditions (Figure 3.11 A). Notably, *Xist*$^{\Delta hs}$ muscles exhibited significantly higher amounts of transcript per volume of the fibre than C57 wild-type mice, demonstrating that dystrophin expression profile differs between strains. The overall dystrophin mRNA distribution pattern was similar between *mdx52* and *mdx52-Xist*$^{\Delta hs}$ animals, however, a reduction in dystrophin mRNA confined to the nuclear region was detected in *mdx52-Xist*$^{\Delta hs}$ but not *mdx52* myofibres relative to controls (Figure 3.11 A, B). Notably, a profound decrease in dystrophin mRNA counts was observed in the perinuclear and cytoplasmic compartments for both *mdx52* and *mdx52-Xist*$^{\Delta hs}$ myofibres (Figure 3.11 C). This suggests that diminished dystrophin transcript abundance is mainly reflected in the loss of mature mRNAs in perinuclear and cytoplasmic regions. Moreover, while mutant and wild-type transcripts cannot be distinguished by the method used, the presence of healthy dystrophin mRNA is expected within the *mdx52-Xist*$^{\Delta hs}$ myofibres. However, the overall transcript dynamics (i.e. abundance and subcellular localisation) were not changed in patchy myofibres as compared to *mdx52*. This suggests that in a dystrophic environment, wild-type transcripts may also be subjected to degradation. Indeed, a study by Dupont *et al.* demonstrated that enhanced ROS-mediated oxidative damage of mRNA in dystrophic conditions leads to diminished transgene mRNA levels in comparison to healthy controls [425].

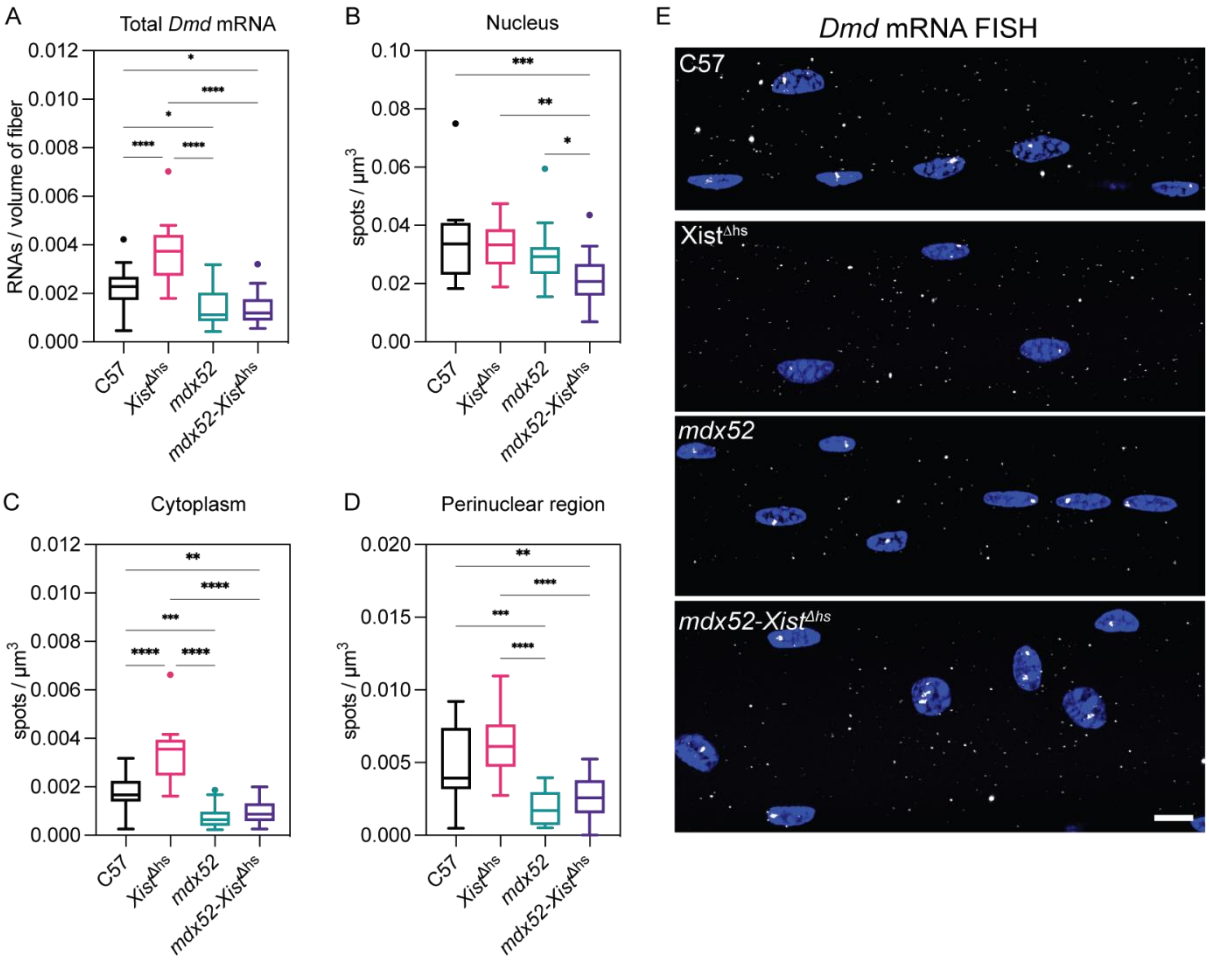

Figure 3.11 Full-length dystrophin mRNA distribution in subcellular compartments of *mdx52-Xist*$^{\Delta hs}$, *mdx52* and healthy controls single isolated EDL myofibres.

Quantification of dystrophin mRNA counts with HCR-RNA FISH followed by analysis as described by Denes *et al.,* 2021. (**A**) Total dystrophin mRNA counts relative to the myofibre volume in C57 (n = 33), *Xist*$^{\Delta hs}$ (n = 19), *mdx52* (n = 26), and *mdx52-Xist*$^{\Delta hs}$ (n = 37) myofibre segments. Dystrophin density in (**B**) nuclear, (**C**) cytoplasmic and (**D**) perinuclear compartments in myofibres of respective genotypes. (**E**) Representative images of dystrophin HCR RNA-FISH in EDL myofibres of C57, *Xist*$^{\Delta hs}$, *mdx52*, *mdx52-Xist*$^{\Delta hs}$ animals. Images taken at ×40 magnification, scale bar represents 10 µm. Statistical analysis: one-way ANOVA with Bonferonni *post hoc* test. *** $P < 0.001$, ** $P < 0.01$, * $P < 0.05$.

3.3.5 Patchy dystrophin inversely correlates with muscle turnover

To assess the impact of non-uniform dystrophin on muscle turnover, the number of centrally nucleated myofibres (CNF) was quantified in TA muscle sections of adult *mdx52-Xist*$^{\Delta hs}$ animals grouped according to their dystrophin expression levels (Figure 3.12). CNFs were quantified using the MuscleJ2 macro for Fiji and expressed as a proportion of total myofibres. The percentage of CNF in low dystrophin-expressing group was comparable to that of age-matched *mdx52* mice, and significantly higher than in *mdx52-Xist*$^{\Delta hs}$ animals expressing non-uniform dystrophin at the medium and high levels (Figure 3.12 B). Specifically, high levels of patchy dystrophin (mean group dystrophin of 30%) resulted in a 3.4-fold reduction in CNF in comparison to low dystrophin expression (mean group dystrophin of 3.5%). Spearman correlation analysis revealed a strong negative relationship between the percentage of patchy dystrophin and CNF in TA muscle (Spearman's r = -0.8632, p = 0.0023, Figure 3.12 C). The overall myofibre size distribution was similar between all analysed genotypes (Figure 3.12 D). However, *mdx52* and low dystrophin expressing *mdx52-Xist*$^{\Delta hs}$ contained significantly higher amount of smallest area myofibres (up to 500 μm^2) relative to medium and high dystrophin expressing *mdx52-Xist*$^{\Delta hs}$ mice (Figure 3.13 A, B). This complements the CNF analysis and demonstrates that level of recently formed, small-calibre myofibres is comparable between dystrophic and *mdx52-Xist*$^{\Delta hs}$ mice expressing low dystrophin levels. Together, these results show that with an increase in sarcolemma coverage by dystrophin, myofibres are more stable and less prone to contraction-induced damage and subsequently, fewer new myofibres are formed. Accordingly, the lowest amount of non-uniformly distributed dystrophin patches does not prevent myofibre necrosis, resulting in *mdx52*-like muscle histopathology.

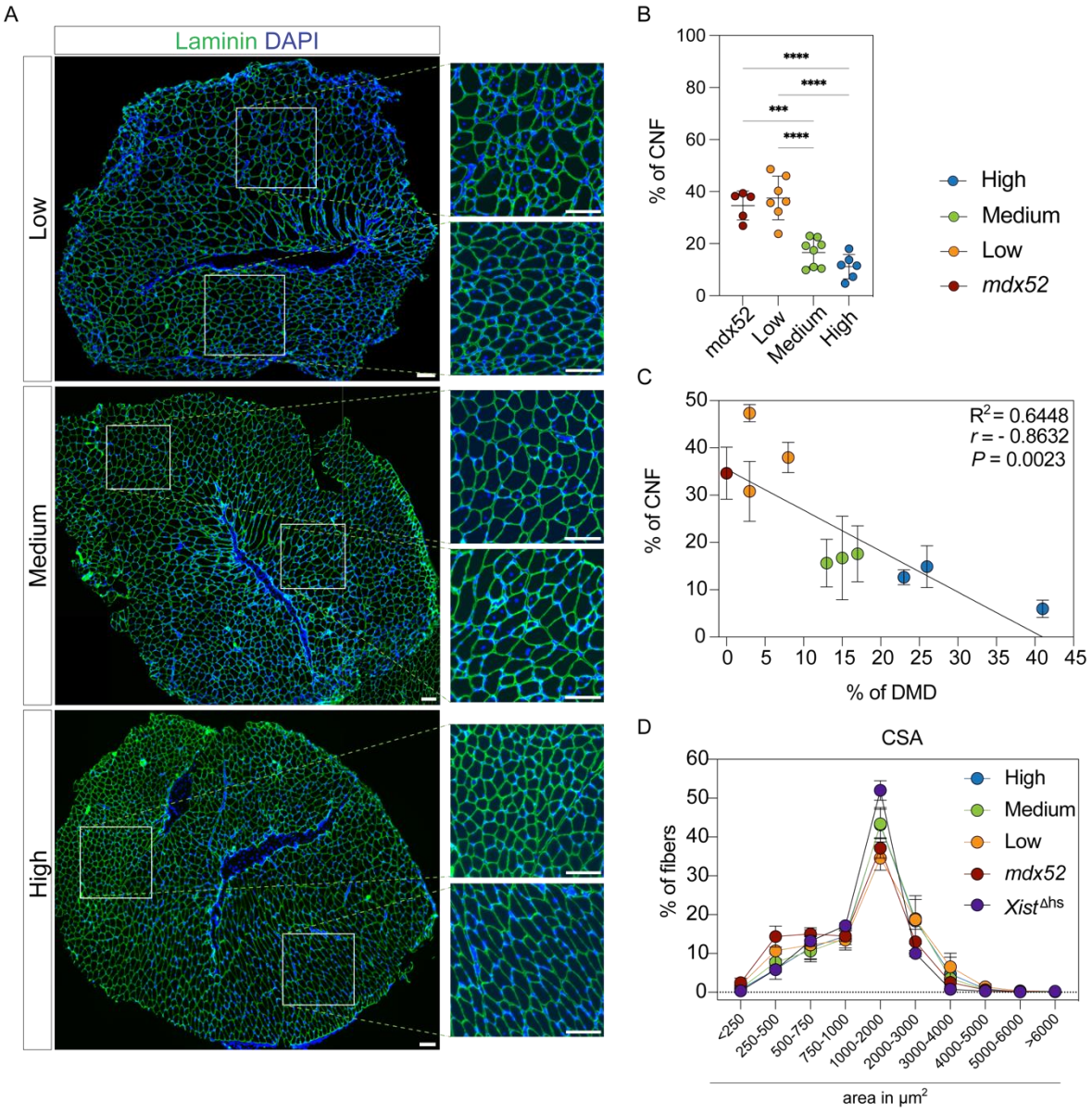

Figure 3.12 Quantification of centrally nucleated myofibres in TA muscle of adult *mdx52-Xist*$^{\Delta hs}$ mice.

(**A**) Representative immunofluorescence images of transverse TA muscle sections stained for laminin (green) as a sarcolemma marker and DAPI (blue) for nuclei visualisation. A magnified view of the sections shows the centrally nucleated fibres (CNF) proportion in two regions of the section. Tiled images were taken at ×10 magnification and stitched in LAS X software. Scale bars represent 100 µm. (**B**) CNF as a proportion of total myofibres analysed per TA section from *mdx52* (*n* = 1 animal, 5 different TA sections) and *mdx52-Xist*$^{\Delta hs}$ animals expressing low, medium, and high dystrophin levels (*n* = 3 animals per group, 2-3 different TA sections per animal). (**C**) Correlation analysis of dystrophin percentage and average

CNF percentage in analysed *mdx52* and *mdx52-Xist*$^{\Delta hs}$ TA sections. Dystrophin protein percentage was derived from western blot analysis. (**D**) Myofibre size variability in TA sections of *mdx52*, *mdx52-Xist*$^{\Delta hs}$ and *Xist*$^{\Delta hs}$ animals visualised through proportion of fibres of specific cross-sectional area (CNS). CNF and CSA were quantified using the MuscleJ2 plugin for Fiji. Statistical analysis: one-way ANOVA with Bonferroni post hoc test. ***P < 0.001, **P < 0.01, *P < 0.05.

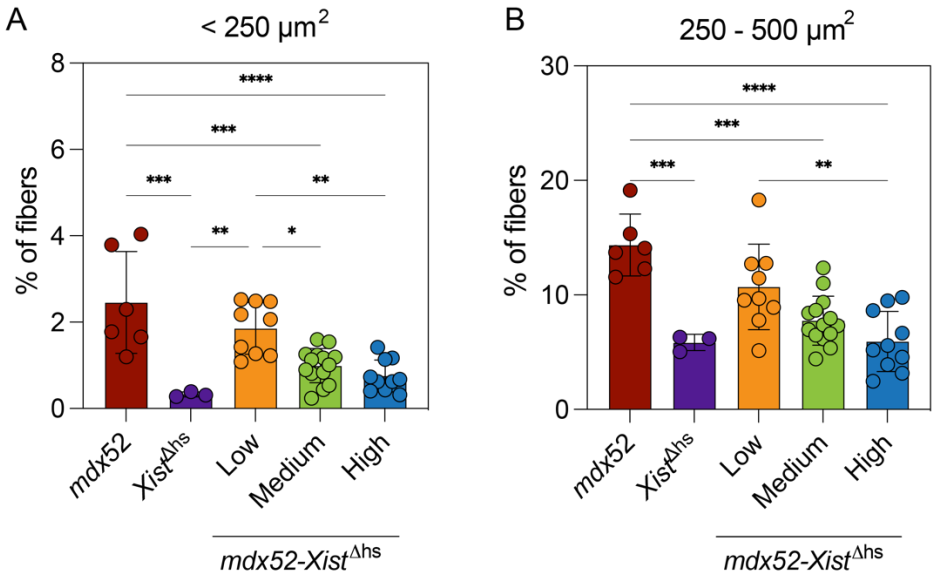

Figure 3.13 Percentage of small area myofibres in adult *mdx52-Xist*$^{\Delta hs}$ mice.

Quantitative analysis of the proportion of myofibres with an area of < 250 µm² (**A**) and 250-500 µm² (**B**) in TA muscle sections of adult *mdx52* (*n* = 1 animal) and *mdx52-Xist*$^{\Delta hs}$ animals expressing high, medium, and low dystrophin (*n* = 3 animals per group). The myofibre percentage was calculated with the MuscleJ2 plugin for Fiji. Statistical analysis: one-way ANOVA with Bonferroni *post hoc* test. ***P < 0.001, **P < 0.01, *P < 0.05.

We have previously shown that the amount of dystrophin restored uniformly at the sarcolemma is strongly anti-correlated with levels of detected extracellular serum myomiRs (further described in results chapter II) [320]. This implies that extracellular myomiRs are good candidates as pharmacodynamic DMD biomarkers. To assess if non-uniformly distributed dystrophin restores the levels of extracellular myomiRs, RT-qPCR for miR-1a-3p, miR-133a-3p and miR-206-3p was performed in serum samples from adult *mdx52-Xist*$^{\Delta hs}$, healthy C57, and dystrophic *mdx52* animals (Figure 3.14 A, B, C). Very low levels of extracellular myomiRs were found in wild-type and *Xist*$^{\Delta hs}$ serum (Figure 3.14 A, B, C). Conversely, *mdx52* animals contained elevated levels of serum myomiRs, indicative of ongoing muscle pathology. The relative abundance of myomiRs was comparable in *mdx52* and low dystrophin expressing *mdx52-Xist*$^{\Delta hs}$ mice. Notably, the myomiR abundance progressively declined in serum of animals expressing medium and high dystrophin *mdx52-Xist*$^{\Delta hs}$ (Figure 3.14 A, B, C). The Spearman correlation analysis revealed a strong negative relationship between levels of patchy dystrophin expressed and relative mount of serum myomiRs biomarkers (Spearman's r = -0.7820; r = -0.8145; r = -0.8772 respectively; P < 0.0001, Figure 3.14 D, E, F). Therefore, patchy dystrophin localisation at the sarcolemma restores extracellular miRNA towards wild-type levels in an expression level-dependent manner.

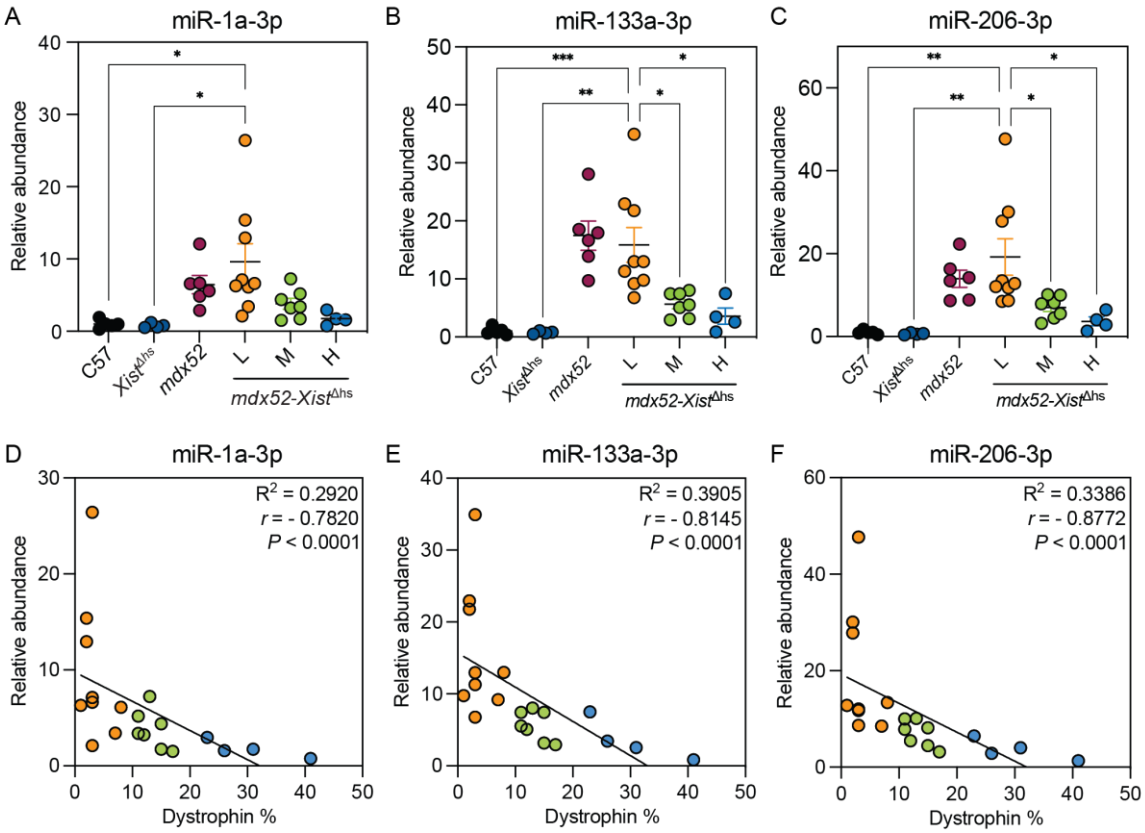

Figure 3.14 Extracellular myomiR biomarkers levels in adult *mdx52-Xist*$^{\Delta hs}$ mice expressing different levels of patchy dystrophin.

RT-qPCR quantification of extracellular myomiRs: miR-1-3p (**A**), miR-133a-3p (**B**) and miR-206-3p (**C**) in serum harvested from adult (6 weeks old) *mdx52-Xist*$^{\Delta hs}$ animals. The values are normalised to internal spike-in control. Spearman correlation analysis of TA dystrophin percentage and relative abundance of serum myomiRs biomarkers for miR-1-3p (**D**), miR-133a-3p (**E**), miR-206-3p (**F**). Statistical analysis: one-way ANOVA with Bonferroni *post hoc* test. *** $P < 0.001$, ** $P < 0.01$, * $P < 0.05$.

3.3.6 Patchy dystrophin and DAPC distribution persist with age

The presence of dystrophin-positive and negative myonuclei within the same myofibre is characteristic of the situation in females heterozygous for mutations in the dystrophin gene [180,181,418]. Early studies of patchy dystrophin localisation in DMD carriers suggested that dystrophin accumulates with age through biochemical (dystrophin diffusion) or genetic (expression from dystrophin-positive satellite cells) correction [180,426]. Accordingly, a progressive increase in dystrophin-positive fibres through the incorporation of dystrophin-expressing satellite cells, as well as expansion of existing dystrophin-positive myonuclear domains, was reported in heterozygous *mdx* mice [419].

To assess if patchy dystrophin distribution is resolved with age in *mdx52-Xist*$^{\Delta hs}$ female muscles, animals were sacrificed at the late time-point of 60 weeks of age (aged, ~14 months, *N* = 21), and skeletal muscle tissues were harvested. The time-point of 60 weeks was selected as reflective of more advanced pathology. Total protein was extracted from TA muscles, and dystrophin protein was measured by western blot and quantified as a percentage of wild-type C57 levels (Figure 3.15 A, B). As in case of adult animals, aged *mdx52-Xist*$^{\Delta hs}$ mice expressed variable levels of dystrophin (Figure 3.15 B). Notably, the overall levels of dystrophin expression were significantly higher in aged versus adult animals (median = 26.5 in aged vs. median = 11.00 in adult, *P* = 0.002), suggesting that dystrophin likely accumulates with age in the analysed cohort. Accordingly, aged animals were assigned into low (~4-20%), medium (~20-46%), and high (~50-94%) dystrophin-expressing groups *post-mortem*.

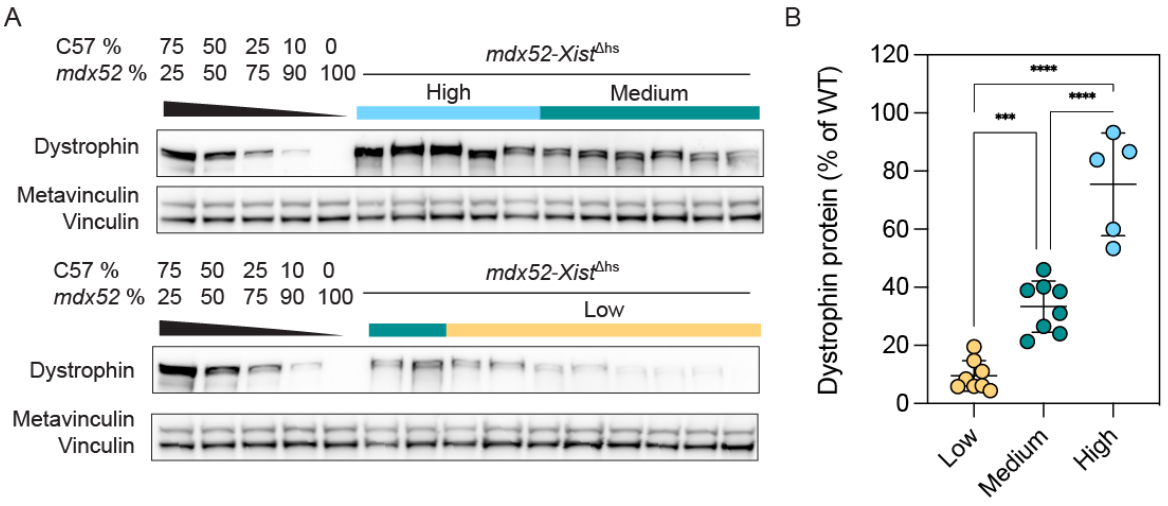

Figure 3.15 Quantification of dystrophin protein expression in aged *mdx52-Xist*$^{\Delta hs}$ muscle.

(**A**) Western blot analysis of dystrophin protein in TA muscle from aged, 60-week-old, *mdx52-Xist*$^{\Delta hs}$. Vinculin was utilised as a loading control, standard curves consisted of mixtures of C57 and *mdx52* TA lysates. (**B**) Quantification of dystrophin western blot as a percentage of wild-type C57. *mdx52-Xist*$^{\Delta hs}$ were assigned to low, medium, or high dystrophin expression groups. Statistical analysis: one-way ANOVA with Bonferroni *post hoc* test. *** $P < 0.001$, ** $P < 0.01$, * $P < 0.05$.

To evaluate the pattern of distribution in aged *mdx52-Xist*$^{\Delta hs}$ dystrophin immunofluorescence was performed in transverse and longitudinal TA muscle sections and in single isolated EDL myofibres (Figure 3.16, Figure 3.17). Strikingly, non-uniform dystrophin localisation was observed in all analysed aged muscles/myofibres regardless of dystrophin expression levels (Figure 3.16, Figure 3.17). In accordance with observations from young *mdx52-Xist*$^{\Delta hs}$ muscles, DAPC components: β-DG and DTNA were non-uniformly distributed and colocalised with dystrophin while nNOS demonstrated uniform localisation along the aged myofibre (Figure 3.17 A, B, C). Together, these results reveal, that spatial restriction of dystrophin is sustained with age, demonstrating that the protein stays confined to its myonuclear domain. Moreover, the progressive incorporation of

satellite cells expressing wild-type dystrophin transcript into myofibres which already express patchy dystrophin likely expanded the pool of protective myonuclear domains. Therefore, the increase in overall dystrophin levels likely reflects the maintenance of increasingly positive myofibres within *mdx52-Xist*$^{\Delta hs}$ muscles.

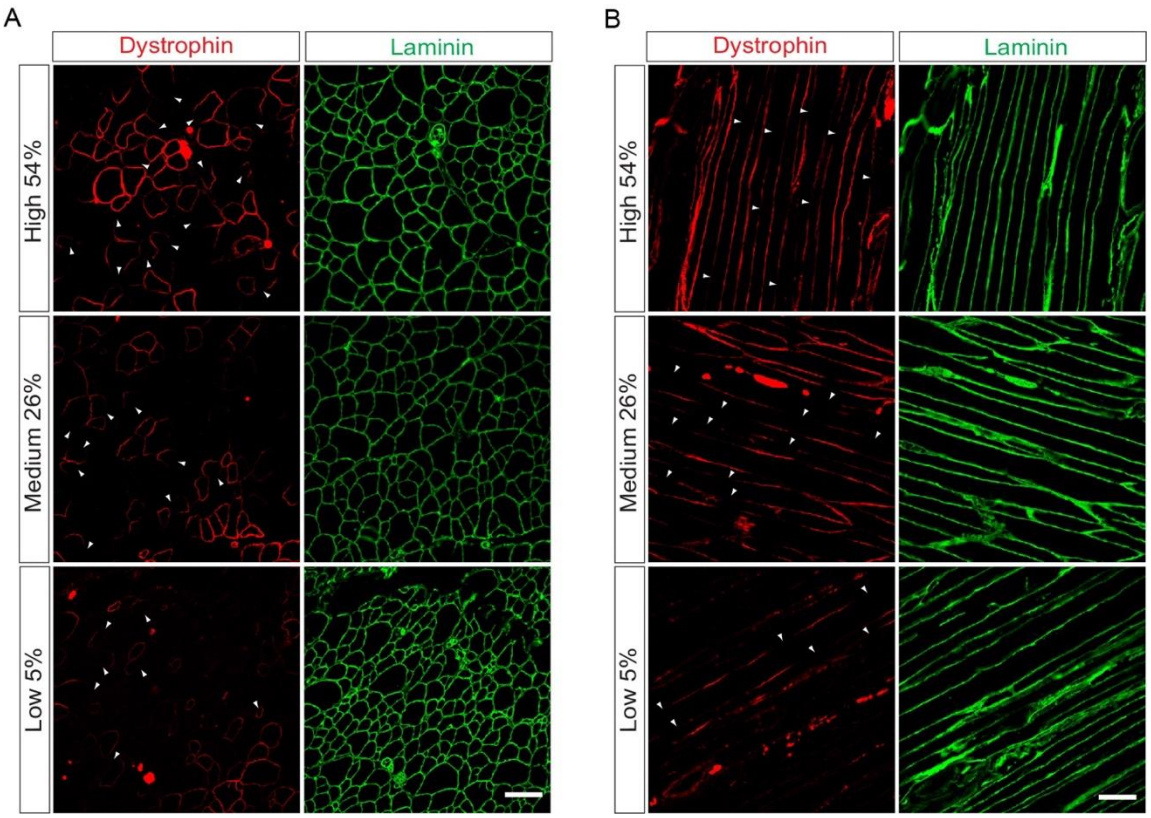

Figure 3.16 Dystrophin localisation in aged *mdx52-Xist*$^{\Delta hs}$ TA muscles.

Representative immunofluorescence staining of dystrophin and laminin in transverse (**A**) and longitudinal (**B**) TA muscle sections of 60-week-old *mdx52-Xist*$^{\Delta hs}$ animals from high, medium, and low dystrophin groups. Within-fibre, patchy dystrophin expression resulting from skewed X-chromosome inactivation indicated with arrowheads. Scale bar indicates 100 μm, images taken at ×20 magnification. Percentage indicates total dystrophin quantification in the animals from which the sections were derived.

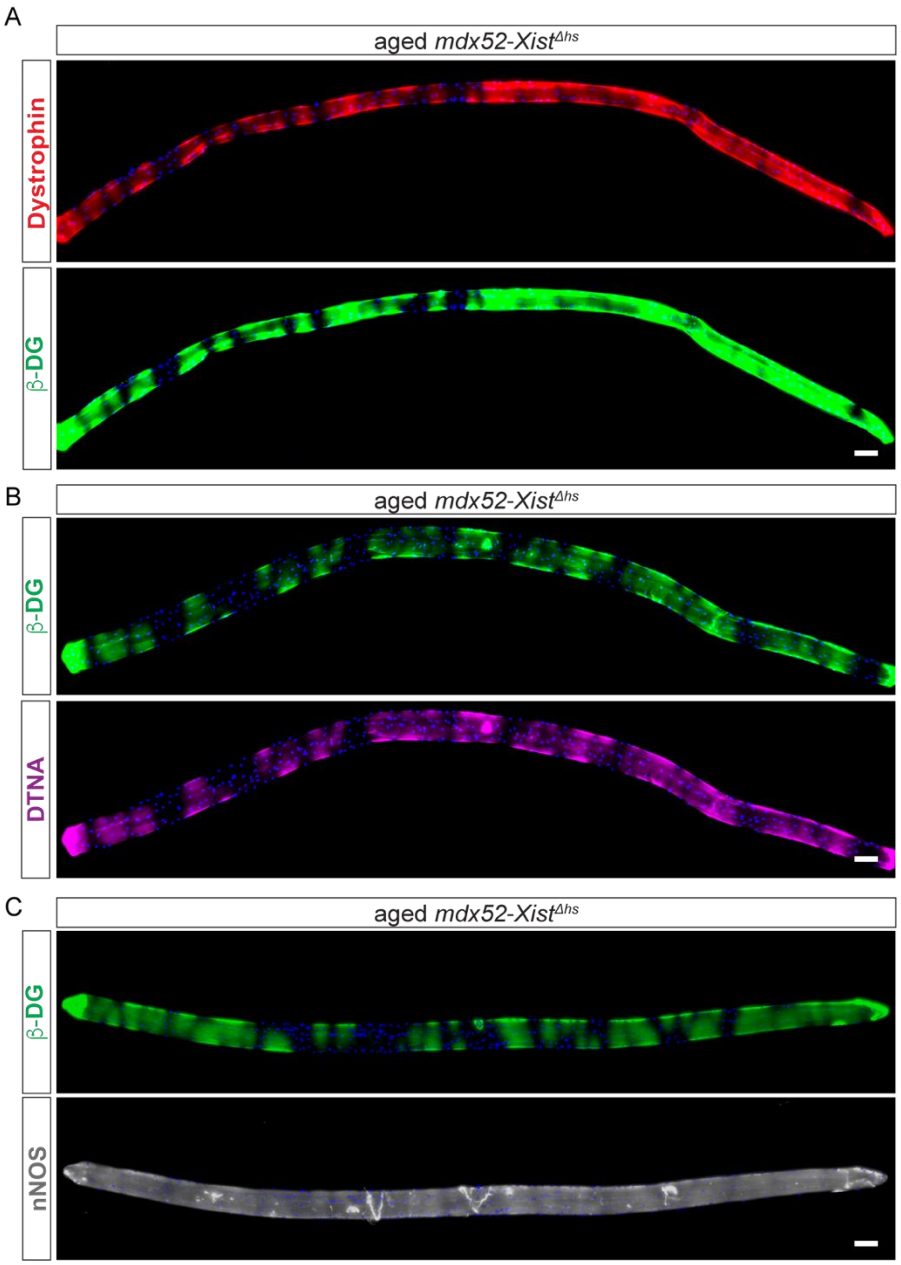

Figure 3.17 Dystrophin and DAPC distribution in aged *mdx52-Xist*$^{\Delta hs}$ EDL myofibres. Representative immunofluorescence co-staining of (**A**) dystrophin and β- DG, (**B**) β-DG and DTNA, (**C**) β-DG and nNOS in isolated EDL single myofibres of *mdx52-Xist*$^{\Delta hs}$. Scale bar indicates 20 µm, tiled images taken at ×10 and stitched in LAS X software. Scale bar indicates 100 µm.

3.3.7 Central nucleation in patchy dystrophin myofibres persist with age

Sustained patchy dystrophin distribution in aged *mdx52-Xist*$^{\Delta hs}$ myofibres indicates that muscles of these animals remain partially unprotected from muscle damage throughout life. To evaluate the markers of muscle turnover in aged animals, analysis of centrally nucleated myofibres in transverse TA sections was performed (Figure 3.18) CNFs were present in all analysed muscles regardless of dystrophin expression level. Their proportion was the highest in the low dystrophin expressing group, with the maximum of 75.5% of the total myofibres in mouse expressing 15% of wild-type dystrophin levels (Figure 3.18 B). The proportion of CNFs was anti-correlated with percentage of dystrophin expressed in TA as measured by western blot (Spearman's r = - 0.5906; P = 0.0078, Figure 3.18 C). The myofibre cross-sectional area analysis revealed no differences between *mdx52-Xist*$^{\Delta hs}$ groups. Together, these results imply that muscles expressing dystrophin in a patchy manner continue to degenerate and regenerate through life and that this process is less pronounced the more non-uniform dystrophin is produced.

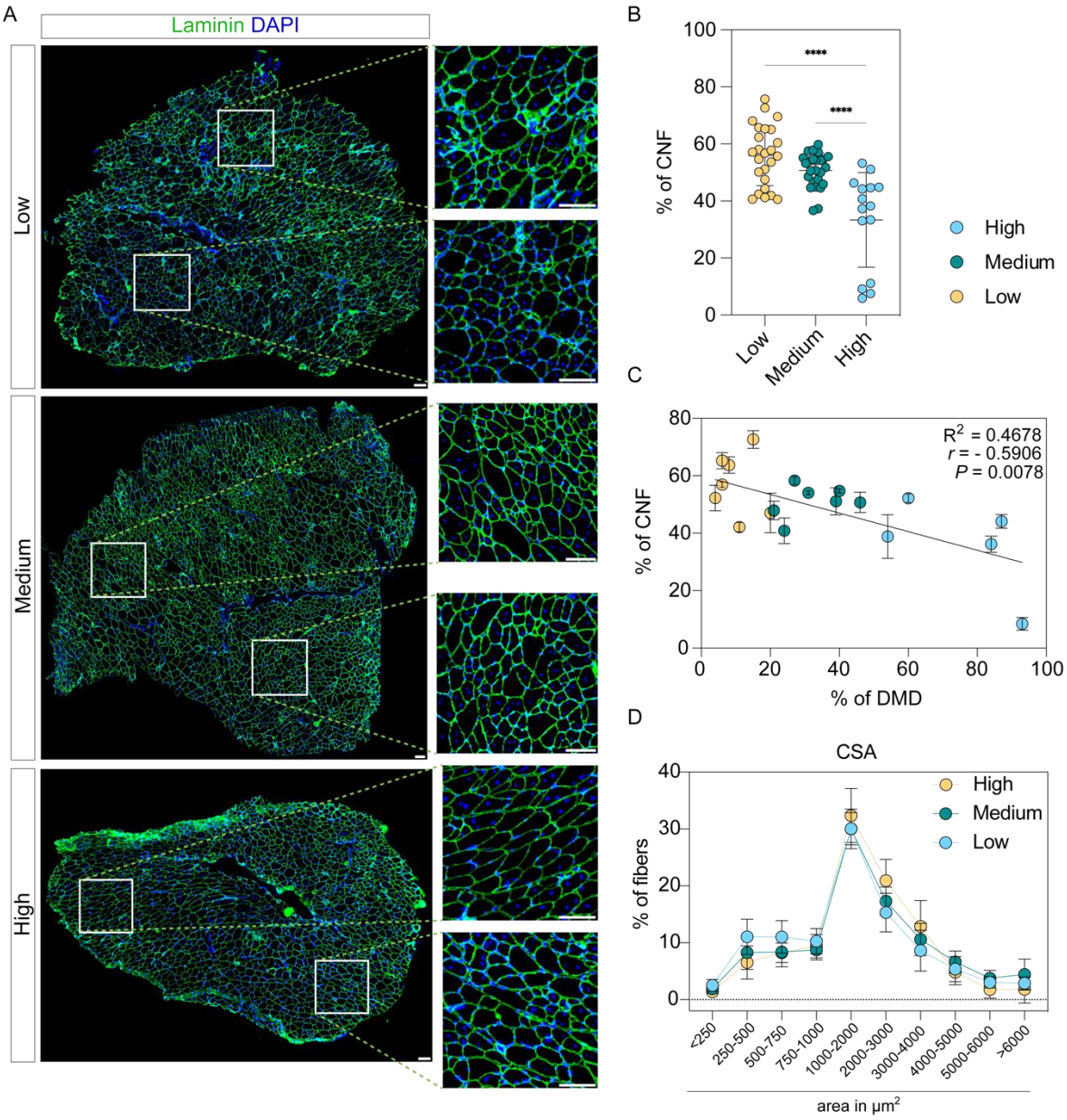

Figure 3.18 Quantification of centrally nucleated myofibres in TA muscle of aged *mdx52-Xist*$^{\Delta hs}$ mice.

(**A**) Representative immunofluorescence images of transverse TA muscle sections from aged (60-week-old) *mdx52-Xist*$^{\Delta hs}$ animals expressing high, medium, and low dystrophin. Sections were stained for laminin (green) as a sarcolemma marker and DAPI (blue) for nuclei visualisation. A magnified view of the sections shows the CNF (centrally nucleated fibres) proportion in two regions of the section. Tiled images were taken at ×10 magnification and stitched in LAS X software. Scale bars represent 100 µm. (**B**) CNF as a proportion of total myofibres analysed per TA section in aged *mdx52-Xist*$^{\Delta hs}$ animals expressing low,

medium, and high dystrophin levels. (**C**) Correlation analysis of dystrophin percentage and average CNF percentage in analysed aged *mdx52-Xist*$^{\Delta hs}$ TA sections. Dystrophin protein percentage was derived from western blot analysis. (**D**) Myofibre size variability in TA sections of *mdx52-Xist*$^{\Delta hs}$ animals expressing high, medium, and low dystrophin visualised through proportion of fibres of specific cross-sectional area (CSA). CNF and CSA were quantified using the MuscleJ2 plugin for Fiji. Statistical analysis: one-way ANOVA with Bonferroni post hoc test. ***$P < 0.001$, **$P < 0.01$, *$P < 0.05$.

Additionally, extracellular myomiRs biomarkers were analysed in the serum of aged *mdx52-Xist*$^{\Delta hs}$ animals. All analysed myomiRs were expressed at a similar level in *mdx52-Xist*$^{\Delta hs}$ regardless of dystrophin expression levels (Figure 3.19 A, B, C). In contrast to adult *mdx52-Xist*$^{\Delta hs}$ mice, no correlation between serum myomiR and dystrophin expression levels was observed for aged animals (Figure 3.19 D, E, F). Notably, a previous study from our group showed that the abundance of extracellular myomiRs in treated *mdx* animals declines with age [107]. Accordingly, the Cq values (quantification cycle of qPCR, where the fluorescent signal of sample crosses the threshold levels) of myomiRs revealed ~ 2 cycle (i.e. ~ 4-fold) difference in myomiR quantity between adult and aged *mdx52-Xist*$^{\Delta hs}$ serum samples (data not shown). As such, it is possible that decrease in myomiR abundance with age results in a loss of correlation between dystrophin and serum myomiR levels. Moreover, this suggests that serum myomiRs are a useful reflection of dystrophin levels, regardless of its distribution only at the early stage of the disease [320].

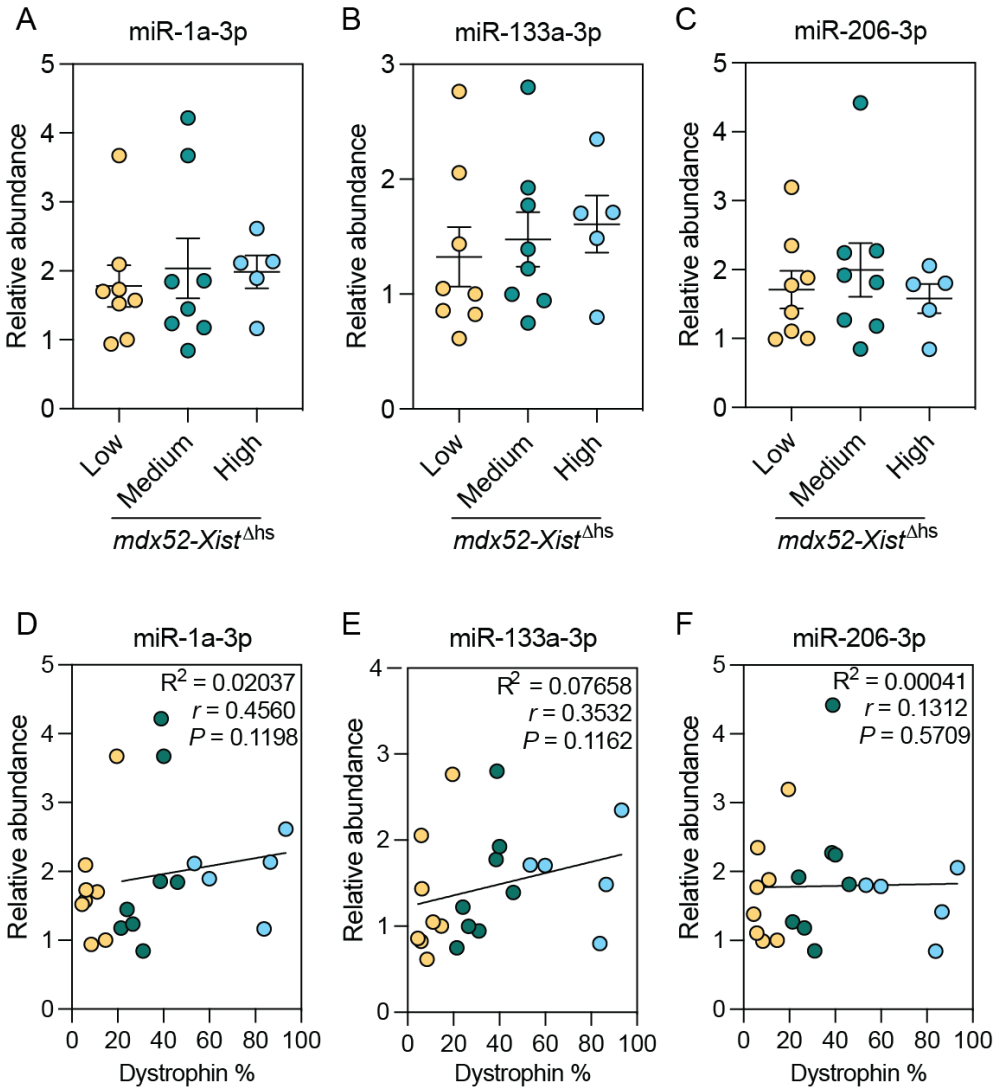

Figure 3.19 Correlation of extracellular myomiRs biomarkers with dystrophin in aged *mdx52-Xist*$^{\Delta hs}$ animals.

RT-qPCR quantification of extracellular myomiRs: miR-1-3p (**A**), miR-133a-3p (**B**) and miR-206-3p (**C**) in serum harvested from aged (60-week-old) *mdx52-Xist*$^{\Delta hs}$ animals. The values are normalised to internal spike-in control. Spearman correlation analysis of TA dystrophin percentage and relative abundance of serum myomiRs biomarkers for miR-1-3p (**D**), miR-133a-3p (**C**), miR-206-3p (**F**).

3.3.8 Centrally nucleated myofibres undergo hypertrophy and nuclear accretion with age

Examination of TA muscle sections and single myofibres from 60-week-old animals revealed a larger myofibre diameter compared to 6-week-old animals, which is indicative of muscle hypertrophy. While progressive muscle hypertrophy is an established component of dystrophic pathology in mice, its quantitative analysis is rarely performed with the distinction between centrally nucleated and peripherally nucleated myofibres [129,427,428]. Utilising the information collected during CNF analysis in adult and aged *mdx52-Xist*$^{\Delta hs}$ muscle, a quantitative comparison of CNF properties (i.e. proportion, multi-nucleation and size) was performed (Figure 3.20). In agreement with a previous study by Massopust *et al.*, an overall increase in the number of CNFs with age was observed (Figure 3.20) [129]. Interestingly, numbers of central nuclei (CN) per CNF also showed an increase with age (Figure 3.20 B). Specifically, a decrease in myofibres containing 1 CN and an increase in ≥2 CN with age was observed, suggesting that CNF acquire more nuclei before the existing central nucleation is resolved (Figure 3.20 B). Accordingly, the minimum Feret diameter and CSA analysis revealed that aged CNF are overall larger in comparison to adult muscle (Figure 3.20 C, D). These results show that CNFs undergo substantial significant hypertrophy, which is likely driven by the progressive accretion of new myonuclei. These observations, together with the limited dispersion of central nuclei to the myofibre periphery observed in mice, show that CNFs at later stages largely do not constitute a population of recently formed muscle cells. Together, these results emphasise the fact that the proportion of CNF at later stages of life in mice reflects the cumulative history of regeneration [136].

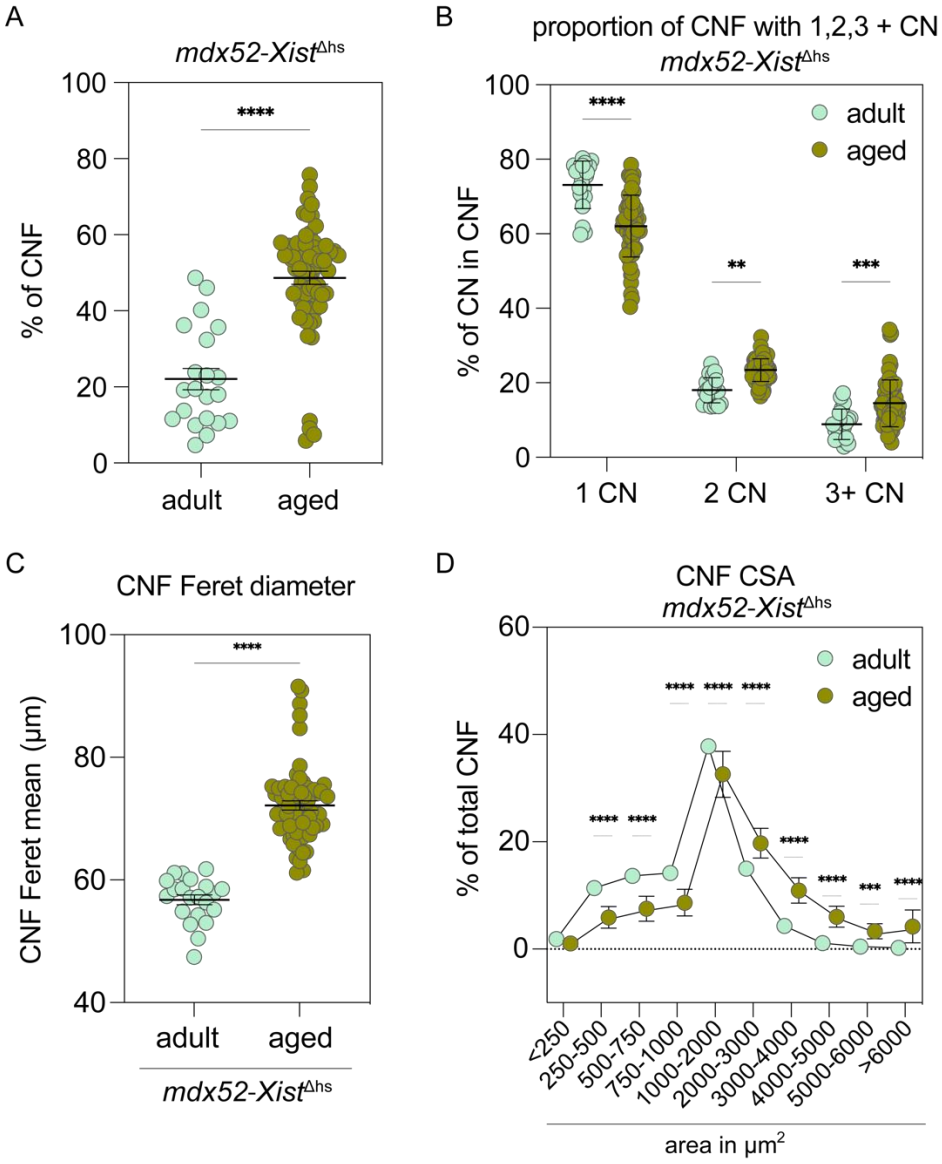

Figure 3.20 Analysis of proportion, multi-nucleation and diameter of centrally nucleated myofibres in transverse TA sections of adult vs. aged *mdx52-Xist*$^{\Delta hs}$ mice.

(**A**) Comparison of CNF levels as a percentage of total myofibres observed in adult and aged *mdx52-Xist*$^{\Delta hs}$ TA muscle. (**B**) Comparison of central nuclei (CN) numbers per CNF observed in adult and aged *mdx52-Xist*$^{\Delta hs}$ TA muscle. (**C**) Comparison of minimal Feret diameter of CNF between adult and aged *mdx52-Xist*$^{\Delta hs}$ TA muscle. (**D**) Distribution of CNF cross-sectional area (CSA) in young vs aged *mdx52-Xist*$^{\Delta hs}$ TA muscle. Statistical analysis: unpaired t-test (A, B, C) and two- ANOVA with Sidak *post hoc* test (D). ***$P < 0.001$, **$P < 0.01$, *$P < 0.05$.

3.3.9 Utrophin does not correlate with patchy dystrophin levels in adult and aged *mdx52-Xist*$^{\Delta hs}$ animals

Utrophin and dystrophin exhibit reciprocal expression patterns during muscle development as well as in dystrophic pathology [429]. Moreover, when expressed together, dystrophin and utrophin localise to the same binding spots at sarcolemma in mouse myofibres [104]. Due to the dystrophic nature of *mdx52-Xist*$^{\Delta hs}$ myofibres, and the presence of dystrophin in positive myonuclear domains, unrestricted availability of binding sites exists within dystrophin-negative regions. As such, it is plausible that utrophin is present in those areas, thereby partially compensating for the lack of dystrophin in patchy myofibres. To test the hypothesis of biological correlation between utrophin and dystrophin in patchy *mdx52-Xist*$^{\Delta hs}$ myofibres, utrophin western blot was performed on muscle lysates from adult and aged animals (Figure 3.21 A, C). Utrophin expression was detected in all analysed animals regardless of age or dystrophin levels (Figure 3.21 A, C). The relative abundance of utrophin was variable between animals. Correlation analysis revealed a lack of relationship between the amount of utrophin and dystrophin percentage in the TA muscle of adult and aged animals (Spearman's r = -0.2807, P = 0.6604 and, r = -0.03506, P = 0.3023 respectively, Figure 3.21 B, D).

To assess the utrophin localisation in patchy dystrophin muscles, immunofluorescence of utrophin was performed in the transverse TA sections of *mdx52-Xist*$^{\Delta hs}$ animals identified to express high utrophin and low dystrophin levels by western blot (Figure 3.22). The 12-week-old *mdx52* tissue sections were used as control where a clear utrophin signal was detected at the membrane of a relatively small, centrally nucleated myofibres organised in densely packed single clusters (Figure 3.22 top panel). Accordingly, several small groups of newly formed CNF with positive utrophin staining were detected in aged *mdx52-Xist*$^{\Delta hs}$ muscle expressing high levels of utrophin. Notably, no utrophin expression was observed at the sarcolemma of larger *mdx52-Xist*$^{\Delta hs}$ TA myofibres (Figure 3.22 middle, bottom panel). As such, utrophin expression in *mdx52-Xist*$^{\Delta hs}$ animals reflects

the ongoing regenerative processes and is not concentrated in the dystrophin-negative myonuclear domains.

Attempts to visualise utrophin staining in longitudinal sections of *mdx52-Xist*$^{\Delta hs}$ TA muscles were inconclusive. As can be seen in transverse sections, majority of the myofibres are utrophin-negative (Figure 3.22). As such, distinguishing positive signal from background in transverse sections was challenging considering the paucity of *bone fide* utrophin positive sarcolemma regions. As such, the localisation of utrophin in mature, patchy-dystrophin myofibers of *mdx52-Xist*$^{\Delta hs}$ mice was not determined.

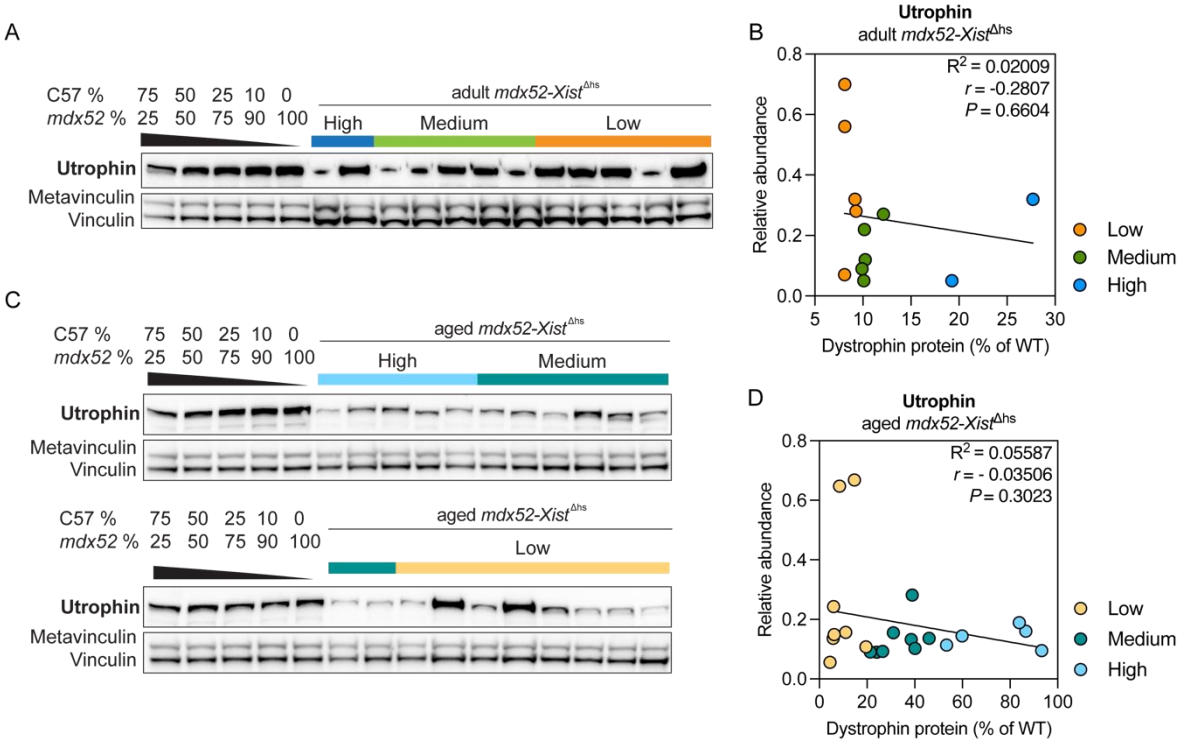

Figure 3.21 Quantification of utrophin protein expression in patchy dystrophin expressing *mdx52-Xist*$^{\Delta hs}$.

Western blot analysis of utrophin protein in TA muscle from (**A**) adult (6 weeks old) and (**C**) aged (60 weeks old) *mdx52-Xist*$^{\Delta hs}$. Vinculin was utilised as a loading control. Labelled, coloured boxes demonstrate levels of dystrophin expressed in respective samples. Spearman correlation analysis of dystrophin percentage and relative utrophin abundance in TA muscles of (**B**) adult and (**D**) aged *mdx52-Xist*$^{\Delta hs}$ animals.

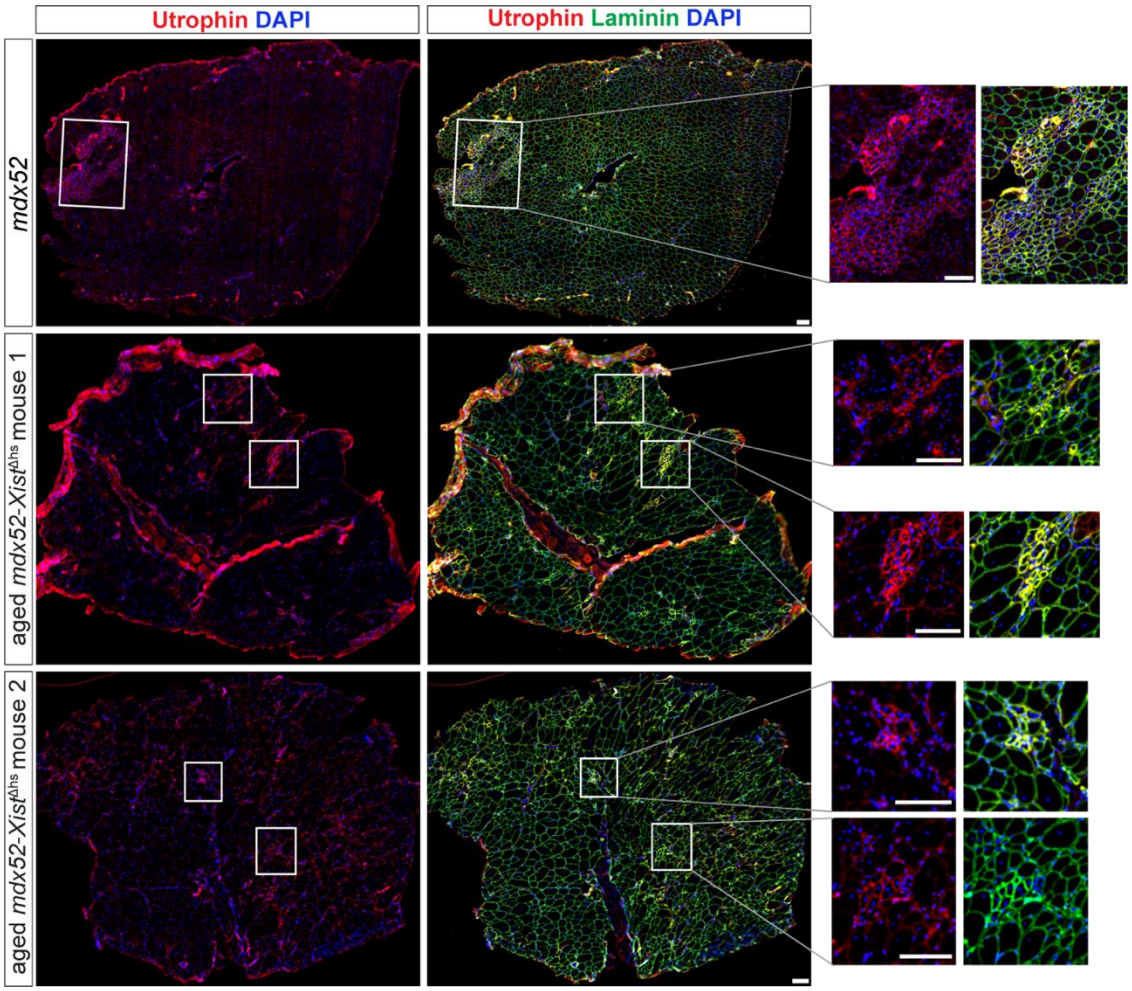

Figure 3.22 Utrophin localisation in aged *mdx52-Xist*$^{\Delta hs}$ TA muscles expressing high utrophin levels.

Immunofluorescence staining of utrophin and laminin in TA muscle sections of 12-week-old *mdx52* mouse and 60-week-old *mdx52-Xist*$^{\Delta hs}$ animals from low dystrophin group expressing high levels of utrophin as quantified with western blot. Insets demonstrate utrophin signal detected in small-calibre centrally nucleated myofibres in control *mdx52* and both *mdx52-Xist*$^{\Delta hs}$ animals. Scale bar indicates 100 µm, tiled images taken at ×20 magnification and stitched using LAS X software.

3.3.10 The microtubule network is disorganised in *mdx52-Xist*$^{\Delta hs}$ animals

One of the hallmarks of correct myofibre organisation is the intricately organised microtubule network that was recently shown to facilitate the active transport of various RNAs and proteins, including the ribosomal machinery, throughout the cell [301,302]. As such, microtubules play a central role in myofibre biology, compensating limited within-fibre diffusion. Notably, dystrophin protein contains a microtubule-binding domain and therefore has been proposed to stabilise the microtubule cytoskeleton in myofibres [49,50]. This role is supported by the fact that the microtubule network is significantly disorganised in dystrophic mice, with costameric (transverse) components being the most severely affected [49,294]. Thus, it is likely that non-uniformly distributed dystrophin can modify the organisation of the microtubules in *mdx52-Xist*$^{\Delta hs}$ mice partially restoring the correct transport route within the cell. Microtubule network organisation was characterised using the texture detection technique (TeDT) developed by Liu *et al*. [290]. The software was designed to identify differences between healthy and dystrophic animals. Specifically, it measures the distribution of microtubule directionality angles in addition to the vertical directionality score which indicates the proportion of transverse microtubules within the myofibre. TeDT analysis of microtubules was performed on images acquired from *mdx52-Xist*$^{\Delta hs}$, *mdx52*, and wild-type C57 EDL myofibres (n = 40, 31 and 32 myofibres respectively). The characteristic peak at the 90° intersection angle representing the transverse microtubules together with a high vertical directionality score was detected in wild-type C57 myofibres (Figure 3.23 A, B). In agreement with existing literature, the microtubule network was visibly disorganised in *mdx52* animals, with significant loss of transverse microtubules (Figure 3.23 A, C) [49,294]. This disorganised pattern was partially restored in *mdx52-Xist*$^{\Delta hs}$ myofibres as confirmed by intermediate microtubule intersection angles distribution (Figure 3.23 A) and vertical directionality scores (Figure 3.23 C). These results show that non-uniformly distributed dystrophin partially restored that wild-type pattern of the microtubule grid organisation.

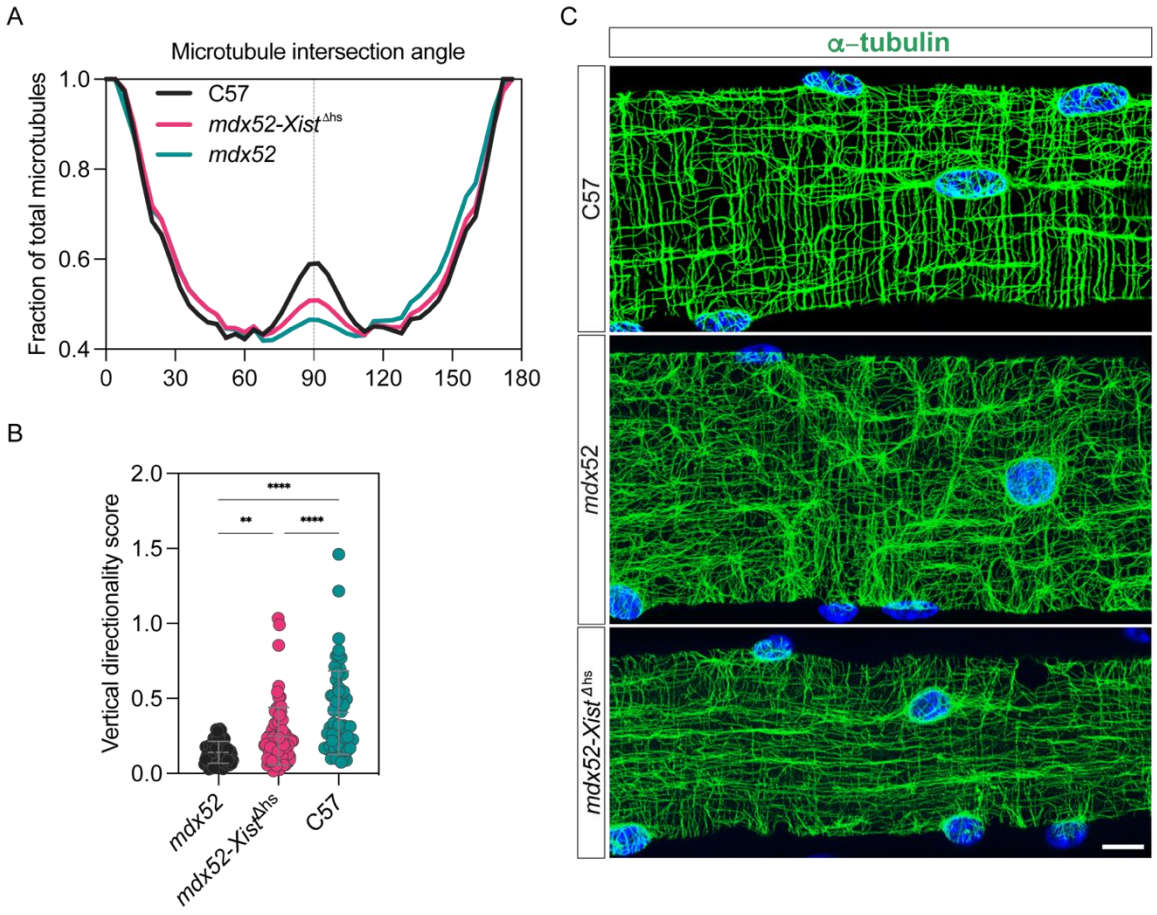

Figure 3.23 Microtubule network organisation in dystrophic, patchy dystrophin and healthy myofibres.

(**A**) Histogram of mean distribution of microtubules of different intersection angles relative to myofibre long axis. Transverse, costameric microtubule peak (90°) is marked with a dotted line. (**B**) Comparison of vertical directionality score reflecting the summed values of microtubules present between 80 to 100 degrees within each fibre. (**C**) Representative immunofluorescence images of cortical microtubule network organisation in C57 wild type, *mdx52* and *mdx52-Xist*$^{\Delta hs}$ single isolated EDL myofibres. Images taken at ×40 magnification, scale bar represents 10 µm. Statistical analysis: one-way ANOVA with Bonferroni post hoc test. *** $P < 0.001$, ** $P < 0.01$, * $P < 0.05$.

The analysis of *mdx52-Xist*$^{\Delta hs}$ microtubules without discriminating between dystrophin-positive and negative myonuclear domains, could hinder the local network stabilisation effects in the dystrophin positive myonuclear domains. As such, a parallel analysis of microtubule network organisation in dystrophin-positive versus dystrophin-negative regions of *mdx52-Xist*$^{\Delta hs}$ myofibres was performed (Figure 3.24). Based on distribution of microtubule intersection angles (Figure 3.24 A) and vertical directionality scores (Figure 3.24 B) no difference in microtubule lattice organisation was observed between the analysed domains. This suggests that the absence of dystrophin alone may not be sufficient to induce cytoskeletal network disruption.

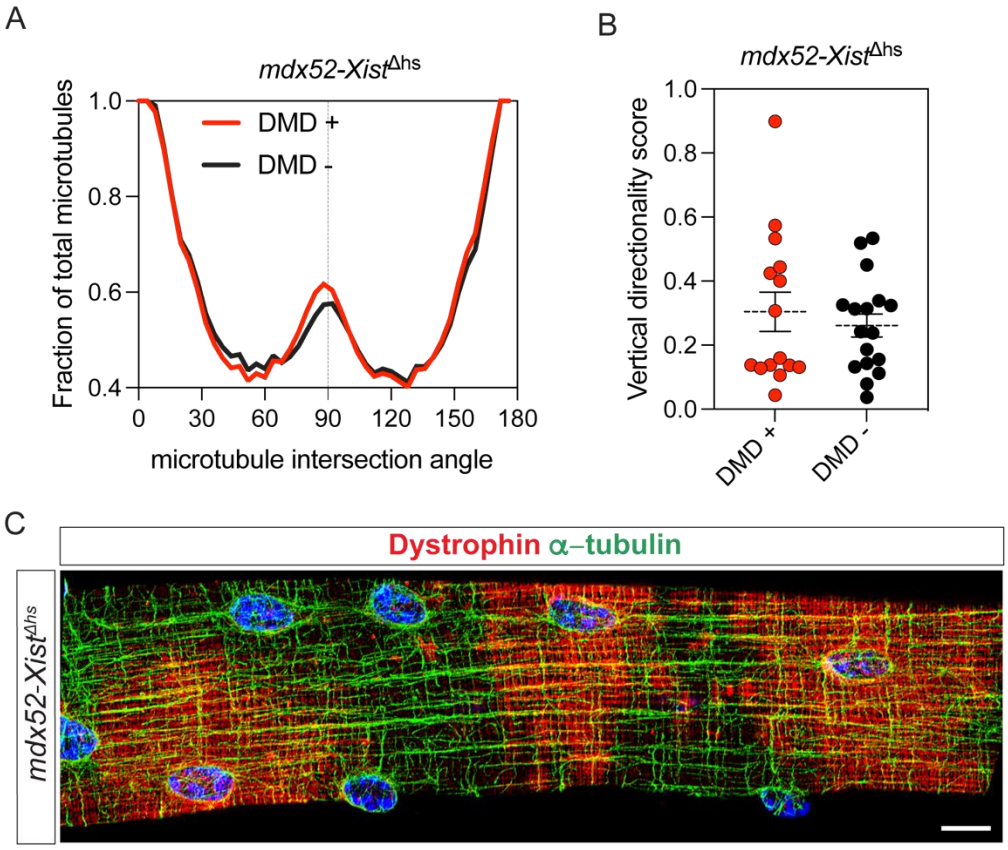

Figure 3.24 Microtubule network organisation in dystrophin positive and dystrophin negative myonuclear domains.

(**A**) Histogram of mean distribution of microtubules of different intersection angles relative to myofibre long axis in dystrophin positive, and negative myonuclear domains of *mdx52-Xist*$^{\Delta hs}$ EDL myofibre. Transverse, costameric microtubule peak (90°) is marked with a

dotted line. (**B**) Comparison of vertical directionality score reflecting the summed values of microtubules present between 80 to 100 degrees within each fibre. (**C**) Representative immunofluorescence images of cortical microtubule network organisation in patchy dystrophin *mdx52-Xist*$^{\Delta hs}$ single isolated EDL myofibre. Image taken at ×40 magnification, scale bar represents 10 μm. Statistical analysis: two-tailed t-test. *** $P < 0.001$, ** $P < 0.01$, * $P < 0.05$.

3.3.11 *mdx52-Xist*$^{\Delta hs}$ muscles contain distinct myofibre classes.

The present study leverages single isolated myofibres, thereby enabling a deeper investigation of the intricate morphological and molecular changes of muscle cells in the context of DMD. Throughout the study, examination of numerous single isolated myofibres revealed significant morphological variations between cells originating from *mdx52-Xist*$^{\Delta hs}$ muscles. This prompted a classification of analysed myofibres into different categories based on their morphology. Specifically, systematic morphological evaluation (see Materials and Methods section 3.2.6) of isolated and stained myofibres revealed the presence of three distinct *mdx52-Xist*$^{\Delta hs}$ myofibre classes based on the location of nuclei within the myofibre: (i) centrally nucleated myofibres indicative of recent or past satellite cell-driven fusion (CNF), (ii) myofibres with all nuclei localised to the cell periphery (non-CNF), and (iii) myofibres containing centrally nucleated segments in otherwise normal fibres (segmented) (Figure 3.25 A, B). Comprehensive visual scoring of 1157, *mdx52-Xist*$^{\Delta hs}$ EDL isolated myofibres (*N* = 13 animals, age: 12–17 weeks old) revealed that the majority (60%) are non-CNF - fully mature myofibres which either did not undergo degeneration/regeneration cycle or underwent full maturation process after regeneration (Figure 3.25 A, B). The second most prevalent group were the segmented myofibres (23.5%), followed by CNF where the central nuclei chain spans the whole length of myofibres reflecting recent or past satellite cell fusion events (16.5%) (Figure 3.25 A, B).

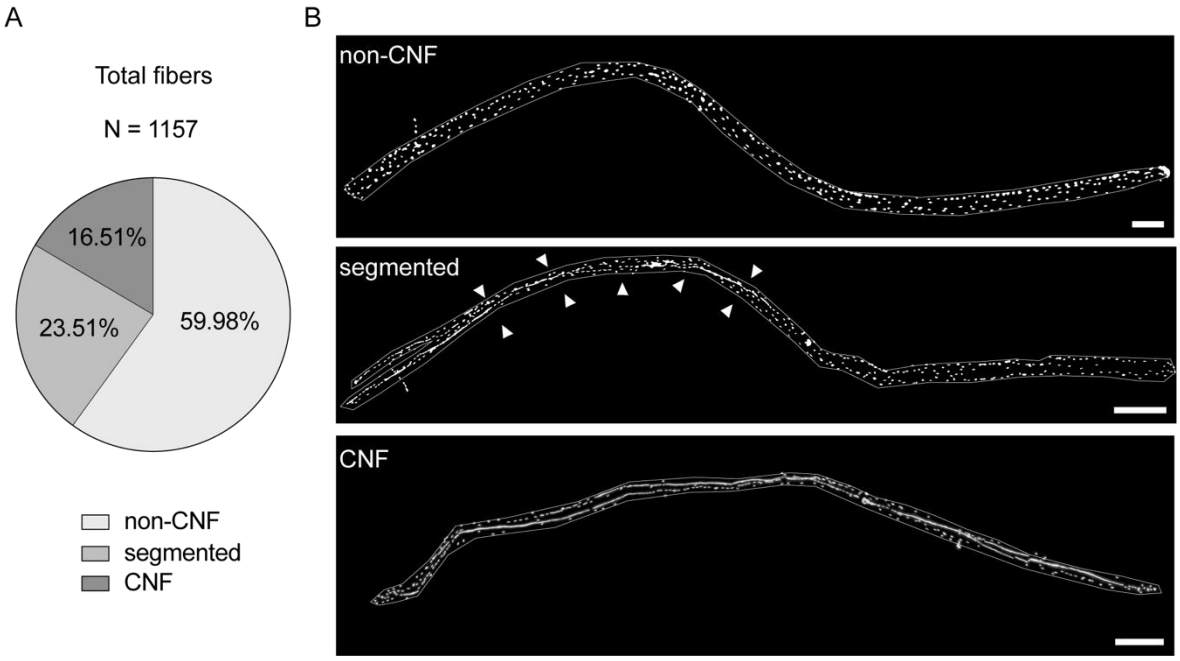

Figure 3.25 Proportion of myofibre classes observed in *mdx52-Xist*$^{\Delta hs}$ EDL muscle.

1157 myofibres from *mdx52-Xist*$^{\Delta hs}$ EDL muscle aged between 12-17 weeks were classified according to the presence of centrally located nuclei (see Materials and Methods section 3.2.6). Representative immunofluorescence images of non-CNF segmented and CNF myofibres. Tiled image was acquired at ×10 magnification and stitched using LAS X software. Scale bar represents 200 µm.

3.3.12 Central nucleation impacts the myofibre morphology and dystrophin expression

The presence of central nuclei within a myofibre is most commonly considered as the marker of myofibre regeneration. Notably, centrally nucleated myofibres can compose up to 100% of muscle in dystrophic animals [126,127,129]. Moreover, as shown in Figure 3.20 and Figure 3.18, central nucleation persists with age in *mdx52-Xist*$^{\Delta hs}$ muscle. As such, CNF constitute an inherent component of the dystrophic pathology in mice. Nevertheless, not much is known regarding the effects of central nucleation on myofibre morphology and biology especially in the context of dystrophin expression. To address this gap, analysis of myonuclei numbers, microtubule network organisation and dystrophin expression was compared among different myofibre classes of dystrophic *mdx52* and *mdx52-Xist*$^{\Delta hs}$ muscles.

3.3.12.1 Centrally nucleated myofibres are hypernucleated

Visual examination of centrally nucleated regions of segmented myofibres and CNF from dystrophic *mdx52* demonstrated several features specific to centrally located nuclei. Specifically, the internalised nuclei were usually packed in dense, long chains with minimal distances between the individual nuclei (Figure 3.26 A, white arrows). In some cases, the distance between adjacent nuclei was challenging to resolve with nuclear staining only. Often, several, parallel chains were observed within one region of interest (Figure 3.26 A, blue arrows). Notably, quantification of myonuclei per myofibre volume revealed a ~ 2-fold increase in nuclei number per myofibre volume in CNF vs. non-CNF (mean = 20.8 and 9.4 respectively, P <0.0001, Figure 3.26 B). Therefore, the CNF are hypernucleated in comparison to non-centrally nucleated myofibres. Notably, increased nuclei number per myofibre volume suggests a reduction of the myonuclear domain in CNF in comparison to non-CNF. It was proposed before that hypernucleation in *mdx* myofibres could represent a compensatory effect of boosted protein production needed for the repair of damaged muscle fibres [129].

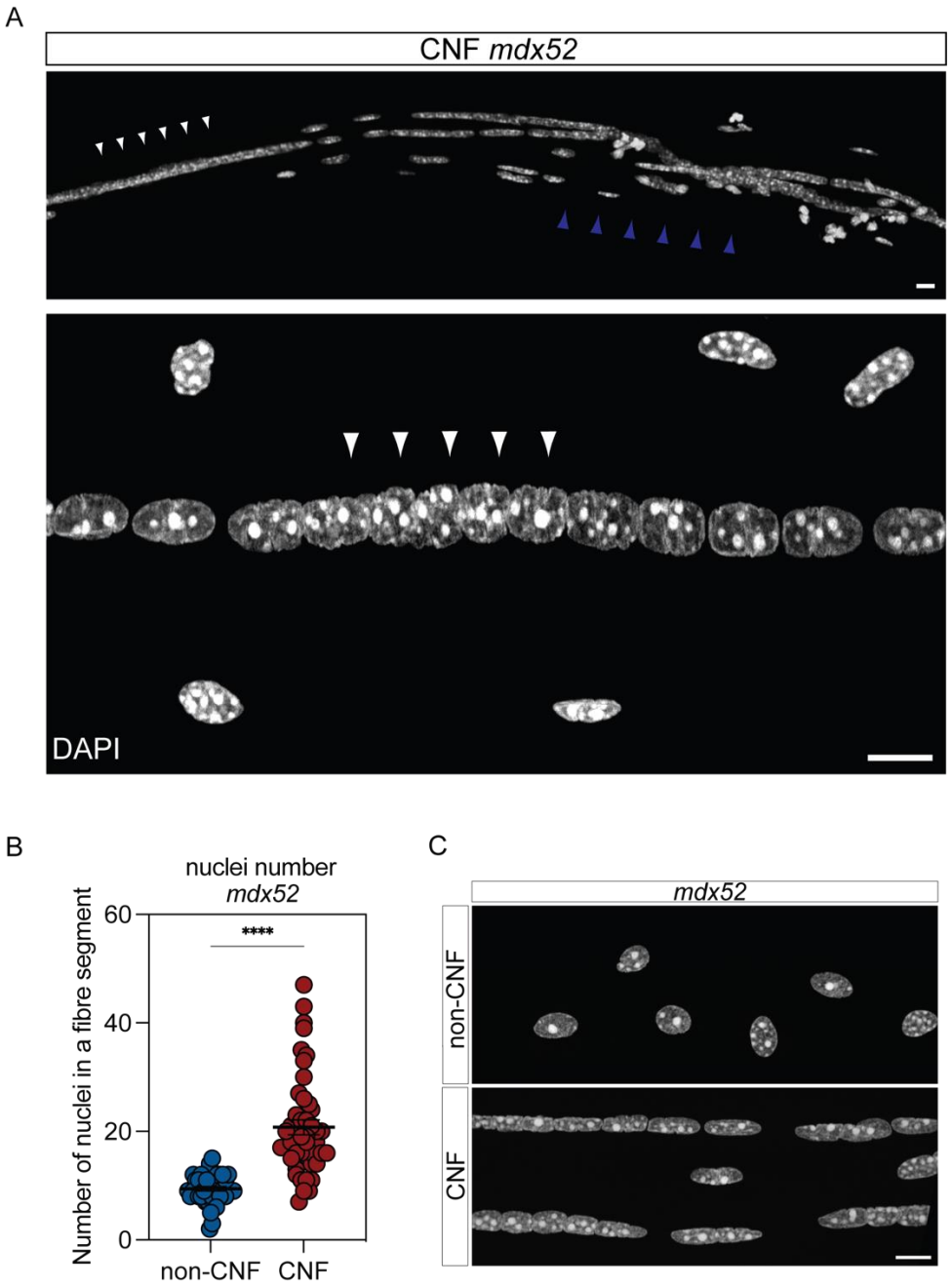

Figure 3.26 Quantification of myonuclei numbers in CNF vs non-CNF.

(**A**) Representative myonuclei staining of centrally nucleated segments in single isolated myofibres from *mdx52* animals. (**B**) Quantification of nuclei numbers in CNF (n = 46) versus non-CNF (n = 41) single isolated *mdx52* EDL myofibres. (**C**) Representative myonuclei staining of CNF vs. non-CNF myofibre segments. Images taken at ×40 magnification, scale bar represents 10 µm. Statistical analysis: two-tailed t-test. *** $P < 0.001$, ** $P < 0.01$, * $P < 0.05$.

3.3.12.2 Microtubule network is more disrupted in CNF

Notably, in mature myofibres, nuclei play a crucial role as a microtubule organisation centre [293,297]. As such the distinct localisations of myonuclei within CNFs and non-CNFs could potentially affect the organisation of microtubule network. To this end, the directionality of cortical microtubules was analysed in CNF and non-CNF EDL myofibres harvested from 12-week-old *mdx52* mice. A significant difference in the lattice organisation was observed, with non-CNF myofibres containing more transverse microtubules (Figure 3.27 A, C). This was also reflected in the higher vertical directionality scores in non-CNF versus CNF myofibres (Figure 3.27 B). These results show, that within dystrophic myofibres, the microtubule lattice is significantly more disrupted in CNF than in non-CNF myofibres. Therefore, the localisation of nuclei is an important factor contributing to the microtubule organisation within the myofibre.

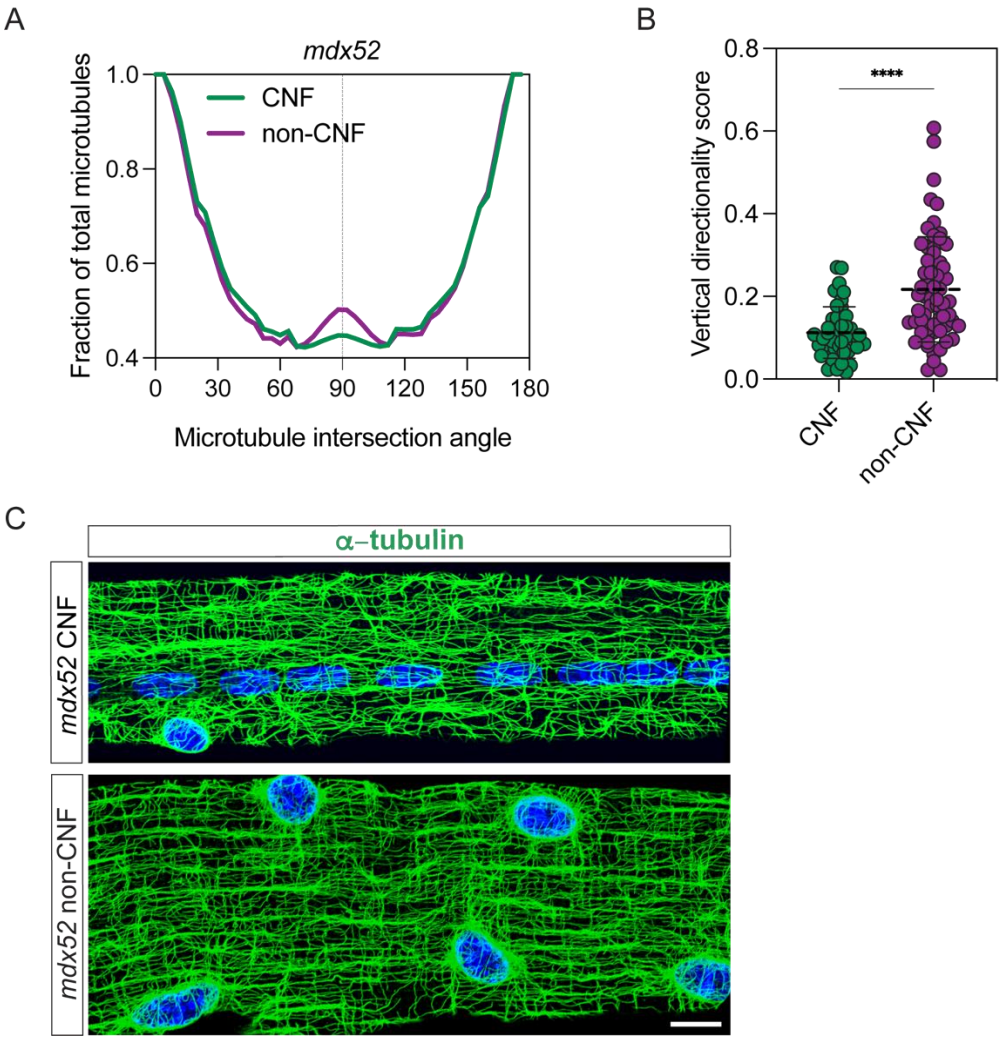

Figure 3.27 Microtubule network organisation in CNF and non-CNF.

(**A**) Histogram of mean distribution of microtubules of different intersection angles relative to myofibre long axis in CNF and non-CNF myofibres of *mdx52* EDL muscle. Transverse, costameric microtubule peak (90°) is marked with a dotted line. (**B**) Comparison of vertical directionality score reflecting the summed values of microtubules with directionality angle 80 to 100 degrees within each fibre. (**C**) Representative immunofluorescence images of cortical microtubule network organisation in CNF and non-CNF *mdx*52 single isolated EDL myofibres. Images taken at ×40 magnification, scale bar represents 10 μm. Statistical analysis: two-tailed t-test. *** $P < 0.001$, ** $P < 0.01$, * $P < 0.05$.

3.3.12.3 Dystrophin mRNA is expressed but not translated in CNF and CN segments

Analysis of dystrophin protein distribution among the different myofibre classes of *mdx52-Xist*$^{\Delta hs}$ EDL muscle revealed a unique feature of dystrophin localisation. Among segmented *mdx52-Xist*$^{\Delta hs}$ myofibres (*n* = 272) analysed for DAPC (i.e. either dystrophin or β-DG expression) in 75.37% (205) the sarcolemmal DAPC signal was observed only in the peripherally nucleated myofibre regions (Figure 3.28 A, B). Within each analysed segmented myofibre, a substantial sarcolemmal coverage of DAPC was noted in non-centrally nucleated regions, suggesting that these fibres are broadly competent to express dystrophin. As such, it can be assumed that a considerable number of nuclei within centrally nucleated regions express functional dystrophin. Notably, this observation was supported by results obtained from classification of dystrophin expression in CNF where 88% of analysed fibres (*n* = 192) completely lacked DAPC at the sarcolemma (Figure 3.29). Importantly, contrary to previous reports, dystrophin mRNA signal was detected in all analysed myonuclei in CNF, segmented and non-CNF myofibres (Figure 3.30 A) [430,431]. This includes a clear dystrophin mRNA signal of a single, large, high intensity ‘blob’ characteristic for dystrophin in all nuclei composing centrally localised chains in CNF (Figure 3.30 A). Together, these results show that dystrophin protein expression is linked to localisation of nuclei within *mdx52-Xist*$^{\Delta hs}$ myofibres. Specifically, dystrophin mRNA is expressed but not translated in centrally nucleated regions, suggesting post-transcriptional repression of dystrophin production in these segments.

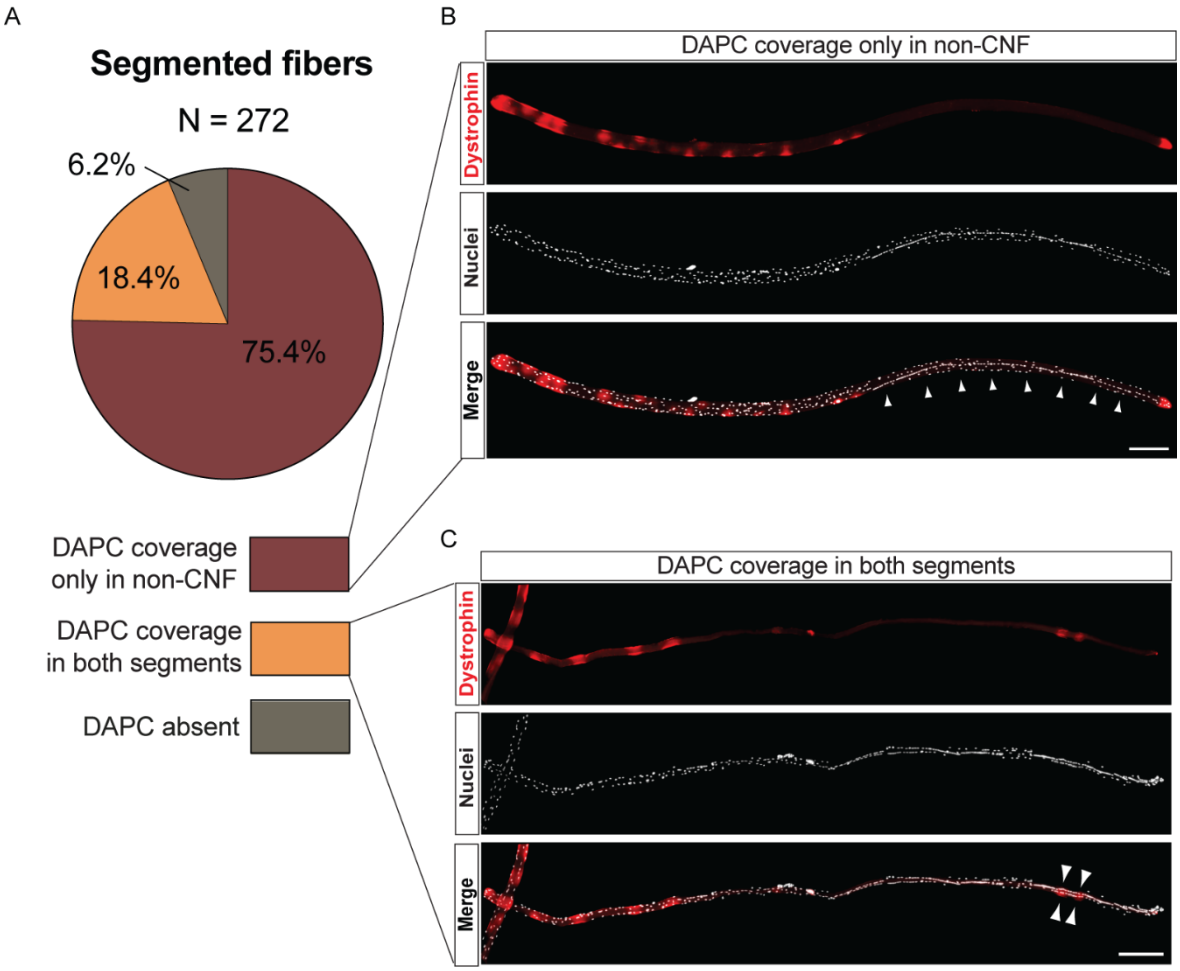

Figure 3.28 Classification of segmented *mdx52-Xist*$^{\Delta hs}$ myofibres based on DAPC presence.

DAPC presence was detected either with dystrophin or β-DG staining. A total of 272 centrally nucleated myofibres from 13 animals were analysed. (**A**) Pie chart representing proportions of centrally nucleated myofibres from adult *mdx52-Xist*$^{\Delta hs}$ animal expressing DAPC in only non-centrally nucleated segment (red), both segments (orange) or not expressing DAPC (grey). Representative immunofluorescence staining of segmented *mdx52-Xist*$^{\Delta hs}$ myofibres (**B**) expressing DAPC only in non-CNF (white arrows indicate the centrally nucleated segment) or (**C**) expressing DAPC in both segments (white arrows indicate the presence of DAPC in the centrally nucleated region). Tiled images were acquired at ×10 magnification and stitched in LAS X Software. Scale bar represents 200 µm.

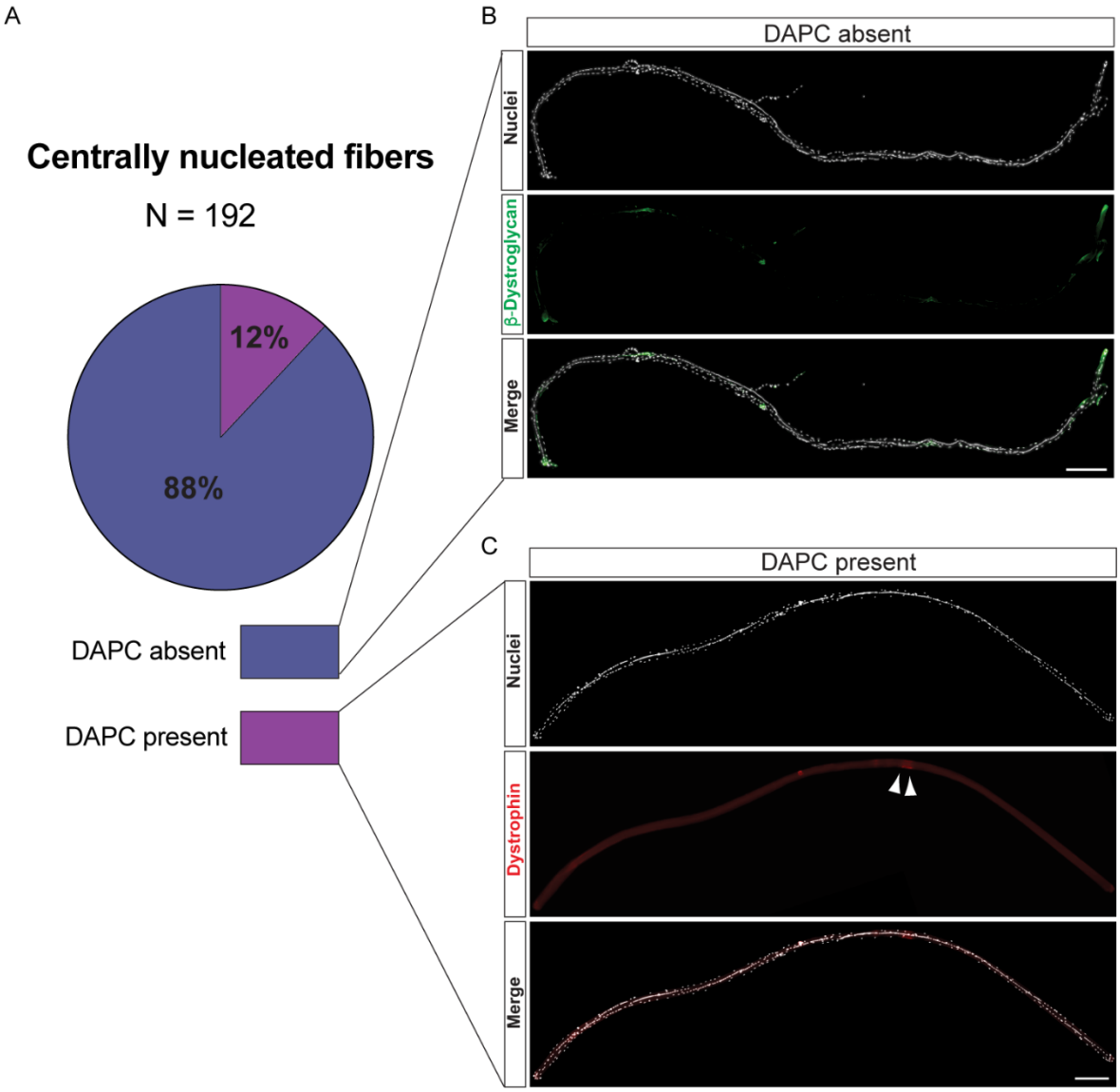

Figure 3.29 Classification of centrally nucleated *mdx52-Xist*$^{\Delta hs}$ myofibres based on DAPC presence.

DAPC presence was detected either with dystrophin or β-DG staining. A total of 192 centrally nucleated myofibres from 13 animals were analysed. (**A**) Pie chart representing proportions of centrally nucleated myofibres from adult *mdx52-Xist*$^{\Delta hs}$ animal expressing (DAPC present) or not expressing (DAPC absent) either dystrophin or β-DG. Representative centrally nucleated *mdx52-Xist*$^{\Delta hs}$ (**B**) myofibres not expressing or (**C**) expressing DAPC (white arrows). Tiled images were acquired at ×10 magnification and stitched in LAS X Software. Scale bar represents 200 µm.

3.3.12.4 Translational repression in CN segments is dystrophin specific

It is possible that various other proteins are translationally repressed in centrally nucleated regions as a part of hierarchical gene expression control connected of myofibre maturation. To assess if other key muscle proteins are similarly absent from CNF regions, the presence of titin, and F-actin was analysed in *mdx52-Xist*$^{\Delta hs}$ myofibres (*n* = 364, and 117 fibres respectively, Figure 3.30 A, B). In contrast to dystrophin, titin and actin were present in the centrally nucleated regions of all analysed myofibres. Moreover, titin exhibited a characteristic sarcomeric striation pattern suggesting that myofibrils are developed (Figure 3.30 A). These results suggest that the observed translational repression in segments with internalised nuclei in *mdx52-Xist*$^{\Delta hs}$ animals is dystrophin-specific. Moreover, centrally nucleated regions contain an organised sarcomeric network and thus can be considered mature.

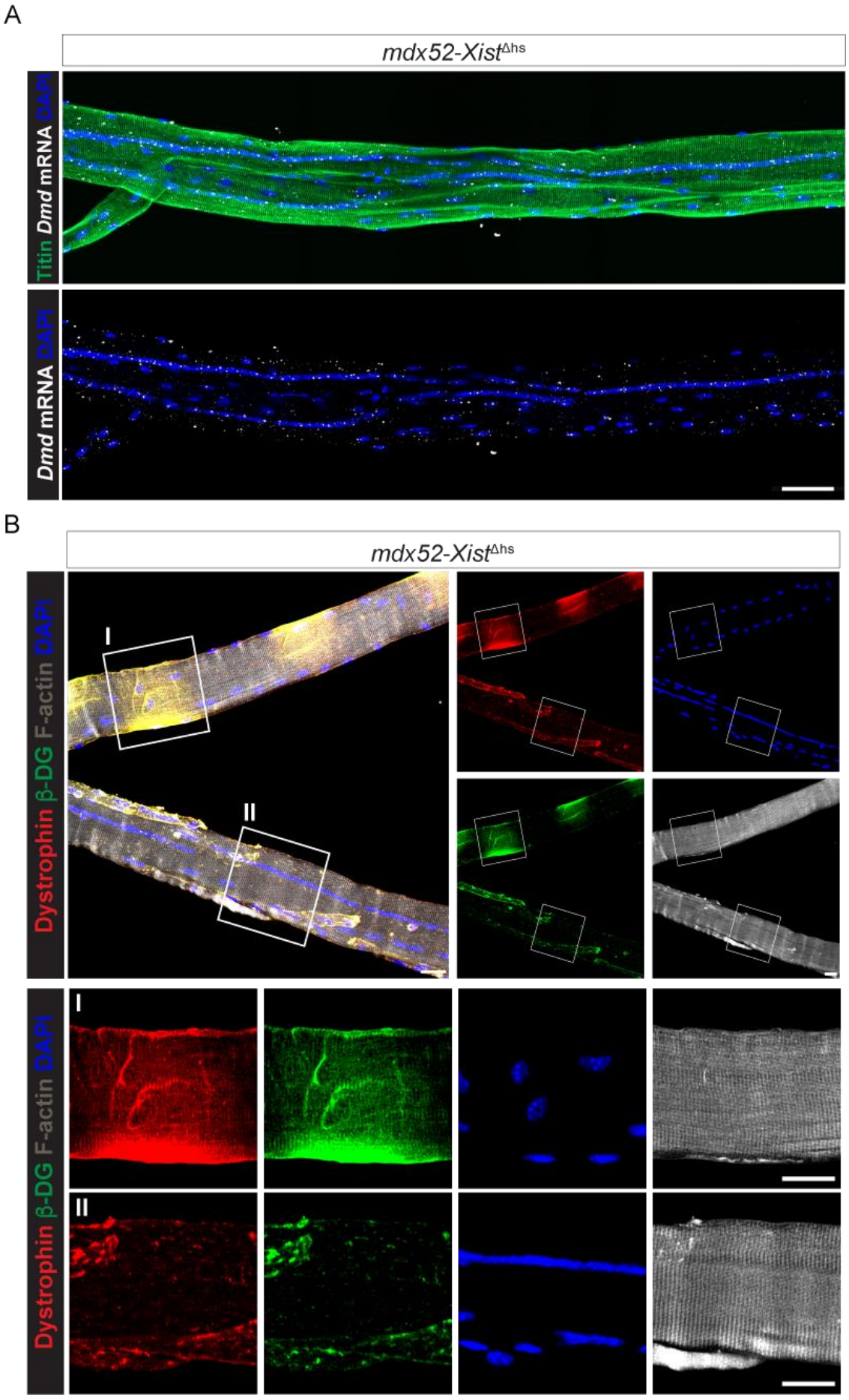
A
mdx52-Xist^Δhs
Titin Dmd mRNA DAPI
Dmd mRNA DAPI
B
mdx52-Xist^Δhs
Dystrophin β-DG F-actin DAPI
I
II
Dystrophin β-DG F-actin DAPI
I
II

Figure 3.30 Localisation of titin, filamentous actin proteins and dystrophin mRNA in centrally nucleated myofibres and segments of *mdx52-Xist*$^{\Delta hs}$ animals.

(**A**) Immunofluorescence image of centrally nucleated *mdx52-Xist*$^{\Delta hs}$ myofibre stained for titin (green) and dystrophin mRNA (white). Nuclei were visualised with DAPI. Tiled image was acquired at ×25 magnification and stitched using ZEN Blue software. Scale bar represents 50 µm. (**B**) Immunofluorescence image of centrally nucleated and non-centrally nucleated myofibres running at an angle from each other. Myofibres are derived from the same *mdx52-Xist*$^{\Delta hs}$ animal. Myofibres were stained for dystrophin (red) β-DG (green), and filamentous actin (gray). Image insets of patchy, non-centrally nucleated segment (I) and centrally nucleated segment (II) are shown enlarged below the main image. Image was acquired at ×25 magnification. Scale bar represents 20 µm.

3.3.12.5 Translational repression of dystrophin persists with age

To assess if translational repression of dystrophin in centrally nucleated segments is an age-specific phenomenon, myofibres from aged *mdx52-Xist*$^{\Delta hs}$ animals were analysed for the presence of DAPC. Notably, the lack of dystrophin in centrally nucleated regions was even more pronounced in aged *mdx52-Xist*$^{\Delta hs}$ animals (Figure 3.31 Figure 3.32). This was partly due to the significant hypertrophy and presence of multiple, parallel centrally nucleated chains in 60-week-old *mdx52-Xist*$^{\Delta hs}$ myofibres (Figure 3.31 B, Figure 3.32, Figure 3.20). Importantly, dystrophin mRNA was expressed in all nuclei analysed from 60-week-old *mdx52-Xist*$^{\Delta hs}$ mice (Figure 3.33). These results show that repression of dystrophin translation is not exclusive to early stages of pathology in *mdx52-Xist*$^{\Delta hs}$ muscle.

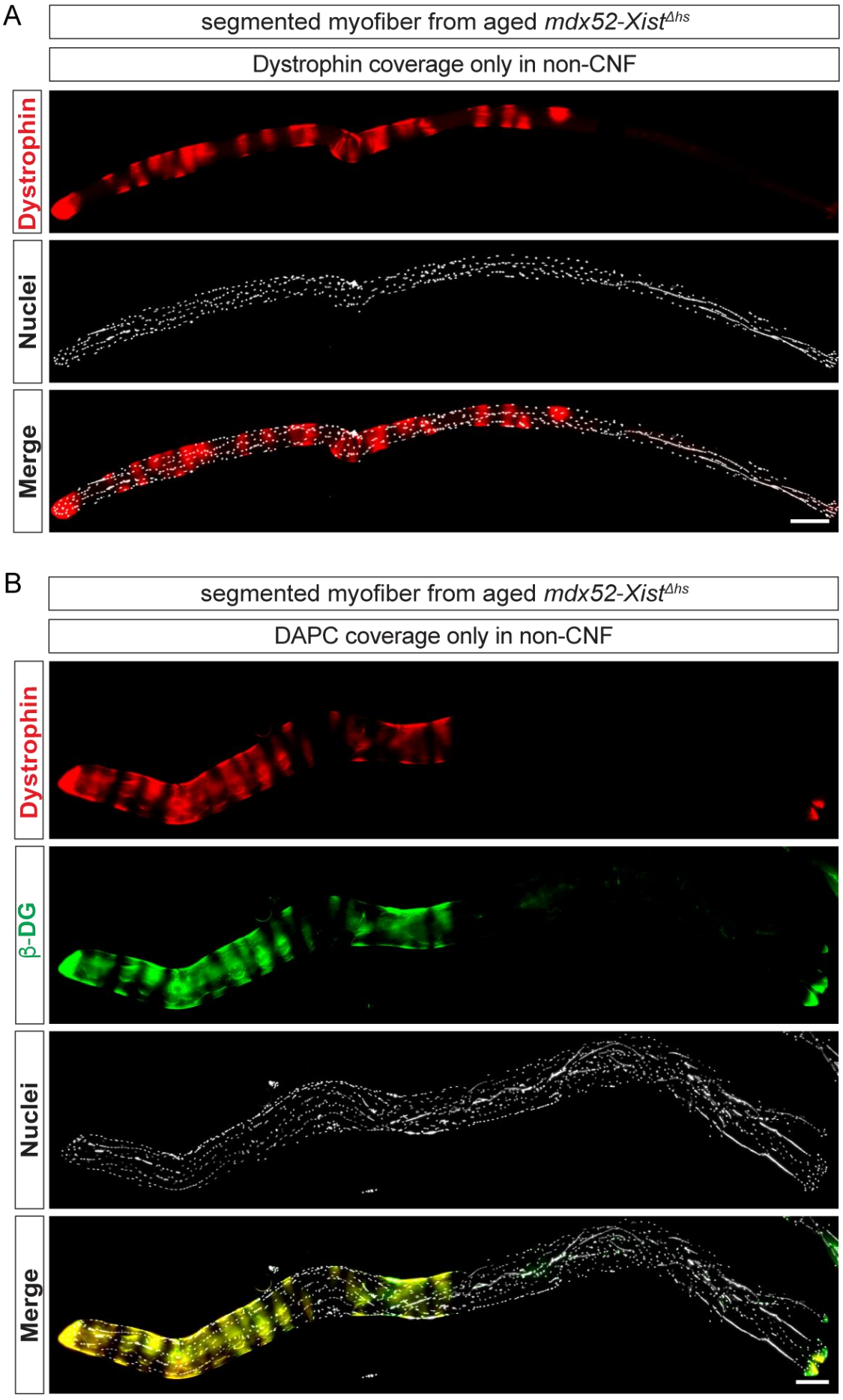
A
segmented myofiber from aged mdx52-Xist^Δhs
Dystrophin coverage only in non-CNF
Dystrophin
Nuclei
Merge
B
segmented myofiber from aged mdx52-Xist^Δhs
DAPC coverage only in non-CNF
Dystrophin
β-DG
Nuclei
Merge

Figure 3.31 DAPC localisation in segmented myofibres of aged *mdx52-Xist*$^{\Delta hs}$ animals.

Representative immunofluorescent staining of dystrophin (**A**) and colocalisation of dystrophin and β-DG (**B**) in single EDL myofibres isolated from 60-week-old *mdx52-Xist*$^{\Delta hs}$ mice. In both cases DAPC is only present in the non-centrally nucleated region of segmented myofibre. Tiled image was acquired at ×10 magnification and stitched using LAS X software. Scale bar represents 200 µm.

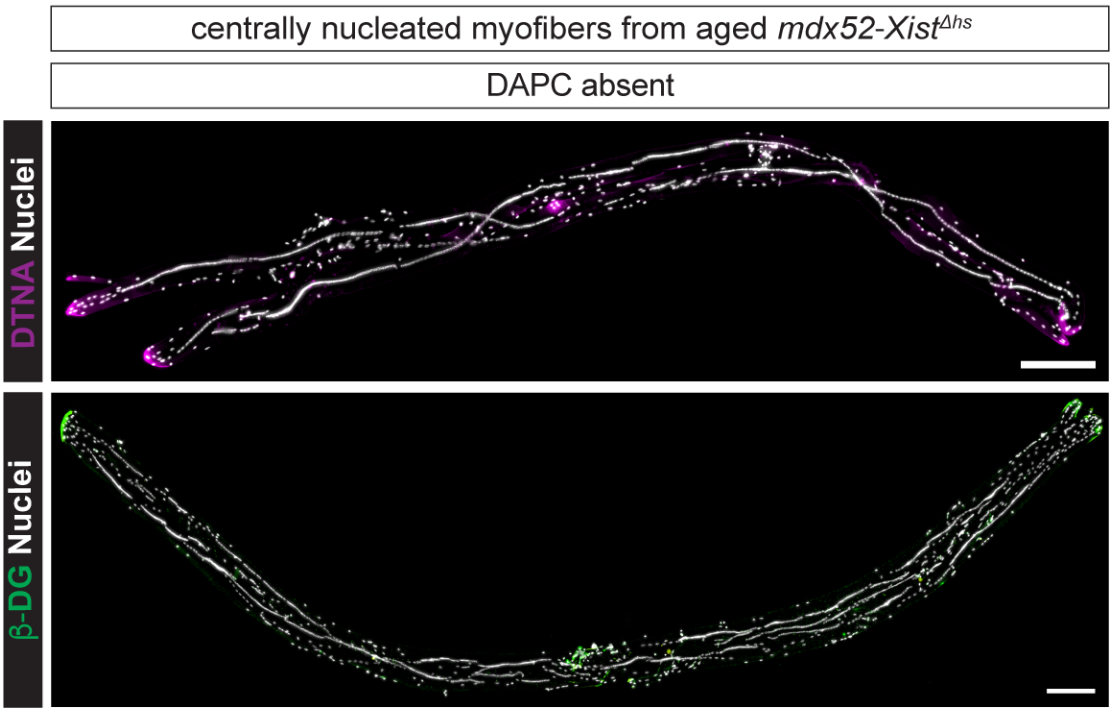

Figure 3.32 Lack of DAPC expression at the sarcolemma of centrally nucleated myofibres from aged *mdx52-Xist*$^{\Delta hs}$.

Representative immunofluorescent staining for DTNA (top) and β-DG (bottom) in single EDL myofibres isolated from60-week-old *mdx52-Xist*$^{\Delta hs}$ mice. For both proteins staining signal is detected only at myotendinous junctions of the myofibre. Tiled image was acquired at 10× magnification and stitched using LAS X software. Scale bar represents 200 µm.

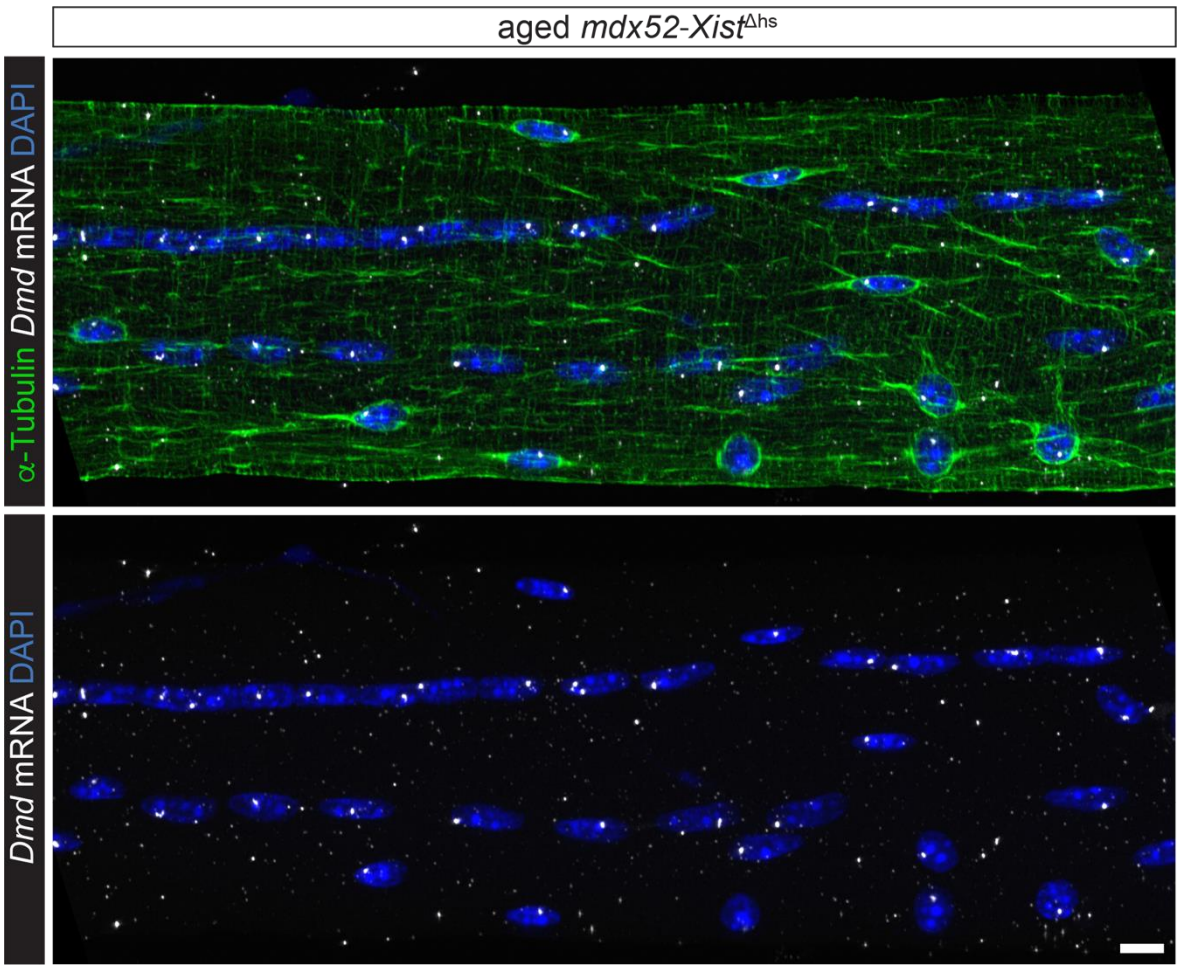

Figure 3.33 Dystrophin mRNA expression in centrally nucleated region of myofibre isolated from aged *mdx52-Xist*$^{\Delta hs}$ mouse.

Immunofluorescence image of centrally nucleated myofibre isolated from aged (60-week-old) *mdx52-Xist*$^{\Delta hs}$ stained for α-tubulin (green) and dystrophin mRNA (white). Nuclei were visualised with DAPI. Image was acquired at ×25 magnification. Scale bar represents 10 µm.

3.4 Discussion

Results presented in this chapter reveal previously under-appreciated, fundamental insights into basic dystrophin biology. These data support the notion that dystrophin protein expression is spatially restricted in accordance with the myonuclear domain theory. More importantly, the spatial restriction of dystrophin does not resolve with age, illustrating the limited capacity for dystrophin-positive regions to become enriched with time. Additionally, I have shown that in centrally nucleated myofibre regions of *mdx52-Xist*$^{\Delta hs}$ dystrophin is translationally repressed. This suggests a novel, spatially restricted mechanism of dystrophin regulation that is likely associated with the dystrophic environment.

Moreover, I show that myofibres expressing patchy dystrophin are partially protected against contraction induced damage, suggesting that higher sarcolemmal coverage by dystrophin is beneficial.

3.4.1 Dystrophin protein expression is myonuclear domain restricted

Dystrophin and the DAPC are expressed in a patchy manner at the sarcolemma of *mdx52-Xist*$^{\Delta hs}$ myofibres regardless of the protein levels and animal age (Figure 3.4, Figure 3.3, Figure 3.15, Figure 3.16, Figure 3.17). This demonstrates that the myonuclear domain theory governs dystrophin protein distribution. Spatial restriction of gene expression products within the vicinity of their myonuclei of origin has been reported previously mainly in heterokaryon muscle cell models *in vitro* [318,319,432]. Notably, one of those studies reported a discrepancy in hybrid myotubes *in vitro* where nuclei-restricted mRNA produced a uniformly dispersed protein [318]. They proposed that mRNAs are locally translated in the proximity of the nucleus, but the protein product can diffuse throughout the myofibre [318]. In fact, some of the dystrophin restoration strategies (i.e., cell therapy) also work on this assumption. However, the results presented in this chapter argue against such a mechanism for dystrophin. In fact, sustained restriction of dystrophin at the sarcolemma up to ~14 months of age in *mdx52-Xist*$^{\Delta hs}$ shows that the protein does not efficiently diffuse

throughout the myofibre. Recently Morin *et al.* presented an elegant study, utilising a model of heterozygous *mdx* mouse with fluorescently labelled wild-type dystrophin expressed on one X chromosome [405]. The authors demonstrated that the dystrophin protein signal is restricted to ~ 80 μm region from the nucleus of origin (longitudinally at the sarcolemma), further demonstrating that dystrophin has limited diffusion [405].

Myonuclear domain restriction is likely protein-specific and could depend on size, function, and site of activity (i.e., sarcomeric, cytoplasmic, nuclear, sarcolemma). For example, nuclear proteins (i.e. proteins with nuclear localisation signal) were shown to readily move between myonuclei in a process termed nuclear propagation [433–435]. Protein diffusion rate through the myofibre was also shown to inversely correlate with size [288,434]. An elegant study by Papadopoulos *et al.* utilised precise microinjection and microspectrophotometry techniques to quantify the longitudinal diffusion of various proteins within single rat EDL and soleus myofibres [288]. They showed that the dispersion rate drops sharply for proteins larger than 100 kDa [288]. As such, the measured diffusion constant for ferritin (450 kDa) was 0.9 $\mu m^2/s$ as compared to 6.2 $\mu m^2/s$ for haemoglobin (64.5 kDa) in EDL myofibres [288]. Accordingly, the earthworm haemoglobin of 3,700 kDa (size similar to titin) was effectively trapped within the myofibrillar lattice, with no diffusion observed [288]. Assuming the diffusion constant for dystrophin is comparable to that of ferritin (based on similar size), some dystrophin dispersion should be therefore observed especially with age. However, unlike cytoplasmic ferritin, dystrophin is a structural protein, stably anchored to the sarcolemma through interactions with DAPC proteins (Figure 1.1,Figure 3.5, Figure 3.17). As such, it is unlikely that significant dystrophin diffusion happens once the protein is correctly localised and the DAPC is formed, especially given the observed long (> 100 days) half-life of dystrophin protein [436]. In fact, constrained movement of dystrophin in comparison to the smaller, readily diffusing β-galactosidase has been reported before for cell transplant experiments in mice and humans [262,435]. Conversely, it has been previously shown that dystrophin can spread up to 500 μm from the

fused donor satellite cell or cover the distance of up to 28 non-dystrophin-expressing nuclei [262,435]. Analogously, dystrophin-positive areas in revertant fibres increase with age, suggesting myonuclear domain expansion [151,153]. Therefore, although extremely limited and slow, it is possible that some dystrophin transport occurs within myofibres. This, in turn could partially explain the overall increase in dystrophin expression levels in aged vs. adult animals (median = 26.5% vs. 11% respectively, Figure 3.3, Figure 3.15).

Recently, Denes *et al.* suggested that mRNAs of several key muscle proteins (titin, myomesin, dystrophin, and vinculin) are not restricted to their myonuclear domains but rather appear dispersed throughout the myofibre [302]. Authors commented that all mRNAs spread readily up to 50 μm away from the closest nuclei [302]. Analogously to their analysis, dystrophin mRNA distribution in healthy controls, *mdx52* and *mdx52-Xist*$^{\Delta hs}$ did not demonstrate a *Dmd* visible transcript accumulation within the proximity of nuclei (Figure 3.10). However, uniform dispersion of gene expression products is not mutually exclusive with the restriction of mRNA to specific myonuclear domains. Myonuclear domain theory is helpful in explaining some features of syncytial skeletal myofibres. Nevertheless, the definition of myonuclear domain is not rigid (i.e. not restricted to specific diameter or distance), but rather abstract and context dependent. Although the size of myonuclear domain can be approximated, it likely varies from cell to cell and protein to protein. For example, several different dystrophin myonuclear domain sizes were proposed: 500 μm, 130 μm, or more recently 80 μm [262,405,417]. Moreover, it is unclear how myonuclear domain theory would apply to centrally nucleated myofibres, which are not only hypernucleated but also contain chains of seemingly compressed nuclei, that often run in parallel to each other (Figure 3.26). As such, the field is complex and results in different myonuclear domain theory definitions which are likely based on individual experimental designs and scientific questions.

The *mdx52-Xist*$^{\Delta hs}$ mouse, as a genetically hybrid mouse model should facilitate the distinction of mutated and healthy dystrophin transcript and their restriction within

myonuclear domains. Specifically, visualisation of exon 52 within the dystrophin-positive myonuclear domain would clearly indicate the myonuclear domain restricted *Dmd* transcript localisation. However, despite extensive efforts, I was unable to detect exon 52 containing transcripts or exon 51-52 junction. Exon 52 is only 118 bp long and thus challenging to detect within thick (up to 100 µm) myofibres, as well as tissue sections where only a specific thin plane of the whole myofibre is preserved. Notably, future directions of the project include single nucleus RNA-sequencing of *mdx52-Xist*$^{\Delta hs}$ myonuclei. We aim to compare gene expression profiles of nuclei expressing functional and mutated dystrophin, distinguishing them based on exon 52 read density. We assume that this analysis will aid identification of distinct signalling pathways in negative versus positive myonuclear domains. This will further facilitate the verification of differentially expressed genes in a spatially resolved context (i.e. through HCR RNA-FISH and immunofluorescence).

3.4.2 Implications of non-uniform dystrophin for DMD therapeutic strategies

The even distribution of corrected dystrophin within a myofibre is largely assumed when considering the efficacy of DMD therapeutic approaches. However, several studies have highlighted that distinct patterns of dystrophin restoration are observed depending on the therapeutic strategy used. We have previously reported that CRISPR-Cas9-mediated gene editing restores dystrophin in a patchy manner along the sarcolemma, while PPMO-mediated exon skipping results in a uniform dystrophin distribution [251,320]. This was attributed to the effective editing of *Dmd* gene only in a portion of myonuclei in the former [251]. As such CRISPR-Cas9-treated dystrophic muscles are comprised of mosaic myofibres, mirroring the situation of *mdx52-Xist*$^{\Delta hs}$ model. Shortly after our studies, Morin and colleagues observed similar patterns of dystrophin restoration upon CRISPR-Cas9 gene editing or exon-skipping using tri-cyclo-DNA (tcDNA) oligomers [405]. Additionally, patchy dystrophin restoration is a hallmark and the expected outcome of cell therapy approaches, where dystrophin-positive myoblasts fuse to dystrophin-negative resident satellite cells and existing fibres in DMD patients and animal models [253,263]. In fact, in

the first study of myoblast transplant into *mdx* mouse, Partridge *et al.* commented that the pattern obtained by successful fusion was patchy and highly similar to non-uniform dystrophin distribution observed in *mdx* heterozygous animals [253]. Additionally, early clinical trials reported that diffusion of wild-type dystrophin from a fused healthy myoblast is limited [262]. Interestingly, the initial study describing the concept of the myonuclear domain noted that histochemical confirmation might be possible in heterozygous DMD female carriers [306]. Moreover, in an early study testing various micro-dystrophin constructs in *mdx* mice Phelps *et al.* demonstrated that dystrophin uniformity within the muscle, rather than its overall expression levels are more important for therapeutic effectiveness [220]. The authors reported that animals expressing dystrophin uniformly, at low levels displayed much greater improvement in muscle pathology (i.e., proportion of centrally nucleated myofibers, CK levels) than mice expressing high dystrophin in variable, inter-fibre pattern within the muscle [220]. Moreover, they suggest that widespread transduction rather than high, spatially localised levels of expression could be critical for the overall therapy effectiveness [220]. Nevertheless, it is currently unclear whether different patterns of within-fibre dystrophin distribution led to variable therapeutic efficacy.

3.4.3 Effects of non-uniform dystrophin on muscle regeneration

Centrally localised myonuclei are a hallmark of regeneration and their presence implies that the containing myofibre has undergone at least one cycle of myonecrosis and satellite-cell mediated repair [132,281,304,340]. As such, analysis of CNF numbers is a standard protocol used to assess the degree of regeneration in DMD [116]. Notably, while the commonly-used term of myonecrosis suggests the simultaneous death of the entire cell, the process of myofibre death and regeneration is thought to be segmental [117,435,437–445]. Specifically, only portions of a myofibre undergo cell death while other segments remain viable at any given time [117,438,440–445]. Indeed, electron microscopy studies of myofibre breakdown and repair in dystrophic muscle reported the compartmentalised death

and repair of DMD myofibres [438,445]. Segmented necrosis follows the generally acknowledged adult regeneration process [440,441,443–445]. Specifically, local myofibre damage leads to immediate myofibril degeneration within the injured region [441,443]. Subsequently, the damage site is infiltrated by immune cells which drive phagocytosis of the necrotic portion of myofibre [440,441,443]. Importantly, within hours the necrotic part is sealed off from a healthy region by a membrane formed through spontaneous aggregation of phospholipids [441,443]. In parallel, satellite cell activation takes place and new myotubes are formed at the site of the degenerated myofibre segment. These fuse with the remaining sarcolemma of the injured myofibre, eventually restoring the continuity of muscle structure [442–445].

Segmented myonecrosis and repair are likely even more pronounced in patchy dystrophin myofibres with dystrophin-negative myonuclear domains being more susceptible to damage and death than dystrophin-positive ones. Indeed, analysis of the proportion of CNFs in *mdx52-Xist*$^{\Delta hs}$ muscle sections revealed a dystrophin level-dependent reduction in muscle regeneration (Figure 3.12) suggesting that higher dystrophin sarcolemma coverage leads to less pronounced muscle turnover. Notably, it has been shown that necrosis can extend up to 630 µm from injury sites before membrane isolation [441]. As such, larger necrotic regions, e.g. in low dystrophin expressing adult *mdx52-Xist*$^{\Delta hs}$ can readily overtake the limited dystrophin-positive sarcolemma, leading to more pronounced myofibre death and satellite cell activation. This scenario is supported by comparable CNF levels observed in both low dystrophin *mdx52-Xist*$^{\Delta hs}$ and *mdx52* mice at 6 weeks of age (Figure 3.12). These results agree with previous reports in the *mdx-Xist*$^{\Delta hs}$ and *mdx*/*utrn*$^{-/-}$/*Xist*$^{\Delta hs}$ models, whereby animals expressing low levels of patchy wild-type dystrophin showed significant CNF accumulation in comparison to other groups [407,410].

Conversely, high dystrophin-expressing adult *mdx52-Xist*$^{\Delta hs}$ mice displayed diminished regeneration with TA containing half the CNF compared to low dystrophin expressors (Figure 3.12). This suggests that < 10% of dystrophin (low expressors),

dispersed in patches throughout the muscle does not protect against myonecrosis. Conversely, dystrophin expressed in a patchy manner, but above a certain threshold (10% of wild-type levels in this study) may be beneficial in improving muscle histopathology. Nevertheless, it remains unclear if this threshold would be the same for therapeutic strategies restoring dystrophin in a uniform manner. A study in BMD patients observed a similar effect whereby >10% of dystrophin resulted in a less severe disease progression [142]. Although the authors noted non-uniform dystrophin expression in some of the patients, this aspect was not included in the correlation analysis [142]. A previous study from our group compared 40% of uniform dystrophin re-expression after exon skipping with the same level of patchy dystrophin in *mdx-Xist*$^{\Delta hs}$ mice [321]. The proportion of the CNF was similar in both dystrophin distribution patterns [321]. Although the *mdx* mice in that study were injected with the exon skipping PPMO conjugate at 6 weeks of age. As such, the CNF percentage in those animals likely reflects the regeneration that occurred prior to the treatment, especially since active myofibre formation was suppressed upon dystrophin restoration as visible through a lack of eMHC^{+} myofibres [321].

Together these results show that non-uniform dystrophin can positively modify the muscle turnover in dystrophic mice at levels above 10% of wild-type dystrophin expression levels. The direct comparison of patchy and uniform myofibres expressing the same amounts of dystrophin should yield further insights into the functionality of patchy myofibres.

3.4.4 Effects of non-uniform dystrophin on serum myomiRs biomarkers

Serum myomiRs (miR-1, miR-133, miR-206) are considered promising pharmacodynamic biomarkers for DMD therapies as their levels can be restored towards wild-type following exon-skipping mediated dystrophin restoration [107,108,320,386,390]. However, we have recently shown that circulating myomiR levels remain elevated after CRISPR-Cas9 dystrophin gene editing [251]. Moreover, only mice with uniform dystrophin achieved through PPMO treatment, and not patchy-dystrophin *mdx-Xist*$^{\Delta hs}$, had their levels

of serum myomiR restored towards wild-type [321]. Together, these results suggested that uniform dystrophin expression is crucial for normalizing serum myomiR abundance [321].

However, patchy dystrophin expressing, adult *mdx52-Xist*$^{\Delta hs}$ mice displayed a decrease in circulating myomiRs that correlated with dystrophin levels (Figure 3.14). Consistent with the CNF results, low (< 10%) patchy dystrophin expression had no impact on serum myomiR levels. However, expression of > 10% of wild-type dystrophin (i.e. medium and high dystrophin expressors) led to a progressive, dystrophin level-dependent increase in circulating myomiRs towards wild-type levels. Although commonly considered as the “leakage” from damaged muscle, studies from our group showed that the serum myomiRs are selectively released from the muscle [386]. Furthermore, serum myomiR levels are influenced not only by myofibre death, but also by regeneration, overall muscle mass, and myomiRs tissue expression levels [107,108,384–386,388,389]. As such, circulating myomiRs reflect the overall muscle turnover dynamic rather than just myofibre death. Serum from low-dystrophin-expressing, adult *mdx52-Xist*$^{\Delta hs}$ mice showed similar levels of myomiRs biomarkers compared to *mdx52* mice, reinforcing the fact, that low dystrophin coverage does not prevent the degeneration and regeneration cycles (Figure 3.14). Consistent with the regeneration analysis, reduced levels of serum myomiRs in medium and high dystrophin expressing *mdx52-Xist*$^{\Delta hs}$ mice suggest that patchy dystrophin does positively influence the dynamic muscle turnover processes within the muscle (Figure 3.14).

Notably, the positive correlation between dystrophin protein and extracellular myomiRs biomarkers was lost in aged *mdx52-Xist*$^{\Delta hs}$ animals (Figure 3.19). This is likely a result of low serum abundance of myomiRs at 60-week-of-age. Results from our group previously showed that serum myomiRs levels decline with age in *mdx* animals [386]. Notably, a reduction in serum myomiRs levels with age has also been shown before in DMD patients [387,389,446]. This phenomenon has been attributed to progressive loss of muscle mass in mice and patients [386,387]. Additionally, it has also been suggested that the

reduction of serum myomiR levels with age could reflect the decline muscle regenerative capacity in older animals [386,447]. However, it was previously shown that the *mdx52* TA muscle retains steady levels of eMHC myofibres up until 18 months of age [136]. Similarly, in *mdx* mice, only a slight decline in regeneration was observed beyond the 65th week of age [135]. Additionally, small-calibre, centrally nucleated and utrophin-positive myofibres were detected in aged *mdx52-Xist*$^{\Delta hs}$ TA muscles indicative of active regeneration even at ~14 months of age (Figure 3.18, Figure 3.22). Utrophin was previously shown to colocalise with eMHC in regenerating *mdx* myofibres at a young age, emphasising its role as the marker of ongoing regeneration [102]. Therefore, a certain level of active regeneration is present in aged *mdx52-Xist*$^{\Delta hs}$ muscles.

3.4.5 Expression of utrophin in patchy dystrophin muscle

Dystrophin and utrophin exhibit a reciprocal expression pattern i.e. high abundance of one protein coincides with low abundance of the other [105,429]. Utrophin, highly expressed during early mouse and human embryonic development, is replaced by dystrophin in the later stages [83,92–95,448]. Moreover, healthy adult muscles with uniformly distributed dystrophin express low levels of utrophin which is restricted to the NMJ and MTJ [99,103,429]. The opposite is true for DMD patients and *mdx* models whereby a lack of dystrophin coincides with elevated extra-junctional utrophin expression [89,96,99,102,103,429]. Additionally, dystrophin and utrophin compete for sarcolemma binding sites, with a total co-labelled density similar to individual measurements, suggestive of a limited quantity of binding sites available [104]. Since dystrophin localisation is patchy in *mdx52-Xist*$^{\Delta hs}$ mice, utrophin abundance was investigated to determine if the protein was preferentially located in dystrophin-negative myonuclear domains. Utrophin expression was detected in all analysed *mdx52-Xist*$^{\Delta hs}$ animals regardless of dystrophin expression levels (Figure 3.21 A, C). However, no correlation was found between dystrophin percentage and utrophin levels in measured samples (Figure 3.21 B, D). Subsequent immunofluorescence

analysis in muscles of *mdx52-Xist*$^{\Delta hs}$ animals expressing the highest levels of utrophin revealed that the protein localises mainly to small-calibre CNF (Figure 3.22). Notably, a study by Mizuno *et al.* reported a clear reciprocal expression pattern of utrophin and dystrophin in DMD patients and healthy controls but found no such relationship in BMD patients and DMD female carriers [429]. Specifically, most of the examined female carriers' myofibres were either strongly negative or positive for both proteins [429]. Other studies confirmed dystrophin and utrophin colocalisation to the same myofibres in transverse muscle sections from DMD carriers [449,450]. Moreover, both proteins were detected within the same segment of revertant fibres in DMD patient biopsies [451]. More recently, the delivery of AAV-encoded micro-dystrophin colocalised with utrophin in *mdx*-Fiona mice which exhibit constitutive utrophin overexpression [98]. As such, it is possible that the presence of some dystrophin (i.e. in DMD carriers, BMD patients and patchy *mdx52-Xist*$^{\Delta hs}$ myofibres) from birth, has an effect on utrophin expression and thus results in a lack of linear relationship between the two proteins [87]. This agrees with the observation in BMD patients whereby lower levels of utrophin are found in biopsies of BMD in contrast to DMD patients [87,451]. As such, the reciprocal expression of dystrophin and utrophin proteins is observed only when the abundance of either protein is low [429].

Analysis of utrophin expression in transverse TA sections of *mdx52-Xist*$^{\Delta hs}$ showed clear staining of small calibre CNF, however, some level of weak sarcolemma signal in larger myofibres has also been observed (Figure 3.22). It is known that staining intensity of utrophin is significantly higher in regenerating than large myofibres in dystrophic samples [87,92–94,450]. However, for these experiments, tissues from dKO mice should be used as a negative control to distinguish between background and signal. Given the lack of reciprocal expression observed in DMD carriers, the non-regeneration dependent utrophin likely would localise within both dystrophin positive and negative myonuclear domains. However, further experiments are needed to confirm utrophin-dystrophin colocalisation in patchy myofibres.

3.4.6 Effects of non-uniform dystrophin on microtubule network

The microtubule network has been shown to play crucial roles in myogenic differentiation (including myofibril formation) as well as correct intracellular transport of mRNAs and proteins along skeletal and cardiac muscle [300–302,452]. Recent studies have demonstrated that inhibition of microtubule polymerisation in muscle prevents mRNA from being distributed along the myofibre and effectively shuts down protein translation throughout the cell [301,302]. As such, the microtubule network is a key component of correct myofibre architecture and function. Several studies have reported increased density and dramatic disorganisation of the microtubule network in dystrophic mouse myofibres [49,50,290,292,294,303]. Increased microtubule density in *mdx* myofibres has been connected to NADPH (reduced-form nicotinamide adenine dinucleotide phosphate) dependent production of ROS, amplification of Ca^{2+} influx and thus exacerbation of myofibre damage [453]. Another study linked the disorganised microtubule network to loss of muscle force production after a single eccentric contraction in *mdx* mice [50].

Dystrophin exhibits high-affinity binding to microtubules via a dedicated microtubule-binding region in repeats 20-23 of the central rod domain [49,50]. This interaction has been demonstrated to regulate microtubule dynamics, with dystrophin capable of pausing microtubule polymerisation [50]. As such, dystrophin is thought to guide and anchor microtubules to the costamere, and thus regulate microtubule network organisation within healthy myofibres [49,50]. Consistently, no such effect was observed for utrophin which lacks the corresponding microtubule binding domain in its structure [50].

Analysis of microtubule organisation in *mdx52-Xist*$^{\Delta hs}$ isolated myofibres revealed an intermediate phenotype, exhibiting a network architecture between healthy and dystrophic muscle (Figure 3.23). This suggests that dystrophin-positive myonuclear domains likely promote organised microtubule networks. However, further analysis revealed no significant difference in microtubule organisation between dystrophin-positive and negative myonuclei

within the same muscle fibres (Figure 3.24). This finding suggests that the role of dystrophin in microtubule organisation may be more complex, possibly involving direct and indirect mechanisms. Mislocalisation of Golgi elements (GE), which are a part of MTOC in mature myofibres, may contribute to microtubule disorganisation in dystrophic muscle [291,293,294]. Healthy muscle fibres exhibit ordered GE aligned longitudinally at the sarcolemma (in groups) and near myonuclei poles [294]. Conversely, dystrophin-deficient mice display disorganised GE, with random scattering throughout both centrally and non-centrally nucleated myofibres [294]. As such, aberrant localisation of GE in dystrophic conditions may disrupt the normal microtubule nucleation process [291,294]. While the presence of dystrophin-positive myonuclear domains might offer some guidance for growing microtubules, the overall disruption caused by GE misplacement prevents a complete restoration of microtubule organisation. In fact, a handful of studies reported variable changes to microtubule organisation upon dystrophin restoration [294,303]. Percival *et al.* demonstrated improvement in the grid organisation upon micro-dystrophin gene therapy, even though the construct used lacked the microtubule-binding domain located in central rod domain repeats 20-23 [49,294]. Additionally, partial restoration of network organisation was reported following mini and micro-dystrophin delivery, and inclusion of the microtubule-binding domain in the construct did not affect the results [50,303].

Notably, microtubule organisation in *mdx52* myofibres appears more severely disrupted in CNF compared to non-CNF fibres (Figure 3.27). This aligns with previous findings by Percival *et al.* who demonstrated aberrant distribution and increased density of GE at the surface of centrally nucleated wild-type fibres after cardiotoxin injury in comparison to non-CNF [294]. Specifically, the authors observed a striking accumulation of GE near central nuclei chains, implying a significant redistribution due to central nucleation [294]. Accordingly, *mdx* CNF fibres also displayed a prominent presence of GE within the inter-myonuclear space [294]. Moreover, centrosome proteins like PCM-1 (a component of the MTOC) were shown to play a role in the alignment of central nuclei during muscle

differentiation [454]. Additionally, CNF fibres are particularly disadvantaged as they lack the peripheral nuclei that contribute to MTOC in mature muscle fibres [293,294]. As such, central nucleation disrupts MTOC organisation more severely. This combined with dystrophin deficiency likely contributes to the more dramatic microtubule disorganisation observed in these fibres.

3.4.7 CNF as accumulated history of muscle regeneration

During muscle development, central nucleation is resolved by re-distribution of the myonuclei to the periphery in a sarcomere-driven process [281]. Live-cell imaging of *in vitro* differentiated mouse myoblasts showed that the myonucleus is slowly squeezed out of myofibre core to the periphery by contracting myofibrils [341]. As such, nuclear localisation to the periphery occurs after myofibril formation and can be considered as one of the final steps of myofibre maturation [281,341]. Indeed, while CNFs are usually considered as recently formed, myofibres with peripheral, uniformly distributed nuclei are usually defined as mature [126,455].

Analysis of CNF in adult vs. aged *mdx52-Xist*$^{\Delta hs}$ TA sections revealed an increase in the CNF proportion with age (Figure 3.20 A). This is consistent with previous observations in TA and EDL muscles of *mdx* animals [126,129,136,427]. Specifically, analysis of TA in *mdx52* mice across various time points revealed minimal reduction in CNF levels from the second to eighteenth month of life [136]. Similarly, all myofibres within *mdx* EDL muscles exhibited 100% of central nuclei from 24 weeks to 2 years (i.e. close to the maximum *mdx* lifespan) [129]. While considered immature at early time points, CNF in aged mice result from lack of nuclei dispersion to the periphery rather than ongoing regeneration [117,126,136,456]. Meyer *et al.* directly confirmed this by demonstrating the presence of CNF in wild-type mice 94 weeks (~ 22 months) after a single dose of cardiotoxin administered at 10 weeks of age [456]. As such, the proportion of CNF at later time points is considered to reflect the accumulated history of regeneration rather than active muscle

repair process [136,456]. Therefore, the increased abundance of CNF in aged *mdx52-Xist*$^{\Delta hs}$ TA sections can be interpreted as the accumulative regeneration that happened in these mice (Figure 3.18). The overall CNF percentage was similar between low and medium dystrophin expressing *mdx52-Xist*$^{\Delta hs}$ animals (mean of 56% and 51% respectively), suggesting that majority of the muscle underwent at least one degeneration and regeneration cycle through life (Figure 3.18 B). Even the animals classified as high dystrophin expressors at 60 weeks of age exhibited significant proportion of regenerated myofibres with over 40% of the CNF in TA muscle (Figure 3.18 B, C). Notably, one aged *mdx52-Xist*$^{\Delta hs}$ animal expressing 93% of dystrophin displayed a significant reduction in CNF in comparison to others, with less than 10% of CNF observed (Figure 3.18 C). Together with results from adult mice (Figure 3.12 and discussion above) these findings indicate that patchy dystrophin expression modifies but does not prevent the muscle turnover that occurs throughout the life of a dystrophic muscle unless expressed at close to normal amounts from birth.

Importantly, since the primary XCI takes place in early embryonic development, medium and high dystrophin expressing *mdx52-Xist*$^{\Delta hs}$ mice contain higher proportions of quiescent satellite cells expressing functional dystrophin protein [166–168,457]. Once incorporated into myofibre, the dystrophin positive satellite cells stabilise the myofibre, preventing further segmented death. As such the process of myofibre repair is likely more efficient in medium and high dystrophin *mdx52-Xist*$^{\Delta hs}$ mice. Moreover, more frequent repair of damaged segments with dystrophin-expressing satellite cells would lead to accumulation of dystrophin positive domains with time, thereby explaining the increase in overall protein levels with time (Figure 3.15). Notably, this points to an important issue for dystrophin restoration strategies that do not target the satellite cells. If dystrophin is not corrected in satellite cells, regeneration will result in addition of non-dystrophin expressing myofibres, thus limiting the clinical benefit. Conflicting results have been obtained for satellite cell

transduction with AAV vectors [244,458–460]. It remains unclear if efficient CRISPR-Cas9 editing or micro-dystrophin delivery of the muscle stem cells can be achieved.

3.4.8 Changes in CNF pathology

The CNF of 12-week-old *mdx52* mice contain more nuclei per myofibre volume than peripherally nucleated myofibres (Figure 3.26 B). This agrees with previous results showing that the hypernucleation observed in dystrophic mice is solely a result of increased numbers of centrally located nuclei while numbers of peripheral nuclei are comparable between wild-type and dystrophic mice [129,306,428]. Additionally, results from *mdx52-Xist*$^{\Delta hs}$ mice suggest that CNFs grow in diameter and progressively acquire more central nuclei as animals age (Figure 3.20 B, C, D). The increase in CNF size likely reflects the progressive hypertrophy characteristic of dystrophic mouse muscles that affects all myofibre classes [129,427]. It is established that the myonuclei number correlates with myofibre size, suggesting that nuclear accretion within the syncytium is regulated [309]. More recently, this was confirmed in CNF occurring after barium chloride muscle injury in wild-type animals whereby the number of central nuclei was correlated with myofibre size during the 28-day post-injury period [461]. As such, increases in myonuclei numbers in CNFs are expected to result in concomitant myofibre hypertrophy. The mechanism and rationale for the lack of re-distribution of mouse nuclei to the periphery is currently unknown. However, it can't be excluded that CNF contribute to the disease progression in mice. Previously, Narita *et al.* identified that CNFs displayed reduced uptake of Evans blue dye compared to non-CNF cells, suggesting less permeable membranes [427]. Moreover, an increase in central myonuclei numbers in CNF could result from the fusion of newly formed myotubes to regenerated CNF that did not distribute the nuclei to the periphery. However, further experiments are needed to confirm this (e.g. lifetime nuclei tracking in *mdx* muscles).

3.4.8.1 Dystrophin is transcribed but not translated in centrally nucleated segments

Notably, the majority of single isolated segmented EDL *mdx52-Xist*$^{\Delta hs}$ myofibres did not express dystrophin in the centrally nucleated region (Figure 3.28). Accordingly, very few CNFs expressed any dystrophin at all (Figure 3.29). HCR-RNA FISH analysis of dystrophin mRNA revealed that dystrophin is readily expressed in those regions, suggesting a translation repression mechanism. Moreover, immunostaining for actin and titin, revealed their correct localisation in centrally nucleated segments, showing that translational repression is specific to dystrophin in *mdx52-Xist*$^{\Delta hs}$ centrally nucleated regions (Figure 3.30).

The morphology of the segmented myofibres resembles the pattern of segmental repair observed previously [435,443]. The centrally nucleated portion of myofibre is likely formed in place of a previously necrotic site which was replaced by newly formed myotubes that fused to the remaining healthy portion of myofibre and are now undergoing a maturation process. Thus, the observed segmented structure supports the hypothesis that satellite cells initially form myotubes, which then integrate with the remaining portion of the undamaged myofibre [435,443]. As described above, the quiescent satellite cells already have established their XCI pattern. As such, if the activated and proliferating satellite cells express mutated dystrophin they could form a fully dystrophin-null myotube explaining the lack of dystrophin expression in centrally nucleated regions. However, in that scenario, all contributing satellite cells would have to exhibit expression of mutated dystrophin. This cannot be excluded but is unlikely for two reasons. Firstly, myofibres that contain centrally nucleated dystrophin negative segments also contain regions of high dystrophin positivity (but still patchy). This indicates that these fibres are broadly competent to express dystrophin and highlights the difference between zebra-like patchy patterns in the non-CNF segments and completely dystrophin-absent CNF segments (Figure 3.28, Figure 3.31). Secondly, satellite cells were previously shown to migrate between adjacent muscles [462–464]. Although generally, the migration of satellite cells is not efficient in populating the

whole muscle, e.g. after myoblast transplant in DMD [252,465], local crush injury was shown to activate satellite cells distal to the damaged region [466]. As such it's unlikely that the segmented myofibre portion results from a proliferation of a limited number of satellite cells that share the same XCI pattern. It would be expected that at least some of cells in newly formed myotubes would be capable of expressing functional dystrophin.

The observed absence of dystrophin translation in centrally nucleated regions and fibres challenges the established understanding of dystrophin expression patterns. Previous studies consistently reported dystrophin presence in CNFs on transverse sections. Some examples include dystrophin-positive centrally nucleated revertant fibres in *mdx* and *mdx52* mice [136,153] or dystrophin expression in CNF after ASO-mediated exon skipping, CRISPR-Cas9 gene editing, gene, and cell therapy [261,467–470]. Additionally, dystrophin localises at the sarcolemma of centronuclear myopathy (CNM) patients, whereby muscles are arrested in a CNF state throughout life [471]. The CNMs are caused by defects in genes which regulate membrane trafficking (e.g., myotubularin, amphiphysin and dynamin 2) [472]. Notably, in CNM muscle, centrally nucleated myofibres are present in the absence of overt necrosis, regeneration, inflammation, and fibrosis [472]. Moreover, the X-linked myotubular myopathy (XLMTM, a form of CNM) mice are born with peripherally localised myonuclei in the majority of skeletal muscles, and progressively accumulate CNFs with age [473]. Thus, although the detailed molecular mechanism linking the genetic mutations in CNM with central nucleation is unclear, it differs from satellite cell-driven myofibre formation. As such, lack of dystrophin protein expression in centrally nucleated regions could be directly connected to multiple secondary pathological changes in dystrophic muscle (e.g., changes in gene expression patterns, molecular signalling from the dystrophic environment, intrinsic satellite cell defects), which are not present in CNMs.

Additionally, it is worth noting that not all of dystrophin restoration studies include the nuclear stain in representative immunofluorescent images, hindering the interpretation of published results [214,241,246,247,251,253,254,321]. This is likely for practical reasons,

as hypernucleation and mononuclear immune cell infiltration can significantly impair image clarity. Nevertheless, the presented potential discrepancy in dystrophin expression patterns in centrally nucleated myofibres warrants further investigation.

Several scenarios could explain the lack of dystrophin protein in centrally nucleated segments and fibres. Unlike utrophin, dystrophin expression at the sarcolemma is not present in early development, suggesting that dystrophin expression and/or translation is switched on at certain stage of myofibre maturation. Notably, differences in the promoter and 3' UTR organization between dystrophin and utrophin suggest distinct regulatory mechanisms governing the expression of these two proteins [474,475]. Unlike dystrophin, the *UTRN* promoter contains numerous CpG islands, which were shown to be associated with the wide-spread tissue expression of the utrophin protein [474]. Additionally, utrophin translation efficacy is modulated by post-transcriptional regulation through several miRNAs, including let-7c, miR-206, and miR-133b, which do not target dystrophin [475]. Additionally, it has been shown before that the transcriptional activity of myonuclei changes depending on the stage of myofibre development or maturation [421]. Accordingly, an early paper by Wassels *et al.* showed that in the 8-week-old human embryo, dystrophin localises first to the cytoplasm and myotendinous junctions, and further spreads through the entire length of the muscle membrane by week 17 [476,477]. Moreover, when comparing the localisation of myogenin and dystrophin transcripts during embryonic development, the latter was identified in elongated cells described as ‘more advanced in differentiation’ [478]. Additionally, early studies in BMD patients suggested a delay in dystrophin expression during myofibre development [479]. In fact, this observation stemmed from the finding that regenerating myofibres lacked dystrophin protein expression [479].

Furthermore, the lack of dystrophin expression from competent nuclei was observed after cell therapy and in DMD female carriers [180,262]. Additionally, Blaveri *et al.* reported silencing of the nuclear β-galactosidase marker in fused donor muscle precursor cells upon grafting, suggesting that newly incorporated myonuclei can be translationally repressed

[435]. Moreover, early studies described a weaker dystrophin staining of smaller myotubes during human fetal development proposing developmental regulation of dystrophin expression [95]. More recently, dystrophin staining was shown to be weak at early stages of injury-induced regeneration [480]. Finally, analysis of expression of various proteins during regeneration led to the conclusion that dystrophin is a marker of myofibre maturity [480].

The lack of dystrophin in centrally nucleated segments and fibres might be connected to the post-transcriptional downregulation of dystrophin by *trans*-acting factors such as miRNAs [481]. For example, miR-31, which was shown to downregulate dystrophin expression, is upregulated in DMD patient biopsies and in *mdx* tissues [108,382]. Thus, local regulation of dystrophin transcripts in the centrally nucleated regions could be connected to spatially restricted expression of miR-31 in those regions. Alternatively, it can be considered that dystrophin is not translated before the nucleus reaches the cell periphery. However, the localised translation scenario does not agree with previous studies detecting dystrophin in the sarcoplasm and perinuclear region in myofibres from centronuclear myopathy patients [471]. Moreover, these results contradict the data from muscle injury experiments in wild-type animals, where centrally nucleated myofibres were shown to express dystrophin at the sarcolemma (Prof. Richard Piercy, personal communication). It can be speculated that translational repression of dystrophin in CNFs is specific to dystrophic conditions. As mentioned above, miR-31 is highly upregulated in *mdx* mice [108,382,481]. While in healthy animals, miR-31 levels decrease once satellite cells are activated, it is possible that high abundance of miR-31 retained in dystrophic conditions has more pronounced effect on dystrophin translation in the therapeutic context [482]. However, such scenario requires further experimental confirmation.

It is unclear if the same phenomenon would readily translate to DMD patients. It has been suggested before that less robust regeneration in DMD patients results in less frequent formation of CNF in comparison to mice [33,134,427,465]. However, analysis of

biopsies from 56 DMD patients aged 1-10 years revealed increased numbers of CNF in older boys [134]. Similar results were obtained more recently by Cardone *et al.* who analysed 24 biopsies from patients aged 1-18 [33]. Although, the proportion of CNFs observed in these studies was lower than what has been observed for *mdx52* and *mdx52-Xist*$^{\Delta hs}$ reaching a maximum of ~ 25% of analysed biopsy at 9 years of age [33]. Notably, myofibre necrosis and regeneration are more prominent in mouse models than in DMD patients [126].

3.5 Conclusions

Results presented in this chapter demonstrate that the dystrophin protein expression (and other DAPC components) is governed by the myonuclear domain theory. Myofibres expressing patchy dystrophin at the sarcolemma are partially protected against damage and result in the restoration of extracellular myomiR biomarkers towards wild-type levels. However, the scale of protective dystrophin function is connected to the level of dystrophin expression, implying that overall higher dystrophin sarcolemma coverage is more beneficial. In fact, the presence of dystrophin-negative myonuclear domains compromises the patchy myofibre integrity and these myofibres progressively degenerate through life regardless of the dystrophin amounts produced. Moreover, non-uniform dystrophin localisation is not resolved with age, although dystrophin protein levels increase most likely through incorporation of satellite cells expressing functional dystrophin.

Additionally, the results presented here clearly demonstrate that central nucleation has profound effects on myofibre morphology and physiology. Centrally nucleated myofibres represent a distinct muscle cell class in terms of myonuclei number, myonuclear domain size, organisation of microtubule network and dystrophin expression. As such, centrally nucleated myofibres should be considered as a separate class of muscle cells.

4 Results II: Dose-dependent rescue of uniform dystrophin after PPMO–mediated exon skipping

4.1 Introduction

DMD clinical trials assess treatment effects through timed functional tests and motor scales performed in controlled settings (e.g., NSAA, 6-minute walk test) [483]. Additionally, the quantity of restored dystrophin is almost always measured using Western blot and immunofluorescence analysis of patient biopsies [484]. While all these methods are widely established, they suffer from several limitations. For example, the mobility tests focus on peak performance rather than real-world motor function [485]. These can be influenced by factors like fatigue or motivation on the day of the assessment [483,485]. Moreover, Western blotting for dystrophin quantification suffers from technical variability between studies. Differences in tissue processing, electrophoresis systems, and antibody selection can significantly hinder effective comparisons of restored dystrophin quantities across trials [486]. Similarly, immunofluorescence is subjected to potential bias resulting from subjective classification of dystrophin-positive fibres [486]. Moreover, both of these techniques utilise patient biopsies which represent a very limited region of the whole muscle, hindering the accurate assessment of restored dystrophin levels. Nevertheless, all these analyses provide complementary information and are crucial for effective evaluation of therapeutic efficacy. This is especially important in the context of immunofluorescent dystrophin detection since variations in the pattern of sarcolemma coverage could potentially impact the effectiveness of the therapeutic outcome [251,320,321,405,487] (Chapter I). Indeed, a complex relationship between dystrophin quantity, distribution, and disease severity has been observed in patients [411]. Specifically, higher dystrophin sarcolemmal coverage has been associated with less severe phenotype [411].

Serum CK is a commonly used minimally invasive biomarker in DMD patients and research. However, this biomarker does not have much utility beyond diagnostics in DMD

patients. This is primarily due to the high interpersonal and seasonal variability as well as an age-related decline connected to increasing fibrosis in DMD muscles [393,394]. As such, there is currently an unmet need for biomarkers that could reflect or predict clinical outcomes and/or the efficiency of therapeutic approaches beyond western blot and immunofluorescence analyses [390,394]. As mentioned above, serum myomiRs have been proposed as minimally invasive biomarkers that can inform on the levels of dystrophin re-expression in muscle [320,390]. Studies from our group have shown that a single-dose injection of PPMO exon skipping conjugate restores not only dystrophin expression but also extracellular myomiR biomarkers towards wild-type levels [107,108,321,395]. Additionally, treatment with two PPMOs of varying potency yielded distinct levels of serum myomiRs restoration [107]. Additionally, results from Chapter I showed that levels of patchy dystrophin in *mdx52-Xist*$^{\Delta hs}$ adult animals are strongly anti-correlated with extracellular myomiR levels (Figure 3.19).

This chapter of the thesis aims to assess whether the PPMO-mediated exon skipping:

1. Elicits a dose-dependent response characterised by uniform dystrophin expression.
2. Restores extracellular myomiR levels in a dose dependent manner.

4.2 Materials and Methods

4.2.1 Synthesis of peptide-PMO conjugates (PPMO)

PPMO conjugates used in this study were comprised of: phosphorodiamidate morpholino oligomer (PMO) targeting 3′ splice junction site of mouse dystrophin exon 23 (5′-GGCCAAACCTCGGCTTACCTGAAAT-3′) and Pip9b peptide. Pip9b is composed of two cationic, arginine-rich regions flanking the hydrophobic core: RXRRBRR FQILY RBRXRB (X, aminohexanoic acid; B, β-alanine). The peptide was synthesised using standard 9-fluorenylmethoxy carbonyl (Fmoc) chemistry [214]. The PMO was purchased from Gene Tools LLC. (Philomath, Oregon, USA). Pip9b was covalently attached to the PMO through amide linkage between peptide C-terminus and 3′ amine end of the PMO as described previously [214]. PPMO conjugates were dissolved in sterile water and passed through 0.22 μm cellulose filters before use.

4.2.2 Injections and tissue harvesting

Male *mdx* animals were treated at 8 weeks of age with a single, intravenous injection of the PPMO at one of three doses: 3, 6, or 12 mg/kg. The compound was diluted in 0.9% sterile saline in nuclease-free water and delivered in equal volumes *via* tail vein. Animals were culled at 10 weeks of age (i.e. 2 weeks after treatment) by increasing CO_2 concentration. Tibialis anterior and serum were harvested immediately after. TA muscles were mounted on corks with O.C.T. Compound Mounting Media for Cryotomy (VWR) and cut into 8 μm transverse and longitudinal sections.

4.2.3 RNA extraction from muscle

TA muscle fragments were placed in Precellys homogenisation tubes containing TRIzol (Thermo Fisher Scientific) and disrupted in two 30 sec cycles at 5,500 rpm (revolutions per minute) using a Precellys 24 Tissue homogeniser (Bertin Technologies).

RNA was extracted from the TRIzol-homogenate according to the manufacturer's instructions. Briefly, 200 µl of chloroform was added, samples were vortexed, and then incubated at room temperature for 10 min to facilitate phase separation. Subsequently, samples were centrifuged at 12,000 *g* for 15 min at 4°C. The aqueous phase containing RNA was transferred to a new tube containing 1 µl of RNAse-free glycogen (Roche). The RNA was precipitated in isopropanol for 10 min at room temperature. Samples were centrifuged for 10 min at 4°C. RNA pellets were washed twice with 75% molecular biology grade ethanol (EtOH). The pellets were air dried at RT, 30 µl of RNase-free water (Life Technologies) was added, and then the samples were incubated at 55°C for 10 min, to improve the RNA solubilisation. RNA samples were stored at -80°C.

4.2.4 Exon skipping RT-qPCR

500 ng of RNA from each sample was reverse transcribed using the High-Capacity cDNA Reverse Transcription Kit (Thermo Fisher Scientific) according to the manufacturer's instructions. The resulting cDNA template was diluted 1:5 prior to the qPCR assay.

cDNA amplification was performed on Step-One Plus Real-Time PCR instrument with TaqMan Universal PCR Master Mix (both Thermo Fisher Scientific, Applied Biosystems) according to the manufacturer's instructions. Samples were analysed in duplicates. Primers and probe sets used in this study were designed to amplify either *Dmd* exons 23 – 24 (unskipped) or *Dmd* exons 22 – 24 (skipped) mature transcripts (Table 4.1). Exon skipping was quantified as a percentage of skipped transcripts relative to total (i.e. skipped and unskipped) by comparing the samples with standard curve composed of serial dilution of skipped and unskipped templates (IDT).

Primer name	Sequence 5' to 3'
qExon22-24-F	CTGAATATGAAATAATGGAGGAGAGACTCG
qExon22-24-R	CTTCAGCCATCCATTTCTGTAAGGT
qExon22-24-Probe	/5FAM/ATGTGATTC/ZEN/TGTAATTTCC/3IABkFQ/
qExon23-24-F	CAGGCCATTCCTCTTTCAGG
qExon23-24-R	GAAACTTTCCTCCCAGTTGGT
qExon23-24-Probe	/5HEX/TCAACTTCA/ZEN/GCCATCCATTTCTGTAAGGT/3IABkFQ/

Table 4.1 Primer and probe sets used in the study.

4.3 Results

4.3.1 PPMO restores dystrophin expression in a dose-dependent manner

The effects of exon-skipping on serum myomiRs levels and pattern of dystrophin expression have been investigated before by our group in a single-dose studies in male *mdx* animals [107,321]. To determine whether the serum myomiRs and dystrophin restoration pattern upon exon-skipping therapy depends on a therapeutic dose, male *mdx* mice were injected intravenously with a single dose of Pip9b2-PMO (PPMO) conjugate targeting 5′ splice site of exon 23 (Figure 4.1 A). Three different doses: 3, 6, and 12 mg/kg (*n* = 7, 9, and 9 animals, respectively) of exon-skipping PPMO conjugates were administered at 8 weeks of age (Figure 4.1 B). By this age, the acute phase of muscle degeneration has stabilised providing a consistent baseline to measure the effects of the treatment [126]. TA muscles and blood serum were harvested two weeks after injection together with age and sex-matched dystrophic (*mdx*, *n* = 9) and wild-type (WT, *n* = 5) controls (Figure 4.1 B).

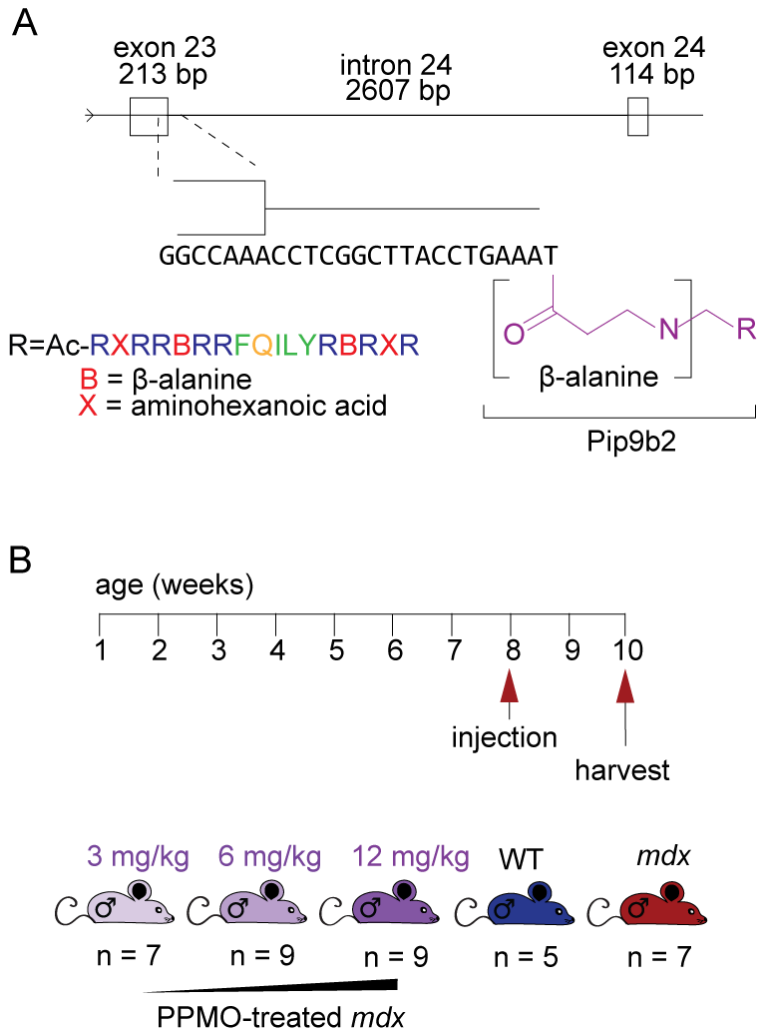

Figure 4.1 Experimental design of PPMO dose response study.

(**A**) Schematic representation of PPMO structure and binding within dystrophin pre-mRNA. Pip9b peptide was conjugated to PMO targeting splice site of exon 23 in mouse dystrophin. The PMO effectively "hides" the splice donor site of mutation-containing exon 23 in *mdx* mice resulting in its exclusion from mature transcript. Pip9b peptide has two cationic arginine (R) rich regions interspersed with β-alanine and aminohexanoic acid which flank the neutrally charged hydrophobic (FQILY) region. Presence of cationic regions facilitates the compound interaction negatively charged cell membrane aiding the efficient membrane penetration and thus cellular uptake. (**B**) Dosage timeline. *mdx* animals were injected intravenously with PPMO conjugates at 8 weeks of age. Three different doses were administered (3, 6, 12 mg/kg). Animals were harvested two weeks after injection alongside relevant controls: C57 wild-type and untreated *mdx*.

Western blot analysis confirmed dose-dependent, PPMO-mediated dystrophin restoration in TA muscle at median values of 3.7% (3 mg/kg), 16.7% (6 mg/kg), and 44.8% (12 mg/kg) of WT levels (Figure 4.2 A, C). No dystrophin protein was observed in TA muscle from *mdx* animals. Levels of transcripts lacking exon 23 (Δ exon 23, skipped transcripts) assessed by RT-qPCR as the percentage of total analysed dystrophin transcripts, demonstrated a similar, PPMO dose-response trend. The median percentage of skipped transcripts was: 1.2% (3 mg/kg), 11.8% (6 mg/kg), and 38% (12 mg/kg). Dystrophin protein expression and *Dmd* exon 23 skipping were strongly positively correlated (Spearman's r = 0.9262, $P < 0.0001$, Figure 4.2 D).

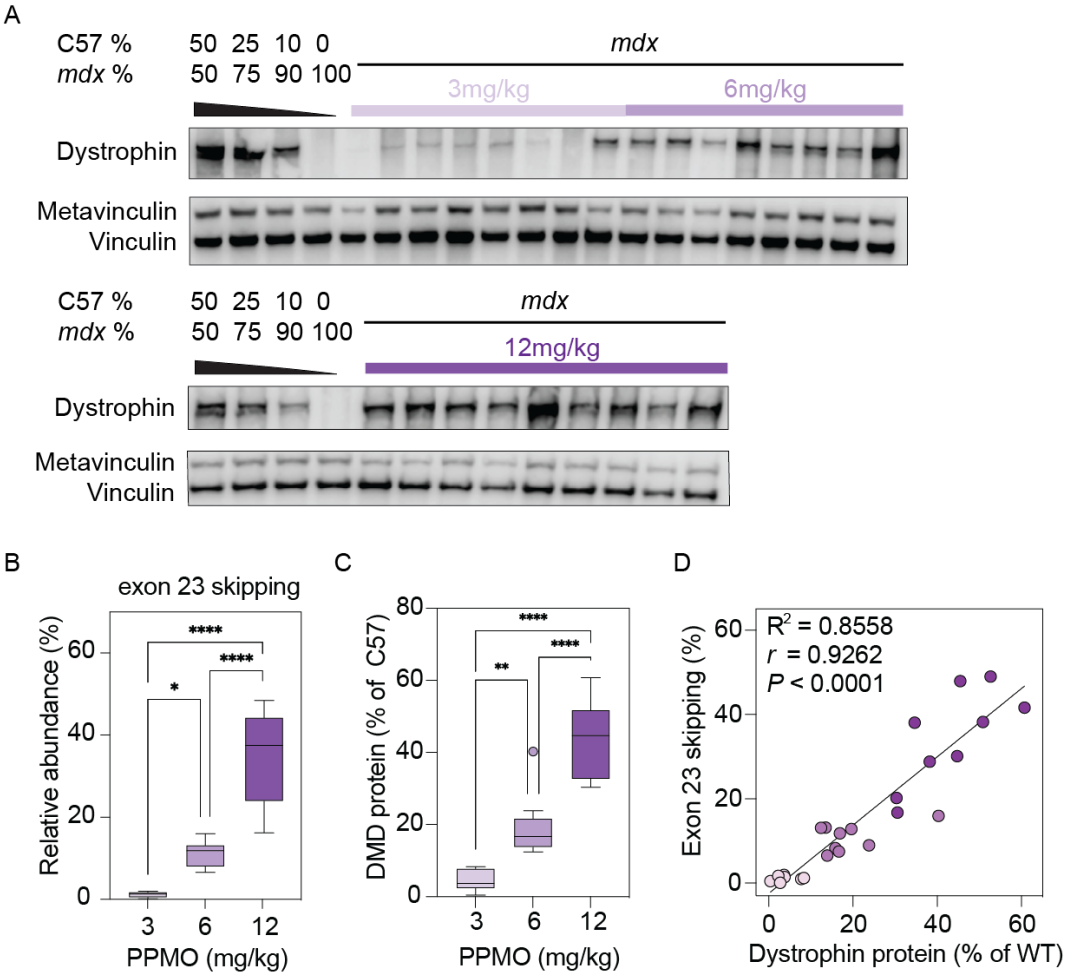

Figure 4.2 Quantification of dystrophin restoration upon treatment with three different doses of exon skipping PPMO conjugate.

(**A**) Western blot analysis of dystrophin protein in TA muscle from *mdx* animals treated with 3,6 and 12 mg/kg of PPMO. Vinculin was utilised as a loading control, standard curves consisted of mixtures of C57 WT and *mdx* TA lysates. (**B**) Tukey box plot of exon skipping levels determined by RT-qPCR. (**C**) Quantification of dystrophin as percentage of wild type levels based on western blot. (**D**) Linear regression and Spearman correlation analysis of dystrophin protein expression and exon skipping levels in *mdx* animals treated with different doses of PPMO. Statistical analysis: one-way ANOVA with Bonferroni *post hoc* test. *** $P < 0.001$, ** $P < 0.01$, * $P < 0.05$.

4.3.2 miR-133a and miR-133b are indistinguishable using a widely used RT-qPCR small RNA assay

miR-133a and miR-133b differing by one nucleotide in their mature sequence, are encoded by two distinct genomic loci. Notably, in contrast to miR-133a, miR-133b is not regulated by MyoD and is thus differentially regulated during myogenesis [376]. Additionally, small RNA sequencing data from our group demonstrated that miR-133b is ~ 5× less abundant than miR-133a in whole muscle lysates [320]. As such, miR-133a/b expression levels are often reported separately. The small-RNA TaqMan RT-qPCR method is a widely used approach to assess the miRNA abundance (Figure 2.1). To determine if this method accurately distinguishes between mature miR-133a and miR-133b, as well as miR-1 and miR-206 a mixture of on- and off-target RT and qPCR assays were performed (Table 4.2). Artificial samples of either miR-1, miR-133a, miR-133b, or miR-206 (50 fmol/sample in water), were reverse transcribed using both correct and off-target stem-loop primers. The resulting cDNA template was subsequently amplified using specific mature miRNA primers and probes.

template	Reaction 1 stem-loop RT primer	Reaction 2 stem-loop RT primer	qPCR
miR-133a	miR-133a	miR-133b	miR-133a and miR-133b
miR-133b	miR-133a	miR-133b	miR133a and miR-133b
miR-1	miR-1	miR-206	miR-1 and miR-206
miR-206	miR-1	miR-206	miR-1 and miR-206

Table 4.2 RT and qPCR reactions to assess the specificity of myomiRs assays.

The miR-1/206 family assays were found to clearly distinguish between the two related myomiRs (Figure 4.3 B). Each of these myomiRs were detected at ~ 40,000-fold higher levels (ΔCq > 15.4) when reverse transcribed with on-target primer, in comparison to the off-target one, indicative of highly specific detection. The amplification of cDNA produced with off-target stem-loop primer was detected ~ 31-35 Cq, suggesting very low levels of template input. Conversely, amplification of miR-133a/b was observed at very similar levels (ΔCq = 0.3, Figure 4.3 C), regardless of whether the on-target or off-target RT primer was used, suggesting that miR-133a/b-specific stem-loops efficiently prime the reverse transcription of both mature miR-133 isoforms.

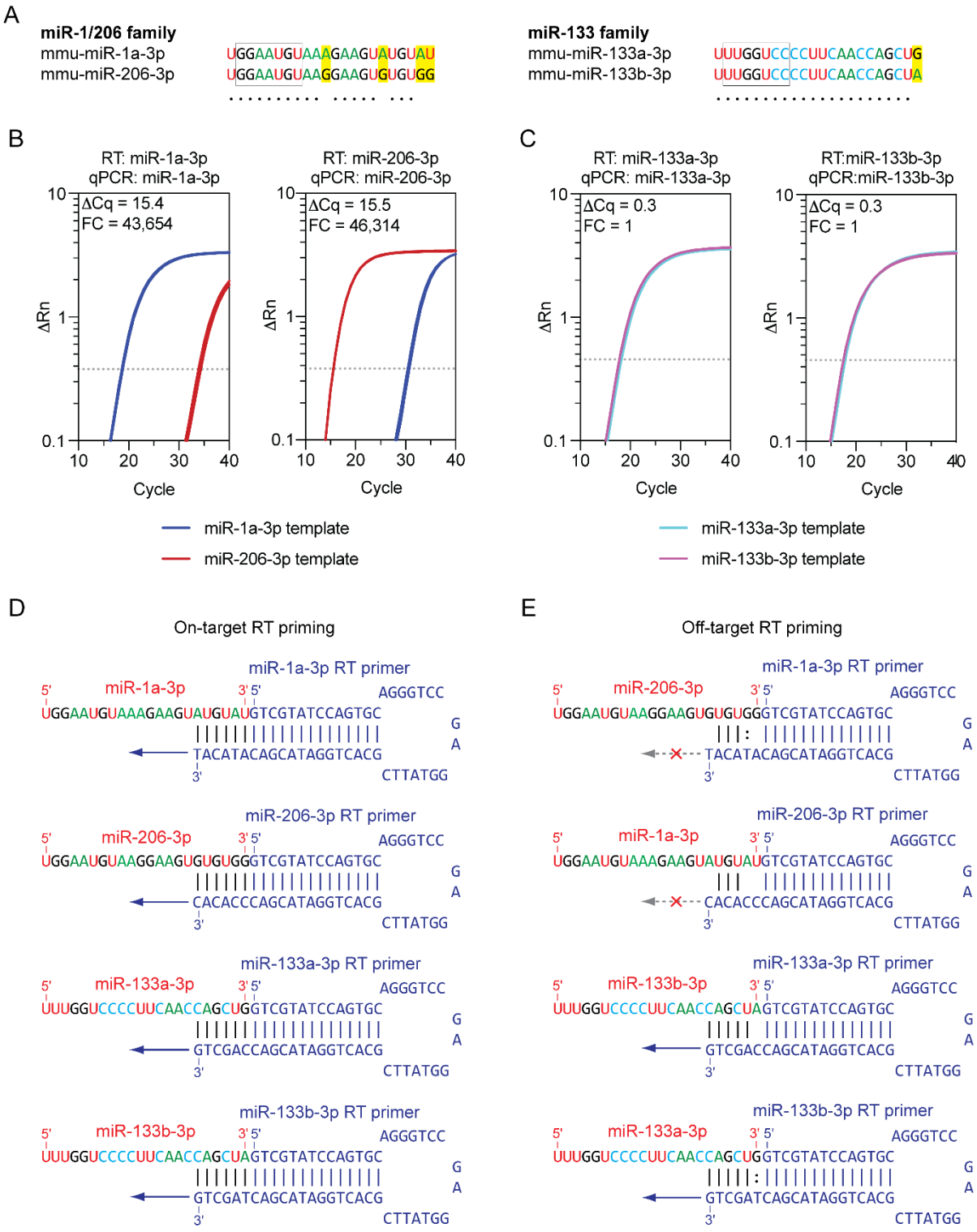

Figure 4.3 Determination of small RNA TaqMan assays reverse transcription specificity in distinguishing closely related miRNA.

(**A**) Sequences of analysed miR-1/206 and miR-133a/133b families. miR-1 and miR-206 differ in four nucleotides, while miR-133a and miR-133b sequences differ only by a single nucleotide at 3′ end. Within families, artificial samples containing 50 fmol of each miRNA

were reverse transcribed using on (e.g., miR-1 primer for miR-1) and off (e.g., miR-206 primer for miR-1) RT primers. Subsequently, on and off-target qPCR assay was performed. qPCR amplification plots are illustrated for (**B**) miR-1-3p and miR-206-3p, (**C**) miR-133a-3p and miR-133b-3p using on/off target RT priming and amplification. On-target (**D**) and off-target (**E**) reverse transcription priming for each miRNA analysed. The Substantial similarity of sequences between miR-133a-3p and miR-133b-3p at the stem-loop primer binding site illustrates the efficient off-target RT priming.

In parallel, on-target RT coupled with off-target qPCR assay did not result in amplification of miR-133a/b nor miR-1/206 indicating that the loss of specificity arises at the RT step (Figure 4.4 A, B). Analysis of interactions between stem-loop primers and both target and non-target miRNAs reveals the underlying cause of cross-reactivity in miR-133 assays (Figure 4.3 D, E). As the stem-loop primers target the 3' end of mature miRNAs, the three mismatches present in the miR-1/-206 family effectively prevent off-target binding (Figure 4.3 E). In contrast, miR-133a and miR-133b differ only by a single, 3' terminal nucleotide. Consequently, most of the stem-loop primer sequence is identical, facilitating the effective priming of both isoforms and thereby contributing to the observed high off-target amplification (Figure 4.3 E).

These results demonstrate the commercially available small RNA MicroRNA TaqMan assays are unable to discriminate between two mature isomers of miR-133 family. These results can potentially be extrapolated onto other small RNAs with minimal 3′ end differences. Given that miR-133a-3p is significantly more abundant, results presented in this thesis report only this isomer, acknowledging concomitant amplification of miR-133b-3p.

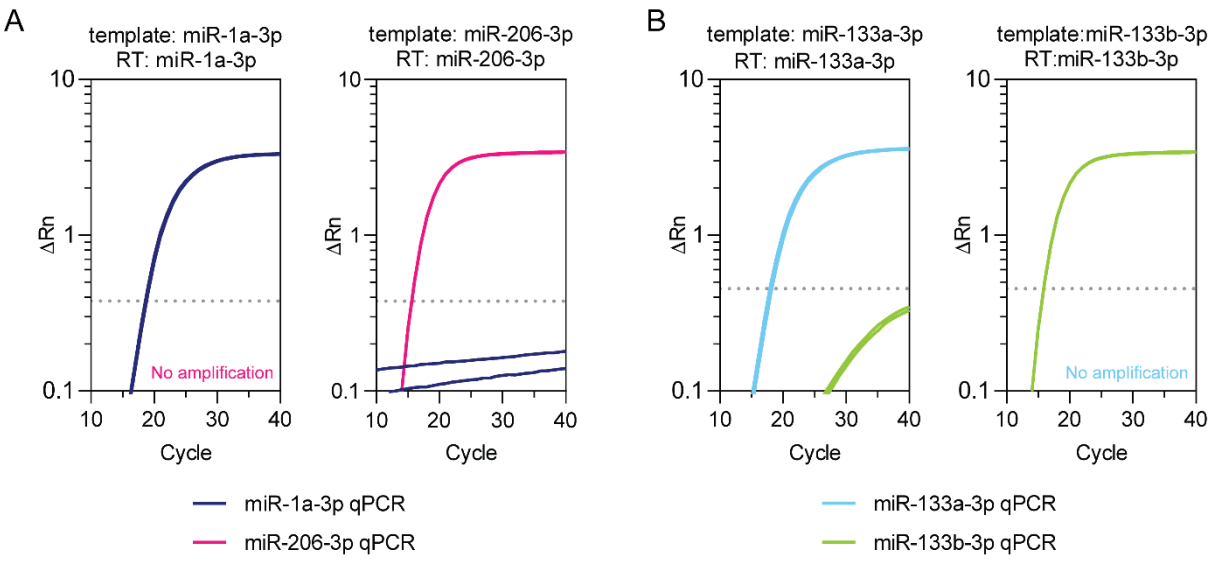

Figure 4.4 Determination of small RNA TaqMan assays specificity in discriminating related miRNAs at qPCR step.

Within miRNA-1/206 and miR-133a/133b families, artificial samples containing 50 fmol of each miRNA were reverse transcribed using on target RT stem loop primer. Subsequently, samples were amplified using on or off target qPCR assay. qPCR amplification plots are illustrated for (**A**) miR-1-3p and miR-206-3p, (**B**) miR-133a-3p and miR-133b-3p using on target reverse transcription and off target qPCR. No amplification of off-target samples was detected.

4.3.3 PPMO treatment induced dose-dependent restoration of extracellular myomiRs in *mdx* serum

To determine effects of PPMO-mediated exon skipping on myomiR biomarkers, RT-qPCR for miR-1-3p miR-206-3p, miR-133a-3p and miR-483-3p was performed in serum of PPMO-treated and control animals, alongside the CK levels analysis. miR-483 was previously identified as a novel candidate of DMD serum biomarkers based on its elevated levels in muscle and serum of *mdx* animals as well as DMD patient sera relative to the control [321,395]. All measured myomiRs, were significantly elevated in *mdx* serum with median fold change of 16 (miR-1-3p), 19.9 (miR-133a-3p), and 48 (miR-206-3p) (Figure 4.5

A, B, C). The upregulation of miR-483-3p (by 12.5-fold) did not reach statistical significance (Figure 4.5 D). PPMO treatment in *mdx* mice resulted in a dose-dependent restoration of myomiRs biomarkers towards WT levels. Notably, the 12 mg/kg group displayed biomarker restoration closest to WT, particularly for miR-1a-3p and miR-133a-3p (Figure 4.5 A, B). Animals treated with PPMO at 6 mg/kg exhibited intermediate serum myomiRs levels, while 3 mg/kg group resembled untreated *mdx*. Importantly, serum CK levels followed a similar trend, with less sample variation resulting in more significant differences between groups (Figure 4.5 E).

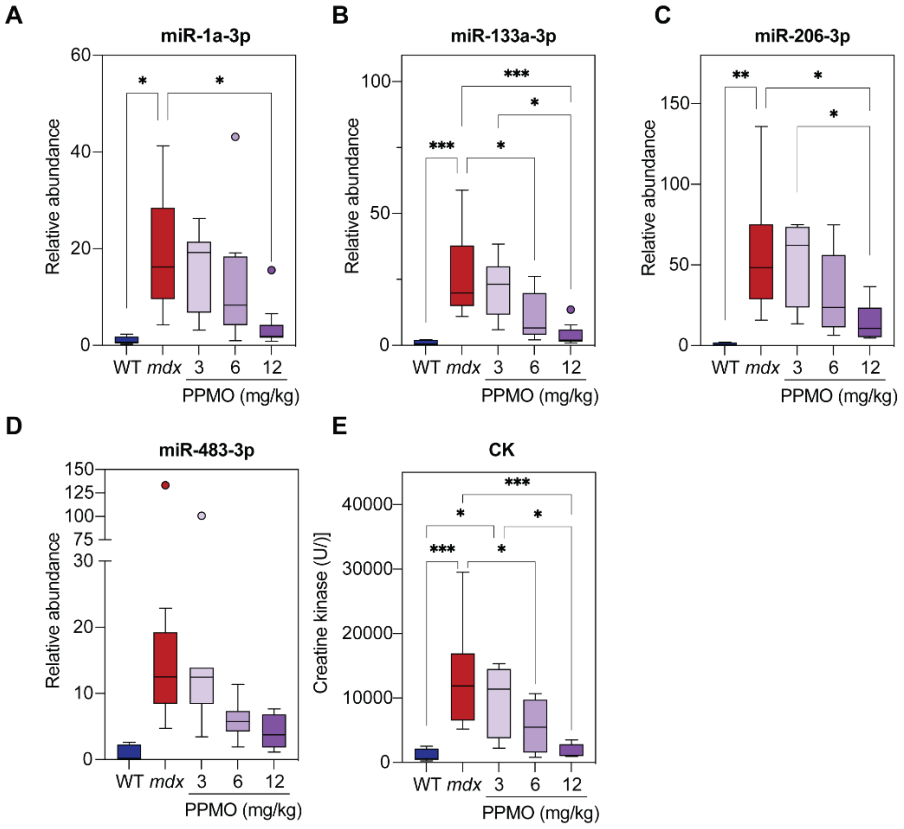

Figure 4.5 Serum myomiR biomarkers levels in *mdx* animals treated with exon-skipping PPMO conjugate.

RT-qPCR quantification of miR-1-3p (**A**), miR-133a-3p (**B**), and miR-206-3p (**C**) and miR-483-3p in serum harvested from 10-week-old PPMO-treated *mdx* mice. The values are normalised to internal spike-in control. Serum from WT and *mdx* mice was used as a control. Statistical analysis: one-way ANOVA with Bonferroni *post hoc* test. *** $P < 0.001$, ** $P < 0.01$, * $P < 0.05$.

4.3.4 Serum myomiRs biomarkers are inversely correlated with dystrophin levels restored by PPMO-mediated exon skipping

Comparison of dystrophin percentage with levels of serum biomarkers revealed a significant inverse correlation with all myomiRs: miR-1-3p r = -0.7185, miR-133a-3p r = -0.7554, miR-206-3p r = -0.640, miR-483-3p r = -0.55 and CK r = -0.7223 (all $P < 0.005$, Figure 4.6). A similar relationship was observed between exon skipping and serum biomarkers levels: miR-1-3p r = -0.6715, miR-133a-3p r = -0.7546, miR-206-3p r = -0.6723, miR-483-3p r = -0.64 and CK r = -0.7687 (all $P < 0.0006$, Figure 4.7). Among the biomarkers analysed, CK and miR-133-3p exhibited the strongest correlation with dystrophin protein and exon skipping levels. The weakest correlation with both measures was observed for miR-483-3p.

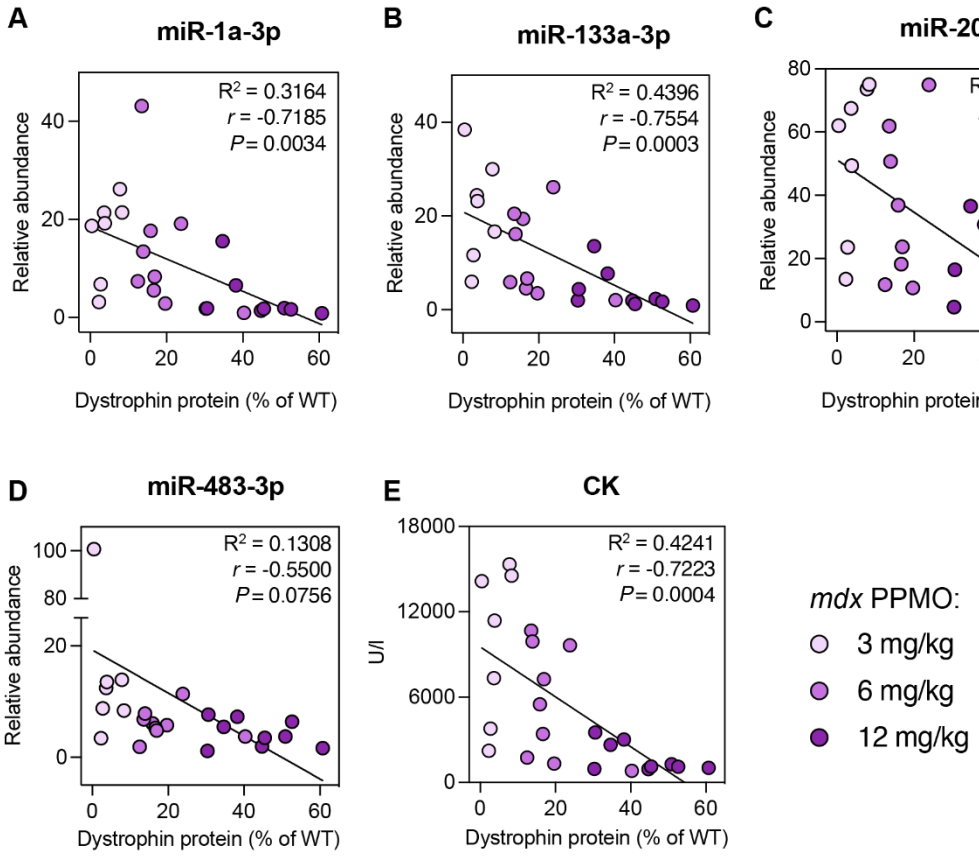

Figure 4.6 Correlation of PPMO-restored dystrophin levels in muscle with serum myomiR biomarkers.

Spearman correlation and linear regression analysis of TA muscle dystrophin levels versus the relative abundance of (**A**) miR-1-3p, (**B**) miR-133a-3p, (**C**) miR-206-3p, (**D**) miR-483-3p and (**E**) CK in serum of *mdx* animals treated with three different doses of PPMO conjugate.

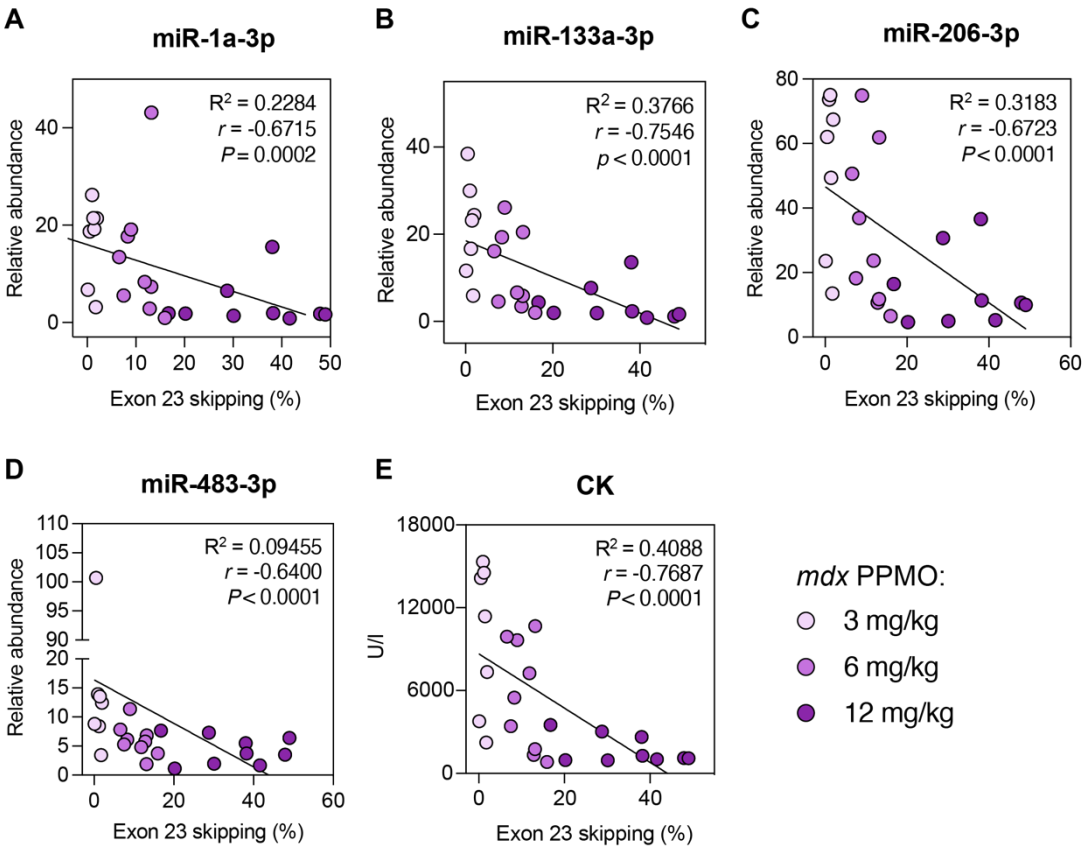

Figure 4.7 Correlation of PPMO-mediated muscle exon skipping levels and serum myomiR biomarkers.

Spearman correlation and linear regression analysis of exon skipping levels in TA muscle versus the relative abundance of (**A**) miR-1-3p, (**B**) miR-133a-3p, (**C**) miR-206-3p, (**D**) miR-483-3p and (**E**) CK in serum of *mdx* animals treated with three different doses of PPMO conjugate.

4.3.5 PPMO-mediated exon-skipping restores dystrophin uniformly at the sarcolemma

Previously, our group contrasted patchy dystrophin distribution at the sarcolemma of *mdx-Xist*$^{\Delta hs}$ with the same levels of uniformly localised dystrophin after a single-dose PPMO treatment at 12.5 mg/kg [321]. To visualise the pattern of pattern of dystrophin restoration, transverse and longitudinal TA muscle sections of animals used in this study were stained for dystrophin and laminin proteins (Figure 4.8). Overall, animals expressed dystrophin uniformly after PPMO-treatment regardless of the dose The staining intensity was the lowest for 3 mg/kg group. Variability in dystrophin signal between myofibres was observed in transverse TA sections from these animals, with some fibres expressing dystrophin and some not. This phenomenon was not apparent in the 6 mg/kg and 12 mg/kg treated animals where most of the myofibres were fully covered with sarcolemmal dystrophin. These results confirm that PPMO-mediated exon-skipping restores dystrophin uniformly at the sarcolemma.

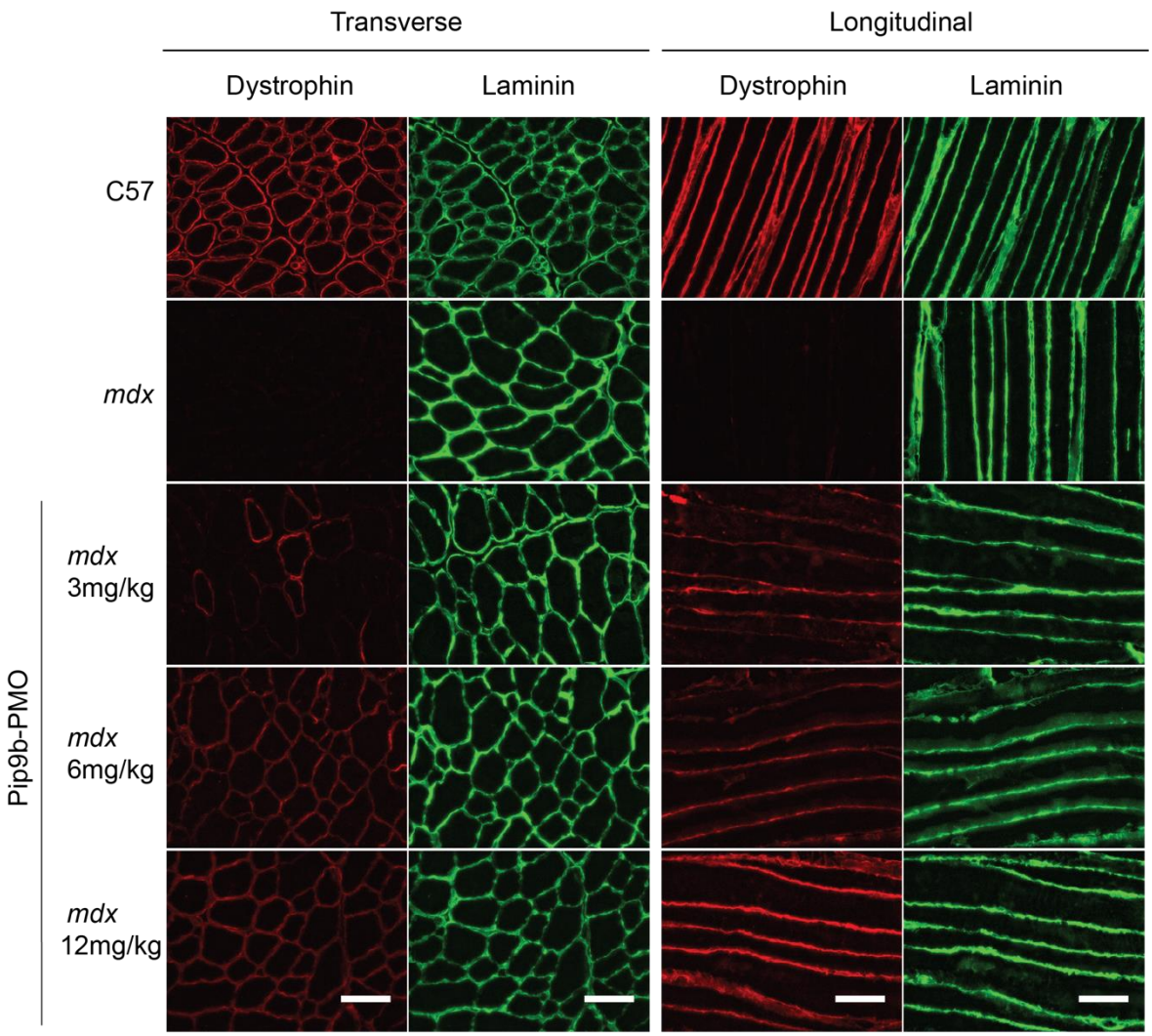

Figure 4.8 Uniform dystrophin protein restoration in *mdx* animals treated with exon-skipping PPMO conjugate.

Representative immunofluorescence staining of dystrophin and laminin in transverse and longitudinal TA muscle sections of 10-week-old mdx animals treated with 3,6 and 12 mg/kg of PPMO conjugate. C57 (WT) and untreated mdx were analysed as controls. Uniform dystrophin restoration at the sarcolemma was detected regardless of the dose used. Scale bar indicates 100 μm, images taken at ×20 magnification.

4.4 Discussion

4.4.1 ASO-mediated exon skipping restore dystrophin uniformly at the sarcolemma

Treatment of *mdx* mice with Pip9b-PMO conjugates resulted in uniform dystrophin restoration at the sarcolemma regardless of the dose (Figure 4.8). This aligns with previous research from our group [321], as well as a recent study by Morin *et al.* [405] and contrasts with the non-uniform pattern of dystrophin restoration observed with CRISPR-Cas9-mediated gene editing [251,405,420]. The differences in the pattern of dystrophin re-expression could result from inherent variabilities of CRISPR-Cas9 and ASO efficacy. The Cas9 protein on its own is 160 kDa while the Pip9b peptide is only ~ 2.5 kDa [235]. Considering that the diffusion of proteins above 100 kDa is significantly restricted within the muscle, it can be assumed that once effectively targeted to the nucleus and translated in the cytoplasm the Cas9 protein would not readily diffuse within the myofibre and thus will be present only in the portion of myonuclei [288]. However, this issue might be partly overcome by incorporating nuclear localisation sequences in the Cas9 plasmids, as commonly done [242,243,246,247,251]. A recent preprint from Poukalov *et al.* demonstrated that attaching a combination of nuclear export and import sequences (termed “Myospreader”) influences the Cas9 nuclear propagation process [420]. Specifically, fusion of Myospreader to Cas9 led to a higher number of targeted nuclei, improved the protein stability, and enhanced the editing efficiency of dystrophin in *mdx* model relative to the Cas9 fused with 2×SV40 nuclear localisation signal [420]. Notably, despite this significant improvement in nuclear propagation of Cas9, editing of exon 23 in *mdx* mice still resulted in patchy dystrophin restoration [420]. Effective gene editing can be achieved only when all CRISPR-Cas9 machinery compounds (i.e. Cas9 protein and sgRNA) are localised to the same nucleus. However, even so, there is still a chance that unproductive gene editing takes place. Specifically, the introduction of secondary lesions (e.g. indels, inversions or even AAV genome integrations that don’t correct the disease-causing mutation) can render the myonucleus refractory to further genetic manipulation [251]. Conversely, PMOs or

PPMOs are likely to easily diffuse throughout the myofibre due to their low molecular mass. Additionally, once in the nucleus the ASOs utilise the host splicing machinery without requirement of delivery of additional exogenous compounds. As such, in principle exon-skipping is much simpler to execute than gene editing and could target a significantly higher amount of myonuclei within the syncytium.

Notably, immunofluorescence analysis of PPMO-restored dystrophin in longitudinal sections exhibited some degree of staining intensity variability between groups treated with different PPMO doses (Figure 4.8). Similarly, Morin *et al.* reported low levels of uniformly distributed dystrophin upon exon-skipping [405]. It is possible that readily diffusing exon-skipping ASOs target and efficiently correct only a portion of nascent dystrophin mRNAs within any given nucleus. This would result in a limited number of functional dystrophin transcripts expressed from most of the nuclei leading to low but uniform dystrophin protein translation. In contrast, CRISPR-Cas9 targeting the underlying DNA mutation indirectly corrects all nascent transcripts but in a limited number of myonuclei. This leads to more robust, but localised dystrophin translation, resulting in the observed patchy pattern of dystrophin expression. Notably, low in intensity but uniform dystrophin was previously detected in two patients carrying out-of-frame *DMD* mutations but exhibiting an intermediate phenotype (i.e. disease progression between that of DMD and BMD) [411].

4.4.2 PPMO-mediated exon skipping restores serum myomiR biomarkers

As mentioned above, Western blot and immunofluorescence-based dystrophin quantification suffer from several limitations including the use of limited fragments of muscle tissue (i.e. patient biopsy) [484]. A surrogate biomarker, by definition, could substitute (or supplement) a clinically meaningful endpoint such as the level of dystrophin restoration [390,394]. Notably, extracellular myomiRs were negatively correlated with corrected dystrophin as well as exon skipping levels in the present study, showing that these molecules reliably reflect the restored levels of dystrophin (Figure 4.6, Figure 4.7).

Importantly, myomiRs can be measured from serum and thus are likely to reflect the general, body-wide change in dystrophin production rather than local variation in a single muscle. As such, results presented here add to the growing literature, supporting the role of serum myomiRs role as pharmacodynamic biomarkers in DMD therapeutic interventions [320,321,386,390].

However, it is important to note, that while serum myomiR levels are correlated with dystrophin levels, other factors influence their presence in the circulation. Specifically, several studies from our group demonstrated that the increase in serum myomiR levels is not merely a reflection of passive 'leakage' from dystrophin-lacking, damaged muscle [107,108,386,398]. MyomiRs can be released to circulation in various physiological conditions, e.g. during healthy perinatal muscle development, after physical exercise or during myotube formation *in vitro* [386]. Accordingly, two peaks of serum myomiRs expression in *mdx* serum are observed [107]. First at an early time point of 4 weeks of age, when massive myofibre necrosis occurs, and a second during the regenerative phase between 12-14 weeks of age [107]. Similarly, elevated serum myomiRs have been shown to correlate with both exercise-induced muscle damage in *mdx* mice, and the subsequent regenerative response [386]. Furthermore, extracellular miR-206 levels were correlated with myogenin expression in the TA muscle, suggesting that serum miR-206 levels mirror the ongoing regenerative processes in muscle [107]. Moreover, the significant upregulation of myomiRs in dystrophic serum (~ 50-100-fold) contrasts with ~ 4-10-fold upregulation of miR-206 in *mdx* tissues, and modest downregulation and steady levels of miR-1 and miR-133a in the muscle [108]. Together, these results show that increased extracellular myomiR levels in dystrophic serum do not passively mirror the myofibre damage but are rather a consequence of selective release at different stages of muscle degeneration/regeneration cycles [386].

4.4.3 Commercially available RT-qPCR assays do not distinguish between miR-133 isoforms

Figure 4.3 shows that the widely used commercial small RNA TaqMan RT-qPCR method assays do not distinguish between miR-133a and miR-133b. Specifically, the stem-loop primer designed for miR-133a and miR-133b binds both isoforms that differ only in a single nucleotide at their 3′ end. This suggest that miRNA specific stem-loop primers tolerate terminal mismatches and lead to off-target amplification and agrees with previous study that did not distinguish between miR-133a/b isoforms [488]. In contrast, Chen *et al.* successfully applied this method to distinguish between different isoforms from *let-7* miRNA family that also differ in single nucleotide at 3′ end [489]. This suggests that other factors (e.g. stability of base-pairing towards 5′ end) could contribute to non-specific reverse transcription priming. The findings emphasise that it is it important to evaluate the specificity of commercially available assays. Notably, some previous studies have reported the expression of miR-133a and miR-133b separately using the analysed method [387,388,490,491].

It's important to note that the lack of specificity of small RNA TaqMan miR-133a/b assays does not point to general limitation of the method, but rather context-specific (i.e. miRNAs differing by a single nucleotide at their 3′ end).

5 Results III: Subcellular distribution of miRNAs during myogenic differentiation

5.1 Introduction

5.1.1 miRNA subcellular localisation

The canonical view is that miRNAs work in the cytoplasm where they target the 3′ UTR of various transcripts inducing their degradation. Indeed, the cytoplasmic localisation of mature mRNAs, as well as the nuclear export of miRNAs during biogenesis suggests that miRNAs are predominantly active in the cytoplasm. As such, alternative aspects of miRNA-mediated gene regulation are often overlooked in the majority of the studies [348,357,492–495]. However, growing evidence suggests that mature miRNAs are not restricted to the cytoplasmic compartment. Notably, nuclear localisation of miRNAs was demonstrated two decades ago [358]. However, this phenomenon was then attributed to cross-contamination between isolated nuclear and cytoplasmic fractions [496]. Since then, multiple small RNA sequencing and microarray studies of mammalian cells have confirmed that almost all miRNAs localise to both nuclear and cytoplasmic compartments [497–503]. In parallel, significant effort was dedicated to elucidating nuclear miRNAs mechanisms of action (reviewed in [504–508]). To date, the proposed roles of miRNAs in the nucleus of mammalian cells include transcriptional activation, transcriptional silencing, and alternative splicing regulation among others (Table 5.1).

Cell line	Origin	Tissue	Mechanism of action
HEK293T	Human	Kidney	• transcriptional repression by miR-671-mediated cleavage of natural antisense transcript [509] • transcriptional activation by miR-24-mediated chromatin modification at enhancer region [510] • transcriptional repression by miR-30b-5p masking of the transcription factor EB binding site [511]
HeLa	Human	Cervical cancer	• transcriptional silencing by miRNA-320-mediated heterochromatin induction at *POLR3D* promoter [512] • RISC-independent regulation of nuclear morphology by miR-29b binding to ANT2 protein [513] • cleavage of cognate nuclear mRNA by let-7 [514] and miR-20 [358]
HepAD38	Human	Hepatoma	• suppression of viral DNA replication by miR-20-induced methylation of viral circular DNA [515]
LN229 U251	Human	Glioblastoma	• splicing alterations by miR-10b binding to U6 small nuclear RNA [516]
HUVEC	Human	Umbilical cord	• activity inhibition by miR-125-5p direct binding to caspase-3 [517]
HCT116	Human	Colon cancer	• alternative splicing regulation by miR-20 and miR-149 binding to intronic sites of *FKBP14* RNA [502]
L929	Mouse	Fibroblasts	• miRNA biogenesis regulation by miR-709 binding to pri-miR-15a/16-1 [518]
HL-1	Mouse	Cardiac	• transcriptional repression by miR-133a-mediated epigenetic changes at the promoter of *Dnmt3b* [519]
C166	Mouse	Endothelium	• transcriptional activation by miR-466c-mediated epigenetic changes at the *Vegfa* promoter [520]
H9C2 NRVC	Rat	Cardiomyocyte	• transcriptional activation by miR-320 binding to *CD36* promoter association [521] • transcriptional activation or repression of various genes by miR-320 interaction with promoter RNAs [501]

Table 5.1 Reported functions of miRNAs in the nucleus.

Additionally, nuclear miRNAs without clearly-defined molecular functions have also been described in: human liver cells [522], human nasopharyngeal carcinoma 5-8F [497], human myotonic dystrophy 1 biopsies [523], SH-SY5Y human neuroblastoma cells [524] , human hepatoma HepAD38 cells [515], mouse liver cells [518], rat primary neurons [500], rat myogenic cells [525], mouse and zebrafish neuronal stem cells [526], mouse heart tissue sections [521]. Moreover, numerous studies have confirmed nuclear localisation of AGO2 [358,498,514,521,526–532], and other RISC components [498,526,527,532] reinforcing the notion of nuclear miRNA activity. As such, nuclear miRNAs are thought to impact plethora of biological processes including viral replication [515], diabetic cardiac dysfunction [521], cell quiescence [526], cell viability [516], hypoxia response [520], proteolysis and apoptosis [517], nuclear morphology [513], senescence [533], lysosome biogenesis and autophagy [511].

5.1.2 C2C12 cell line – an *in vitro* model of muscle regeneration

The most widely studied *in vitro* model of muscle differentiation and regeneration is the C2C12 mouse myoblast line. Originally established in 1977, C2C12 cells have become a widely used model system for studying skeletal muscle development and differentiation [334,335,534]. Under high foetal bovine serum conditions, C2C12 exhibit a fibroblast-like morphology and undergo rapid expansion. Conversely, low serum induces cell cycle arrest, withdrawal from proliferation and efficient myotube formation within days [535]. C2C12 cells recapitulate well-established myogenic gene expression patterns [369]. Accordingly, myomiRs are not expressed (or expressed at low levels) in proliferating mouse and human myoblasts but increase upon induction of cellular differentiation [369,376,380]. Notably, the inhibition of miR-206 by antagomirs (i.e. a single-stranded oligos binding to miRNA and supressing its function) has been shown to delay the formation of C2C12 myotubes *in vitro* through lack of *Pol1a* (DNA polymerase) mRNA suppression [369,378]. Similarly, miR-133 knock-down resulted in lack of ERK1/2 pathway inhibition leading to repressed C2C12

differentiation [380,536]. While existing evidence highlights the importance of nuclear miRNA in diverse biological processes (Table 5.1), the potential role of nuclear myomiRs in skeletal muscle biology remains unexplored. Accordingly, very few studies consider the subcellular localisation of the myomiRs [519,525].

Subcellular fractionation is one of the methods that enables the parallel analysis of the RNA and protein compositions for both cytoplasmic and nuclear compartments within cells and tissues [537]. Although many methods to separate nuclei from cytoplasm exist in the literature, utilisation of hypotonic lysis buffer is one of the most practical. Hypotonic lysis buffer is formulated to contain a lower solute (e.g., salts) concentration than that observed inside the cell. As such, when cells are suspended in hypotonic lysis buffer osmotic pressure drives water molecules from the buffer into the cells. This results in cell swelling, leading to eventually membrane rupture and release of the cytoplasmic components to the buffer. By carefully adjusting the buffer composition, the nuclear bilayer membrane remains intact. As such, protein and RNA extraction can be performed separately from each fraction.

In this chapter of the thesis subcellular localisation of myomiRs during myogenic differentiation is investigated.

5.2 Material and Methods

5.2.1 Cell Culture

C2C12 murine myoblasts were obtained from ATCC (cat no. CRL-1772). The cells were maintained in Dulbecco's Modified Eagle Medium growth media (DMEM; Thermo Fisher Scientific) supplemented with 15% (v/v) foetal bovine serum (FBS; Gibco) and 1% PSA (Thermo Fisher Scientific). C2C12 myotube differentiation was induced when cells reached ~ 90% confluency by switching to differentiation media composed of DMEM supplemented with 2% horse serum, 1%, PSA (both Thermo Fisher Scientific). Cells were differentiated for at least 4 days; differentiation media was changed every 2 days.

Immortalised human myoblasts were obtained from MRC CNMD Biobank, London (L954/1284 M-I). The cells were maintained in skeletal muscle cell growth medium (PromoCell, Heidelberg, Germany) with supplement mix (PromoCell), 10% (v/v) FBS and 1× GlutaMAX, and 1× PSA (all Thermo Fisher Scientific). For myotube differentiation, at 90% confluency cells were switched to skeletal muscle differentiation medium (PromoCell) supplemented with 1× Differentiation Medium SupplementMix (PromoCell) and differentiated for at least 4 days. During differentiation, media was changed every 2 days.

All cultured cells were maintained in a humidified incubator at 37°C and 5% CO_2 and were regularly tested for *Mycoplasma* contamination.

5.2.2 Nuclear-cytoplasmic fractionation

C2C12 myoblasts and myotubes were trypsinised, pelleted (1,000 *g*, 5 min, 4°C), resuspended in 1 ml of PBS and aliquoted into four equal parts. Two parts for protein and RNA analysis of whole cell (WC) and two parts for separation into cytoplasmic (C) and nuclear (N) fractions. Cells were pelleted at (1,000 *g*, 5 min, 4°C), supernatant was discarded. One whole cell aliquot was frozen dry for protein analysis, and 750 µl of TRIzol LS reagent was added to second aliquot for RNA analysis. Further two aliquots were

incubated in 400 µl of hypotonic lysis buffer (HLB; 10 mM Tris-HCl, pH 7.4, 10 mM NaCl, 3 mM MgCl2 and 0.5% (v/v) NP-40) for 10 minutes on ice. Nuclei were pelleted (800 *g*, 10 min, 4°C). The supernatant was collected as cytoplasmic fraction: for protein analysis, 8 µl of 50× protease inhibitor cocktail (Roche, Basel, Switzerland) was added, for RNA analysis, 1.2 ml TRIzol LS was added and frozen dry. Nuclear pellets were washed with 1 ml of HLB and immediately centrifuged at (800 *g*, 10 min, 4°C). One nuclear pellet was dry frozen for protein analysis and 750 µl of Trizol LS was added to second pellet for RNA analysis. All samples were stored in - 80°C until ready for processing.

5.2.3 Chromatin, nucleoplasm, and cytoplasmic fractionation

Chromatin, nucleoplasm, and cytoplasmic fractions were isolated as described previously [537]. C2C12 myoblasts and myotubes were harvested by trypsinisation and centrifuged (1,000 *g*, 5 min, 4°C). Pellets were resuspended in PBS and divided into four equal aliquots. Two aliquots for protein and RNA analysis of whole cell (WC) and two aliquots for separation into cytoplasmic (CYT), nucleoplasm (NP) and chromatin (CH) fractions. Aliquots were centrifuged at (1,000 *g*, 5 min, 4°C), supernatant was discarded. One whole cell aliquot was frozen dry for protein analysis, and 750 µl of TRIzol LS reagent was added to a second aliquot for RNA analysis. Fractionation aliquots were resuspended in 400 µl of (HLB; 10 mM Tris, pH 7.5, 10 mM NaCl, 3 mM MgCl2, 0.3% NP-40 (v/v), and 10% glycerol (v/v)) incubated 10 min on ice, briefly vortexed and centrifuged (1,000 *g*, 10 min, 4°C). The supernatant was collected as cytoplasmic fraction: for protein analysis, 8 µl of 50× cOmplete PI (Roche) was added, for RNA analysis and frozen dry, 1.2 ml TRIzol LS was added and frozen dry. The pellet (nuclei) was washed with 1 ml of HLB and immediately centrifuged (1,000 *g*, 10 min, 4°C). The supernatant was discarded, and nuclear pellets were resuspended in 400 µl of Modified Wuarin-Schibler buffer (MWS; 10 mM Tris-HCl, pH 7.0, 4 mM EDTA, 0.3 M NaCl, 1 M urea, 1% NP-40 (v/v)), vortexed for 30 sec, incubated for 5 min on ice, vortexed once again and incubated for another 10 min on ice. After that time,

samples were centrifuged (500 *g* ,10 min, 4°C). The supernatant was collected as nucleoplasmic fraction: for protein analysis, 8 µl of 50× cOmplete PI cocktail was added, for RNA analysis 1.2 ml TRIzol LS was added and frozen dry. The pellet (chromatin) was washed with 1 ml of MWS, centrifuged at (1,000 *g*, 10 min, 4°C), supernatant was discarded. One chromatin aliquot was frozen dry for protein analysis, and 750 µl of TRIzol LS reagent was added to second aliquot for RNA analysis.

5.2.4 RNA extraction from subcellular fractions

RNA was extracted with TRIzol LS reagent according to manufacturer's instructions with some modifications. TRIzol LS samples collected during subcellular fractionation were thawed on ice. For chromatin, nucleoplasm, and cytoplasmic fractionation, 10 µl of 0.5 M EDTA was added and each sample was incubated at 65°C with vortexing until the pellet had dissolved [537]. This heating step aided the efficient release of RNAs from chromatin and insoluble RNA-protein complexes [537]. 3 µl of 5 nM exogenous spike-in mix was added to each sample, vortexed vigorously for 10 s and incubated for 10 min at room temperature. Chloroform was added to each sample and vortexed again. Samples were centrifuged at 12,000 *g*, 20 min, 4ºC. The aqueous phase was transferred to a fresh tube and supplemented with RNase-free glycogen (Roche) as an inert carrier to aid the extraction. RNA was precipitated with isopropanol for 10 min at room temperature. Samples were centrifuged at 12,000 *g*, 20 min, 4ºC. RNA pellets were washed with 70% ethanol, air-dried, and resuspended in 30 µl nuclease-free water, incubated for 10 min at 55ºC, and stored at - 80ºC.

5.2.5 Protein extraction from cell culture

For nuclear and cytoplasmic fractionation, whole cell and nuclear pellets were resuspended in 400 µl of RIPA buffer (Thermo Fisher Scientific) supplemented with 8 µl of

50× cOmplete PI cocktail (Roche). Samples were vortexed and incubated on ice for 10 min with vortexing every 2 min to lyse the cells/nuclei. The cell debris was pelleted (14,000 *g*, 10 min, 4ºC), and the supernatant was transferred to a fresh microcentrifuge tube as the final protein lysate. Protein concentrations were determined using Pierce BCA Protein Assay Kit.

For chromatin, nucleoplasm, and cytoplasmic fractionation whole cell and chromatin pellets were resuspended in 400 µl of RIPA buffer supplemented with PI. All samples were passed six times through 25 G syringe and sonicated using a Qsonica Q125 sonicator (Qsonica, Newtown, CT, USA) at 20% power for 5 min: 30 sec on, 30 sec off on ice. Protein was precipitated overnight with 1 ml of ice-cold acetone at -20ºC. Samples were centrifuged (14,000 *g*, 10 min, 4ºC) to pellet the acetone-precipitated protein. Pellets were resuspended in 100 µl of ddH_2O and protein concentration was determined using Pierce BCA Protein Assay Kit.

5.2.6 Western Blotting

For fractionation confirmation, equal volumes of all fractions were loaded onto 8 - 12% Bis-Tris gels. For chromatin, nucleoplasm, and cytoplasmic fractionation, equal volumes of fractions were loaded and whole cell lysate was loaded at 50% of the fraction volume to avoid signal saturation. Electrophoresis was performed at 100 V for 2 hr in (3-(N-Morpholino) propanesulfonic acid (MOPS) SDS running buffer (Thermo Fisher Scientific). Proteins were transferred to 0.45 µm PVDF membrane at 30 V for 2 hr. Whole protein was visualised using Fast-Green stain (Sigma-Aldrich). Membranes were blocked with Odyssey blocking buffer (LI-COR Biosciences) and incubated with primary antibodies overnight (Table 2.3). After washes, membranes were incubated with secondary HRP-conjugated antibodies (Table 2.4) for 1-2 hr room temperature. Chemiluminescent signal was detected using Clarity Western ECL substrate (Bio-Rad).

5.2.7 RT-qPCR of subcellular-compartment specific RNAs

To ensure a consistent comparison of RNA abundance across subcellular compartments, equal volumes of RNA from each fraction were reverse transcribed. This approach controls for potential variations that may arise due to the natural distribution of RNA within the cell, where some compartments, like the nucleus, typically contain more RNA than others. All reagents were purchased from Thermo Fisher Scientific.

5.2.7.1 tRNA RT

For tRNA analysis, RT was performed as described before [503]. The RNA was incubated with gene specific primer at 65ºC for 5 min and then on ice for > 1 min. Multiscribe RT enzyme and buffer were added to the mix and samples were incubated for further 30 min at 37ºC. cDNA was diluted 1:5 and amplified on step-one real time PCR instrument using SYBR Green gene expression Master Mix.

Primer name	Species	Sequence 5' to 3'
tRNA-Lys-TTT	Human / mouse	CGCCCGAACAGGGACTTG
tRNA-Met-CAT	Human / mouse	TGCCCCGTGTGAGGATCG

Table 5.2 List of gene-specific tRNA reverse transcription primers used in this study.

5.2.7.2 miRNA RT

For miRNA analysis, equal volumes of RNA were reversed transcribed, and cDNA was amplified as described above (Section 2.3.3) and previously [386].

5.2.7.3 lncRNA RT

For lncRNA analysis, equal volumes of RNA were reverse transcribed using High-Capacity cDNA Synthesis kit using a random priming strategy according to the manufacturer’s instruction. cDNA was diluted 1:5 and amplified on step-one real time PCR instrument using SYBR Green gene expression master mix.

Primer name	Species	Sequence 5' to 3'
Malat1 FWD	Human	GCGTAATGGAAAGTAAAGCCC
Malat 1 REV	Human	CAAACACCTCACAAAACCCC
Neat 1 FWD	Human	GACTCTCCATTTCCCCATCTG
Neat 1 REV	Human	CATTTACCCGCATTTCACAGAC
Rnu1a1 FWD	Mouse	GGAGATACCATGATCACGAAGG
Rnu1a1 REV	Mouse	TTATGCAGTCGAGTTTCCCG
Malat1 FWD	Mouse	GCTGGTAACCGCTGCTATAA
Malat 1 REV	Mouse	CAGAGAATCCAGACCCAGTAAG
Neat 1 FWD	Mouse	CGCTACTGACCACAGACTTTAC
Neat 1 REV	Mouse	GTTGGATTGGGTCTCCTTCTAC
tRNA-Lys-TTT FWD	Human / mouse	GCCCGGATAGCTCAGTCG
tRNA-Lys-TTT REV	Human / mouse	CGCCCGAACAGGGACTTG
tRNA-Met-CAT FWD	Human / mouse	GCCTCGTTAGCGCAGTAG
tRNA-Met-CAT REV	Human / mouse	TGCCCCGTGTGAGGATCG

Table 5.3 List of qPCR primers used in this study.

5.2.8 Cell transfection

3′-biotinylated miR-133a-3p, miR-206-3p and cel-miR-67-3p as well as miR-133-5p, miR-206-5p and cel-miR-67-5p mimics were purchased from IDT. Single-stranded miRNAs of the same family were annealed in equimolar amounts of mimics with annealing buffer (30 mM 4-(2-hydroxyethyl)-1-piperazineethanesulfonic acid (HEPES)-KOH pH 7.4, 100 mM KCl, 2 mM $MgCl_2$, 50 mM NH_4Ac) and incubated at 90°C for 1 min and then at room temperature for 45 min. The duplexes were stored at - 20°C until ready for use.

C2C12 were seeded in GM at the 1.6×10^5 density in 6-well plate and switched to DM two days after to induce myotube differentiation. Cells were transfected with 25 nM biotinylated miRNA mimics on the second day of differentiation using Lipofectamine RNAiMAX Transfection Reagent (Thermo Fisher Scientific) according to manufacturer’s instructions. Transfection complexes were prepared in Opti-MEM Reduced Serum Medium (Thermo

Fisher Scientific). Untransfected sample served as a control. Nuclear-cytoplasmic fractionation and biotin pull-down were performed 48 hr after transfection.

5.2.9 Immunofluorescence in cells

The immunofluorescent staining for myosin heavy chain (MHC) was performed in a 6-well format. On the day of the staining, cells were washed 3-times with 1 ml of PBS (Thermo Fisher Scientific) and fixed for 10 min at room temperature with 4% PFA in PBS. Subsequently, cells were washed 3 times with 1 ml of PBS and permeabilised with 0.25% of Triton-X100 (Sigma) in PBS for 10 min at room temperature. Non-specific antigens were blocked with 5% BSA (Sigma) in PBS (blocking buffer) for 1 hr at room temperature. MHC was detected using the primary MF20 antibody (Table 2.3) diluted in blocking buffer for 2 hr at room temperature. Subsequently, cells were washed 3 times with PBS and incubated with anti-mouse secondary antibody (Table 2.4) for 2 hr at room temperature in darkness. Cells were washed 3 times with PBS and once with DAPI diluted in PBS (1:5000, Thermo Fisher Scientific) 5 minutes each time. Cells were kept in PBS for imaging. Imaging was performed on EVOS Digital Inverted Fluorescence Microscope (Thermo Fisher Scientific).

5.2.10 Biotinylated miRNA mimics pull-down

Biotinylated miRNAs were pulled down from cytoplasmic and nuclear fractions. Subcellular fractionation was performed as described in section 5.2.2 and 10% of each fraction was collected as an input control before the pull-down. The biotin pull-down was performed as described previously [538]. Dynabeads MyOneStreptavidin C1 (Thermo Fisher Scientific) were resuspended by vortexing and transferred to a new microcentrifuge tube at a volume of 30 µl/sample. The tubes were placed on the magnetic rack for 2 min and then washed with 30 µl of bead washing buffer (Tris-HCl 5 mM, EDTA 0.6 mM and NaCl 1M) three times. After the third wash, beads were resuspended in 100 µl of solution A (100

mM NaOH, 50 mM NaCl in nuclease free water), mixed by pipetting and incubated at room temperature for 2 min twice. Subsequently, beads were incubated with solution B (100 mM NaCl in nuclease free water). Beads incubation with solution A and B facilitated removal of any RNase contamination. The beads were then blocked with 1 µg/µl ultrapure BSA, 1 µg/µl yeast t-RNA blocking buffer for 30 min at room temperature with rotation to prevent unspecific binding of proteins and RNAs to the beads. This blocking step prevents direct, non-specific binding of abundant proteins and RNAs to the beads. Subsequently, beads were washed with washing buffer (10 mM KCl,1.5 mM $MgCl_2$,10 mM Tris-Cl pH 7.5, 5 mM DTT, 0.5% NP-40) with the addition of RNase OUT Ribonuclease Inhibitor (Thermo Fisher Scientific) and 1× cOmplete PI (Roche). After the third wash, the fractionated samples were mixed with beads and incubated for 30 min at room temperature with rotation to facilitate biotin-streptavidin binding. Samples were then washed 4 times with wash buffer and resuspended in 200 µl of PBS.

Protein was isolated from the pulled-down beads through denaturing elution. 100 µl of sample was transferred to a new microcentrifuge tube and placed on the magnetic rack for 2 minutes. The supernatant was removed, and protein-bound beads were resuspended in 20 µl of 1× NuPAGE LDS + NuPAGE Sample Reducing Agent (Thermo Fisher Scientific) diluted in PBS. Samples were heated for 10 min at 70°C to allow for proteins to be released to the suspension. Beads were removed by placing the tube on a magnetic rack for 2 minutes. Supernatant containing eluted protein fraction was stored in - 80°C until ready for analysis.

RNA was isolated using TRIzol reagent directly from the remaining 100 µl of fraction-specific pulled-down samples as described in section 5.2.4.

5.2.11 Generation of stable, inducible FLAG-His-tagged AGO2 C2C12 cell line

A C2C12 cell line expressing inducible AGO2 protein fused to triple-FLAG (3×FLAG) and a poly-histidine (8×His) tag was established using the PiggyBac (PB) transposon system. In the PiggyBac system, a sequence of interest is inserted into the PiggyBac vector plasmid in between the inverted terminal repeats (ITR) [539]. The ITRs are recognised by the co-transfected transposase enzyme which facilitates the 'cut-and-paste' mechanism of flanked sequence into the host genome within sites containing the TTAA sequence. A full-length sequence of mouse AGO2 cDNA was acquired from the NCBI database (NM153178.5). The gene fragment (g-block) of the desired sequence was designed to contain a codon-optimised triple FLAG tag sequence (5'-GACTACAAGGACCACGACGGCGATTATAAGGATCACGACATCGACTACAAAGACGAC GACGATAAG-3') and eight histidine amino acids separated by a linker composed of four alanine amino acids fused to N-terminus of AGO2 protein. The g-block was purchased from IDT (Belgium). Subsequently, the tagged-AGO2 g-block was cloned into the linearised PB vector, which also carries sequences of the tetracycline-inducible system (Tet-on) by Gibson assembly using the Gibson Assembly Master Mix (New England Biolabs, MA, USA). The sequence of obtained PB-3×FLAG-8×His-AGO2 plasmid was confirmed by Sanger sequencing. The transgene containing plasmid was electroporated together with transposase encoding helper plasmid into C2C12 myoblasts using the Neon Electroporation system (Thermo Fisher Scientific) according to the manufacturer's instructions. To obtain a stable cell line, electroporated C2C12 were placed under puromycin selection for 2 weeks. Untransfected C2C12 cells served as a control to assess puromycin selection. Plasmids were purchased from VectorBuilder (vector id: VB010000-949, Neu-Isenburg, Germany)

5.3 Results

5.3.1 MyomiRs are enriched in the nucleus of differentiated human myoblasts.

The role of myomiRs in the control of muscle cell differentiation is well established [371]. All studies investigating mechanisms by which myomiRs control muscle development have to-date considered only the cytoplasmic function of myomiRs in PTGS of genes crucial for myogenesis. However, unpublished data from our group suggests that myomiRs are upregulated primarily in the nuclear compartment during the differentiation of murine C2C12 myoblasts (Figure 5.1, figure by Dr Thomas Roberts and Dr Sofia Stenler). Specifically, small RNA sequencing of nuclear and cytoplasmic fractions of undifferentiated C2C12 myoblasts (MB) or differentiated C2C12 myotubes (MT) revealed that upregulation of miRNA expression in whole cell are mainly reflected in the nuclear fraction of the cells (Figure 5.1 G).

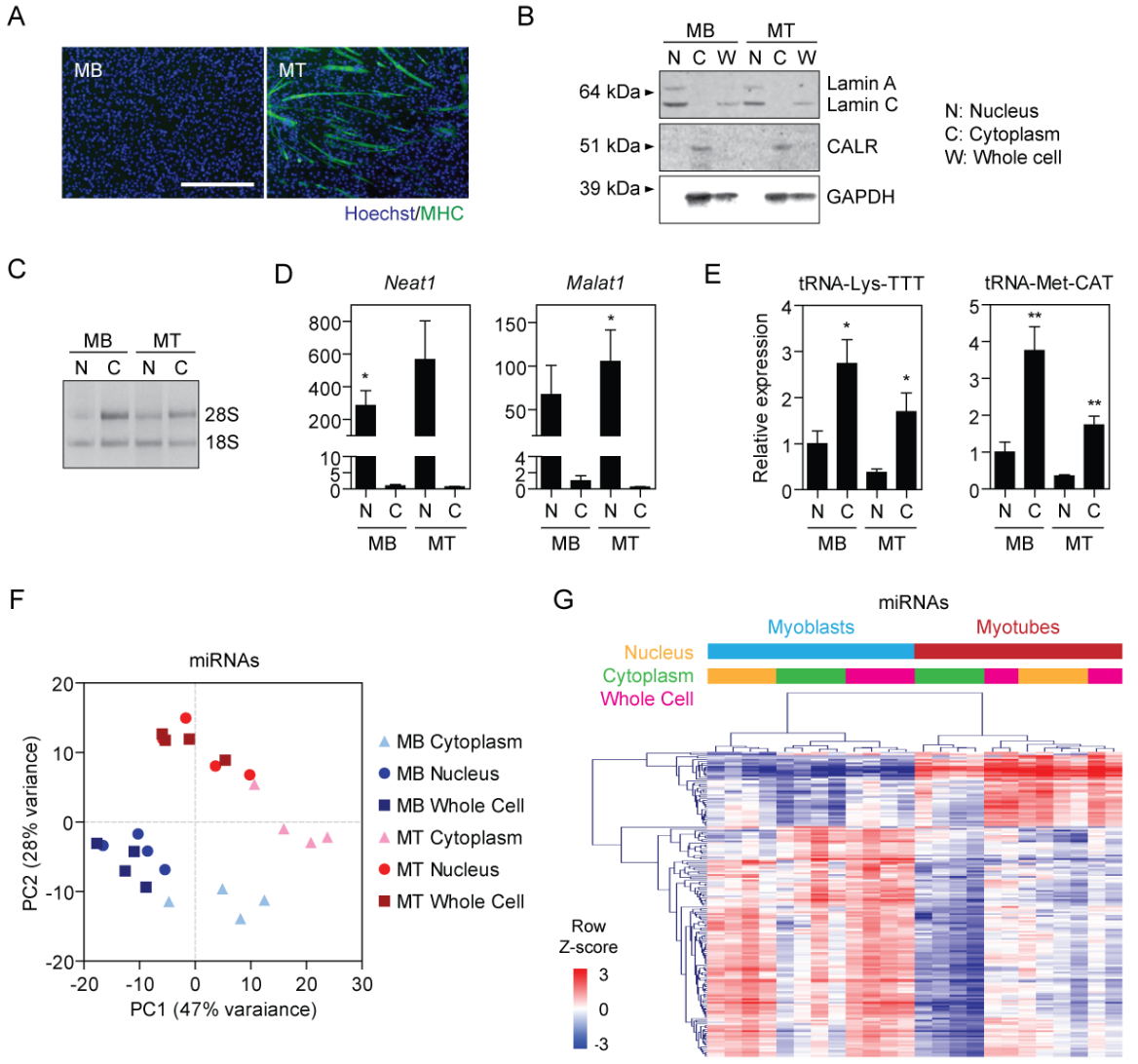

Figure 5.1 Sub-cellular miRNA profiling during mouse C2C12 myogenic differentiation.

Undifferentiated human myoblasts (MB) or differentiated myotubes (MT) were separated into nuclear (N), cytoplasmic (C) and whole cell (WC) fractions and harvested in parallel (n=4). (**A**) Immunofluorescence staining of myosin heavy chain (green) in MB (left) and differentiated MT (right) confirming the myotube formation. Nuclei visualised with Hoechst stain. (**B**) Confirmation of successful subcellular fractionation. Western blot for nuclear (Lamin A/C), cytoplasmic (GAPDH), and endoplasmic reticulum (CALR) markers in each fraction. (**C**) Nuclear and cytoplasmic fractions were analysed by RT-qPCR for nuclear (Neat1 and Malat1) and cytoplasmic (tRNA-Lys-TT and tRNA-Met-CAT) markers. (**D, E**) Total RNA from nuclear and cytoplasmic fractions was separated by agarose gel

electrophoresis and 18S and 28S rRNA visualised with ethidium bromide. Small RNA-seq counts data were visualised for (**F, G**) miRNAs. Data collection and figure preparation by Dr Thomas Roberts and Dr Stofia Stenler.

To assess if a similar phenomenon is observed in human cells, cytoplasmic and nuclear fractions were collected from immortalised human myoblasts at the stage of MB or MT. The same number of cells was used for subcellular fractionation as for the whole cell analysis. Myogenic differentiation was confirmed by immunofluorescence staining for myosin heavy chain (MHC) characteristic for mature myofibres [540] (Figure 5.2 A). Nuclear-cytoplasmic fractionation was confirmed by differential localisation of known nuclear and cytoplasm-enriched proteins: nuclear lamina protein lamin A/C, calreticulin localising to the endoplasmic reticulum and cytoplasmic GAPDH glycolytic enzyme (Figure 5.2 B). In parallel, subcellular compartment-specific RNAs were analysed by qPCR: lysine (Lys) and methionine (Met) carrying cytoplasmic transfer RNAs (tRNA), and nucleus-specific Neat1 and Malat1 lncRNA (Figure 5.2 C). RT-qPCR quantification of the myomiRs: miR-1a-3p, miR-133a-3p and miR-206-3p demonstrated their significant upregulation in differentiated myotubes, consistent with previous observations in C2C12 cells (Figure 5.2 D). Upregulation was observed in both: the cytoplasmic and nuclear compartments of human myoblasts with a slight trend of higher expression in the nucleus as compared with the cytoplasm. These results confirm, that myomiRs are abundant in the nucleus of human myoblasts and are upregulated in the nuclear compartment during differentiation.

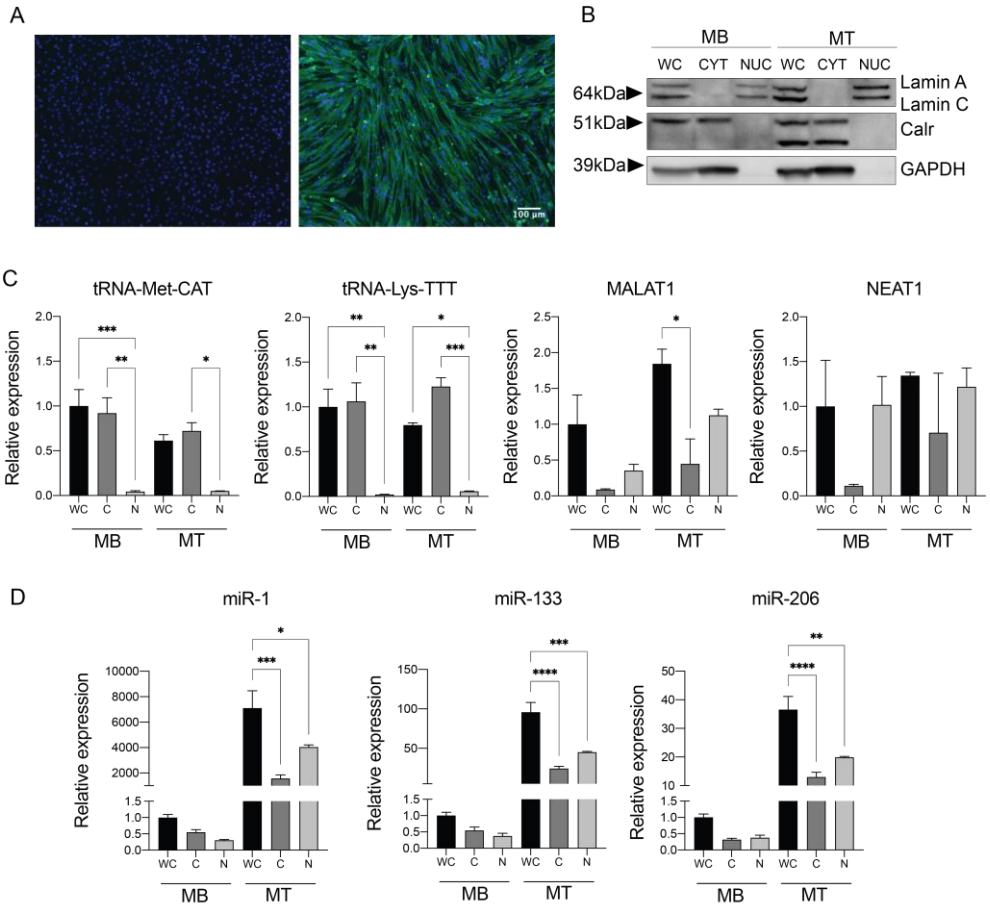

Figure 5.2 Sub-cellular enrichment of muscle specific miRNA during human myoblast differentiation.

Undifferentiated human myoblasts (MB) or differentiated myotubes (MT) were separated into nuclear (N), cytoplasmic (C) and whole cell (WC) fractions and harvested in parallel (*n* = 3). (**A**) Immunofluorescence staining of myosin heavy chain (green) in MB (left) and differentiated MT (right) confirming the myotube formation. Nuclei visualised with Hoechst stain. (**B**) Western blot for nuclear (lamin A/C), endoplasmic-reticulum specific Calreticulin (Calr) and cytoplasmic GAPDH in each fraction. (**C**) RT-qPCR analysis of cytoplasmic (tRNAs,) and nuclear (Malat1, Neat1) markers in each fraction. (**D**) RT-qPCR analysis of miR-1, -133a, -206 relative to exogenous, synthetic oligonucleotide spike in each fraction. Statistical analysis: one-way ANOVA and Bonferroni correction. All values are mean + SEM, n = 3, ***$P < 0.001$, **$P < 001$, *$P < 0.05$.

5.3.2 MyomiRs are localised in the nucleoplasm of differentiated mouse muscle cells

To explore the localisation of miRNAs in the nucleus more precisely, a more rigorous fractionation protocol separating nucleoplasm and chromatin fractions was employed on mouse muscle cells. Differentiated C2C12 myotubes were separated into cytoplasmic (CYT), nucleoplasm (NP) and chromatin (CH) fractions. The number of cells used for fractionation was the same as for the whole cell analysis. Fractionation efficiency was confirmed by RT-qPCR (Figure 5.3 A) and western blot (Figure 5.3 B) detection of fraction-specific RNA and protein markers including nucleoplasm-enriched U1 spliceosomal RNA (*Rnu1a1)*, heterogeneous nuclear RNP (hnRNP) A1, and DNA binding Histone H3 [541,542]. RT-qPCR analysis showed a significant enrichment of myomiRs in the nucleoplasm fraction (Figure 5.3 C). Similarly, western blot analysis revealed AGO2 protein enrichment in the nucleoplasm (Figure 5.3 B). Notably, miRNAs and AGO2 detected in the chromatin fraction were present at very low levels.

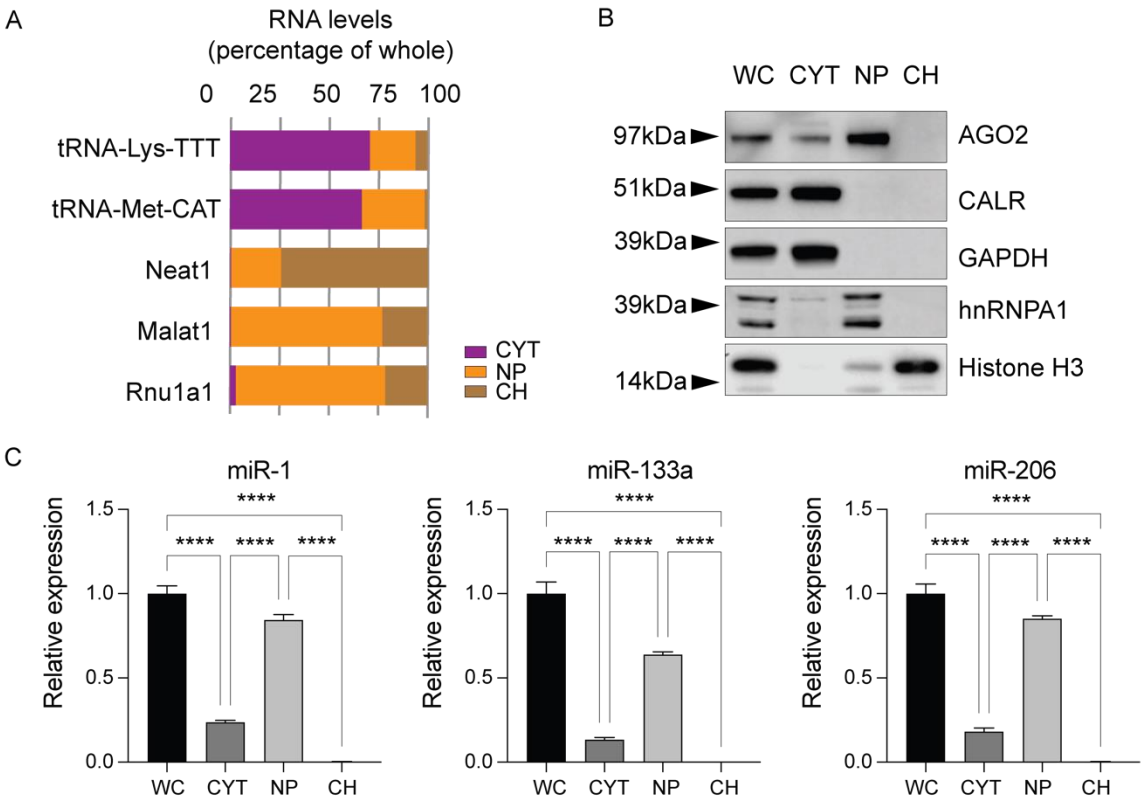

Figure 5.3 Primary myomiRs localisation to the nucleoplasm in differentiated C2C12 murine myotubes.

(**A**) Cytoplasmic (CYT), nucleoplasm (NP) and chromatin (CH) fractionation markers analysed by RT-qPCR. (**B**) Western blot analysis of fraction markers and AGO2 protein. (**C**) RT-qPCR analysis of miR-1, -133a, -206 relative to exogenous, synthetic oligonucleotide spike in each fraction. All three myomiRs exhibit strong nucleoplasm localisation. Statistical analysis: one-way ANOVA with Bonferroni correction. ***$P < 0.001$, **$P < 001$, *$P < 0.05$.

5.3.3 Nuclear miR-206 and miR-133a are AGO2-bound

miRNA exhibit their function as a part of RISC complex, at which core lies the enzymatically active AGO2 protein capable of cleaving the target mRNA. As such, incorporation of nuclear miRNAs into RISC by binding to AGO2 indicates active RNAi mechanism in the nucleus [498]. To investigate if myomiRs are bound to AGO2 protein within the nucleus, differentiating C2C12 cells were transfected with biotinylated miR-133a or miR-206 mimic oligonucleotides (Figure 5.4 A). *C. elegans* biotinylated miR-67 and untreated cells served as controls. Samples were separated into nuclear and cytoplasmic fractions and miRNAs were precipitated with streptavidin beads two days after transfection. RT-qPCR analysis of miR-133a and miR-206 levels (Figure 5.4C) confirmed efficient and specific pulldown of biotinylated miRNAs. Signal was detected in both, cytoplasmic and nuclear fractions. Both miRNAs constituted a larger fraction of input in the nucleus as compared to cytoplasmic fraction, suggesting efficient transport of the exogenous miRNA mimics into the nuclear compartment (Figure 5.4 B). Importantly, western blot analysis showed the presence of AGO2 protein in both fractions of cells transfected with biotinylated miR-133a, suggesting that miR-133a is bound to a RISC-like complex in the nucleus, similarly to that of the cytoplasm (Figure 5.4 D).

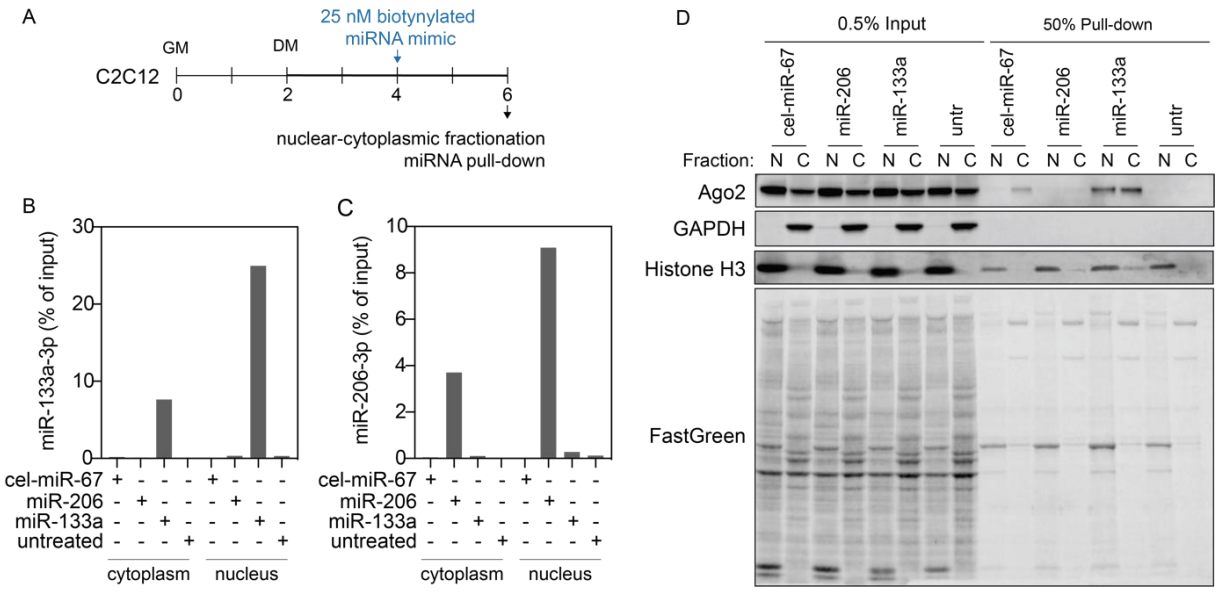

Figure 5.4 Biotinylated miR-133a and miR-206 mimics are bound to AGO2 protein in the nucleus of differentiated C2C12 murine muscle cells.

(**A**) experiment timeline. C2C12 cells were seeded in growth medium (GM) and switched to differentiation medium (DM) two days after. Cells were transfected with biotinylated miRNA duplex on day 4. Fractionation was performed on day 6 and miRNA were precipitated with streptavidin beads. RT-qPCR confirmation of efficient biotinylated (**B**) miR-133a mimic and (**C**) miR-206 mimic from both nuclear and cytoplasmic fraction. (**D**) AGO2 western blot. Strong signal of AGO2 protein was detected in biotinylated miR-133a transfected nuclear and cytoplasmic fractions subjected to streptavidin pull down. GAPDH and Histone H3 protein are showed as fractionation confirmation. Fast Green stain shows total amount of protein loaded.

5.3.4 The majority of AGO2 is localised in the nucleus during myoblast differentiation

To investigate the distribution of AGO2 protein during myotube formation, C2C12 cells were separated into nuclear and cytoplasmic fractions in 24 hr intervals during a 7-day differentiation time course (Figure 5.5 A). The formation of myotubes was visualised by immunofluorescence staining for MHC at each time point (Figure 5.5 B). Western blot analysis of protein isolated from cytoplasmic and nuclear fraction revealed that levels of AGO2 protein were enriched in the nucleus relative to cytoplasm at all differentiation time points (Figure 5.5 C left). At the same time, the whole cell abundance of AGO2 remained relatively constant throughout the process (Figure 5.5 C right). These results confirm that the majority of AGO2 population in differentiating mouse myoblasts is contained to the nucleus. The analysis was also performed using same volume loading strategy and resulted in the same expression pattern (data not shown).

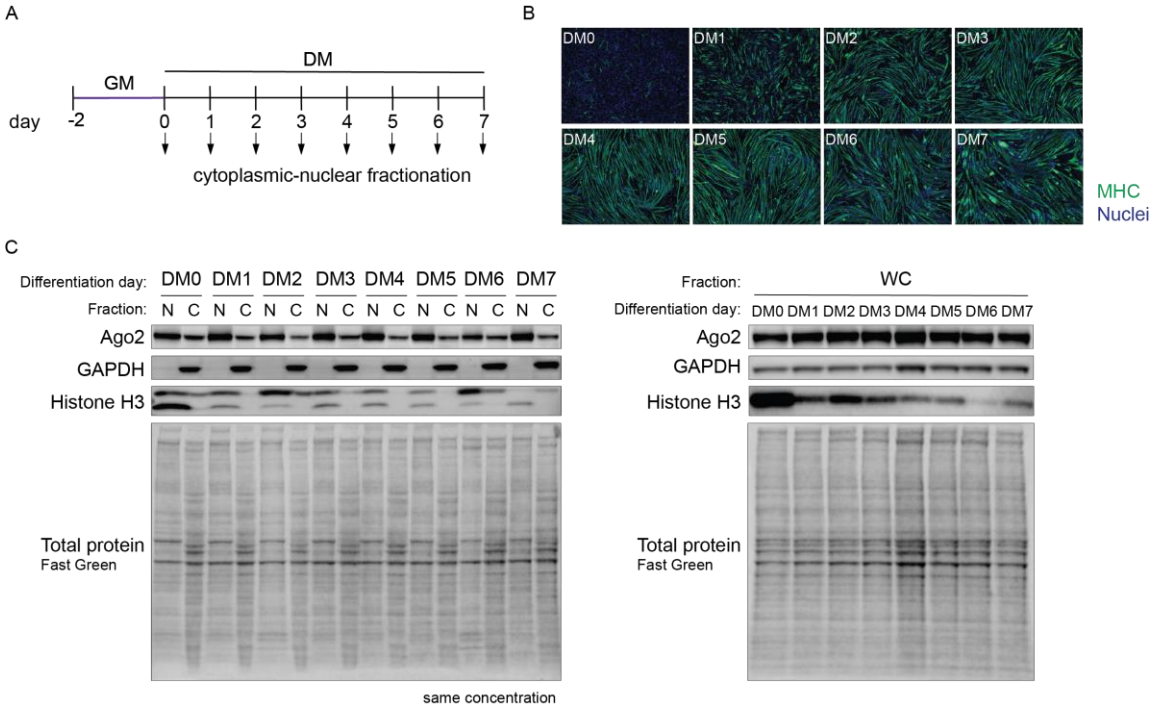

Figure 5.5 Analysis of AGO2 expression in nucleus and cytoplasm of differentiating C2C12 mouse myoblasts.

(**A**) Experiment timeline. C2C12 were seeded in growth medium (GM) and switched to differentiation medium (DM) 2 days after. Cells were maintained in DM for further 7 days. Subcellular fractionation was performed in 24 hr intervals. (**B**) Myosin heavy chain (MHC) as a confirmation of myotube formation during differentiation. (**C**) AGO2 western blot. Strong signal of AGO2 protein was detected in nuclear fractions at all differentiation timepoints. GAPDH and Histone H3 protein are showed as fractionation confirmation. The same concentration of proteins from each fraction was loaded for all timepoints. Fast Green stain shows total amount of protein loaded.

5.3.5 Development of inducible tagged-AGO2 mouse muscle cell line

Current studies suggest that nuclear AGO2-miRNA can act through several mechanisms, which largely depend on the identity of target molecules. To facilitate the identification of nuclear AGO2-myomiRs targets during muscle differentiation a doxycycline-inducible expression system for tagged AGO2 was generated using C2C12 mouse myoblasts. The sequence of mouse AGO2 cDNA was fused with a triple-FLAG (3×FLAG) and a poly-Histidine (8×His) tag and cloned into a PiggyBac transposon vector [539]. The tagged-AGO2 was placed under control of the doxycycline-inducible, *trans*-regulatory element (TRE) Tight promoter in the puromycin-resistant vector (Figure 5.6 A). In the absence of doxycycline, reverse transcriptional activator (rtTA) does not bind the TRE Tight located upstream of transgene sequence (i.e. AGO2) (Figure 5.6 B). The presence of doxycycline induces a conformational change in rtTA factor allowing it to efficiently bind the TRE element facilitating recruitment of RNA polymerase and thus controlling the gene expression activation (Figure 5.6C) [543].

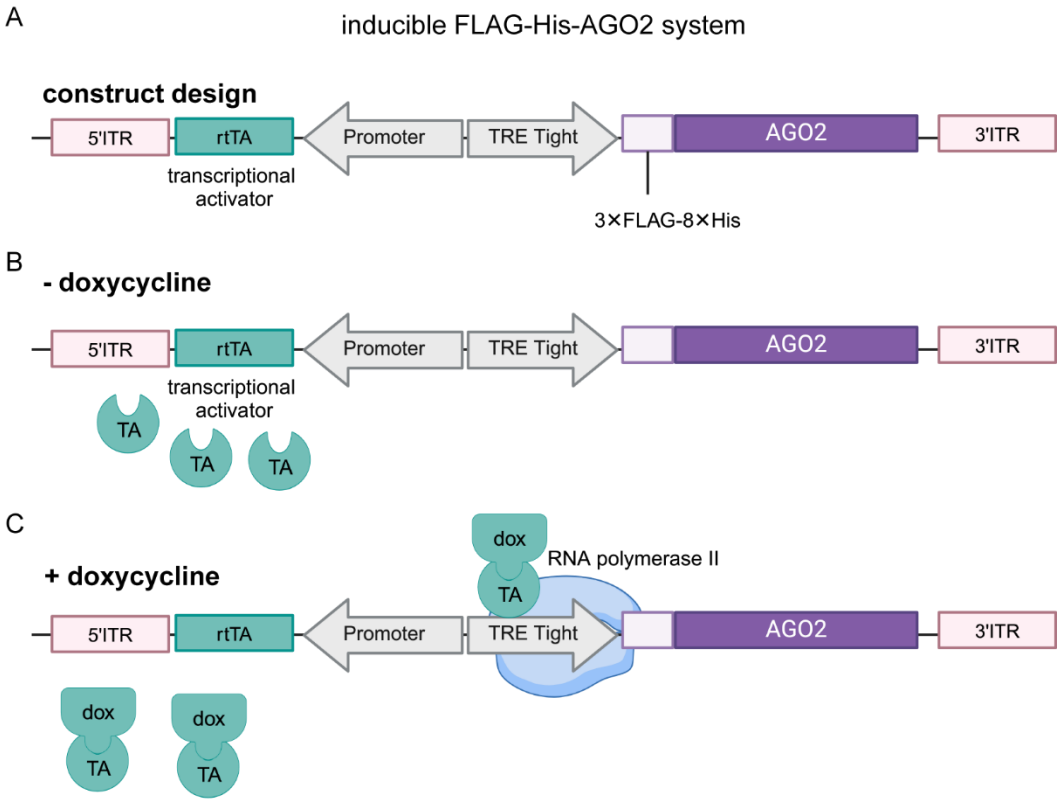

Figure 5.6 Schematic design of inducible tagged-AGO2 system used in this study.

(**A**) AGO2 protein fused to triple FLAG and eight histidines was cloned into the Piggy Bac (PB) vector plasmid between the inverse terminal repeats (ITRs) under the TRE (*trans*-regulatory element) Tight promoter. (**B**) When doxycycline is lacking the reverse transcriptional activator (rtTA) does not bind to the TRE Tight promoter. (**C**) When present in the cell medium, doxycycline binds the rtTA and induces conformational changes in the activator, allowing for binding to TRE Tight promoter and effective recruitment of RNA polymerase II complex for transcription initiation of the tagged AGO2 protein.

C2C12 cells were nucleofected with the tagged-AGO2 plasmid and placed under puromycin selective pressure for 2 weeks. The myogenic differentiation capability of C2C12 stably expressing 3×FLAG-8×His-AGO2 was confirmed with immunofluorescence staining for MHC (Figure 5.7 A). Cells were treated with five different doses (5, 10, 25, 50 ng/ml) of doxycycline to induce expression of tagged AGO2 protein. Western blot analysis demonstrated a dose-dependent induction of FLAG expression and an increase in AGO2 protein amounts (Figure 5.7 B). These data confirm the generation of a novel 3×FLAG-8×His-AGO2 inducible mouse myoblast cell line. This cell line will be used as a tool investigating nuclear miRNA targets using the cross-linking and sequencing of hybrids (CLASH) method [544].

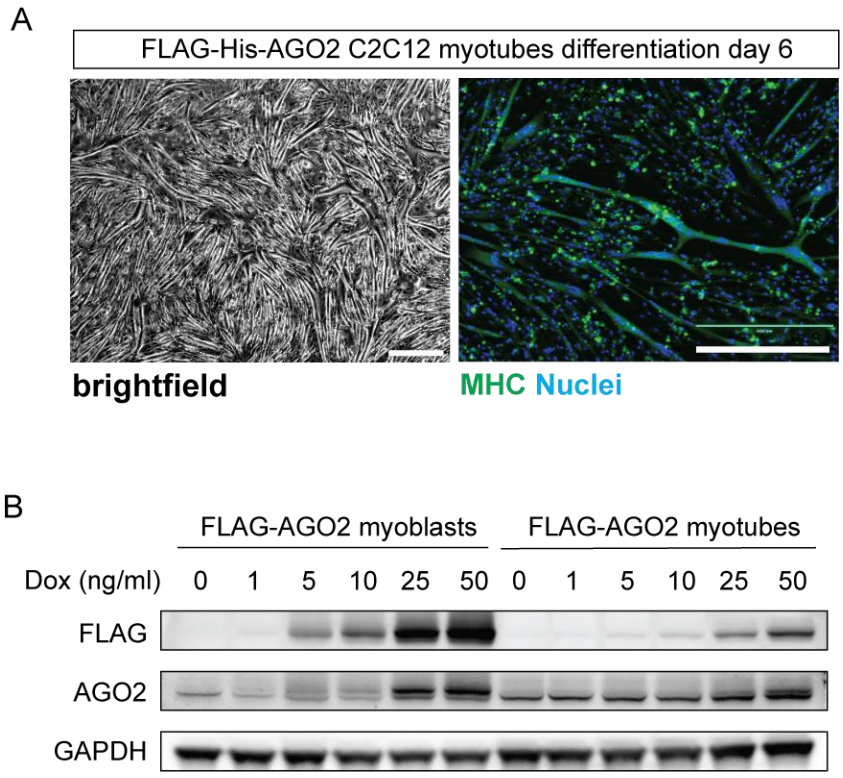

Figure 5.7 Induction of tagged-AGO2 expression in stable C2C12 cell line.

(**A**) Confirmation of 3×FLAG-8×His-AGO2 C2C12 differentiation into myotubes. Clear, multinucleated cells expressing MHC differentiation marker (right) are visible 6 days after induction of differentiation. Scale bar represents 400 µm. (**B**) Western blot analysis of FLAG and AGO2 protein levels upon induction with six different doses of doxycycline. FLAG and AGO2 protein localised to a band of similar molecular weight.

5.4 Discussion

New insights into miRNA functions, extend beyond their canonical roles in cytoplasmic post-transcriptional gene silencing. A variety of studies have established that miRNA interactions are not limited to 3' UTR regions, and target sites have been identified in 5' UTRs, coding sequences and introns of mRNA [502,532,545,546]. Moreover, the observed formation of miRNA-DNA triplexes confirms that miRNA can directly bind to the chromatin [547]. In fact, millions of potential miRNA target sites have been identified within human promoter regions [548,549] and promoter binding was proposed as a key mechanism of miRNA-mediated transcriptional gene regulation [501,512,519,550,551]. Additionally, miRNAs have been demonstrated to interact with protein partners other than AGO, expanding their roles beyond classical RNAi [552]. Therefore, the scope of miRNA functions is likely much broader than currently assumed and not limited to the single cellular compartment. Indeed, a wide range of miRNA functions is proposed in the nucleus (Table 5.1) and mitochondria [505].

This chapter explores the nuclear localisation of muscle-specific myomiRs during the *in vitro* myogenic differentiation. MyomiRs localise to the nucleus of human and murine muscle cells *in vitro* (Figure 5.1, Figure 5.2, Figure 5.3). Their upregulation occurs in both cytoplasmic and nuclear compartment during differentiation, as observed in mouse C2C12 cells (Figure 5.1) and human myoblasts (Figure 5.2). In differentiated mouse myotubes myomiRs as well as AGO2 reside primarily in the soluble nucleoplasm fraction (Figure 5.3), suggesting they are not bound to DNA. Exogenous, biotinylated miR-133 and miR-206 mimics are readily transported to the nucleus during differentiation (Figure 5.4). Moreover, exogenous miR-133 binds AGO2 (Figure 5.4) in both subcellular compartments, highlighting the potential of RISC-mediated gene regulation in the nucleus. This finding is further supported by high levels of nuclear AGO2 throughout the C2C12 differentiation, suggesting a previously unknown aspect of myogenesis regulation.

Additionally, to facilitate further investigations of nuclear myomiRs target in the context of myogenic differentiation, a novel, stable mouse myoblast cell line expressing inducible 3×FLAG-8×His-tagged-AGO2 protein was generated (Figure 5.6). Introduction of a tag and overexpression of AGO2 protein did not affect the cell myogenic potential as observed through efficient myotube formation (Figure 5.7). A clear induction of tagged protein was achieved at undifferentiated and differentiated stages, confirming successful establishment of this novel cell line.

5.4.1 MyomiRs localise to the nucleus of differentiating myoblasts

Comprehensive research efforts have established critical roles of muscle-specific myomiRs in myogenic differentiation [368]. As shown here, these are significantly upregulated during myotube formation *in vitro* for both human and mouse muscle cells (Figure 5.1, Figure 5.2, Figure 5.3). Notably, the results presented in this thesis provide an insight into the previously under-appreciated subcellular distribution of myomiRs. Unpublished data from our group showed that myomiR upregulation during differentiation of mouse C2C12 cells primarily occurs in the nuclear compartment (Figure 5.1). Similarly, in differentiating human myoblasts, myomiRs were increased in both the nucleus and cytoplasm (Figure 5.2). This is suggestive of conserved of myomiR nuclear enrichment mechanisms between species, implying its potential significance in the differentiation process.

This study shows, for the first time, the nuclear localisation of myomiRs in human myoblasts (Figure 5.2). Previously, myomiRs have been identified in other cell lines by two independent studies. Politz *et al*. showed an increase of miR-206 levels in the nucleus and cytoplasm of differentiating rat L6 myocytes [525]. Mauro *et al*. demonstrated that upon inactivation of the Wnt signalling pathway, miR-133 shuttles to the nucleus of cardiac myocytes where it represses transcription of the *Dnmt3b* gene [519]. Notably, the Wnt pathway plays a crucial role as a positive regulator of adult muscle stem cells self-renewal

[323] whereas the *Dnmt3b* knock-out was shown to have the opposite effects [553]. Therefore, translocation of miR-133 to the nucleus of differentiating myoblasts could potentially trigger their switch from proliferation to differentiation programme. Especially given that *Dnmt3b* knock-down was shown to inhibit proliferation and trigger differentiation of rhabdomyosarcoma cells [554]. However, such a scenario warrants further investigation and experimental confirmation.

5.4.2 Sub-nuclear localisation of myomiRs

Since the nucleus is functionally compartmentalised, the specific subnuclear localisation of myomiRs could provide further insight into their potential functions. In differentiated mouse myoblasts, all investigated myomiRs primarily occupied the nucleoplasm (Figure 5.3 C). Notably, AGO2 protein mirrored this distribution, implying the incorporation of nucleoplasmic myomiRs into active RISC complexes (Figure 5.3 B). This aligns with previous reports of AGO2 primary localisation in the nucleoplasm of mammalian embryonic stem cells, and RNAi activity in the nucleoplasm of HeLa cells [498,532]. Despite the robust fractionation of the nucleus as confirmed by RT-qPCR and western blot (Figure 5.3 A, B), neither myomiRs nor AGO2 were found to localise to chromatin fraction. Contrary to the existing studies demonstrating the role of AGO2-miRNAs in transcriptional regulation by binding to the promoter regions [502,509,511,512,521,533,550,551,555], myomiR nuclear functions are more likely to act through interaction with nucleoplasmic targets. The array of these targets is vast and not limited to small nuclear RNAs (snRNA), pri-miRNAs, mRNAs, and long non-coding RNAs (lncRNA). Indeed, targeting of snRNA and pri-miRNA by nuclear miRNA has been demonstrated previously [516,518].

While a previous study identified miR-206 in the nucleoplasm of rat muscle cells, the authors specifically focused on its concentration in the nucleolus [525]. Notably, various other miRNAs have been localised to that structure [528]. As the centre of ribosome biogenesis, the nucleolus is enriched for ribosomal RNA (rRNA). Many putative miRNA binding sites within rRNAs have been identified and miRNA-mediated interaction of AGO2

with rRNA has been reported previously [528]. The subnuclear fractionation method used in this chapter, does not distinguish between the nucleoplasm and nucleolus [537]. As such, nucleoplasm likely contains multiple nucleolus-specific myomiRs. Nevertheless, the interplay between miRNAs and ribosomal biogenesis machinery remains elusive and is probably not exclusive to myogenic differentiation. Such interaction could rather represent additional layer of miRNA involvement in cellular homeostasis through global protein synthesis regulation.

5.4.3 Nuclear myomiRs in differentiation

The crucial role of miRNAs in development is manifested by embryonic lethality of mice lacking miRNA processing (Dicer mutants) and loading (AGO2 mutants) machinery [556,557]. Notably, mice without Dicer activity in muscle, suffer extensive muscle mass loss and die perinatally, suggesting the essential contribution of miRNA to myogenic development [558].

Previously, a study by Sarshad *et al*. demonstrated that nuclear enrichment of AGO2 protein is characteristic of differentiation-competent cells and that high levels of nuclear AGO2-miRNAs complexes can alone induce embryonic stem cells differentiation [532]. Accordingly, nuclear enrichment of AGO2 in the nucleus of C2C12 and human primary myoblasts was shown [532]. Similarly, a robust nuclear translocation of AGO2 and miR-9 was identified in mouse neuronal stem cells [526]. Notably, Sarshad *et al*. showed that, during a short 2-day C2C12 differentiation protocol, AGO2 increases mainly in the nucleus, mirroring the nuclear upregulation of myomiRs previously identified by our group in the same cell line (Figure 5.1) [532]. In contrast, several papers noted equal subcellular distribution of AGO2 in HEK293, neuroblastoma, embryonic carcinoma, healthy and cancerous epithelial cells as well as fibroblasts [498,527,532]. All studies showed [498,526,527,532] or assumed [527] that nuclear AGO2 proteins are bound to miRNA.

Limited evidence suggests that miRNAs and AGO2 protein change their localisation in specific cellular or environmental contexts. For example, retinoic acid-induced

granulopoiesis and doxorubicin-induced senescence trigger the nuclear import of miR-223 and *let*-7-AGO2 respectively [533,551]. Once in the nucleus, these molecules were shown to regulate processes that prompted their relocation [533,551]. Moreover, miRNA-320-AGO2 was increased mainly in the nucleus of obese mouse cardiomyocytes, but not in wild-type cells [521]. Similarly, nuclear miR-9 was found only in quiescent and not proliferating neuronal stem cells [526].

Together with data presented in this chapter, this suggests a possible scenario where the differentiation stimuli trigger myomiRs and AGO2 protein upregulation and their enhanced translocation to the nucleus, where they can regulate the differentiation process itself. Notably, it has been suggested, that AGO2 proteins constantly shuttle between cytoplasm and nucleus, rather than remain at a steady state [559]. Thus, serum withdrawal as in the case of *in vitro* muscle differentiation, and other factors may influence that process towards enhanced nuclear import, fine-tuning the myogenesis regulation.

The restrictive focus of current miRNA target prediction tools on mRNAs limits the experimental validation of potential targets. Since the exact role of nuclear myomiRs in differentiation control highly depends on the nature of their targets, their identification will allow to describe a more generalised mechanism of nuclear myomiRs role.

5.4.4 Nuclear-cytoplasmic transport of myomiRs

Exogenous, biotinylated miR-133 and miR-206 transfected into differentiating C2C12 myoblasts show were found to localise to both cytoplasmic and nuclear subcellular compartments (Figure 5.4 B, C). Additionally, precipitation of miR-133 mimics eluted significant amount of AGO2 protein fractions (Figure 5.4 D). These findings suggest the presence of efficient cytoplasmic-nuclear shuttling mechanism for miRNAs and AGO2 proteins. The current understanding of that process is that miRNAs are first loaded into RISC in the cytoplasm and the mature complex is subsequently shuttled to the nucleus

[358,359,497,498,513–515,522,526]. It has been demonstrated that this mechanism is target-independent and relies on AGO2-miRNA interaction as unloaded AGO2 and miRNAs are unstable and quickly degraded [348,359,495].

Importin 8 (IPO8) has been suggested to mediate the process of miRNA cytoplasmic nuclear translocation [560]. IPO8 knockdown was shown to specifically block the nuclear import of miR-709 in mouse fibroblasts [560]. Importantly, Di Mauro *et al*. showed, that miR-133a shuttling to the nucleus of cardiac cells is dependent on the IPO8 route [519]. However, alternative scenarios cannot be excluded. Active miR-9 shuttling, dependent on TNRC6A protein, which is a component of RISC, was shown *in vivo* in the zebrafish model [526]. Additionally, miR-126-5p was shown to shuttle to the nucleus via AGO2 interaction with Mex3a [517]. Moreover, some studies have proposed small-RNA independent roles for Ago2 in the nucleus [530]. Therefore, it is possible that several independent routes of nuclear miRNA import exist. Some of those might be actively regulated, responding to external and internal cues, and thus increasing the nuclear presence of miRNA in specific environmental contexts.

Many proteins rely on short peptide motifs (nuclear localisation signals, NLS) for their efficient transport to the nucleus [561]. Some studies attempted to find a corresponding RNA sequence that could prompt the nuclear localisation of miRNA [497,562]. It has been reported that the nuclear localisation of miR-29b strongly relies on the specific AGUGUU motif at its 3' end [562]. In contrast co-transcribed miR-29a which lacks this sequence is primarily cytoplasmic [562]. Incorporation of the AGUGUU sequence into siRNA was sufficient to induce its nuclear import. As such, identified hexanucleotide motif was defined as a miRNA nuclear localisation signal [562]. At the same time, deep sequencing of small RNAs in the nucleus, revealed that there’s no conserved or common motif between nuclear miRNAs [497].

5.4.5 Defining the function of nuclear myomiRs

It can be speculated, that upregulation of myomiRs in the nuclear compartment during differentiation is suggestive of important regulatory mechanisms that are distinct from the canonical functions of the miRNAs. Although myomiRs targets during myogenesis are well-established, and more are being experimentally validated, extrapolating available data to their nuclear function is challenging. In theory, any of the abovementioned mechanisms of nuclear miRNA action are plausible. Target prediction tools delineated thousands of putative miR-206 and miR-133a binding sites within 5' UTR, coding-sequences, long non-coding RNAs and more (unpublished results). However, the specific subcellular distribution of these targets is hard to predict, especially for abundant RIKEN transcripts targets which represent currently unannotated RNAs of unknown function [563]. As such, to define specific nuclear myomiRs targets, precise experimental methodology and less restrictive target prediction tools must be applied. Several methods to detect miRNA-bound targets have been established [544,546,564]. One of them involves sequencing of miRNA-mRNA complexes captured by streptavidin pull-down of biotinylated miRNA [564]. The sequencing of miR-133a and miR-206-bound RNA eluted from cytoplasmic and nuclear fractions in this study failed due to a high level of non-specific signal (Figure 5.4). As such, other methods need to be applied. The tagged-AGO2 C2C12 cell line was designed to facilitate a robust purification of AGO2-miRNA complexes as a part of cross-linking and sequencing of hybrids method (CLASH) [544]. CLASH allows for an unambiguous detection of miRNA-bound targets by employing an important RNA-RNA ligation step which forms hybrids composed of miRNA and its direct target [544]. These hybrids are then sequenced, facilitating the precise definition of direct miRNA targets. This and other confirmatory experiments (i.e., RT-qPCR, *in vitro* functional assays) will determine the mechanisms of nuclear myomiRs interaction. However, results presented in this chapter, as well as a well-defined role in muscle allows to assume that nuclear myomiRs impact myogenic differentiation pathways.

5.4.6 Conclusions

Results presented in this chapter demonstrate a previously unappreciated distribution of muscle-specific myomiRs during myogenic differentiation *in vitro*. I showed that regulation of myotube formation by myomiRs does not occur only in the cytoplasmic compartment via a well-established post-transcriptional gene silencing mechanism. The regulatory mechanisms are rather concentrated in the nucleus, where the majority of myomiR upregulation happens as myoblasts fuse to each other. Additionally, I showed, that nuclear myomiRs are incorporated into the effector RISC complex by binding to AGO2, further strengthening the validity of their nuclear roles. Accordingly, an established tagged-AGO2 cell line will facilitate further experimental work focused on elucidating myomiR targets during myogenic differentiation. These results are of key significance to the miRNA and muscle biology field as they demonstrate that alternative functions and distribution of miRNA need to be considered when investigating the regulation of key cellular processes, and especially myogenesis.

6 Discussion and conclusions

6.1 Spatial biology of dystrophin and DMD therapeutic approaches

A plethora of DMD therapeutic approaches are currently under development, with four ASOs and one gene therapy approved in the USA [6]. The efficiency of the ASO drugs is considered to be relatively poor, with a maximum of 5.9% of healthy dystrophin levels restored after repeated, weekly dosing for around 6 months (as in the case of Viltolarsen) [10,198]. Several other ASO-based drugs are currently in development including peptide-conjugated PMOs by Sarepta (SRP-5051 Vesleteplirsen), PepGen (PGN-EDO51) and Entrada (ENTR-601-44) [6]. The interim phase 2 data of SRP-5051 trial revealed mean 11% of exon skipping and 5.7% of dystrophin expression after 7 monthly doses [565]. In the PepGen trial, a single PGN-EDO51 dose resulted in 2% of exon skipping in healthy volunteers [566]. Efficacy details for ENTR-601-44 are currently undisclosed. Moreover, Dyne Therapeutics and Avidity Biosciences are currently conducting clinical trials (DYNE-251 NCT05524883 and AOC 1044, NCT05670730) of PMO ASOs conjugated to transferrin receptor 1 (Trf1) Fab fragments and antibodies, respectively [6]. Both studies are currently in phase 1, and the interim results revealed modest induction of exon skipping reaching only 1.5% (AOC 1044, in healthy volunteers, single dose) and 0.8% (DYNE-251, in DMD patients, 6 monthly injections) [567,568]. Notably, in an ongoing trial of PN-ASO designed to skip exon 51 (Wave Life Sciences, WVE-N531, NCT04906460), investigators reported an impressive 53% of exon skipping in DMD patients after 3 biweekly doses [207]. Nevertheless, these levels of RNA correction are contrasted with a very low levels of detected dystrophin protein at 0.27% (mean) [207]. Importantly, this result illustrates an important discrepancy between mRNA and protein levels observed in other ASO DMD clinical trials [10]. For example, Viltolarsen induced an 43.9% increase in exon-skipping which resulted only in production of 5.9% of the wild-type dystrophin levels [10]. However, it is important to note that such inconsistences between levels of corrected transcripts and dystrophin protein can stem from the differences in assay design. As such, although the

majority of these trials are not concluded (and/or in early phases), the available results allow to speculate that the efficacy of investigated compounds may not differ substantially from the currently approved ASOs. Notably, recently approved Delandistrogene moxeparvovec gene replacement therapy restored almost 40% of dystrophin protein levels in patients (assessed by western blot) [569]. Notably, in a parallel micro-dystrophin study sponsored by Genethon, investigators observed up to 85% of dystrophin positive myofibres by immunofluorescence [570]. However, the gene replacement approach is likely to result in diminished pseudo-dystrophin production with time due to vector genome loss, epigenetic silencing of the transgene, and the dilution effect of non-transduced nuclei as a consequence of muscle growth and repair. Notably, repeat administration with AAV is currently not possible as the patient is effectively immunised to the treatment after the first dose [569]. Moreover, AAV poses a substantial safety risk with some clinical trials previously reporting fatal immune adverse effects using high doses of the viral vectors [223]. As such, the search for efficacious and safe DMD therapeutics is far from over, with ASOs, gene therapy, utrophin upregulation, and CRISPR-Cas9 all showing high promise. While most of these strategies mimic dystrophin protein (gene replacement) and target dystrophin mRNA (ASOs) or gene (CRISPR-Cas9) numerous aspects of dystrophin biology remain underexplored. For example, while the protein structure is well-established, relatively little is known about the specific mechanisms governing correct dystrophin localisation to the sarcolemma.

Although clearly pointed out by early cell therapy studies, the aspect of spatial restriction of dystrophin has only recently received more attention. CRISPR-Cas9 is the only approach that could correct the underlying DNA mutation in patients effectively providing a cure for DMD. Such approaches have been shown to be efficacious in DMD mouse and dog models with some studies reporting restoration of 90% of wild-type dystrophin levels [241–247]. However, none of the proof-of-concept CRISPR-Cas9 studies focused on the re-expressed dystrophin localisation pattern. In fact, only in the past two years, research

from our group and others showed that, similar to cell therapy, CRISPR-Cas9-treatment results in patchy dystrophin expression at the sarcolemma [251,405,420]. Similarly, other investigated therapeutic approaches (i.e. gene therapy, ASO-mediated exon skipping) rarely consider dystrophin restoration pattern as therapeutic efficacy factor. While results presented in Chapter II of this thesis show that ASO-mediated exon skipping results in uniform dystrophin expression gene replacement effects on dystrophin distribution are currently unknown [320,321,405]. However, assuming that the challenges of safety, production, and delivery of sufficient AAV vector genomes can be overcome, it remains to be demonstrated if the AAV genome, and therefore micro-dystrophin expression, are uniformly distributed throughout the myofibre [218,288,569]. It can be speculated, that the AAV vectors will not uniformly transduce the entire length of the myofibre and thus the micro-dystrophin transgene will be expressed from a subset of myonuclei. However, since the produced pseudo-dystrophin is of significantly smaller size than full-length protein, it is possible that its diffusion throughout the cell could be more efficient.

Our group and others have highlighted the importance of within-fibre dystrophin distribution when considered dystrophin restoration strategies [239,487]. Results presented in the Chapter I of this thesis, demonstrate that patchy dystrophin can effectively limit muscle turnover and restore levels of dystrophic biomarkers towards wild type as long as it is expressed at relatively high levels. This is also supported, by previous work in *mdx-Xist*$^{\Delta hs}$ and *mdx/utrn* $^{-/-}$*/ Xist*$^{\Delta hs}$ animals which reported dystrophin level-dependent benefits, even when expressed in a patchy manner [407,410]. Perhaps the most convincing result comes from improved survival dKO animals expressing dystrophin in a patchy manner [410]. Specifically, while dKO animal lifespan is usually around 12 weeks of age, expression of patchy dystrophin at > 4% of wild type levels resulted in increased animal survival up to 43 weeks with mild to moderate disease symptoms [410]. Notably, we have previously shown that re-expression of patchy dystrophin at 5.7% of wild type levels upon CRISPR-Cas9-mediated gene editing, did not prolong the survival of dKO mice [251]. At the same time,

one *mdx/utrn* $^{-/-}$/ *Xist*$^{\Delta hs}$ expressing 27% of dystrophin survived until 24.5 months (wild-type mouse lifespan) with moderate dystrophic changes observed in these animals [410]. These findings suggest that a greater extent of dystrophin coverage on the sarcolemma is more effective in mitigating the dystrophic phenotype. This implies that achieving similar clinical benefits might be possible with lower levels dystrophin, as long as its distribution is uniform. We have recently demonstrated such an effect in a study where dKO animals were treated with exon-skipping PN-ASOs [206]. In this study, PN-ASO-mediated exon 23 skipping in dKO animals resulting in 12% rescue of dystrophin protein in gastrocnemius muscle not only increased mouse survival beyond 9 months when study was terminated, but also significantly improved muscle specific force and restored serum myomiRs and CK towards wild-type levels [206]. Nevertheless, direct comparisons between different studies are challenging due to different technical details of analysis (i.e. dystrophin quantification based on standard versus capillary western blot system) [206,410].

Notably, low levels of uniform dystrophin are difficult to model unless treatment (e.g. ASO-mediated exon skipping) is included. Moreover, it is unclear how low abundance, but homogenous dystrophin localisation is achieved at the sarcolemma. This in turn, leads back to the fact that not much is known about regulation of dystrophin gene expression and protein localisation. Indeed, the literature on translational regulation of dystrophin is limited [481,571,572]. Similarly, models of dystrophin transcription have emerged only recently and require further experimental validation [573].

Given the importance of dystrophin function its transcript and protein levels are relatively scarce comprising 0.01–0.001% of total skeletal muscle RNA and 0.002% of total protein [574,575]. Recent studies have reported that due to the large size of the *Dmd* gene, the majority of detected dystrophin transcript is nascent, while the overall *Dmd* transcript is imbalanced with 5' portion of the gene detected at higher levels than the 3' end [430,573,576]. Notably, results of this thesis add to the literature describing dystrophin transcript dynamics and its changes in dystrophic conditions (Figure 3.11). Specifically, the

observed reduction of dystrophin mRNA in the cytoplasm of *mdx52* and *mdx52-Xist*$^{\Delta hs}$ myofibres agree with data from *in vitro* DMD patient cells and muscle biopsies [577]. Moreover, the observation of reduced nuclear transcripts observed in *mdx52-Xist*$^{\Delta hs}$ animals supports the notion that dystrophin transcription is initiated less frequently in *mdx* mice in comparison to wild-type animals [430,573]

Another key finding of this thesis is the translational repression of dystrophin within centrally nucleated regions of segmented *mdx52-Xist*$^{\Delta hs}$ myofibres. As mentioned above, regulation of dystrophin translation is currently not well understood. However, it has been shown before that reporter constructs downstream of the dystrophin 5' UTR are translated with low efficiency in both C2C12 myoblasts and myotubes [571]. This was partly due to suboptimal Kozak sequence which facilitates correct ribosome assembly and recognition of translation start codon [571]. Dystrophin transcript abundance was shown to be regulated by highly conserved dystrophin 3' UTR region which common to all isoforms (with the exception of Dp40), through largely unknown mechanisms [571]. Different *trans*-acting factors could potentially regulate dystrophin expression through interaction with the 3' UTR (e.g. RNA-binding proteins, lncRNAs), however, miRNAs are one of the most likely candidates. The *Dmd* 3' UTR contains binding sites for multiple miRNAs, including miR-31, miR-146b, miR-374, and miR-233 [108,382,481]. A study by Fiorillo *et al.* demonstrated that miR-146b/-374/-31 inhibit dystrophin expression *in vivo* via intramuscular injection of the miRNA mimic mix to notexin-injured TA of healthy mouse [572]. Moreover, miR-146a and miR-223 were shown to be inflammation associated, as their expression is induced by pro-inflammatory NF-κB pathway in a myositis mouse model, whereby they also downregulate dystrophin expression [578]. A study by Cacchiarelli *et al.* demonstrated that miR-31 reduces expression of dystrophin reporter construct, while inhibition of miR-31 enhances exon skipping efficacy *in vitro* [481]. Similarly, miR-146a, miR-374, miR-223 miR-328, and miR-320a were shown to correlate with dystrophin levels restored by PMO-mediated exon-skipping [572]. Therefore, local inhibition of dystrophin translation mediated by miRNAs is

one plausible explanation for the deficiency in dystrophin translation observed in the centrally nucleated regions of *mdx52-Xist*$^{\Delta hs}$ myofibres. Notably, miR-31 was shown to be highly upregulated in dystrophic mouse muscle ~ 100-fold relative to the healthy control [108,382]. I propose that miR-31 is upregulated in CNF regions where it represses dystrophin translation, and thus may affect the outcome of dystrophin restoration strategies.

It would be important to determine whether such *trans*-acting factors exhibit similar patterns of spatial restriction that may provide a mechanistic explanation for these findings. Targeted RNA FISH or spatially resolved imaging and sequencing are required to test these hypotheses. Alternatively, it is plausible that dystrophin translation is only initiated when myonucleus and dystrophin mRNA reach the cell periphery. Notably, puromycin labelling in single isolated myofibres revealed that while active sites of protein translation are localised throughout the myofibre, they are highly concentrated at the myofibre surface [302]. It is possible, that extensive translation of sarcomeric proteins inside the core of myofibre (e.g., titin or actin), limits the availability of ribosomes to produce other proteins in that region. Indeed, given the size of dystrophin and its site of action, it could be reasoned that production of the protein in the myofibre centre and its subsequent transport through the dense myofibrils network would be energetically unfavourable. Instead, local translation of mRNA might be much more efficient. However, a lack of dystrophin in segmented myofibres containing both centrally and peripherally localised nuclei argues against localised translation (Figure 3.31, Figure 3.32). Similarly, the presence of dystrophin in centrally nucleated regions of injured wild-type muscle (Richard Piercy, personal communication) and CNMs muscle suggests that the observed translational repression might be specific to dystrophic conditions. Nevertheless, further studies in single isolated myofibres are needed to elucidate the control of dystrophin translation within centrally nucleated regions. For example, chemical injury of the healthy muscle (e.g., cardiotoxin injury) could provide more information regarding discussed mechanisms.

The absence of dystrophin protein expression specifically in centrally nucleated myofibre regions has not been reported previously (to the best of my knowledge). Notably, the *mdx52-Xist*$^{\Delta hs}$ (and *mdx-Xist*$^{\Delta hs}$) mouse model, uniquely allows for the tracking of dystrophin expression dynamics. It distinctively leverages the dystrophic pathology features (i.e. myofibre degeneration and regeneration, upregulation of dystrophic serum biomarkers) with variable expression levels of full-length dystrophin protein from a subset of nuclei. This contrasts with fully dystrophin-positive muscle of healthy animals lacking signs of pathology and dystrophin-null *mdx* mice. Notably, analysis of treated *mdx* animals, would not provide the same insight as the lack of dystrophin in this setting might be attributed to inefficient correction rather than translational repression mechanism. Nevertheless, a notable limitation of the model is the fact, that only female *mdx52-Xist*$^{\Delta hs}$ are characterised by patchy dystrophin expression. Since DMD is an X-linked disorder, male animals are most commonly used in pre-clinical research. Differential hormonal homeostasis in male and female models could therefore be contributing to variabilities in muscle physiology.

6.2 Diverse roles of myomiRs

Results of Chapter III reveal another novel phenomenon relevant to spatial organisation of the muscle. Specifically, the well-established phenomenon of myomiR upregulation during myogenic differentiation was found to occur predominantly in the nucleus, with the majority of cellular AGO2-bound myomiRs localising to the nucleoplasm. While myomiRs have been widely researched, their nuclear localisation has not been reported before in the context of myogenic differentiation. This finding is especially significant, as it suggests additional roles for myomiRs in muscle, beyond the canonical dogma of cytoplasmic post-transcriptional gene regulation. Future studies aim to elucidate those functions in detail, utilising a C2C12 cell line expressing inducible, tagged AGO2 protein that I have generated and validated (Figure 5.7). From a DMD therapeutics perspective, an interesting aspect of nuclear miRNA function is the observation that small

interfering RNAs (siRNAs) can act as splicing regulators. Previously, Liu *et al.* showed that AGO2-bound exogenous siRNAs can alter splicing of *SMN2* and dystrophin pre-mRNAs [360]. By targeting exon 51 in DMD patient's fibroblasts containing 45-50 deletions, they were able to restore the dystrophin ORF, resulting in production of truncated but functional protein [360]. Currently, miRNA target prediction is usually limited to mature mRNAs. However, to further investigate if endogenous molecules can act in the same way, miRNA target prediction tools, should expand to dystrophin pre-mRNA sequences, especially around splice sites of commonly affected exons.

In addition to direct regulatory roles for myomiRs, results of Chapter I and II show, that these molecules have potential utility as pharmacodynamic serum biomarkers of dystrophin restoration levels, further supporting our previous observations, and those of others [107,206,321]. Pharmacodynamic biomarkers, in principle, demonstrate that the therapeutic has reached its targets and produced a desired effect [374]. Currently, target engagement of dystrophin restoration therapeutics is tested mainly through western blot-based quantification of dystrophin protein in DMD trials [484]. While in general the western blot-based dystrophin quantification protocol is well established, it does not facilitate a robust comparison of dystrophin quantities between different trials [486]. Specifically, the use of different control samples within various laboratories can significantly skew the quantification, further compromising efficient comparison of different therapeutic approaches [484]. It has recently been noted that while dystrophin was considered previously completely absent in DMD biopsies, it is now clear that most DMD patients produce very low levels of the protein (i.e. revertant fibres and dystrophin traces) [145,149,150]. This further complicates correct selection of controls and underscores the need for measuring changes in dystrophin expression relative to a pre-treatment baseline [484,486]. Additionally, patient muscle biopsies necessarily represent a very limited fraction of the whole musculature. As such, results obtained from these samples are not representative of the systemic changes which can significantly skew the interpretation.

Conversely, correlation of extracellular myomiRs presented in chapter I and II, shows, that they can reliably reflect the approximate level of dystrophin expression in skeletal muscle regardless of dystrophin expression pattern. Although further analyses using other muscle types (i.e. diaphragm or heart) should be included, myomiRs have the potential to provide an estimate of an overall dystrophin levels restored upon treatment. Moreover, there is a need for protocols for serum myomiR quantification to be standardised across different groups (i.e. using the small RNA TaqMan assay used in this study). As such, measurement of serum myomiRs could significantly support the evaluation of dystrophin restoration treatments.

6.3 Limitations of these studies

The limitations of studies included in this thesis are for the most part associated to the models utilised. Firstly, the *mdx* and *mdx52* mouse models do not recapitulate the disease progression observed in patients accurately. However, due to lack of better, readily available models, these animals are commonly used in the laboratory practice. Secondly, while *mdx52-Xist*$^{\Delta hs}$ is an excellent model to investigate effects of patchy dystrophin expression on muscle, it must be noted, that due to their genetics, these animals express certain levels of full-length dystrophin from birth. This is especially significant as proportion of satellite cells in these animals expresses functional dystrophin. Moreover, this is also the case in other studies utilising *mdx/utrn* $^{-/-}$*/ Xist*$^{\Delta hs}$ or *mdx-Xist*$^{\Delta hs}$ models [321,407–410,579]. In contrast, patchy restoration of dystrophin with CRISPR-Cas9 or cell therapy will introduce dystrophin positive myonuclear domains at certain stage of disease progression, without guaranteeing correction of satellite cell genome [244,458–460]. As such, although the comparison of myofibre morphology and molecular biology is justified between the two models, the regenerative response of CRISPR-Cas9 treated myofibres will largely depend on the ability to edit the satellite cells.

Additionally, while C2C12 myoblasts are widely used as *in vitro* models of muscle differentiation, they do not reflect the complexity of mature myofibre architecture upon differentiation [580–582]. Specifically, C2C12 grown on commonly used tissue culture dishes exhibit disorganised contractile proteins, with minimal formation of aligned sarcomeres and thus lack the characteristic muscle striation [581,583]. This random orientation reflects the pre-myofibril stage of myofibrillogenesis, and thus reiterates that C2C12 myotubes are immature relative to fully developed myofibres [280,287]. Accordingly, the signalling pathways observed in C2C12 cultures do not accurately reflect those of mature muscle [582]. Therefore, while useful in determining the regulatory mechanisms of early myogenic differentiation, C2C12 myotubes cannot be easily compared with mature myofibres. Notably, more mature sarcomeric structures *in vitro* can be achieved using tissue cultured dishes coated with micropatterned hydrogels that facilitate myoblast alignment which in turn leads to advanced myogenic maturation of cells [581,583]. This includes more robust organisation of sarcomeres, resulting in observable striated pattern, as well as enhanced expression of sarcomeric organisation proteins relative to C2C12 cultured on unpatterned hydrogels [583]. Additionally, more advanced technologies including 3D organoid-like cultures or scaffold-based platforms are in development and include establishment of advanced disease models from muscular dystrophy patient derived cells [584–586].

Additionally, while most muscle biology studies rely on transverse muscle sections, this orientation of muscle tissue restricts the comprehensiveness of analysis. Each mouse muscle fibre can be millimeters in length (as shown in Chapter I). At the same time, transverse section which are usually ~8-10 μm in thickness, represent an extremely limited portion of the entire sarcolemma which is the approximate length of a single myonucleus. As such, analysis of transverse muscle sections alone reduces the field of analysis to a very limited part of each myofibre. Notably, the patchy dystrophin pattern observed in *mdx52-Xist*$^{\Delta hs}$ is not as clear on transverse sections in comparison to sections in the longitudinal

orientation (Figure 3.4). As such, the reliance on transverse muscle sections in initial CRISPR-Cas9-mediated dystrophin restoration studies may partially explain the lack of reported patchy dystrophin restoration [241–247]. In fact, none of those studies reported data from longitudinal muscle sections [241–247]. Nevertheless, in several cases incomplete sarcolemma staining on some transverse muscle images could be observed [242,243,245]. However, it is important to note that some of the CRISPR-Cas9 studies demonstrated extremely high efficiencies of dystrophin restoration (reaching 100% of wild-type protein levels in certain studies), at which levels patchiness is likely undetected [241,246,247].

As presented in Chapter I, utilising single isolated myofibres can provides spatial information that cannot be obtained, or is ambiguous, when analysing tissue sections to the performed analyses. Specifically, systematic classification of different myofibres into distinct groups could not be performed in analysis of the whole tissue. Longitudinal muscle sections, while advantageous, present challenges in clearly distinguishing continuity of closely adjacent myofibres. Additionally, similarly to transverse orientation, variable plane of 8-10 μm sections between makes it difficult to assess the morphology of the whole myofibre that can reach up to 80-100 μm in thickness (based on my analyses). Nevertheless, it is important to note that while single myofibres provide a unique insight into myofibre morphology, the isolation procedure yields are variable and lead to loss of significant proportion of cells. For example, dissociating single myofibres from dystrophic tissue can be technically challenging.

6.4 Conclusions

In conclusion, the effects of patchy dystrophin distribution as a model of CRISPR-Cas9 restored pattern on muscle morphology and molecular biology were analysed in this thesis. The utilisation of a unique *mdx52-Xist*$^{\Delta hs}$ model, yielded additional findings with regards to impact of central nucleation on myofibre morphology and dystrophin expression. Patchy dystrophin expression was contrasted with uniformly distributed protein upon PPMO-mediated exon skipping treatment. Moreover, the utility of myomiRs as pharmacodynamic biomarkers of dystrophin restoration was demonstrated, regardless of the observed dystrophin expression pattern. Additionally, the upregulation of myomiRs during myogenic differentiation was shown to primarily occur in the nucleus, suggesting that their functions are also spatially restricted during muscle formation at the sub-cellular level. Together, these results demonstrate the complexities of the spatial organisation of gene expression within skeletal muscle and highlight the implications of myofibre architecture for dystrophin restoration strategies and studies of muscle regeneration.

7 References

1. Benarroch L, Bonne G, Rivier F, et al. (2023) The 2023 version of the gene table of neuromuscular disorders (nuclear genome). *Neuromuscular Disorders* 33: 76–117.

2. Ricci G, Torri F, Bianchi F, et al. (2022) Frailties and critical issues in neuromuscular diseases highlighted by SARS-CoV-2 pandemic: how many patients are still “invisible”? *Acta Myologica* 41: 24.

3. Mercuri E, Bönnemann CG, Muntoni F (2019) Muscular dystrophies. *The Lancet* 394: 2025–2038.

4. Dowling JJ, Weihl CC, Spencer MJ (2021) Molecular and Cellular Basis of Genetically Inherited Skeletal Muscle Disorders. *Nat Rev Mol Cell Biol* 22: 713.

5. Younger DS (2023) Childhood muscular dystrophies. *Handb Clin Neurol* 195: 461–496.

6. Roberts TC, Wood MJA, Davies KE (2023) Therapeutic approaches for Duchenne muscular dystrophy. *Nat Rev Drug Discov* 22: 917–934.

7. Shirley M (2021) Casimersen: First Approval. *Drugs* 81: 875–879.

8. Heo Y-A (2020) Golodirsen: First Approval. *Drugs 2020 80:3* 80: 329–333.

9. Hoy SM (2023) Delandistrogene Moxeparvovec: First Approval. *Drugs* 83: 1323–1329.

10. Roshmi RR, Yokota T (2023) Viltolarsen: From Preclinical Studies to FDA Approval. *Methods Mol Biol* 2587: 31–41.

11. Hoffman EP, Brown RH, Kunkel LM (1987) Dystrophin: The protein product of the duchenne muscular dystrophy locus. *Cell* 51: 919–928.

12. Duchenne G-B (1806-1875). A du texte (1868) De la paralysie musculaire pseudo-hypertrophique, ou paralysie myo-sclérosique / par le Dr Duchenne (de Boulogne).

13. Tyler KL (2003) Origins and early descriptions of “Duchenne muscular dystrophy”. *Muscle Nerve* 28: 402–422.

14. Buzin CH, Feng J, Yan J, et al. (2005) Mutation rates in the dystrophin gene: a hotspot of mutation at a CpG dinucleotide. *Hum Mutat* 25: 177–188.

15. Bushby KMD, Thambyayah M, Gardner-Medwin D (1991) Prevalence and incidence of Becker muscular dystrophy. *Lancet* 337: 1022–1024.

16. Vengalil S, Preethish-Kumar V, Polavarapu K, et al. (2017) Duchenne Muscular Dystrophy and Becker Muscular Dystrophy Confirmed by Multiplex Ligation-Dependent Probe Amplification: Genotype-Phenotype Correlation in a Large Cohort. *Journal of Clinical Neurology* 13: 91–97.

17. Magri F, Govoni A, D’Angelo MG, et al. (2011) Genotype and phenotype characterization in a large dystrophinopathic cohort with extended follow-up. *J Neurol* 258: 1610–1623.

18. Gazzoli I, Pulyakhina I, Verwey NE, et al. (2016) Non-sequential and multi-step splicing of the dystrophin transcript. *RNA Biol* 13: 290.

19. Tennyson CN, Klamut HJ, Worton RG (1995) The human dystrophin gene requires 16 hours to be transcribed and is cotranscriptionally spliced. *Nat Genet* 9: 184–190.

20. Muntoni F, Torelli S, Ferlini A (2003) Dystrophin and mutations: one gene, several proteins, multiple phenotypes. *Lancet Neurol* 2: 731–740.

21. Aartsma-Rus A, Van Deutekom JCT, Fokkema IF, et al. (2006) Entries in the Leiden Duchenne muscular dystrophy mutation database: An overview of mutation types and paradoxical cases that confirm the reading-frame rule. *Muscle Nerve* 34: 135–144.

22. Bladen CL, Salgado D, Monges S, et al. (2015) The TREAT-NMD DMD Global Database: analysis of more than 7,000 Duchenne muscular dystrophy mutations. *Hum Mutat* 36: 395–402.

23. Duan D, Goemans N, Takeda S, et al. (2021) Duchenne muscular dystrophy. *Nat Rev Dis Primers* 7: 13.

24. England SB, Nicholson LVB, Johnson MA, et al. (1990) Very mild muscular dystrophy associated with the deletion of 46% of dystrophin. *Nature* 343: 180–182.

25. Guo R, Zhu G, Zhu H, et al. (2015) DMD mutation spectrum analysis in 613 Chinese patients with dystrophinopathy. *Journal of Human Genetics 2015 60:8* 60: 435–442.

26. Oudet C, Hanauer A, Clemens P, et al. (1992) Two hot spots of recombination in the DMD gene correlate with the deletion prone regions. *Hum Mol Genet* 1: 599–603.

27. Findlay AR, Wein N, Kaminoh Y, et al. (2015) Clinical phenotypes as predictors of the outcome of skipping around DMD exon 45. *Ann Neurol* 77: 668.

28. Beggs AH, Hoffman EP, Snyder JR, et al. (1991) Exploring the molecular basis for variability among patients with Becker muscular dystrophy: dystrophin gene and protein studies. *Am J Hum Genet* 49: 54.

29. Anthony K, Cirak S, Torelli S, et al. (2011) Dystrophin quantification and clinical correlations in Becker muscular dystrophy: implications for clinical trials. *Brain* 134: 3544.

30. Hoffman EP (2020) Causes of clinical variability in Duchenne and Becker muscular dystrophies and implications for exon skipping therapies. *Acta Myologica* 39: 179.

31. Harper SQ, Hauser MA, DelloRusso C, et al. (2002) Modular flexibility of dystrophin: Implications for gene therapy of Duchenne muscular dystrophy. *Nature Medicine 2002 8:3* 8: 253–261.

32. Vo AH, McNally EM (2015) Modifier Genes and their effect on Duchenne Muscular Dystrophy. *Curr Opin Neurol* 28: 528.

33. Cardone N, Taglietti V, Baratto S, et al. (2023) Myopathologic trajectory in Duchenne muscular dystrophy (DMD) reveals lack of regeneration due to senescence in satellite cells. *Acta Neuropathol Commun* 11: 1–11.

34. Birnkrant DJ, Bushby K, Bann CM, et al. (2018) Diagnosis and management of Duchenne muscular dystrophy, part 1: diagnosis, and neuromuscular, rehabilitation, endocrine, and gastrointestinal and nutritional management. *Lancet Neurol* 17: 251–267.

35. Mercuri E, Muntoni F, Buccella F, et al. (2022) P.22 Age at loss of ambulation in patients with DMD from the STRIDE registry and the CINRG natural history study: A matched cohort analysis. *Neuromuscular Disorders* 32: S52.

36. Szabo SM, Salhany RM, Deighton A, et al. (2021) The clinical course of Duchenne muscular dystrophy in the corticosteroid treatment era: a systematic literature review. *Orphanet J Rare Dis* 16: 1–13.

37. LoMauro A, Romei M, Gandossini S, et al. (2018) Evolution of respiratory function in Duchenne muscular dystrophy from childhood to adulthood. *European Respiratory Journal* 51: 1701418.

38. Fayssoil A, Ogna A, Chaffaut C, et al. (2018) Natural history of cardiac function in Duchenne and Becker muscular dystrophies on home mechanical ventilation. *Medicine* 97.

39. Iodice F, Testa G, Averardi M, et al. (2015) Implantation of a left ventricular assist device as a destination therapy in Duchenne muscular dystrophy patients with end stage cardiac failure: management and lessons learned. *Neuromuscul Disord* 25: 19–23.

40. Florczyk-Soluch U, Polak K, Dulak J (2021) The multifaceted view of heart problem in Duchenne muscular dystrophy. *Cellular and Molecular Life Sciences* 78: 5447–5468.

41. Passamano L, Taglia A, Palladino A, et al. (2012) Improvement of survival in Duchenne Muscular Dystrophy: retrospective analysis of 835 patients. *Acta Myologica* 31: 121.

42. Clemens PR, Niizawa G, Feng J, et al. (2020) The CINRG Becker Natural History Study: Baseline characteristics. *Muscle Nerve* 62: 369–376.

43. Zatz M, Rapaport D, Vainzof M, et al. (1991) Serum creatine-kinase (CK) and pyruvate-kinase (PK) activities in Duchenne (DMD) as compared with Becker (BMD) muscular dystrophy. *J Neurol Sci* 102: 190–196.

44. Kim EY, Lee JW, Suh MR, et al. (2017) Correlation of Serum Creatine Kinase Level With Pulmonary Function in Duchenne Muscular Dystrophy. *Ann Rehabil Med* 41: 306.

45. Szigyarto CA-K, Spitali P (2018) Biomarkers of Duchenne muscular dystrophy: current findings. *Degener Neurol Neuromuscul Dis* 8: 1.

46. Ervasti JM (2013) Structure and Function of the Dystrophin-Glycoprotein Complex.

47. Gao QQ, McNally EM (2015) The Dystrophin Complex: structure, function and implications for therapy. *Compr Physiol* 5: 1223.

48. Norwood FLM, Sutherland-Smith AJ, Keep NH, et al. (2000) The structure of the N-terminal actin-binding domain of human dystrophin and how mutations in this domain may cause Duchenne or Becker muscular dystrophy. *Structure* 8: 481–491.

49. Prins KW, Humston JL, Mehta A, et al. (2009) Dystrophin is a microtubule-associated protein. *Journal of Cell Biology* 186: 363–369.

50. Belanto JJ, Mader TL, Eckhoff MD, et al. (2014) Microtubule binding distinguishes dystrophin from utrophin. *Proc Natl Acad Sci U S A* 111: 5723–5728.

51. Lai Y, Thomas GD, Yue Y, et al. (2009) Dystrophins carrying spectrin-like repeats 16 and 17 anchor nNOS to the sarcolemma and enhance exercise performance in a mouse model of muscular dystrophy. *J Clin Invest* 119: 624–635.

52. Adams ME, Odom GL, Kim MJ, et al. (2018) Syntrophin binds directly to multiple spectrin-like repeats in dystrophin and mediates binding of nNOS to repeats 16–17. *Hum Mol Genet* 27: 2978.

53. Constantin B (2014) Dystrophin complex functions as a scaffold for signalling proteins. *Biochimica et Biophysica Acta (BBA) - Biomembranes* 1838: 635–642.

54. Sadoulet-Puccio HM, Rajala M, Kunkel LM (1997) Dystrobrevin and dystrophin: An interaction through coiled-coil motifs. *Proc Natl Acad Sci U S A* 94: 12413–12418.

55. Nakamori M, Takahashi MP (2011) The Role of Alpha-Dystrobrevin in Striated Muscle. *Int J Mol Sci* 12: 1660.

56. Jung D, Yang B, Meyer J, et al. (1995) Identification and characterization of the dystrophin anchoring site on beta-dystroglycan. *J Biol Chem* 270: 27305–27310.

57. Zhao J, Kodippili K, Yue Y, et al. (2016) Dystrophin contains multiple independent membrane-binding domains. *Hum Mol Genet* 25: 3647–3653.

58. Montanaro F, Lindenbaum M, Carbonetto S (1999) α-Dystroglycan Is a Laminin Receptor Involved in Extracellular Matrix Assembly on Myotubes and Muscle Cell Viability. *J Cell Biol* 145: 1325.

59. Hack AA, Ly CT, Jiang F, et al. (1998) γ-Sarcoglycan Deficiency Leads to Muscle Membrane Defects and Apoptosis Independent of Dystrophin. *J Cell Biol* 142: 1279.

60. Turk R, Sterrenburg E, de Meijer EJ, et al. (2005) Muscle regeneration in dystrophin-deficient mdx mice studied by gene expression profiling. *BMC Genomics* 6: 1–15.

61. Ervasti JM (2003) Costameres: The Achilles' heel of Herculean muscle. *Journal of Biological Chemistry* 278: 13591–13594.

62. Gorza L, Sorge M, Seclì L, et al. (2021) Master Regulators of Muscle Atrophy: Role of Costamere Components. *Cells 2021, Vol 10, Page 61* 10: 61.

63. Bloch RJ, Gonzalez-Serratos H (2003) Lateral force transmission across costameres in skeletal muscle. *Exerc Sport Sci Rev* 31: 73–78.

64. Mayer U, Saher G, Fässler R, et al. (1997) Absence of integrin alpha 7 causes a novel form of muscular dystrophy. *Nat Genet* 17: 318–323.

65. Guo C, Willem M, Werner A, et al. (2006) Absence of α7 integrin in dystrophin-deficient mice causes a myopathy similar to Duchenne muscular dystrophy. *Hum Mol Genet* 15: 989–998.

66. Vainzof M, Passos-Bueno MR, Canovas M, et al. (1996) The sarcoglycan complex in the six autosomal recessive limb-girdle muscular dystrophies. *Hum Mol Genet* 5: 1963–1969.

67. Godfrey C, Foley AR, Clement E, et al. (2011) Dystroglycanopathies: coming into focus. *Curr Opin Genet Dev* 21: 278–285.

68. Straub V, Rafael JA, Chamberlain JS, et al. (1997) Animal Models for Muscular Dystrophy Show Different Patterns of Sarcolemmal Disruption. *J Cell Biol* 139: 375.

69. Le S, Yu M, Hovan L, et al. (2018) Dystrophin As a Molecular Shock Absorber. *ACS Nano* 12: 12140–12148.

70. Petrof BJ, Shrager JB, Stedman HH, et al. (1993) Dystrophin protects the sarcolemma from stresses developed during muscle contraction. *Proc Natl Acad Sci U S A* 90: 3710.

71. Stamler JS, Meissner G (2001) Physiology of nitric oxide in skeletal muscle. *Physiol Rev* 81: 209–237.

72. Thomas GD, Shaul PW, Yuhanna IS, et al. (2003) Vasomodulation by Skeletal Muscle–Derived Nitric Oxide Requires α-Syntrophin–Mediated Sarcolemmal Localization of Neuronal Nitric Oxide Synthase. *Circ Res* 92: 554–560.

73. Kobzik L, Reid MB, Bredt DS, et al. (1994) Nitric oxide in skeletal muscle. *Nature 1994 372:6506* 372: 546–548.

74. Thomas GD, Sander M, Lau KS, et al. (1998) Impaired metabolic modulation of α-adrenergic vasoconstriction in dystrophin-deficient skeletal muscle. *Proc Natl Acad Sci U S A* 95: 15090–15095.

75. Thomas GD, Victor RG (1998) Nitric oxide mediates contraction-induced attenuation of sympathetic vasoconstriction in rat skeletal muscle. *J Physiol* 506: 817.

76. Reid MB (1998) Role of nitric oxide in skeletal muscle: synthesis, distribution and functional importance. *Acta Physiol Scand* 162: 401–409.

77. Filippin LI, Cuevas MJ, Lima E, et al. (2011) Nitric oxide regulates the repair of injured skeletal muscle. *Nitric Oxide* 24: 43–49.

78. Anderson JE (2000) A Role for Nitric Oxide in Muscle Repair: Nitric Oxide–mediated Activation of Muscle Satellite Cells. *Mol Biol Cell* 11: 1859.

79. Brenman JE, Chao DS, Xia H, et al. (1995) Nitric oxide synthase complexed with dystrophin and absent from skeletal muscle sarcolemma in Duchenne muscular dystrophy. *Cell* 82: 743–752.

80. Thomas GD (2013) Functional muscle ischemia in Duchenne and Becker muscular dystrophy. *Front Physiol* 4.

81. Leyva-Leyva M, Sandoval A, Felix R, et al. (2018) Biochemical and Functional Interplay Between Ion Channels and the Components of the Dystrophin-Associated Glycoprotein Complex. *J Membr Biol* 251: 535–550.

82. Mareedu S, Million ED, Duan D, et al. (2021) Abnormal Calcium Handling in Duchenne Muscular Dystrophy: Mechanisms and Potential Therapies. *Front Physiol* 12.

83. Schofield J, Houzelstein D, Davies K, et al. (1993) Expression of the dystrophin-related protein (utrophin) gene during mouse embryogenesis. *Dev Dyn* 198: 254–264.

84. Pearce M, Blake DJ, Tinsley JM, et al. (1993) The utrophin and dystrophin genes share similarities in genomic structure. *Hum Mol Genet* 2: 1765–1772.

85. Szwec S, Kapłucha Z, Chamberlain JS, et al. (2023) Dystrophin- and Utrophin-Based Therapeutic Approaches for Treatment of Duchenne Muscular Dystrophy: A Comparative Review. *BioDrugs 2023 38:1* 38: 95–119.

86. Tinsley JM, Blake DJ, Roche A, et al. (1992) Primary structure of dystrophin-related protein. *Nature* 360: 591–593.

87. Janghra N, Morgan JE, Sewry CA, et al. (2016) Correlation of Utrophin Levels with the Dystrophin Protein Complex and Muscle Fibre Regeneration in Duchenne and Becker Muscular Dystrophy Muscle Biopsies. *PLoS One* 11.

88. Tinsley JM, Potter AC, Phelps SR, et al. (1996) Amelioration of the dystrophic phenotype of mdx mice using a truncated utrophin transgene. *Nature* 384: 349–353.

89. Matsumura K, Ervasti JM, Ohlendieck K, et al. (1992) Association of dystrophin-related protein with dystrophin-associated proteins in mdx mouse muscle. *Nature 1992 360:6404* 360: 588–591.

90. Blake DJ, Tinsley JM, Davies KE (1996) Utrophin: A Structural and Functional Comparison to Dystrophin. *Brain Pathology* 6: 37–47.

91. Li D, Bareja A, Judge L, et al. (2010) Sarcolemmal nNOS anchoring reveals a qualitative difference between dystrophin and utrophin. *J Cell Sci* 123: 2008.

92. Khurana TS, Watkins SC, Chafey P, et al. (1991) Immunolocalization and developmental expression of dystrophin related protein in skeletal muscle. *Neuromuscular Disorders* 1: 185–194.

93. Clerk A, Morris GE, Dubowitz V, et al. (1993) Dystrophin-related protein, utrophin, in normal and dystrophic human fetal skeletal muscle. *The Histochemical Journal 1993 25:8* 25: 554–561.

94. Rigoletto C, Prelle A, Ciscato P, et al. (1995) Utrophin expression during human fetal development. *International Journal of Developmental Neuroscience* 13: 585–593.

95. Clerk A, Strong PN, Sewry CA (1992) Characterisation of dystrophin during development of human skeletal muscle. *Development* 114: 395–402.

96. Vainzof M, Passos-Bueno MR, Nguyen Thi Man, et al. (1995) Absence of correlation between utrophin localization and quantity and the clinical severity in Duchenne/Becker dystrophies. *Am J Med Genet* 58: 305–309.

97. Pons F, Nicholson LVB, Robert A, et al. (1993) Dystrophin and dystrophin-related protein (utrophin) distribution in normal and dystrophin-deficient skeletal muscles. *Neuromuscular Disorders* 3: 507–514.

98. Krishna S, Piepho AB, Lake DM, et al. (2024) Gene therapy delivered micro-dystrophins co-localize with transgenic utrophin in dystrophic skeletal muscle fibers. *Neuromuscular Disorders* 36: 1–5.

99. Nguyen TM, Ellis JM, Love DR, et al. (1991) Localization of the DMDL gene-encoded dystrophin-related protein using a panel of nineteen monoclonal antibodies: presence at neuromuscular junctions, in the sarcolemma of dystrophic skeletal muscle, in vascular and other smooth muscles, and in proliferating brain cell lines. *J Cell Biol* 115: 1695.

100. Galvagni F, Cantini M, Oliviero S (2002) The utrophin gene is transcriptionally up-regulated in regenerating muscle. *Journal of Biological Chemistry* 277: 19106–19113.

101. Helliwell TR, Nguyen thi M, Morris GE, et al. (1992) The dystrophin-related protein, utrophin, is expressed on the sarcolemma of regenerating human skeletal muscle fibres in dystrophies and inflammatory myopathies. *Neuromuscul Disord* 2: 177–184.

102. Guiraud S, Edwards B, Squire SE, et al. (2019) Embryonic myosin is a regeneration marker to monitor utrophin-based therapies for DMD. *Hum Mol Genet* 28: 307–319.

103. Weir AP, Morgan JE, Davies KE (2004) A-utrophin up-regulation in mdx skeletal muscle is independent of regeneration. *Neuromuscular Disorders* 14: 19–23.

104. Cullen MJ, Walsh JM, Tinsley JM, et al. (2001) Immunogold confirmation that utrophin is localized to the normal position of dystrophin in dystrophin-negative transgenic mouse muscle. *Histochemical Journal* 33: 579–583.

105. Gorokhova S, Schessl J, Zou Y, et al. (2023) Unusually severe muscular dystrophy upon in-frame deletion of the dystrophin rod domain and lack of compensation by membrane-localized utrophin. *Med* 4: 245-251.e3.

106. Mokri B, Engel AG (1975) Duchenne dystrophy: Electron microscopic findings pointing to a basic or early abnormality in the plasma membrane of the muscle fiber. *Neurology* 25: 1111–1120.

107. Roberts TC, Godfrey C, McClorey G, et al. (2013) Extracellular microRNAs are dynamic non-vesicular biomarkers of muscle turnover. *Nucleic Acids Res* 41: 9500–9513.

108. Roberts TC, Blomberg KEM, McClorey G, et al. (2012) Expression analysis in multiple muscle groups and serum reveals complexity in the microRNA transcriptome of the mdx mouse with implications for therapy. *Mol Ther Nucleic Acids* 1: e39.

109. Turner PR, Fong P, Denetclaw WF, et al. (1991) Increased calcium influx in dystrophic muscle. *J Cell Biol* 115: 1701–1712.

110. Jung C, Martins AS, Niggli E, et al. (2008) Dystrophic cardiomyopathy: amplification of cellular damage by Ca2+ signalling and reactive oxygen species-generating pathways. *Cardiovasc Res* 77: 766–773.

111. Terrill JR, Radley-Crabb HG, Iwasaki T, et al. (2013) Oxidative stress and pathology in muscular dystrophies: focus on protein thiol oxidation and dysferlinopathies. *FEBS J* 280: 4149–4164.

112. Rosenberg AS, Puig M, Nagaraju K, et al. (2015) Immune-mediated pathology in Duchenne muscular dystrophy. *Sci Transl Med* 7: 299rv4.

113. Mauro A (1961) Satellite cell of skeletal muscle fibers. *J Biophys Biochem Cytol* 9: 493.

114. Seale P, Sabourin LA, Girgis-Gabardo A, et al. (2000) Pax7 Is Required for the Specification of Myogenic Satellite Cells. *Cell* 102: 777–786.

115. Tajbakhsh S (2009) Skeletal muscle stem cells in developmental versus regenerative myogenesis. *J Intern Med* 266: 372–389.

116. Dubuisson N, Versele R, Planchon C, et al. (2022) Histological Methods to Assess Skeletal Muscle Degeneration and Regeneration in Duchenne Muscular Dystrophy. *Int J Mol Sci* 23: 16080.

117. Madry H, Pizza FX, Buckley KH (2023) Regenerating Myofibers after an Acute Muscle Injury: What Do We Really Know about Them? *International Journal of Molecular Sciences 2023, Vol 24, Page 12545* 24: 12545.

118. Zammit PS, Heslop L, Hudon V, et al. (2002) Kinetics of Myoblast Proliferation Show That Resident Satellite Cells Are Competent to Fully Regenerate Skeletal Muscle Fibers. *Exp Cell Res* 281: 39–49.

119. Desguerre I, Mayer M, Leturcq F, et al. (2009) Endomysial fibrosis in Duchenne muscular dystrophy: a marker of poor outcome associated with macrophage alternative activation. *J Neuropathol Exp Neurol* 68: 762–773.

120. Kodippili K, Rudnicki MA (2023) Satellite cell contribution to disease pathology in Duchenne muscular dystrophy. *Front Physiol* 14.

121. Boldrin L, Zammit PS, Morgan JE (2015) Satellite cells from dystrophic muscle retain regenerative capacity. *Stem Cell Res* 14: 20.

122. Gaina G, (Gruianu) AP (2021) Muscular dystrophy: Experimental animal models and therapeutic approaches (Review). *Exp Ther Med* 21.

123. Bulfield G, Siller WG, Wight PAL, et al. (1984) X chromosome-linked muscular dystrophy (mdx) in the mouse. *Proc Natl Acad Sci U S A* 81: 1189.

124. Sicinski P, Geng Y, Ryder-Cook AS, et al. (1989) The molecular basis of muscular dystrophy in the mdx mouse: A point mutation. *Science (1979)* 244: 1578–1580.

125. Isken O, Maquat LE (2008) The multiple lives of NMD factors: balancing roles in gene and genome regulation. *Nat Rev Genet* 9: 699–712.

126. Coulton GR, Morgan JE, Partrige TA, et al. (1988) The mdx mouse skeletal muscle myopathy: I. A histological, morphometric and biochemical investigation. *Neuropathol Appl Neurobiol* 14: 53–70.

127. Tanabe Y, Esaki K, Nomura T (1986) Skeletal muscle pathology in X chromosome-linked muscular dystrophy (mdx) mouse. *Acta Neuropathol* 69: 91–95.

128. Merrick D, Stadler LKJ, Larner D, et al. (2009) Muscular dystrophy begins early in embryonic development deriving from stem cell loss and disrupted skeletal muscle formation. *Dis Model Mech* 2: 374–388.

129. Massopust RT, Lee Y il, Pritchard AL, et al. (2020) Lifetime analysis of mdx skeletal muscle reveals a progressive pathology that leads to myofiber loss. *Scientific Reports 2020 10:1* 10: 1–16.

130. Villalta SA, Nguyen HX, Deng B, et al. (2009) Shifts in macrophage phenotypes and macrophage competition for arginine metabolism affect the severity of muscle pathology in muscular dystrophy. *Hum Mol Genet* 18: 482–496.

131. Giovarelli M, Arnaboldi F, Zecchini S, et al. (2022) Characterisation of Progressive Skeletal Muscle Fibrosis in the Mdx Mouse Model of Duchenne Muscular Dystrophy: An In Vivo and In Vitro Study. *Int J Mol Sci* 23.

132. DiMario JX, Uzman A, Strohman RC (1991) Fiber regeneration is not persistent in dystrophic (MDX) mouse skeletal muscle. *Dev Biol* 148: 314–321.

133. Chamberlain JS, Metzger J, Reyes M, et al. (2007) Dystrophin-deficient mdx mice display a reduced life span and are susceptible to spontaneous rhabdomyosarcoma. *The FASEB Journal* 21: 2195–2204.

134. Peverelli L, Testolin S, Villa L, et al. (2015) Histologic muscular history in steroid-treated and untreated patients with Duchenne dystrophy. *Neurology* 85: 1886.

135. Pastoret C, Sebille A (1995) mdx mice show progressive weakness and muscle deterioration with age. *J Neurol Sci* 129: 97–105.

136. Echigoya Y, Lee J, Rodrigues M, et al. (2013) Mutation Types and Aging Differently Affect Revertant Fiber Expansion in Dystrophic Mdx and Mdx52 Mice. *PLoS One* 8: 69194.

137. Kornegay JN, Childers MK, Bogan DJ, et al. (2012) The Paradox of Muscle Hypertrophy in Muscular Dystrophy. *Phys Med Rehabil Clin N Am* 23: 149.

138. Deconinck AE, Rafael JA, Skinner JA, et al. (1997) Utrophin-dystrophin-deficient mice as a model for Duchenne muscular dystrophy. *Cell* 90: 717–727.

139. Tinsley J, Deconinck N, Fisher R, et al. (1998) Expression of full-length utrophin prevents muscular dystrophy in mdx mice. *Nat Med* 4: 1441–1444.

140. Araki E, Nakamura K, Nakao K, et al. (1997) Targeted Disruption of Exon 52 in the Mouse Dystrophin Gene Induced Muscle Degeneration Similar to That Observed in Duchenne Muscular Dystrophy. *Biochem Biophys Res Commun* 238: 492–497.

141. Kameya S, Araki E, Katsuki M, et al. (1997) Dp260 Disrupted Mice Revealed Prolonged Implicit Time of the b-Wave in ERG and Loss of Accumulation of β-Dystroglycan in the Outer Plexiform Layer of the Retina. *Hum Mol Genet* 6: 2195–2203.

142. Van Den Bergen JC, Wokke BH, Janson AA, et al. (2014) Dystrophin levels and clinical severity in Becker muscular dystrophy patients. *J Neurol Neurosurg Psychiatry* 85: 747–753.

143. Neri M, Torelli S, Brown S, et al. (2007) Dystrophin levels as low as 30% are sufficient to avoid muscular dystrophy in the human. *Neuromuscular Disorders* 17: 913–918.

144. de Feraudy Y, Ben Yaou R, Wahbi K, et al. (2021) Very Low Residual Dystrophin Quantity Is Associated with Milder Dystrophinopathy. *Ann Neurol* 89: 280–292.

145. Nicholson LVB, Johnson MA, Bushby KMD, et al. (1993) Functional significance of dystrophin positive fibres in Duchenne muscular dystrophy. *Arch Dis Child* 68: 632–636.

146. Wells DJ, Wells KE, Asante EA, et al. (1995) Expression of human full-length and minidystrophin in transgenic mdx mice: implications for gene therapy of Duchenne muscular dystrophy. *Hum Mol Genet* 4: 1245–1250.

147. Godfrey C, Muses S, McClorey G, et al. (2015) How much dystrophin is enough: the physiological consequences of different levels of dystrophin in the mdx mouse. *Hum Mol Genet* 24: 4225–4237.

148. Wasala NB, Yue Y, Vance J, et al. (2017) Uniform low-level dystrophin expression in the heart partially preserved cardiac function in an aged mouse model of Duchenne cardiomyopathy. *J Mol Cell Cardiol* 102: 45–52.

149. Arechavala-Gomeza V, Kinali M, Feng L, et al. (2010) Revertant fibres and dystrophin traces in Duchenne muscular dystrophy: implication for clinical trials. *Neuromuscul Disord* 20: 295–301.

150. Lu QL (2021) Revertant Phenomenon in DMD and LGMD2I and Its Therapeutic Implications: A Review of Study Under Mentorship of Terrence Partridge. *J Neuromuscul Dis* 8: S359.

151. Lu QL, Morris GE, Wilton SD, et al. (2000) Massive idiosyncratic exon skipping corrects the nonsense mutation in dystrophic mouse muscle and produces functional revertant fibers by clonal expansion. *J Cell Biol* 148: 985–995.

152. Hoffman EP, Morgan JE, Watkins SC, et al. (1990) Somatic reversion/suppression of the mouse mdx phenotype in vivo. *J Neurol Sci* 99: 9–25.

153. Yokota T, Lu QL, Morgan JE, et al. (2006) Expansion of revertant fibers in dystrophic mdx muscles reflects activity of muscle precursor cells and serves as an index of muscle regeneration. *J Cell Sci* 119: 2679–2687.

154. Penny GD, Kay GF, Sheardown SA, et al. (1996) Requirement for Xist in X chromosome inactivation. *Nature* 379: 131–137.

155. Lyon MF (1961) Gene action in the X-chromosome of the mouse (Mus musculus L.). *Nature* 190: 372–373.

156. Brockdorff N, Ashworth A, Kay GF, et al. (1992) The product of the mouse Xist gene is a 15 kb inactive X-specific transcript containing no conserved ORF and located in the nucleus. *Cell* 71: 515–526.

157. Wang J, Mager J, Chen Y, et al. (2001) Imprinted X inactivation maintained by a mouse Polycomb group gene. *Nat Genet* 28: 371–375.

158. Plath K, Mlynarczyk-Evans S, Nusinow DA, et al. (2002) Xist RNA and the mechanism of X chromosome inactivation. *Annu Rev Genet* 36: 233–278.

159. Amos-Landgraf JM, Cottle A, Plenge RM, et al. (2006) X Chromosome–Inactivation Patterns of 1,005 Phenotypically Unaffected Females. *Am J Hum Genet* 79: 493.

160. Belmont JW (1996) Genetic control of X inactivation and processes leading to X-inactivation skewing. *Am J Hum Genet* 58: 1101.

161. Shvetsova E, Sofronova A, Monajemi R, et al. (2018) Skewed X-inactivation is common in the general female population. *European Journal of Human Genetics 2018 27:3* 27: 455–465.

162. Migeon BR (1998) Non-random X chromosome inactivation in mammalian cells. *Cytogenet Cell Genet* 80: 142–148.

163. Puck JM, Willard HF (1998) X Inactivation in Females with X-Linked Disease. *New England Journal of Medicine* 338: 325–328.

164. Newall AET, Duthie S, Formstone E, et al. (2001) Primary non-random X inactivation associated with disruption of Xist promoter regulation. *Hum Mol Genet* 10: 581–589.

165. Panning B (2008) X-chromosome inactivation: The molecular basis of silencing. *J Biol* 7: 1–4.

166. Brown CJ, Robinson WP (2000) The causes and consequences of random and non-random X chromosome inactivation in humans. *Clin Genet* 58: 353–363.

167. Sun BK, Lee JT (2006) X-Chromosome Inactivation. *Encyclopedic Reference of Genomics and Proteomics in Molecular Medicine* 2013–2019.

168. Puck JM, Stewart CC, Nussbaum RL (1992) Maximum-likelihood analysis of human T-cell X chromosome inactivation patterns: normal women versus carriers of X-linked severe combined immunodeficiency. *Am J Hum Genet* 50: 742.

169. Lyon MF (1974) Mechanisms and evolutionary origins of variable X-chromosome activity in mammals. *Proc R Soc Lond B Biol Sci* 187: 243–268.

170. Vandenberg SG, Mckusick VA, Mckusick AB (1962) Twin Data in Support of the Lyon Hypothesis. *Nature 1962 194:4827* 194: 505–506.

171. Muers MR, Sharpe JA, Garrick D, et al. (2007) Defining the Cause of Skewed X-Chromosome Inactivation in X-Linked Mental Retardation by Use of a Mouse Model. *Am J Hum Genet* 80: 1138.

172. Young JI, Zoghbi HY (2004) X-chromosome inactivation patterns are unbalanced and affect the phenotypic outcome in a mouse model of rett syndrome. *Am J Hum Genet* 74: 511–520.

173. Plenge RM, Stevenson RA, Lubs HA, et al. (2002) Skewed X-Chromosome Inactivation Is a Common Feature of X-Linked Mental Retardation Disorders. *Am J Hum Genet* 71: 168.

174. Wengler G, Gorlin JB, Williamson JM, et al. (1995) Nonrandom inactivation of the X chromosome in early lineage hematopoietic cells in carriers of Wiskott-Aldrich syndrome. *Blood* 85: 2471–2477.

175. Okumura K, Fujimori Y, Takagi A, et al. (2008) Skewed X chromosome inactivation in fraternal female twins results in moderately severe and mild haemophilia B. *Haemophilia* 14: 1088–1093.

176. Migeon BR (2020) X-linked diseases: susceptible females. *Genetics in Medicine* 22: 1156.

177. Viggiano E, Ergoli M, Picillo E, et al. (2016) Determining the role of skewed X-chromosome inactivation in developing muscle symptoms in carriers of Duchenne muscular dystrophy. *Human Genetics 2016 135:7* 135: 685–698.

178. Finsterer J, Stollberger C (2018) Muscle, cardiac, and cerebral manifestations in female carriers of dystrophin variants. *J Neurol Sci* 388: 107–108.

179. Matthews PM, Benjamin D, Van Bakel I, et al. (1995) Muscle X-inactivation patterns and dystrophin expression in Duchenne muscular dystrophy carriers. *Neuromuscular Disorders* 5: 209–220.

180. Pegoraro E, Schimke RN, Garcia C, et al. (1995) Genetic and biochemical normalization in female carriers of Duchenne muscular dystrophy: evidence for failure of dystrophin production in dystrophin-competent myonuclei. *Neurology* 45: 677–690.

181. Richards CS, Watkins SC, Hoffman EP, et al. (1990) Skewed X inactivation in a female MZ twin results in Duchenne muscular dystrophy. *Am J Hum Genet* 46: 672.

182. Viggiano E, Picillo E, Cirillo A, et al. (2013) Comparison of X-chromosome inactivation in Duchenne muscle/myocardium-manifesting carriers, non-manifesting carriers and related daughters. *Clin Genet* 84: 265–270.

183. Mercier S, Toutain A, Toussaint A, et al. (2013) Genetic and clinical specificity of 26 symptomatic carriers for dystrophinopathies at pediatric age. *European Journal of Human Genetics* 21: 855.

184. Sun MX, Jing M, Hua Y, et al. (2024) A female patient carrying a novel DMD mutation with non-random X-chromosome inactivation from a DMD family. *BMC Med Genomics* 17: 1–7.

185. Birnkrant DJ, Bushby K, Bann CM, et al. (2018) Diagnosis and management of Duchenne muscular dystrophy, part 2: respiratory, cardiac, bone health, and orthopaedic management. *Lancet Neurol* 17: 347–361.

186. Bushby K, Finkel R, Birnkrant DJ, et al. (2010) Diagnosis and management of Duchenne muscular dystrophy, part 1: diagnosis, and pharmacological and psychosocial management. *Lancet Neurol* 9: 77–93.

187. Quattrocelli M, Zelikovich AS, Salamone IM, et al. (2021) Mechanisms and Clinical Applications of Glucocorticoid Steroids in Muscular Dystrophy. *J Neuromuscul Dis* 8: 39.

188. Guglieri M, Clemens PR, Perlman SJ, et al. (2022) Efficacy and Safety of Vamorolone vs Placebo and Prednisone Among Boys With Duchenne Muscular Dystrophy: A Randomized Clinical Trial. *JAMA Neurol* 79: 1005–1014.

189. Mercuri E, Osorio AN, Muntoni F, et al. (2023) Safety and effectiveness of ataluren in patients with nonsense mutation DMD in the STRIDE Registry compared with the CINRG Duchenne Natural History Study (2015–2022): 2022 interim analysis. *J Neurol* 270: 3896.

190. EMA confirms recommendation for non-renewal of authorisation of Duchenne muscular dystrophy medicine Translarna | European Medicines Agency Available from: https://www.ema.europa.eu/en/news/ema-confirms-recommendation-non-renewal-authorisation-duchenne-muscular-dystrophy-medicine-translarna.

191. Aartsma-Rus A, Straub V, Hemmings R, et al. (2017) Development of Exon Skipping Therapies for Duchenne Muscular Dystrophy: A Critical Review and a Perspective on the Outstanding Issues. *Nucleic Acid Ther* 27: 251–259.

192. Roberts TC, Langer R, Wood MJA (2020) Advances in oligonucleotide drug delivery. *Nature Reviews Drug Discovery 2020 19:10* 19: 673–694.

193. Brad Wan W, Seth PP (2016) The Medicinal Chemistry of Therapeutic Oligonucleotides. *J Med Chem* 59: 9645–9667.

194. Aartsma-Rus A, Fokkema I, Verschuuren J, et al. (2009) Theoretic applicability of antisense-mediated exon skipping for Duchenne muscular dystrophy mutations. *Hum Mutat* 30: 293–299.

195. Summerton J, Weller D (1997) Morpholino antisense oligomers: design, preparation, and properties. *Antisense Nucleic Acid Drug Dev* 7: 187–195.

196. Amantana A, Iversen PL (2005) Pharmacokinetics and biodistribution of phosphorodiamidate morpholino antisense oligomers. *Curr Opin Pharmacol* 5: 550–555.

197. Lim KRQ, Maruyama R, Yokota T (2017) Eteplirsen in the treatment of Duchenne muscular dystrophy. *Drug Des Devel Ther* 11: 533.

198. Clemens PR, Rao VK, Connolly AM, et al. (2020) Safety, Tolerability, and Efficacy of Viltolarsen in Boys With Duchenne Muscular Dystrophy Amenable to Exon 53 Skipping: A Phase 2 Randomized Clinical Trial. *JAMA Neurol* 77: 982–991.

199. Aartsma-Rus A, Goemans N (2019) A Sequel to the Eteplirsen Saga: Eteplirsen Is Approved in the United States but Was Not Approved in Europe. *Nucleic Acid Ther* 29: 13–15.

200. Vincik LY, Dautel AD, Staples AA, et al. (2024) Evolving Role of Viltolarsen for Treatment of Duchenne Muscular Dystrophy. *Adv Ther*.

201. Wagner K, Cripe L, Eagle M, et al. (2019) EP.83Design of a Phase 2/3 randomized controlled trial of suvodirsen (WVE-210201) in patients with Duchenne muscular dystrophy amenable to exon 51 skipping. *Neuromuscular Disorders* 29: S176–S177.

202. Aartsma-Rus A, Corey DR (2020) The 10th Oligonucleotide Therapy Approved: Golodirsen for Duchenne Muscular Dystrophy. *https://home.liebertpub.com/nat* 30: 67–70.

203. Goemans N, Mercuri E, Belousova E, et al. (2018) A randomized placebo-controlled phase 3 trial of an antisense oligonucleotide, drisapersen, in Duchenne muscular dystrophy. *Neuromuscul Disord* 28: 4–15.

204. Markati T, De Waele L, Schara-Schmidt U, et al. (2021) Lessons Learned from Discontinued Clinical Developments in Duchenne Muscular Dystrophy. *Front Pharmacol* 12.

205. Kandasamy P, Liu Y, Aduda V, et al. (2022) Impact of guanidine-containing backbone linkages on stereopure antisense oligonucleotides in the CNS. *Nucleic Acids Res* 50: 5401–5423.

206. Kandasamy P, McClorey G, Shimizu M, et al. (2022) Control of backbone chemistry and chirality boost oligonucleotide splice switching activity. *Nucleic Acids Res* 50: 5443.

207. Tillinger M, Lake S, Servais L, et al. (2023) P22 WVE-N531 yields 53% mean exon 53 skipping in skeletal muscle of boys with Duchenne muscular dystrophy (DMD) after three biweekly doses. *Neuromuscular Disorders* 33: S102.

208. Echigoya Y, Lim KRQ, Nakamura A, et al. (2018) Multiple Exon Skipping in the Duchenne Muscular Dystrophy Hot Spots: Prospects and Challenges. *J Pers Med* 8.

209. Aoki Y, Yokota T, Nagata T, et al. (2012) Bodywide skipping of exons 45-55 in dystrophic mdx52 mice by systemic antisense delivery. *Proc Natl Acad Sci U S A* 109: 13763–13768.

210. van Vliet L, de Winter CL, van Deutekom JCT, et al. (2008) Assessment of the feasibility of exon 45-55 multiexon skipping for Duchenne muscular dystrophy. *BMC Med Genet* 9.

211. Servais L, Mercuri E, Straub V, et al. (2022) Long-Term Safety and Efficacy Data of Golodirsen in Ambulatory Patients with Duchenne Muscular Dystrophy Amenable to Exon 53 Skipping: A First-in-human, Multicenter, Two-Part, Open-Label, Phase 1/2 Trial. *Nucleic Acid Ther* 32: 29.

212. Nicolau S, Malhotra J, Kaler M, et al. (2024) Increase in Full-Length Dystrophin by Exon Skipping in Duchenne Muscular Dystrophy Patients with Single Exon Duplications: An Open-label Study. *J Neuromuscul Dis* Preprint: 1–7.

213. Tsoumpra MK, Fukumoto S, Matsumoto T, et al. (2019) Peptide-conjugate antisense based splice-correction for Duchenne muscular dystrophy and other neuromuscular diseases. *EBioMedicine* 45: 630–645.

214. Betts C, Saleh AF, Arzumanov AA, et al. (2012) Pip6-PMO, A New Generation of Peptide-oligonucleotide Conjugates With Improved Cardiac Exon Skipping Activity for DMD Treatment. *Mol Ther Nucleic Acids* 1: e38.

215. McClorey G, Banerjee S (2018) Cell-Penetrating Peptides to Enhance Delivery of Oligonucleotide-Based Therapeutics. *Biomedicines* 6.

216. Davies KE, Guiraud S (2019) Micro-dystrophin Genes Bring Hope of an Effective Therapy for Duchenne Muscular Dystrophy. *Molecular Therapy* 27: 486–488.

217. Blankinship MJ, Gregorevic P, Chamberlain JS (2006) Gene Therapy Strategies for Duchenne Muscular Dystrophy Utilizing Recombinant Adeno-associated Virus Vectors. *Molecular Therapy* 13: 241–249.

218. Wang D, Tai PWL, Gao G (2019) Adeno-associated virus vector as a platform for gene therapy delivery. *Nature Reviews Drug Discovery 2019 18:5* 18: 358–378.

219. Li N, Song Y (2022) Strategies for Bottlenecks of rAAV-Mediated Expression in Skeletal and Cardiac Muscle of Duchenne Muscular Dystrophy. *Genes 2022, Vol 13, Page 2021* 13: 2021.

220. Phelps SF, Hauser MA, Cole NM, et al. (1995) Expression of full-length and truncated dystrophin mini-genes in transgenic mdx mice. *Hum Mol Genet* 4: 1251–1258.

221. Bönnemann CG, Belluscio BA, Braun S, et al. (2023) Dystrophin Immunity after Gene Therapy for Duchenne's Muscular Dystrophy. *New England Journal of Medicine* 388: 2294–2296.

222. Tabebordbar M, Lagerborg KA, Stanton A, et al. (2021) Directed evolution of a family of AAV capsid variants enabling potent muscle-directed gene delivery across species. *Cell* 184: 4919-4938.e22.

223. High-dose AAV gene therapy deaths (2020) *Nat Biotechnol* 38: 910.

224. Ertl HCJ (2022) Immunogenicity and toxicity of AAV gene therapy. *Front Immunol* 13.

225. Dosing paused in Pfizer DMD gene therapy trial after patient death Available from: https://musculardystrophynews.com/news/dosing-pause-after-patient-death-pfizer-dmd-gene-therapy-trial/.

226. Jinek M, Chylinski K, Fonfara I, et al. (2012) A programmable dual-RNA-guided DNA endonuclease in adaptive bacterial immunity. *Science* 337: 816–821.

227. Wiedenheft B, Sternberg SH, Doudna JA (2012) RNA-guided genetic silencing systems in bacteria and archaea. *Nature 2012 482:7385* 482: 331–338.

228. Brouns SJJ, Jore MM, Lundgren M, et al. (2008) Small CRISPR RNAs guide antiviral defense in prokaryotes. *Science* 321: 960–964.

229. Modell JW, Jiang W, Marraffini LA (2017) CRISPR-Cas systems exploit viral DNA injection to establish and maintain adaptive immunity. *Nature* 544: 101.

230. Jansen R, Van Embden JDA, Gaastra W, et al. (2002) Identification of genes that are associated with DNA repeats in prokaryotes. *Mol Microbiol* 43: 1565–1575.

231. Barrangou R, Fremaux C, Deveau H, et al. (2007) CRISPR provides acquired resistance against viruses in prokaryotes. *Science* 315: 1709–1712.

232. McGinn J, Marraffini LA (2018) Molecular mechanisms of CRISPR–Cas spacer acquisition. *Nature Reviews Microbiology 2018 17:1* 17: 7–12.

233. Liao C, Beisel CL (2021) The tracrRNA in CRISPR biology and technologies. *Annu Rev Genet* 55: 161.

234. Deltcheva E, Chylinski K, Sharma CM, et al. (2011) CRISPR RNA maturation by trans-encoded small RNA and host factor RNase III. *Nature* 471: 602–607.

235. Anders C, Jinek M (2014) In vitro Enzymology of Cas9. *Methods Enzymol* 546: 1.

236. Ledford H, Callaway E (2020) Pioneers of revolutionary CRISPR gene editing win chemistry Nobel. *Nature* 586: 346–347.

237. Gaj T, Gersbach CA, Barbas CF (2013) ZFN, TALEN and CRISPR/Cas-based methods for genome engineering. *Trends Biotechnol* 31: 397.

238. Scully R, Panday A, Elango R, et al. (2019) DNA double-strand break repair-pathway choice in somatic mammalian cells. *Nature Reviews Molecular Cell Biology 2019 20:11* 20: 698–714.

239. Hanson B, Wood MJA, Roberts TC (2021) Molecular correction of Duchenne muscular dystrophy by splice modulation and gene editing. *https://doi.org/101080/1547628620211874161* 18: 1048–1062.

240. Erkut E, Yokota T (2022) CRISPR Therapeutics for Duchenne Muscular Dystrophy. *Int J Mol Sci* 23.

241. Long C, McAnally JR, Shelton JM, et al. (2014) Prevention of muscular dystrophy in mice by CRISPR/Cas9-mediated editing of germline DNA. *Science* 345: 1184–1188.

242. Nelson CE, Hakim CH, Ousterout DG, et al. (2016) In vivo genome editing improves muscle function in a mouse model of Duchenne muscular dystrophy. *Science (1979)* 351: 403–407.

243. Long C, Amoasii L, Mireault AA, et al. (2016) Postnatal genome editing partially restores dystrophin expression in a mouse model of muscular dystrophy. *Science (1979)* 351: 400–403.

244. Tabebordbar M, Zhu K, Cheng JKW, et al. (2016) In vivo gene editing in dystrophic mouse muscle and muscle stem cells. *Science (1979)* 351: 407–411.

245. Ousterout DG, Kabadi AM, Thakore PI, et al. (2015) Multiplex CRISPR/Cas9-based genome editing for correction of dystrophin mutations that cause Duchenne muscular dystrophy. *Nat Commun* 6: 1–13.

246. Amoasii L, Long C, Li H, et al. (2017) Single-cut genome editing restores dystrophin expression in a new mouse model of muscular dystrophy. *Sci Transl Med* 9.

247. Amoasii L, Hildyard JCW, Li H, et al. (2018) Gene editing restores dystrophin expression in a canine model of Duchenne muscular dystrophy. *Science (1979)* 362: 86–91.

248. Liao HK, Hatanaka F, Araoka T, et al. (2017) In Vivo Target Gene Activation via CRISPR/Cas9-Mediated Trans-epigenetic Modulation. *Cell* 171: 1495-1507.e15.

249. Lek A, Wong B, Keeler A, et al. (2023) Unexpected Death of a Duchenne Muscular Dystrophy Patient in an N-of-1 Trial of rAAV9-delivered CRISPR-transactivator. *medRxiv* 2023.05.16.23289881.

250. Olson EN (2021) Toward the correction of muscular dystrophy by gene editing. *Proceedings of the National Academy of Sciences* 118.

251. Hanson B, Stenler S, Ahlskog N, et al. (2022) Non-uniform dystrophin re-expression after CRISPR-mediated exon excision in the dystrophin/utrophin double-knockout mouse model of DMD. *Mol Ther Nucleic Acids* 30: 379–397.

252. Choi S, Ferrari G, Tedesco FS (2020) Cellular dynamics of myogenic cell migration: molecular mechanisms and implications for skeletal muscle cell therapies. *EMBO Mol Med* 12.

253. Partridge TA, Morgan JE, Coulton GR, et al. (1989) Conversion of mdx myofibres from dystrophin-negative to -positive by injection of normal myoblasts. *Nature* 337: 176–179.

254. Morgan JE, Hoffman EP, Partridge TA (1990) Normal myogenic cells from newborn mice restore normal histology to degenerating muscles of the mdx mouse. *J Cell Biol* 111: 2437.

255. Law PK, Goodwin TG, Fang Q, et al. (1991) Myoblast Transfer Therapy for Duchenne Muscular Dystrophy. *Pediatrics International* 33: 206–215.

256. Huard J, Bouchard JP, Roy R, et al. (1992) Human myoblast transplantation: Preliminary results of 4 cases. *Muscle Nerve* 15: 550–560.

257. Law PK, Goodwin TG, Fang Q, et al. (1992) Feasibility, Safety, and Efficacy of Myoblast Transfer Therapy on Duchenne Muscular Dystrophy Boys. *http://dx.doi.org/101177/0963689792001002-305* 1: 235–244.

258. Akat A, Karaöz E (2024) Cell Therapy Strategies on Duchenne Muscular Dystrophy: A Systematic Review of Clinical Applications. *Stem Cell Rev Rep* 20: 138–158.

259. Tedesco FS, Dellavalle A, Diaz-Manera J, et al. (2010) Repairing skeletal muscle: regenerative potential of skeletal muscle stem cells. *J Clin Invest* 120: 11.

260. Motohashi N, Shimizu-Motohashi Y, Roberts TC, et al. (2019) Potential Therapies Using Myogenic Stem Cells Combined with Bio-Engineering Approaches for Treatment of Muscular Dystrophies. *Cells* 8.

261. Skuk D, Goulet M, Roy B, et al. (2006) Dystrophin Expression in Muscles of Duchenne Muscular Dystrophy Patients After High-Density Injections of Normal Myogenic Cells. *J Neuropathol Exp Neurol* 65: 371–386.

262. Gussoni E, Blau HM, Kunkel LM (1997) The fate of individual myoblasts after transplantation into muscles of DMD patients. *Nat Med* 3: 970–974.

263. Gussoni E, Pavlath GK, Lanctot AM, et al. (1992) Normal dystrophin transcripts detected in Duchenne muscular dystrophy patients after myoblast transplantation. *Nature 1992 356:6368* 356: 435–438.

264. Karpati G, Carpenter S (1986) Small-caliber skeletal muscle fibers do not suffer deleterious consequences of dystrophic gene expression. *Am J Med Genet* 25: 653–658.

265. Cossu G, Previtali SC, Napolitano S, et al. (2015) Intra-arterial transplantation of HLA -matched donor mesoangioblasts in Duchenne muscular dystrophy . *EMBO Mol Med* 7: 1513–1528.

266. Cossu G, Tonlorenzi R, Brunelli S, et al. (2022) Mesoangioblasts at 20: From the embryonic aorta to the patient bed. *Front Genet* 13.

267. McDonald CM, Marbán E, Hendrix S, et al. (2022) Repeated intravenous cardiosphere-derived cell therapy in late-stage Duchenne muscular dystrophy (HOPE-2): a multicentre, randomised, double-blind, placebo-controlled, phase 2 trial. *The Lancet* 399: 1049–1058.

268. Deconinck N, Tinsley J, De Backer F, et al. (1997) Expression of truncated utrophin leads to major functional improvements in dystrophin-deficient muscles of mice. *Nature Medicine 1997 3:11* 3: 1216–1221.

269. Tinsley JM, Fairclough RJ, Storer R, et al. (2011) Daily Treatment with SMTC1100, a Novel Small Molecule Utrophin Upregulator, Dramatically Reduces the Dystrophic Symptoms in the mdx Mouse. *PLoS One* 6.

270. Tinsley J, Robinson N, Davies KE (2015) Safety, tolerability, and pharmacokinetics of SMT C1100, a 2-arylbenzoxazole utrophin modulator, following single- and multiple-dose administration to healthy male adult volunteers. *J Clin Pharmacol* 55: 698–707.

271. Muntoni F, Tejura B, Spinty S, et al. (2019) A Phase 1b Trial to Assess the Pharmacokinetics of Ezutromid in Pediatric Duchenne Muscular Dystrophy Patients on a Balanced Diet. *Clin Pharmacol Drug Dev* 8: 922–933.

272. Ricotti V, Spinty S, Roper H, et al. (2016) Safety, Tolerability, and Pharmacokinetics of SMT C1100, a 2-Arylbenzoxazole Utrophin Modulator, following Single- and Multiple-Dose Administration to Pediatric Patients with Duchenne Muscular Dystrophy. *PLoS One* 11.

273. Guiraud S, Roblin D, Kay DE (2018) The potential of utrophin modulators for the treatment of Duchenne muscular dystrophy. *Expert Opin Orphan Drugs* 6: 179–192.

274. Chatzopoulou M, Claridge TDW, Davies KE, et al. (2020) Isolation, Structural Identification, Synthesis, and Pharmacological Profiling of 1,2- trans-Dihydro-1,2-diol Metabolites of the Utrophin Modulator Ezutromid. *J Med Chem* 63: 2547–2556.

275. Guiraud S, Squire SE, Edwards B, et al. (2015) Second-generation compound for the modulation of utrophin in the therapy of DMD. *Hum Mol Genet* 24: 4212–4224.

276. Yin W, Rogge M (2019) Targeting RNA: A Transformative Therapeutic Strategy. *Clin Transl Sci* 12: 98–112.

277. Joyce Chen CN, Thompson LDV, Snow LA (2017) Muscle Structure and Function. *Orthopaedic Physical Therapy Secrets: Third Edition* 1–9.

278. Sanger JW, Kang S, Siebrands CC, et al. (2005) How to build a myofibril. *J Muscle Res Cell Motil* 26: 343–354.

279. Sanger JW, Chowrashi P, Shaner NC, et al. (2002) Myofibrillogenesis in skeletal muscle cells. *Clin Orthop Relat Res* 403.

280. Sanger JW, Wang J, Fan Y, et al. (2010) Assembly and Dynamics of Myofibrils. *J Biomed Biotechnol* 2010.

281. Roman W, Gomes ER (2018) Nuclear positioning in skeletal muscle. *Semin Cell Dev Biol* 82: 51–56.

282. Clarke M (2008) Muscle sliding filaments. *Nature Reviews Molecular Cell Biology 2008 9:1* 9: s7–s7.

283. Lange S, Pinotsis N, Agarkova I, et al. (2020) The M-band: The underestimated part of the sarcomere. *Biochimica et Biophysica Acta (BBA) - Molecular Cell Research* 1867: 118440.

284. Peter AK, Cheng H, Ross RS, et al. (2011) The costamere bridges sarcomeres to the sarcolemma in striated muscle. *Prog Pediatr Cardiol* 31: 83.

285. Siebrands CC, Sanger JM, Sanger JW (2004) Myofibrillogenesis in skeletal muscle cells in the presence of taxol. *Cell Motil Cytoskeleton* 58: 39–52.

286. Sparrow JC, Schöck F (2009) The initial steps of myofibril assembly: integrins pave the way. *Nature Reviews Molecular Cell Biology 2009 10:4* 10: 293–298.

287. Myhre JL, Pilgrim DB (2012) At the start of the sarcomere: A previously unrecognized role for myosin chaperones and associated proteins during early myofibrillogenesis. *Biochem Res Int*.

288. Papadopoulos S, Jürgens KD, Gros G (2000) Protein diffusion in living skeletal muscle fibers: dependence on protein size, fiber type, and contraction. *Biophys J* 79: 2084.

289. Lucas L, Cooper TA (2023) Insights into Cell-Specific Functions of Microtubules in Skeletal Muscle Development and Homeostasis. *Int J Mol Sci* 24.

290. Liu W, Ralston E (2014) A new directionality tool for assessing microtubule pattern alterations. *Cytoskeleton (Hoboken)* 71: 230–240.

291. Oddoux S, Randazzo D, Kenea A, et al. (2019) Misplaced Golgi Elements Produce Randomly Oriented Microtubules and Aberrant Cortical Arrays of Microtubules in Dystrophic Skeletal Muscle Fibers. *Front Cell Dev Biol* 7: 176.

292. Ralston E, Lu Z, Ploug T (1999) The Organization of the Golgi Complex and Microtubules in Skeletal Muscle Is Fiber Type-Dependent. *Journal of Neuroscience* 19: 10694–10705.

293. Bugnard E, Zaal KJM, Ralston E (2005) Reorganization of microtubule nucleation during muscle differentiation. *Cell Motil Cytoskeleton* 60: 1–13.

294. Percival JM, Gregorevic P, Odom GL, et al. (2007) rAAV6-Microdystrophin Rescues Aberrant Golgi Complex Organization in mdx Skeletal Muscles. *Traffic* 8: 1424–1439.

295. Sanchez AD, Feldman JL (2017) Microtubule-organizing centers: from the centrosome to non-centrosomal sites. *Curr Opin Cell Biol* 44: 93.

296. Ralston E (1993) Changes in architecture of the Golgi complex and other subcellular organelles during myogenesis. *J Cell Biol* 120: 399.

297. Oddoux S, Zaal KJ, Tate V, et al. (2013) Microtubules that form the stationary lattice of muscle fibers are dynamic and nucleated at Golgi elements. 203.

298. Lu Z, Joseph D, Bugnard E, et al. (2001) Golgi Complex Reorganization during Muscle Differentiation: Visualization in Living Cells and Mechanism. *Mol Biol Cell* 12: 795.

299. Pizon V, Gerbal F, Diaz CC, et al. (2005) Microtubule-dependent transport and organization of sarcomeric myosin during skeletal muscle differentiation. *EMBO J* 24: 3781–3792.

300. Perez OD, Chang YT, Rosania G, et al. (2002) Inhibition and reversal of myogenic differentiation by purine-based microtubule assembly inhibitors. *Chem Biol* 9: 475–483.

301. Scarborough EA, Uchida K, Vogel M, et al. (2021) Microtubules orchestrate local translation to enable cardiac growth. *Nature Communications 2021 12:1* 12: 1–13.

302. Denes LT, Kelley CP, Wang ET (2021) Microtubule-based transport is essential to distribute RNA and nascent protein in skeletal muscle. *Nature Communications 2021 12:1* 12: 1–19.

303. Nelson DM, Lindsay A, Judge LM, et al. (2018) Variable rescue of microtubule and physiological phenotypes in mdx muscle expressing different miniaturized dystrophins. *Hum Mol Genet* 27: 2090.

304. Cadot B, Gache V, Gomes ER (2015) Moving and positioning the nucleus in skeletal muscle-one step at a time.

305. Hansson KA, Eftestøl E, Bruusgaard JC, et al. (2020) Myonuclear content regulates cell size with similar scaling properties in mice and humans. *Nature Communications 2020 11:1* 11: 1–14.

306. Landing BH, Dixon LG, Wells TR (1974) Studies on isolated human skeletal muscle fibers, including a proposed pattern of nuclear distribution and a concept of nuclear territories. *Hum Pathol* 5: 441–461.

307. Aman F, El Khatib E, AlNeaimi A, et al. (2023) Is the myonuclear domain ceiling hypothesis dead? *Singapore Med J* 64: 415–422.

308. Prasad V, Millay DP (2021) Skeletal muscle fibers count on nuclear numbers for growth. *Semin Cell Dev Biol*.

309. Cramer AAWW, Prasad V, Eftestøl E, et al. (2020) Nuclear numbers in syncytial muscle fibers promote size but limit the development of larger myonuclear domains. *Nature Communications 2020 11:1* 11: 1–14.

310. Qaisar R, Larsson L (2014) What determines myonuclear domain size? *Indian J Physiol Pharmacol* 58: 1–12.

311. Gundersen K, Sanes JR, Merlie JP (1993) Neural regulation of muscle acetylcholine receptor epsilon- and alpha- subunit gene promoters in transgenic mice. *J Cell Biol* 123: 1535.

312. Merlie JP, Sanes JR (1985) Concentration of acetylcholine receptor mRNA in synaptic regions of adult muscle fibres. *Nature* 317: 66–68.

313. Sanes JR, Johnson YR, Kotzbauer PT, et al. (1991) Selective expression of an acetylcholine receptor-lacZ transgene in synaptic nuclei of adult muscle fibers. *Development* 113: 1181–1191.

314. Fontaine B, Sassoon D, Buckingham M, et al. (1988) Detection of the nicotinic acetylcholine receptor alpha-subunit mRNA by in situ hybridization at neuromuscular junctions of 15-day-old chick striated muscles. *EMBO J* 7: 603.

315. Chal J, Pourquié O (2017) Making muscle: skeletal myogenesis in vivo and in vitro. *Development* 144: 2104–2122.

316. Hui T, Jing H, Lai X (2021) Neuromuscular junction-specific genes screening by deep RNA-seq analysis. *Cell Biosci* 11: 1–15.

317. Jasmin BJ, Lee RK, Rotundo RL (1993) Compartmentalization of Acetylcholinesterase mRNA and Enzyme at the Vertebrate Neuromuscular Junction. *Neuron* 11: 467–477.

318. Ralston E, Hall ZW (1992) Restricted distribution of mRNA produced from a single nucleus in hybrid myotubes. *J Cell Biol* 119: 1063–1068.

319. Pavlath GK, Rich K, Webster SG, et al. (1989) Localization of muscle gene products in nuclear domains. *Nature 1989 337:6207* 337: 570–573.

320. Chwalenia K, Oieni J, Zemła J, et al. (2022) Exon skipping induces uniform dystrophin rescue with dose-dependent restoration of serum miRNA biomarkers and muscle biophysical properties. *Mol Ther Nucleic Acids* 29: 955–968.

321. van Westering TLE, Lomonosova Y, Coenen-Stass AML, et al. (2020) Uniform sarcolemmal dystrophin expression is required to prevent extracellular microRNA release and improve dystrophic pathology. *J Cachexia Sarcopenia Muscle* 11: 578–593.

322. Marsh S, Hanson B, Wood MJA, et al. (2020) Application of CRISPR-Cas9-Mediated Genome Editing for the Treatment of Myotonic Dystrophy Type 1. *Mol Ther* 28: 2527–2539.

323. Bentzinger CF, Wang YX, Rudnicki MA (2012) Building Muscle: Molecular Regulation of Myogenesis. *Cold Spring Harb Perspect Biol* 4: a008342.

324. Ge Y, Chen J (2011) MicroRNAs in skeletal myogenesis. *Cell Cycle* 10.

325. Ott MO, Bober E, Lyons G, et al. (1991) Early expression of the myogenic regulatory gene, myf-5, in precursor cells of skeletal muscle in the mouse embryo. *Development* 111: 1097–1107.

326. Zhang M, McLennan IS (1995) During secondary myotube formation, primary myotubes preferentially absorb new nuclei at their ends. *Dev Dyn* 204: 168–177.

327. Ross JJ, Duxson MJ, Harris AJ (1987) Formation of primary and secondary myotubes in rat lumbrical muscles. *Development* 100: 383–394.

328. Schiaffino S, Rossi AC, Smerdu V, et al. (2015) Developmental myosins: Expression patterns and functional significance. *Skelet Muscle* 5: 1–14.

329. Asfour HA, Allouh MZ, Said RS (2018) Myogenic regulatory factors: The orchestrators of myogenesis after 30 years of discovery. *Exp Biol Med* 243: 118.

330. Tajbakhsh S, Rocancourt D, Cossu G, et al. (1997) Redefining the genetic hierarchies controlling skeletal myogenesis: Pax- 3 and Myf-5 act upstream of MyoD. *Cell* 89: 127–138.

331. Ishibashi J, Perry RL, Asakura A, et al. (2005) MyoD induces myogenic differentiation through cooperation of its NH2- and COOH-terminal regions. *J Cell Biol* 171: 471.

332. Cao Y, Kumar RM, Penn BH, et al. (2006) Global and gene-specific analyses show distinct roles for Myod and Myog at a common set of promoters. *EMBO J* 25: 502–511.

333. Venuti JM, Morris JH, Vivian JL, et al. (1995) Myogenin is required for late but not early aspects of myogenesis during mouse development. *J Cell Biol* 128: 563–576.

334. Andrés V, Walsh K (1996) Myogenin expression, cell cycle withdrawal, and phenotypic differentiation are temporally separable events that precede cell fusion upon myogenesis. *Journal of Cell Biology* 132: 657–666.

335. Guo K, Wang J, Andrés V, et al. (1995) MyoD-induced expression of p21 inhibits cyclin-dependent kinase activity upon myocyte terminal differentiation. *Mol Cell Biol* 15: 3823.

336. Adhikari A, Kim W, Davie J (2021) Myogenin is required for assembly of the transcription machinery on muscle genes during skeletal muscle differentiation. *PLoS One* 16.

337. Millay DP, Sutherland LB, Bassel-Duby R, et al. (2014) Myomaker is essential for muscle regeneration. *Genes Dev* 28: 1641.

338. Millay DP, O'Rourke JR, Sutherland LB, et al. (2013) Myomaker is a membrane activator of myoblast fusion and muscle formation. *Nature* 499: 301–305.

339. Quinn ME, Goh Q, Kurosaka M, et al. (2017) Myomerger induces fusion of non-fusogenic cells and is required for skeletal muscle development. *Nature Communications 2017 8:1* 8: 1–9.

340. Cadot B, Gache V, Vasyutina E, et al. (2012) Nuclear movement during myotube formation is microtubule and dynein dependent and is regulated by Cdc42, Par6 and Par3. *EMBO Rep* 13: 741.

341. Roman W, Martins JP, Carvalho FA, et al. (2017) Myofibril contraction and crosslinking drive nuclear movement to the periphery of skeletal muscle. *Nature Cell Biology 2017 19:10* 19: 1189–1201.

342. Zammit PS, Golding JP, Nagata Y, et al. (2004) Muscle satellite cells adopt divergent fates: a mechanism for self-renewal? *J Cell Biol* 166: 347–357.

343. Zammit PS, Relaix F, Nagata Y, et al. (2006) Pax7 and myogenic progression in skeletal muscle satellite cells. *J Cell Sci* 119: 1824–1832.

344. Yin H, Price F, Rudnicki MA (2013) Satellite Cells and the Muscle Stem Cell Niche. *Physiol Rev* 93: 23.

345. Dumont NA, Wang YX, Von Maltzahn J, et al. (2015) Dystrophin expression in muscle stem cells regulates their polarity and asymmetric division. *Nat Med* 21: 1455.

346. Bartel DP (2009) MicroRNAs: Target Recognition and Regulatory Functions. *Cell* 136: 215–233.

347. Wilson RC, Doudna JA (2013) Molecular Mechanisms of RNA Interference. *https://doi.org/101146/annurev-biophys-083012-130404* 42: 217–239.

348. Shang R, Lee S, Senavirathne G, et al. (2023) microRNAs in action: biogenesis, function and regulation. *Nature Reviews Genetics 2023 24:12* 24: 816–833.

349. Cai X, Hagedorn CH, Cullen BR (2004) Human microRNAs are processed from capped, polyadenylated transcripts that can also function as mRNAs. *RNA* 10: 1957.

350. Lee Y, Kim M, Han J, et al. (2004) MicroRNA genes are transcribed by RNA polymerase II. *EMBO J* 23: 4051.

351. Lee Y, Ahn C, Han J, et al. (2003) The nuclear RNase III Drosha initiates microRNA processing. *Nature 2003 425:6956* 425: 415–419.

352. Yi R, Qin Y, Macara IG, et al. (2003) Exportin-5 mediates the nuclear export of pre-microRNAs and short hairpin RNAs. *Genes Dev* 17: 3011–3016.

353. Hutvágner G, McLachlan J, Pasquinelli AE, et al. (2001) A cellular function for the RNA-interference enzyme Dicer in the maturation of the let-7 small temporal RNA. *Science* 293: 834–838.

354. Iwakawa H oki, Tomari Y (2022) Life of RISC: Formation, action, and degradation of RNA-induced silencing complex. *Mol Cell* 82: 30–43.

355. Medley JC, Panzade G, Zinovyeva AY (2021) microRNA strand selection: Unwinding the rules. *Wiley Interdiscip Rev RNA* 12.

356. Friedman RC, Farh KKH, Burge CB, et al. (2009) Most mammalian mRNAs are conserved targets of microRNAs. *Genome Res* 19: 92.

357. Filipowicz W, Bhattacharyya SN, Sonenberg N (2008) Mechanisms of post-transcriptional regulation by microRNAs: are the answers in sight? *Nature Reviews Genetics 2008 9:2* 9: 102–114.

358. Meister G, Landthaler M, Patkaniowska A, et al. (2004) Human Argonaute2 mediates RNA cleavage targeted by miRNAs and siRNAs. *Mol Cell* 15: 185–197.

359. Ohrt T, Mütze J, Staroske W, et al. (2008) Fluorescence correlation spectroscopy and fluorescence cross-correlation spectroscopy reveal the cytoplasmic origination of loaded nuclear RISC in vivo in human cells. *Nucleic Acids Res* 36: 6439.

360. Liu J, Hu J, Corey DR (2012) Expanding the action of duplex RNAs into the nucleus: redirecting alternative splicing. *Nucleic Acids Res* 40: 1240–1250.

361. Liu J, Carmell MA, Rivas F V., et al. (2004) Argonaute2 is the catalytic engine of mammalian RNAi. *Science (1979)* 305: 1437–1441.

362. Jo MH, Shin S, Jung SR, et al. (2015) Human Argonaute 2 Has Diverse Reaction Pathways on Target RNAs. *Mol Cell* 59: 117–124.

363. Ivey KN, Srivastava D (2015) microRNAs as Developmental Regulators. *Cold Spring Harb Perspect Biol* 7: 1–9.

364. Sempere LF, Freemantle S, Pitha-Rowe I, et al. (2004) Expression profiling of mammalian microRNAs uncovers a subset of brain-expressed microRNAs with possible roles in murine and human neuronal differentiation. *Genome Biol* 5: R13.

365. Mok GF, Lozano-Velasco E, Münsterberg A (2017) microRNAs in skeletal muscle development. *Semin Cell Dev Biol* 72: 67–76.

366. Williams AH, Liu N, Rooij E van, et al. (2009) MicroRNA Control of Muscle Development and Disease. *Curr Opin Cell Biol* 21: 461.

367. Safa A, Bahroudi Z, Shoorei H, et al. (2020) miR-1: A comprehensive review of its role in normal development and diverse disorders. *Biomedicine & Pharmacotherapy* 132: 110903.

368. Koutsoulidou A, Mastroyiannopoulos NP, Furling D, et al. (2011) Expression of miR-1, miR-133a, miR-133b and miR-206 increases during development of human skeletal muscle. *BMC Dev Biol* 11: 1–9.

369. Kim HK, Lee YS, Sivaprasad U, et al. (2006) Muscle-specific microRNA miR-206 promotes muscle differentiation. *J Cell Biol* 174: 677.

370. Ma G, Wang Y, Li Y, et al. (2015) MiR-206, a Key Modulator of Skeletal Muscle Development and Disease. *Int J Biol Sci* 11: 345.

371. Horak M, Novak J, Bienertova-Vasku J (2016) Muscle-specific microRNAs in skeletal muscle development. *Dev Biol* 410: 1–13.

372. Mitchelson KR, Qin W-Y (2015) Roles of the canonical myomiRs miR-1, -133 and -206 in cell development and disease. *World J Biol Chem* 6: 162.

373. Liu N, Bezprozvannaya S, Williams AH, et al. (2008) microRNA-133a regulates cardiomyocyte proliferation and suppresses smooth muscle gene expression in the heart. *Genes Dev* 22: 3242.

374. McCarthy JJ (2008) MicroRNA-206: the skeletal muscle-specific myomiR. *Biochim Biophys Acta* 1779: 682.

375. Anderson C, Catoe H, Werner R (2006) MIR-206 regulates connexin43 expression during skeletal muscle development. *Nucleic Acids Res* 34: 5863.

376. Rao PK, Kumar RM, Farkhondeh M, et al. (2006) Myogenic factors that regulate expression of muscle-specific microRNAs. *Proc Natl Acad Sci U S A* 103: 8721–8726.

377. Rosenberg MI, Georges SA, Asawachaicharn A, et al. (2006) MyoD inhibits Fstl1 and Utrn expression by inducing transcription of miR-206. *J Cell Biol* 175: 77–85.

378. Chen J-F, Tao Y, Li J, et al. (2010) microRNA-1 and microRNA-206 regulate skeletal muscle satellite cell proliferation and differentiation by repressing Pax7. *Journal of Cell Biology* 190: 867–879.

379. Lu J, McKinsey TA, Zhang CL, et al. (2000) Regulation of Skeletal Myogenesis by Association of the MEF2 Transcription Factor with Class II Histone Deacetylases. *Mol Cell* 6: 233–244.

380. Chen J-FF, Mandel EM, Thomson JM, et al. (2006) The role of microRNA-1 and microRNA-133 in skeletal muscle proliferation and differentiation. *Nat Genet* 38: 228–233.

381. Lee A, Moon J, Yu J, et al. (2022) MicroRNAs in Dystrophinopathy. *Int J Mol Sci* 23.

382. Greco S, De Simone M, Colussi C, et al. (2009) Common micro-RNA signature in skeletal muscle damage and regeneration induced by Duchenne muscular dystrophy and acute ischemia. *FASEB J* 23: 3335–3346.

383. Yuasa K, Hagiwara Y, Ando M, et al. (2008) MicroRNA-206 is highly expressed in newly formed muscle fibers: implications regarding potential for muscle regeneration and maturation in muscular dystrophy. *Cell Struct Funct* 33: 163–169.

384. Meng Q, Zhang J, Zhong J, et al. (2022) Novel miRNA Biomarkers for Patients With Duchenne Muscular Dystrophy. *Front Neurol* 13: 921785.

385. Mizuno H, Nakamura A, Aoki Y, et al. (2011) Identification of muscle-specific microRNAs in serum of muscular dystrophy animal models: promising novel blood-based markers for muscular dystrophy. *PLoS One* 6.

386. Coenen-Stass AML, Betts CA, Lee YF, et al. (2016) Selective release of muscle-specific, extracellular microRNAs during myogenic differentiation. *Hum Mol Genet* 25: 3960.

387. Zaharieva IT, Calissano M, Scoto M, et al. (2013) Dystromirs as Serum Biomarkers for Monitoring the Disease Severity in Duchenne Muscular Dystrophy. *PLoS One* 8: 80263.

388. Vignier N, Amor F, Fogel P, et al. (2013) Distinctive Serum miRNA Profile in Mouse Models of Striated Muscular Pathologies. *PLoS One* 8: e55281.

389. Cacchiarelli D, Legnini I, Martone J, et al. (2011) miRNAs as serum biomarkers for Duchenne muscular dystrophy. *EMBO Mol Med* 3: 258.

390. Coenen-Stass AML, Wood MJA, Roberts TC (2017) Biomarker Potential of Extracellular miRNAs in Duchenne Muscular Dystrophy. *Trends Mol Med* 23: 989–1001.

391. Mazzone E, Martinelli D, Berardinelli A, et al. (2010) North Star Ambulatory Assessment, 6-minute walk test and timed items in ambulant boys with Duchenne muscular dystrophy. *Neuromuscul Disord* 20: 712–716.

392. Baird MF, Graham SM, Baker JS, et al. (2012) Creatine-Kinase- and Exercise-Related Muscle Damage Implications for Muscle Performance and Recovery. *J Nutr Metab* 2012: 13.

393. Zygmunt AM, Wong BL, Horn PS, et al. (2023) A longitudinal study of creatine kinase and creatinine levels in Duchenne muscular dystrophy. *Muscle Nerve* 67: 138–145.

394. Aartsma-Rus A, Spitali P (2015) Circulating Biomarkers for Duchenne Muscular Dystrophy. *J Neuromuscul Dis* 2: S49.

395. Coenen-Stass AML, Sork H, Gatto S, et al. (2018) Comprehensive RNA-Sequencing Analysis in Serum and Muscle Reveals Novel Small RNA Signatures with Biomarker Potential for DMD. *Mol Ther Nucleic Acids* 13: 1–15.

396. Goyenvalle A, Babbs A, Wright J, et al. (2012) Rescue of severely affected dystrophin/utrophin-deficient mice through scAAV-U7snRNA-mediated exon skipping. *Hum Mol Genet* 21: 2559–2571.

397. Deconinck AE, Potter AC, Tinsley JM, et al. (1997) Postsynaptic Abnormalities at the Neuromuscular Junctions of Utrophin-deficient Mice. *J Cell Biol* 136: 883.

398. Roberts TC, Coenen-Stass AML, Betts CA, et al. (2014) Detection and quantification of extracellular microRNAs in murine biofluids. *Biol Proced Online* 16: 5.

399. Roberts TC, Coenen-Stass AML, Wood MJA (2014) Assessment of RT-qPCR normalization strategies for accurate quantification of extracellular microRNAs in murine serum. *PLoS One* 9.

400. Pfaffl MW (2001) A new mathematical model for relative quantification in real-time RT-PCR. *Nucleic Acids Res* 29: E45.

401. Schindelin J, Arganda-Carreras I, Frise E, et al. (2012) Fiji: an open-source platform for biological-image analysis. *Nature Methods 2012 9:7* 9: 676–682.

402. Nawrotzki R, Loh NY, Ruegg MA, et al. (1998) Characterisation of alpha-dystrobrevin in muscle. *J Cell Sci* 111 (Pt 17): 2595–2605.

403. Blake DJ, Hawkes R, Benson MA, et al. (1999) Different Dystrophin-like Complexes Are Expressed in Neurons and Glia. *J Cell Biol* 147: 645.

404. Nevalainen M, Kaakinen M, Metsikkö K (2013) Distribution of mRNA transcripts and translation activity in skeletal myofibers. *Cell Tissue Res* 353: 539–548.

405. Morin A, Stantzou A, Petrova ON, et al. (2023) Dystrophin myonuclear domain restoration governs treatment efficacy in dystrophic muscle. *Proc Natl Acad Sci U S A* 120: e2206324120.

406. Watkins SC, Hoffman P, Slayter HS, et al. (1989) Dystrophin distribution in heterozygote mdx mice. *Muscle Nerve* 12: 861–868.

407. Putten M van, Hulsker M, Nadarajah VD, et al. (2012) The Effects of Low Levels of Dystrophin on Mouse Muscle Function and Pathology. *PLoS One* 7: 31937.

408. van der Pijl EM, van Putten M, Niks EH, et al. (2018) Low dystrophin levels are insufficient to normalize the neuromuscular synaptic abnormalities of mdx mice. *Neuromuscular Disorders* 28: 427–442.

409. Van Putten M, Van der Pijl EM, Hulsker M, et al. (2014) Low dystrophin levels in heart can delay heart failure in mdx mice. *J Mol Cell Cardiol* 69: 17–23.

410. Van Putten M, Hulsker M, Young C, et al. (2013) Low dystrophin levels increase survival and improve muscle pathology and function in dystrophin/utrophin double-knockout mice. *FASEB J* 27: 2484–2495.

411. Torelli S, Scaglioni D, Sardone V, et al. (2021) High-Throughput Digital Image Analysis Reveals Distinct Patterns of Dystrophin Expression in Dystrophinopathy Patients. *J Neuropathol Exp Neurol*.

412. Danckaert A, Trignol A, Le Loher G, et al. (2023) MuscleJ2: a rebuilding of MuscleJ with new features for high-content analysis of skeletal muscle immunofluorescence slides. *Skelet Muscle* 13: 1–14.

413. Keire P, Shearer A, Shefer G, et al. (2013) Isolation and Culture of Skeletal Muscle Myofibers as a Means to Analyze Satellite Cells. *Methods Mol Biol* 946: 431.

414. Wu X, Hammer JA (2021) ZEISS Airyscan: Optimizing usage for fast, gentle, super-resolution imaging. *Methods Mol Biol* 2304: 111.

415. Van Der Walt S, Schönberger JL, Nunez-Iglesias J, et al. (2014) scikit-image: image processing in Python. *PeerJ* 2.

416. Biressi S, Filareto A, Rando TA (2020) Stem cell therapy for muscular dystrophies. *J Clin Invest* 130: 5652–5664.

417. Kinoshita I, Vilquin JT, Asselin I, et al. (1998) Transplantation of myoblasts from a transgenic mouse overexpressing dystrophin produced only a relatively small increase of dystrophin-positive membrane. *Muscle Nerve 1998 Jan* 91–103.

418. Arahata K, Ishihara T, Kamakura K, et al. (1989) Mosaic expression of dystrophin in symptomatic carriers of Duchenne's muscular dystrophy. *N Engl J Med* 320: 138–142.

419. Zubrzycka-Gaarn EE, Bulman DE, Ray PN, et al. (1990) Age-Related Conversion of Dystrophin-Negative to -Positive Fiber Segments of Skeletal but not Cardiac Muscle Fibers in Heterozygote mdx Mice. *J Neuropathol Exp Neurol* 49: 96–105.

420. Poukalov KK, Valero MC, Muscato DR, et al. (2023) Myospreader improves gene editing in skeletal muscle by myonuclear propagation. *bioRxiv* 2023.11.06.565807.

421. Newlands S, Levitt LK, Robinson CS, et al. (1998) Transcription occurs in pulses in muscle fibers. *Genes Dev* 12: 2748–2758.

422. Kim M, Franke V, Brandt B, et al. (2020) Single-nucleus transcriptomics reveals functional compartmentalization in syncytial skeletal muscle cells. *Nature Communications 2020 11:1* 11: 1–14.

423. Petrany MJ, Swoboda CO, Sun C, et al. (2020) Single-nucleus RNA-seq identifies transcriptional heterogeneity in multinucleated skeletal myofibers. *Nature Communications 2020 11:1* 11: 1–12.

424. Choi HMT, Schwarzkopf M, Fornace ME, et al. (2018) Third-generation in situ hybridization chain reaction: Multiplexed, quantitative, sensitive, versatile, robust. *Development (Cambridge)* 145.

425. Dupont JB, Tournaire B, Georger C, et al. (2015) Short-lived recombinant adeno-associated virus transgene expression in dystrophic muscle is associated with oxidative damage to transgene mRNA. *Mol Ther Methods Clin Dev* 2: 15010.

426. Wenger SL, Steele MW, Hoffman EP, et al. (1992) X inactivation and dystrophin studies in a t(X;12) female: Evidence for biochemical normalization in Duchenne muscular dystrophy carriers. *Am J Med Genet* 43: 1012–1015.

427. Narita S, Yorifuji H (1999) Centrally nucleated fibers (CNFs) compensate the fragility of myofibers in mdx mouse. *Neuroreport* 10: 3233–3235.

428. Duddy W, Duguez S, Johnston H, et al. (2015) Muscular dystrophy in the mdx mouse is a severe myopathy compounded by hypotrophy, hypertrophy and hyperplasia. *Skelet Muscle* 5.

429. Mizuno Y, Nonaka I, Hirai S, et al. (1993) Reciprocal expression of dystrophin and utrophin in muscles of Duchenne muscular dystrophy patients, female DMD-carriers and control subjects. *J Neurol Sci* 119: 43–52.

430. Hildyard JCW, Rawson F, Wells DJ, et al. (2020) Multiplex in situ hybridization within a single transcript: RNAscope reveals dystrophin mRNA dynamics. *PLoS One* 15: e0239467.

431. Kann AP, Krauss RS (2019) Multiplexed RNAscope and immunofluorescence on whole-mount skeletal myofibers and their associated stem cells. *Development (Cambridge)* 146.

432. Hall ZW, Ralston E (1989) Nuclear domains in muscle cells. *Cell* 59: 771–772.

433. Masschelein E, D'Hulst G, Zvick J, et al. (2020) Exercise promotes satellite cell contribution to myofibers in a load-dependent manner. *Skelet Muscle* 10: 1–15.

434. Taylor-Weiner H, Grigsby CL, Ferreira DMS, et al. (2020) Modeling the transport of nuclear proteins along single skeletal muscle cells Hermes, National Academy of Sciences.

435. Blaveri K, Heslop L, Yu DS, et al. (1999) Patterns of Repair of Dystrophic Mouse Muscle: Studies on Isolated Fibers. *Dev Dyn* 216: 244–256.

436. Verhaart IEC, Van Vliet-Van Den Dool L, Sipkens JA, et al. (2014) The Dynamics of Compound, Transcript, and Protein Effects After Treatment With 2OMePS Antisense Oligonucleotides in mdx Mice. *Mol Ther Nucleic Acids* 3: e148.

437. Elbrink J, Malhotra SK, Elleker MG (1987) Duchenne muscular dystrophy: pathogenesis and pharmacology. *Trends Pharmacol Sci* 8: 109–113.

438. Bischoff R (1994) The satellite cell and muscle regeneration. *Myology : basic and clinical*.

439. Khalifa AA, Ali MA, Elsokkary NH, et al. (2023) Mitochondrial modulation of amplified preconditioning influences of remote ischemia plus erythropoietin against skeletal muscle ischemia/reperfusion injury in rats. *Life Sci* 329: 121979.

440. Fridén J, Lieber RL (1998) Segmental muscle fiber lesions after repetitive eccentric contractions. *Cell Tissue Res* 293: 165–171.

441. Stirling S, George G (1989) Segmental Necrosis and its Demarcation in Experimental Micropuncture Injury of Skeletal Muscle Fibers. *J Neuropathol Exp Neurol* 48: 154–170.

442. Äärimaa V, Kääriäinen M, Vaittinen S, et al. (2004) Restoration of myofiber continuity after transection injury in the rat soleus. *Neuromuscular Disorders* 14: 421–428.

443. Robertson TA, Papadimitriou JM, Grounds MD (1993) Fusion of myogenic cells to the newly sealed region of damaged myofibres in skeletal muscle regeneration. *Neuropathol Appl Neurobiol* 19: 350–358.

444. Roth D, Oron U (1985) Repair mechanisms involved in muscle regeneration following partial excision of the rat gastrocnemius muscle. *Exp Cell Biol* 53: 107–114.

445. Schmalbruch H (1984) Regenerated muscle fibers in duchenne muscular dystrophy: A serial section study. *Neurology* 34: 60–65.

446. Trifunov S, Natera-de Benito D, Exposito Escudero JM, et al. (2020) Longitudinal Study of Three microRNAs in Duchenne Muscular Dystrophy and Becker Muscular Dystrophy. *Front Neurol* 11: 530097.

447. Blau HM, Cosgrove BD, Ho ATV (2015) The central role of muscle stem cells in regenerative failure with aging. *Nat Med* 21: 854.

448. Tomé FMS, Matsumura K, Chevallay M, et al. (1994) Expression of dystrophin-associated glycoproteins during human fetal muscle development: a preliminary immunocytochemical study. *Neuromuscul Disord* 4: 343–348.

449. Sewry CA, Matsumura K, Campbell KP, et al. (1994) Expression of dystrophin-associated glycoproteins and utrophin in carriers of Duchenne muscular dystrophy. *Neuromuscular Disorders* 4: 401–409.

450. Sewry CA (2000) Immunocytochemical Analysis of Human Muscular Dystrophy. *Microsc Res Tech* 48: 142–154.

451. Taylor J, Muntoni F, Dubowitz V, et al. (1997) The abnormal expression of utrophin in Duchenne and Becker muscular dystrophy is age related. *Neuropathol Appl Neurobiol* 23: 399–405.

452. Dhanyasi N, VijayRaghavan K, Shilo BZ, et al. (2021) Microtubules provide guidance cues for myofibril and sarcomere assembly and growth. *Developmental Dynamics* 250: 60–73.

453. Khairallah RJ, Shi G, Sbrana F, et al. (2012) Microtubules underlie dysfunction in duchenne muscular dystrophy. *Sci Signal* 5.

454. Espigat-Georger A, Dyachuk V, Chemin C, et al. (2016) Nuclear alignment in myotubes requires centrosome proteins recruited by nesprin-1. *J Cell Sci* 129: 4227–4237.

455. Bruusgaard JC, Liestøl K, Ekmark M, et al. (2003) Number and spatial distribution of nuclei in the muscle fibres of normal mice studied in vivo. *J Physiol* 551: 467–478.

456. Meyer GA (2018) Evidence of induced muscle regeneration persists for years in the mouse. *Muscle Nerve* 58: 858.

457. Gartler SM, Goldman MA (2005) X-Chromosome Inactivation. *Encyclopedia of Life Sciences*.

458. Nance ME, Shi R, Hakim CH, et al. (2019) AAV9 Edits Muscle Stem Cells in Normal and Dystrophic Adult Mice. *Mol Ther* 27: 1568–1585.

459. Kwon JB, Ettyreddy AR, Vankara A, et al. (2020) In Vivo Gene Editing of Muscle Stem Cells with Adeno-Associated Viral Vectors in a Mouse Model of Duchenne Muscular Dystrophy. *Mol Ther Methods Clin Dev* 19: 320.

460. Arnett AL, Konieczny P, Ramos JN, et al. (2014) Adeno-associated viral vectors do not efficiently target muscle satellite cells. *Mol Ther Methods Clin Dev* 1: 14038.

461. Buckley KH, Nestor-Kalinoski AL, Pizza FX (2022) Positional Context of Myonuclear Transcription During Injury-Induced Muscle Regeneration. *Front Physiol* 13.

462. Jockusch H, Voigt S (2003) Migration of adult myogenic precursor cells as revealed by GFP/nLacZ labelling of mouse transplantation chimeras. *J Cell Sci* 116: 1611–1616.

463. Watt DJ, Morgan JE, Clifford MA, et al. (1987) The movement of muscle precursor cells between adjacent regenerating muscles in the mouse. *Anat Embryol (Berl)* 175: 527–536.

464. Hughes SM, Blau HM (1990) Migration of myoblasts across basal lamina during skeletal muscle development. *Nature* 345: 350–353.

465. Karpati G, Ajdukovic D, Arnold D, et al. (1993) Myoblast transfer in duchenne muscular dystrophy. *Ann Neurol* 34: 8–17.

466. Schultz E, Jaryszak DL, Valliere CR (1985) Response of satellite cells to focal skeletal muscle injury. *Muscle Nerve* 8: 217–222.

467. Novak JS, Hogarth MW, Boehler JF, et al. (2017) Myoblasts and macrophages are required for therapeutic morpholino antisense oligonucleotide delivery to dystrophic muscle. *Nat Commun* 8.

468. Cohen SA, Bar-Am O, Fuoco C, et al. (2022) In vivo restoration of dystrophin expression in mdx mice using intra-muscular and intra-arterial injections of hydrogel microsphere carriers of exon skipping antisense oligonucleotides. *Cell Death Dis* 13.

469. Liu M, Yue Y, Harper SQ, et al. (2005) Adeno-Associated virus-mediated microdystrophin expression protects young mdx muscle from contraction-induced injury. *Molecular Therapy* 11: 245–256.

470. Egorova T V., Polikarpova A V., Vassilieva SG, et al. (2023) CRISPR-Cas9 correction in the DMD mouse model is accompanied by upregulation of Dp71f protein. *Mol Ther Methods Clin Dev* 30: 161–180.

471. Mora M, Morandi L, Merlini L, et al. (1994) Fetus-like dystrophin expression and other cytoskeletal protein abnormalities in centronuclear myopathies. *Muscle Nerve* 17: 1176–1184.

472. Gómez-oca R, Cowling BS, Laporte J (2021) Common Pathogenic Mechanisms in Centronuclear and Myotubular Myopathies and Latest Treatment Advances. *Int J Mol Sci* 22.

473. Buj-Bello A, Laugel V, Messaddeq N, et al. (2002) The lipid phosphatase myotubularin is essential for skeletal muscle maintenance but not for myogenesis in mice. *Proc Natl Acad Sci U S A* 99: 15060.

474. Dennis CL, Tinsley JM, Deconinck AE, et al. (1996) Molecular and functional analysis of the utrophin promoter. *Nucleic Acids Res* 24: 1646.

475. Basu U, Lozynska O, Moorwood C, et al. (2011) Translational Regulation of Utrophin by miRNAs. *PLoS One* 6.

476. Wessels A, Ginjaar IB, Moorman AFM, et al. (1991) Different localization of dystrophin in developing and adult human skeletal muscle. *Muscle Nerve* 14: 1–7.

477. Ginjaar IB, Bakker E, Dunnen JTD, et al. (1989) IMMUNOLOGICAL STUDY OF DYSTROPHIN IN DUCHENNE FETUS. *The Lancet* 334: 1212–1213.

478. Houzelstein D, Lyons GE, Chamberlain J, et al. (1992) Localization of dystrophin gene transcripts during mouse embryogenesis. *J Cell Biol* 119: 811.

479. Fanin M, Pegoraro E, Angelini C (1994) Absence of dystrophin and spectrin in regenerating muscle fibers from Becker dystrophy patients. *J Neurol Sci* 123: 88–94.

480. Yoshimoto Y, Ikemoto-Uezumi M, Hitachi K, et al. (2020) Methods for Accurate Assessment of Myofiber Maturity During Skeletal Muscle Regeneration. *Front Cell Dev Biol* 8: 267.

481. Cacchiarelli D, Incitti T, Martone J, et al. (2011) miR-31 modulates dystrophin expression: new implications for Duchenne muscular dystrophy therapy. *EMBO Rep* 12: 136.

482. Crist CG, Montarras D, Buckingham M (2012) Muscle Satellite Cells Are Primed for Myogenesis but Maintain Quiescence with Sequestration of Myf5 mRNA Targeted by microRNA-31 in mRNP Granules. *Cell Stem Cell* 11: 118–126.

483. Straub V, Mercuri E (2018) Report on the workshop: Meaningful outcome measures for Duchenne muscular dystrophy, London, UK, 30-31 January 2017. *Neuromuscul Disord* 28: 690–701.

484. Anthony K, Arechavala-Gomeza V, Taylor LE, et al. (2014) Dystrophin quantification: Biological and translational research implications. *Neurology* 83: 2062.

485. Servais L, Camino E, Clement A, et al. (2021) First Regulatory Qualification of a Novel Digital Endpoint in Duchenne Muscular Dystrophy: A Multi-Stakeholder Perspective on the Impact for Patients and for Drug Development in Neuromuscular Diseases. *Digit Biomark* 5: 183.

486. Aartsma-Rus A, Morgan J, Lonkar P, et al. (2019) Report of a TREAT-NMD/World Duchenne Organisation Meeting on Dystrophin Quantification Methodology. *J Neuromuscul Dis* 6: 147.

487. Wells DJ (2019) What is the level of dystrophin expression required for effective therapy of Duchenne muscular dystrophy? *Journal of Muscle Research and Cell Motility 2019 40:2* 40: 141–150.

488. Ikeda S, He A, Kong SW, et al. (2009) MicroRNA-1 negatively regulates expression of the hypertrophy-associated calmodulin and Mef2a genes. *Mol Cell Biol* 29: 2193–2204.

489. Chen C, Ridzon DA, Broomer AJ, et al. (2005) Real-time quantification of microRNAs by stem–loop RT–PCR. *Nucleic Acids Res* 33: e179.

490. Koutsoulidou A, Kyriakides TC, Papadimas GK, et al. (2015) Elevated Muscle-Specific miRNAs in Serum of Myotonic Dystrophy Patients Relate to Muscle Disease Progress. *PLoS One* 10.

491. Perfetti A, Greco S, Bugiardini E, et al. (2014) Plasma microRNAs as biomarkers for myotonic dystrophy type 1. *Neuromuscul Disord* 24: 509–515.

492. Frédérick PM, Simard MJ (2022) Regulation and different functions of the animal microRNA-induced silencing complex. *Wiley Interdiscip Rev RNA* 13: e1701.

493. Bartel DP (2004) MicroRNAs: Genomics, Biogenesis, Mechanism, and Function. *Cell* 116: 281–297.

494. Naeli P, Winter T, Hackett AP, et al. (2023) The intricate balance between microRNA-induced mRNA decay and translational repression. *FEBS J* 290: 2508–2524.

495. O'Brien J, Hayder H, Zayed Y, et al. (2018) Overview of microRNA biogenesis, mechanisms of actions, and circulation. *Front Endocrinol (Lausanne)* 9: 388354.

496. Holding C (2005) RNAi active in the nucleus? *Genome Biol* 6: 1–3.

497. Liao JY, Ma LM, Guo YH, et al. (2010) Deep sequencing of human nuclear and cytoplasmic small RNAs reveals an unexpectedly complex subcellular distribution of miRNAs and tRNA 3' trailers. *PLoS One* 5.

498. Gagnon KT, Li L, Chu Y, et al. (2014) RNAi Factors are Present and Active in Human Cell Nuclei. *Cell Rep* 6: 211.

499. Park CW, Zeng Y, Zhang X, et al. (2010) Mature microRNAs identified in highly purified nuclei from HCT116 colon cancer cells. *RNA Biol* 7: 606–614.

500. Khudayberdiev SA, Zampa F, Rajman M, et al. (2013) A comprehensive characterization of the nuclear microRNA repertoire of post-mitotic neurons. *Front Mol Neurosci* 6.

501. Li H, Zhan J, Zhao Y, et al. (2020) Identification of ncRNA-Mediated Functions of Nucleus-Localized miR-320 in Cardiomyocytes. *Mol Ther Nucleic Acids* 19: 132–143.

502. CHU Y, YOKOTA S, LIU J, et al. (2021) Argonaute binding within human nuclear RNA and its impact on alternative splicing. *RNA* 27: 991–1003.

503. Turunen TA, Roberts TC, Laitinen P, et al. (2019) Changes in nuclear and cytoplasmic microRNA distribution in response to hypoxic stress. *Sci Rep* 9: 1–12.

504. Roberts TC (2014) The MicroRNA biology of the Mammalian nucleus. *Mol Ther Nucleic Acids* 3: e188.

505. Leung AKL (2015) The Whereabouts of microRNA Actions: Cytoplasm and Beyond. *Trends Cell Biol* 25: 601–610.

506. Catalanotto C, Cogoni C, Zardo G (2016) MicroRNA in Control of Gene Expression: An Overview of Nuclear Functions.

507. Huang V, Li LC (2012) miRNA goes nuclear. *RNA Biol* 9: 269.

508. Hu X, Yin G, Zhang Y, et al. (2023) Recent advances in the functional explorations of nuclear microRNAs. *Front Immunol* 14.

509. Hansen TB, Wiklund ED, Bramsen JB, et al. (2011) MiRNA-dependent gene silencing involving Ago2-mediated cleavage of a circular antisense RNA. *EMBO Journal* 30: 4414–4422.

510. Xiao M, Li J, Li W, et al. (2017) MicroRNAs activate gene transcription epigenetically as an enhancer trigger. *RNA Biol* 14: 1326–1334.

511. Guo H, Pu M, Tai Y, et al. (2020) Nuclear miR-30b-5p suppresses TFEB-mediated lysosomal biogenesis and autophagy. *Cell Death Differ* 28: 320–336.

512. Kim DH, Sætrom P, Snøve O, et al. (2008) MicroRNA-directed transcriptional gene silencing in mammalian cells. *Proc Natl Acad Sci U S A* 105: 16230–16235.

513. Kriegel AJ, Terhune SS, Greene AS, et al. (2018) Isomer-specific effect of microRNA miR-29b on nuclear morphology. *J Biol Chem* 293: 14080–14088.

514. Robb GB, Brown KM, Khurana J, et al. (2005) Specific and potent RNAi in the nucleus of human cells. *Nature Structural & Molecular Biology 2005 12:2* 12: 133–137.

515. Moon IY, Choi JH, Chung JW, et al. (2019) MicroRNA-20 induces methylation of hepatitis B virus covalently closed circular DNA in human hepatoma cells. *Mol Med Rep* 20: 2285–2293.

516. El Fatimy R, Zhang Y, Deforzh E, et al. (2022) A nuclear function for an oncogenic microRNA as a modulator of snRNA and splicing. *Mol Cancer* 21.

517. Santovito D, Egea V, Bidzhekov K, et al. (2020) Noncanonical inhibition of caspase-3 by a nuclear microRNA confers endothelial protection by autophagy in atherosclerosis. *Sci Transl Med* 12.

518. Tang R, Li L, Zhu D, et al. (2012) Mouse miRNA-709 directly regulates miRNA-15a/16-1 biogenesis at the posttranscriptional level in the nucleus: Evidence for a microRNA hierarchy system. *Cell Res* 22: 504–515.

519. Di Mauro V, Crasto S, Colombo FS, et al. (2019) Wnt signalling mediates miR-133a nuclear re-localization for the transcriptional control of Dnmt3b in cardiac cells. *Scientific Reports 2019 9:1* 9: 1–15.

520. Laitinen P, Väänänen MA, Kolari IL, et al. (2022) Nuclear microRNA-466c regulates Vegfa expression in response to hypoxia. *PLoS One* 17.

521. Li H, Fan J, Zhao Y, et al. (2019) Nuclear miR-320 Mediates Diabetes-Induced Cardiac Dysfunction by Activating Transcription of Fatty Acid Metabolic Genes to Cause Lipotoxicity in the Heart. *Circ Res* 125: 1106–1120.

522. Foldes-Papp Z, Konig K, Studier H, et al. (2009) Trafficking of mature miRNA-122 into the nucleus of live liver cells. *Curr Pharm Biotechnol* 10: 569–578.

523. Gambardella S, Rinaldi F, Lepore SM, et al. (2010) Overexpression of microRNA-206 in the skeletal muscle from myotonic dystrophy type 1 patients. *J Transl Med* 8.

524. Goldie BJ, Fitzsimmons C, Weidenhofer J, et al. (2017) miRNA Enriched in Human Neuroblast Nuclei Bind the MAZ Transcription Factor and Their Precursors Contain the MAZ Consensus Motif. *Front Mol Neurosci* 10.

525. Politz JCR, Zhang F, Pederson T (2006) MicroRNA-206 colocalizes with ribosome-rich regions in both the nucleolus and cytoplasm of rat myogenic cells. *Proc Natl Acad Sci U S A* 103: 18957–18962.

526. Katz S, Cussigh D, Urbán N, et al. (2016) A Nuclear Role for miR-9 and Argonaute Proteins in Balancing Quiescent and Activated Neural Stem Cell States. *Cell Rep* 17: 1383–1398.

527. Roya K, Jessica AH, Liande LI, et al. (2016) Stable association of RNAi machinery is conserved between the cytoplasm and nucleus of human cells. *RNA* 22: 1085–1098.

528. Atwood BL, Woolnough JL, Lefevre GM, et al. (2016) Human Argonaute 2 Is Tethered to Ribosomal RNA through MicroRNA Interactions. *J Biol Chem* 291: 17919–17928.

529. Janowski BA, Huffman KE, Schwartz JC, et al. (2006) Involvement of AGO1 and AGO2 in mammalian transcriptional silencing. *Nat Struct Mol Biol* 13: 787–792.

530. Woolnough JL, Atwood BL, Giles KE (2015) Argonaute 2 Binds Directly to tRNA Genes and Promotes Gene Repression in cis. *Mol Cell Biol* 35: 2278.

531. Johnson KC, Kilikevicius A, Hofman C, et al. (2023) Nuclear Localization of Argonaute is affected by Cell Density and May Relieve Repression by microRNAs. *bioRxiv*.

532. Sarshad AA, Juan AH, Muler AIC, et al. (2018) Argonaute-miRNA Complexes Silence Target mRNAs in the Nucleus of Mammalian Stem Cells. *Mol Cell* 71: 1040-1050.e8.

533. Benhamed M, Herbig U, Ye T, et al. (2012) Senescence is an Endogenous Trigger for microRNA-Directed Transcriptional Gene Silencing in Human Cells. *Nat Cell Biol* 14: 266.

534. Yaffe D, Saxel O (1977) Serial passaging and differentiation of myogenic cells isolated from dystrophic mouse muscle. *Nature 1977 270:5639* 270: 725–727.

535. Lawson MA, Purslow PP (2000) Differentiation of Myoblasts in Serum-Free Media: Effects of Modified Media Are Cell Line-Specific. *Cells Tissues Organs* 167: 130–137.

536. Feng Y, Niu L-L, Wei W, et al. (2013) A feedback circuit between miR-133 and the ERK1/2 pathway involving an exquisite mechanism for regulating myoblast proliferation and differentiation. *Cell Death & Disease 2013 4:11* 4: e934–e934.

537. Gagnon KT, Li L, Janowski BA, et al. (2014) Analysis of Nuclear RNA Interference (RNAi) in Human Cells by Subcellular Fractionation and Argonaute Loading. *Nat Protoc* 9: 2045.

538. Wani S, Cloonan N (2014) Profiling direct mRNA-microRNA interactions using synthetic biotinylated microRNA-duplexes. *bioRxiv* 005439.

539. Wilson MH, Coates CJ, George AL (2007) PiggyBac transposon-mediated gene transfer in human cells. *Mol Ther* 15: 139–145.

540. S S, C R (1996) Molecular diversity of myofibrillar proteins: gene regulation and functional significance. *Physiol Rev* 76: 371–423.

541. Siomi H, Dreyfuss G (1995) A nuclear localization domain in the hnRNP A1 protein. *J Cell Biol* 129: 551–560.

542. Rossi M, Bucci G, Rizzotto D, et al. (2019) LncRNA EPR controls epithelial proliferation by coordinating Cdkn1a transcription and mRNA decay response to TGF-β. *Nat Commun* 10.

543. Das AT, Tenenbaum L, Berkhout B (2016) Tet-On Systems For Doxycycline-inducible Gene Expression. *Curr Gene Ther* 16: 156.

544. Helwak A, Tollervey D (2014) Mapping the miRNA interactome by cross-linking ligation and sequencing of hybrids (CLASH). *Nat Protoc* 9: 711–728.

545. Lytle JR, Yario TA, Steitz JA (2007) Target mRNAs are repressed as efficiently by microRNA-binding sites in the 5’ UTR as in the 3’ UTR. *Proc Natl Acad Sci U S A* 104: 9667–9672.

546. Guo ZW, Xie C, Yang JR, et al. (2015) MtiBase: a database for decoding microRNA target sites located within CDS and 5′UTR regions from CLIP-Seq and expression profile datasets. *Database* 2015.

547. Paugh SW, Coss DR, Bao J, et al. (2016) MicroRNAs Form Triplexes with Double Stranded DNA at Sequence-Specific Binding Sites; a Eukaryotic Mechanism via which microRNAs Could Directly Alter Gene Expression. *PLoS Comput Biol* 12: 1004744.

548. Piriyapongsa J, Bootchai C, Ngamphiw C, et al. (2012) microPIR: An Integrated Database of MicroRNA Target Sites within Human Promoter Sequences. *PLoS One* 7.

549. Toms D, Pan B, Bai Y, et al. (2021) Small RNA sequencing reveals distinct nuclear microRNAs in pig granulosa cells during ovarian follicle growth. *J Ovarian Res* 14: 1–12.

550. Place RF, Li LC, Pookot D, et al. (2008) MicroRNA-373 induces expression of genes with complementary promoter sequences. *Proc Natl Acad Sci U S A* 105: 1608.

551. Zardo G, Ciolfi A, Vian L, et al. (2012) Polycombs and microRNA-223 regulate human granulopoiesis by transcriptional control of target gene expression. *Blood* 119: 4034–4046.

552. Zealy RW, Wrenn SP, Davila S, et al. (2017) microRNA-binding proteins: specificity and function. *Wiley Interdiscip Rev RNA* 8: e1414.

553. Naito M, Mori M, Inagawa M, et al. (2016) Dnmt3a Regulates Proliferation of Muscle Satellite Cells via p57Kip2. *PLoS Genet* 12: 1006167.

554. Megiorni F, Camero S, Ceccarelli S, et al. (2016) DNMT3B in vitro knocking-down is able to reverse embryonal rhabdomyosarcoma cell phenotype through inhibition of proliferation and induction of myogenic differentiation. *Oncotarget* 7: 79342.

555. Bai Y, Pan B, Zhan X, et al. (2021) Microrna 195-5p targets foxo3 promoter region to regulate its expression in granulosa cells. *Int J Mol Sci* 22.

556. Bernstein E, Kim SY, Carmell MA, et al. (2003) Dicer is essential for mouse development. *Nat Genet* 35: 215–217.

557. Morita S, Horii T, Kimura M, et al. (2007) One Argonaute family member, Eif2c2 (Ago2), is essential for development and appears not to be involved in DNA methylation. *Genomics* 89: 687–696.

558. O'Rourke JR, Georges SA, Seay HR, et al. (2007) Essential role for Dicer during skeletal muscle development. *Dev Biol* 311: 359–368.

559. Schraivogel D, Schindler SG, Danner J, et al. (2015) Importin-β facilitates nuclear import of human GW proteins and balances cytoplasmic gene silencing protein levels. *Nucleic Acids Res* 43: 7447–7461.

560. Wei Y, Li L, Wang D, et al. (2014) Importin 8 regulates the transport of mature microRNAs into the cell nucleus. *J Biol Chem* 289: 10270–10275.

561. Lu J, Wu T, Zhang B, et al. (2021) Types of nuclear localization signals and mechanisms of protein import into the nucleus. *Cell Communication and Signaling* 19: 1–10.

562. Hwang HW, Wentzel EA, Mendell JT (2007) A hexanucleotide element directs microRNA nuclear import. *Science (1979)* 315: 97–100.

563. Hayashizaki Y (2003) RIKEN mouse genome encyclopedia. *Mech Ageing Dev* 124: 93–102.

564. Dash S, Balasubramaniam M, Dash C, et al. (2018) Biotin-based Pulldown Assay to Validate mRNA Targets of Cellular miRNAs. *J Vis Exp* 2018: 57786.

565. Sarepta Therapeutics Announces Positive Data from Part B of MOMENTUM, a Phase 2 Study of SRP-5051 in Patients with Duchenne Muscular Dystrophy Amenable to Skipping Exon 51 | Sarepta Therapeutics, Inc. Available from: https://investorrelations.sarepta.com/news-releases/news-release-details/sarepta-therapeutics-announces-positive-data-part-b-momentum.

566. Larkindale J, Lonkar P, Goyal J, et al. (2023) P44 Phase 1 study of PGN-EDO51 demonstrates tolerability, delivery and high levels of exon skipping for treatment of Duchenne muscular dystrophy (DMD). *Neuromuscular Disorders* 33: S69.

567. Avidity Biosciences Reports Positive Data Demonstrating AOC 1044 Delivers Unprecedented Concentrations of PMO in Muscle Following a Single Dose in Healthy Volunteers from Phase 1/2 EXPLORE44™ Trial for Duchenne Muscular Dystrophy Available from: https://www.prnewswire.com/news-releases/avidity-biosciences-

reports-positive-data-demonstrating-aoc-1044-delivers-unprecedented-concentrations-of-pmo-in-muscle-following-a-single-dose-in-healthy-volunteers-from-phase-12-explore44-trial-for-duchenne-muscular-dystrophy-302013456.html.

568. Dyne Reports Positive Phase 1/2 Data for Duchenne Agent DYNE-251 Available from: https://www.neurologylive.com/view/dyne-reports-positive-phase-1-2-data-duchenne-agent-dyne-251.

569. Mendell JR, Shieh PB, McDonald CM, et al. (2023) Expression of SRP-9001 dystrophin and stabilization of motor function up to 2 years post-treatment with delandistrogene moxeparvovec gene therapy in individuals with Duchenne muscular dystrophy. *Front Cell Dev Biol* 11.

570. First Clinical Trial Results of Gene Therapy (GNT0004) for Duchenne Muscular Dystrophy presented at International Myology 2024 Congress Available from: https://www.genethon.com/first-clinical-trial-results-of-gene-therapy-gnt0004-for-duchenne-muscular-dystrophy-presented-at-international-myology-2024-congress/.

571. Larsen CA, Howard MT (2014) Conserved regions of the DMD 3' UTR regulate translation and mRNA abundance in cultured myotubes. *Neuromuscul Disord* 24: 693.

572. Fiorillo AA, Heier CR, Novak JS, et al. (2015) TNFα-induced microRNAs control dystrophin expression in Becker muscular dystrophy. *Cell Rep* 12: 1678.

573. Hildyard JCW, Piercy RJ (2023) When Size Really Matters: The Eccentricities of Dystrophin Transcription and the Hazards of Quantifying mRNA from Very Long Genes. *Biomedicines* 11: 2082.

574. Hoffman EP, Monaco AP, Feener CC, et al. (1987) Conservation of the Duchenne muscular dystrophy gene in mice and humans. *Science (1979)* 238: 347–350.

575. Brown KJ, Marathi R, Fiorillo AA, et al. (2013) Accurate Quantitation of Dystrophin Protein in Human Skeletal Muscle Using Mass Spectrometry. *J Bioanal Biomed* Suppl 7.

576. Spitali P, Van Den Bergen JC, Verhaart IEC, et al. (2013) DMD transcript imbalance determines dystrophin levels. *FASEB J* 27: 4909–4916.

577. Falzarano MS, Mietto M, Fortunato F, et al. (2023) mRNA in situ hybridization exhibits unbalanced nuclear/cytoplasmic dystrophin transcript repartition in Duchenne myogenic cells and skeletal muscle biopsies. *Scientific Reports 2023 13:1* 13: 1–13.

578. Kinder TB, Heier CR, Tully CB, et al. (2020) Muscle Weakness in Myositis: MicroRNA-Mediated Dystrophin Reduction in a Myositis Mouse Model and Human Muscle Biopsies. *Arthritis and Rheumatology* 72: 1170–1183.

579. Marchal GA, van Putten M, Verkerk AO, et al. (2021) Low human dystrophin levels prevent cardiac electrophysiological and structural remodelling in a Duchenne mouse model. *Sci Rep* 11: 9779.

580. Abdelmoez AM, Puig LS, Smith JAB, et al. (2020) Comparative profiling of skeletal muscle models reveals heterogeneity of transcriptome and metabolism. *Am J Physiol Cell Physiol* 318: C615–C626.

581. Hosseini V, Ahadian S, Ostrovidov S, et al. (2012) Engineered Contractile Skeletal Muscle Tissue on a Microgrooved Methacrylated Gelatin Substrate. *Tissue Eng Part A* 18: 2453.

582. Deshmukh AS, Murgia M, Nagaraj N, et al. (2015) Deep proteomics of mouse skeletal muscle enables quantitation of protein isoforms, metabolic pathways, and transcription factors. *Molecular and Cellular Proteomics* 14: 841–853.

583. Denes LT, Riley LA, Mijares JR, et al. (2019) Culturing C2C12 myotubes on micromolded gelatin hydrogels accelerates myotube maturation. *Skelet Muscle* 9: 1–10.

584. Jalal S, Dastidar S, Tedesco FS (2021) Advanced models of human skeletal muscle differentiation, development and disease: Three-dimensional cultures, organoids and beyond. *Curr Opin Cell Biol* 73: 92.

585. Maffioletti SM, Sarcar S, Henderson ABH, et al. (2018) Three-Dimensional Human iPSC-Derived Artificial Skeletal Muscles Model Muscular Dystrophies and Enable Multilineage Tissue Engineering. *Cell Rep* 23: 899–908.

586. Pinton L, Khedr M, Lionello VM, et al. (2023) 3D human induced pluripotent stem cell-derived bioengineered skeletal muscles for tissue, disease and therapy modeling. *Nat Protoc* 18: 1337–1376.

8 Appendix

8.1 Manuscripts accepted for publication

Chwalenia K, Oieni J, Zemła J, Lekka M, Ahlskog N, Coenen-Stass AML, McClorey G, Wood MJA, Lomonosova Y, Roberts TC. *Exon skipping induces uniform dystrophin rescue with dose-dependent restoration of serum miRNA biomarkers and muscle biophysical properties*. Mol Ther Nucleic Acids. 2022

Hanson B, Stenler S, Ahlskog N, Chwalenia K, Svrzikapa N, Coenen-Stass AML, Weinberg MS, Wood MJA, Roberts TC. *Non-uniform dystrophin re-expression after CRISPR-mediated exon excision in the dystrophin/utrophin double-knockout mouse model of DMD*. Mol Ther Nucleic Acids. 2022

8.2 Conferences attended

1. **European Muscle Conference,** 2-6th September 2023, Florence, Italy

   Poster: Chwalenia K., Oieni J., Hanson B, Lomonosova Y., Aartsma-Rus A., van Putten M., Kelly C., Wang E., Wood MJA., Roberts TC. *Myonuclear domain-dependent spatial restriction of the dystrophin and associated proteins in dystrophic myofibers.*

2. **Advances in Skeletal Muscle Biology Conference,** 15-17th March 2023, University of Florida, Gainesville, US

   Poster: Chwalenia K., Kelly C., Aartsma-Rus A., van Putten M., Wang E., Wood MJA., Roberts TC. *Single myofiber analysis in a novel mouse model that exhibits non-uniform dystrophin expression.*

3. **Oxford-Harrington Rare Disease Centre Symposium,** 13-15th September 2022, Pembroke College, Oxford, UK

   Poster: Chwalenia K., Oieni J., Hanson B, Lomonosova Y., Aartsma-Rus A., van Putten M., Kelly C., Wang E., Wood MJA., Roberts TC. *Effects of dystrophin distribution on therapies for Duchenne muscular dystrophy.*

4. **MDUK Oxford Neuromuscular Centre Annual Meeting,** 14th July 2022, Saïd Business School, Oxford, UK

   Poster: Chwalenia K., Oieni J., Hanson B, Lomonosova Y., Aartsma-Rus A., van Putten M., Kelly C., Wang E., Wood MJA., Roberts TC. *Effect of myonuclear domain structure on therapies for Duchenne muscular dystrophy.*